

# **Thermal Properties of Polymers and Hybrid Material Thin Films**

## **Dissertation**

zur Erlangung des akademischen Grades  
eines Doktors der Naturwissenschaften (Dr. rer. nat.)

in der Bayreuther Graduiertenschule  
für Mathematik und Naturwissenschaften (BayNat)  
der Universität Bayreuth

vorgelegt von

**Patrick Hummel**

geboren in Nürtingen

Bayreuth, 2020



Die vorliegende Arbeit wurde in der Zeit von Juni 2015 bis Februar 2019 in Bayreuth am Lehrstuhl Physikalische Chemie I unter Betreuung von Herrn Prof. Dr. Markus Retsch angefertigt.

Vollständiger Abdruck der von der Bayreuther Graduiertenschule für Mathematik und Naturwissenschaften (BayNAT) der Universität Bayreuth genehmigten Dissertation zur Erlangung des akademischen Grades eines Doktors der Naturwissenschaften (Dr. rer. nat.).

Dissertation eingereicht am: 11.05.2020

Zulassung durch das Leitungsgremium: 26.05.2020

Wissenschaftliches Kolloquium: 30.09.2020

Amtierender Direktor: Prof. Dr. Markus Lippitz

Prüfungsausschuss:

Prof. Dr. Markus Retsch	(Gutachter)
Prof. Dr. Andreas Greiner	(Gutachter)
Prof. Dr. Georg Papastavrou	(Vorsitz)
Prof. Dr. Birgit Weber	







# Contents

<b>List of publications</b>	<b>V</b>
<b>List of contributions</b>	<b>VI</b>
<b>List of abbreviations</b>	<b>VII</b>
<b>Summary</b>	<b>1</b>
<b>Zusammenfassung</b>	<b>3</b>
<b>1 Introduction</b>	<b>7</b>
<b>2 Theoretical overview</b>	<b>11</b>
2.1 Heat transfer . . . . .	11
2.1.1 Macroscopic Heat transfer . . . . .	11
2.1.2 Microscopic heat transfer . . . . .	13
2.1.3 Thermal transport in hybrid structures . . . . .	16
2.2 Photoacoustic method . . . . .	22
2.2.1 Solving the heat equation . . . . .	22
2.2.2 The photoacoustic signal . . . . .	26
2.2.3 The photoacoustic method to determine the thermal properties of a sample . . . . .	27
<b>3 Materials and Methods</b>	<b>31</b>
3.1 Materials . . . . .	31
3.1.1 Nanoparticles . . . . .	31
3.1.2 Polymer synthesis . . . . .	34
3.1.3 Nanocomposites . . . . .	40
3.1.4 Sample preparation for PA measurements . . . . .	44

3.2	Methods . . . . .	44
3.2.1	Photoacoustic method . . . . .	44
3.2.2	Further methods . . . . .	47
<b>4</b>	<b>References</b>	<b>55</b>
<b>5</b>	<b>Thesis overview</b>	<b>63</b>
5.1	Synopsis . . . . .	63
5.2	Individual contributions to joint publications . . . . .	77
<b>6</b>	<b>Simple and High Yield Synthesis of Metal-Polymer Nanocomposites: The Role of Theta-Centrifugation as an Essential Purification Step</b>	<b>81</b>
6.1	Introduction . . . . .	82
6.2	Materials and Methods . . . . .	83
6.2.1	Materials . . . . .	83
6.2.2	RAFT synthesis . . . . .	83
6.2.3	Nanoparticle synthesis . . . . .	84
6.2.4	Ligand exchange . . . . .	85
6.2.5	Characterization . . . . .	85
6.3	Results and Discussion . . . . .	87
6.4	Conclusion . . . . .	96
<b>7</b>	<b>Well-defined metal-polymer nanocomposites: The interplay of structure, thermoplasmonics, and elastic mechanical properties</b>	<b>101</b>
7.1	Introduction . . . . .	103
7.2	Experimental . . . . .	105
7.2.1	Materials . . . . .	105
7.2.2	Film preparation and characterization . . . . .	105
7.2.3	Optical spectroscopy . . . . .	105
7.2.4	Transmission electron microscopy . . . . .	106
7.2.5	Electron tomography . . . . .	106
7.2.6	Small-Angle-X-ray Scattering . . . . .	106

7.2.7	Brillouin light scattering spectroscopy <sup>[Alonso-Redondo2015]</sup> . . .	106
7.2.8	Differential scanning calorimetry . . . . .	107
7.2.9	Thermographic measurements . . . . .	107
7.3	Results and Discussion . . . . .	108
7.3.1	Materials . . . . .	108
7.3.2	Structural changes induced by thermal annealing . . . . .	115
7.4	Conclusion . . . . .	118
7.5	Supporting Information . . . . .	120
7.5.1	Annealing procedure . . . . .	120
7.5.2	Video TEM tilt series . . . . .	120
7.5.3	SAXS characterization . . . . .	120
7.5.4	Effective medium analysis . . . . .	123
7.5.5	Glass Transition . . . . .	125
7.5.6	Absorption coefficients . . . . .	127
7.5.7	Annealing effects . . . . .	133
7.5.8	Collective heating effect . . . . .	134
7.6	Appendix . . . . .	137
7.6.1	Thermal conductivity of one-component nanocomposites . .	137

**8 Anisotropic thermal transport in spray coated single-phase 2D materials: synthetic clay vs. graphene oxide 145**

8.1	Introduction . . . . .	146
8.2	Results and Discussion . . . . .	147
8.3	Conclusion . . . . .	153
8.4	Materials and Methods . . . . .	154
8.4.1	Sample preparation and characterization . . . . .	154
8.4.2	Thermal conductivity measurements . . . . .	155
8.5	Supporting Information . . . . .	157
8.5.1	Sample preparation and characterization . . . . .	157
8.5.2	Thermal measurements . . . . .	163

<b>9 Tunable thermoelastic anisotropy in hybrid Bragg stacks with extreme polymer confinement</b>	<b>173</b>
9.1 Introduction . . . . .	174
9.2 Results and Discussion . . . . .	176
9.3 Conclusion . . . . .	186
9.4 Experimental Section . . . . .	187
9.5 Supporting Information . . . . .	190
9.5.1 Sample preparation . . . . .	190
9.5.2 Thermal measurements . . . . .	194
9.5.3 Brillouin light spectroscopy . . . . .	199
9.5.4 Evaluation of interfacial thermal conductance . . . . .	205
9.5.5 Uncertainty analysis . . . . .	207
<b>10 Thermal Transport in Ampholytic Polymers: The Role of Hydrogen Bonding and Water Uptake</b>	<b>213</b>
10.1 Introduction . . . . .	214
10.2 Materials and Methods . . . . .	216
10.3 Results and Discussion . . . . .	220
10.4 Conclusions . . . . .	227
10.5 Supporting information . . . . .	231
10.5.1 Thermal conductivity measurements . . . . .	231
10.5.2 IR Spectroscopy of dry samples . . . . .	231
10.5.3 Humidity dependent IR spectra . . . . .	238
10.5.4 DSC measurements . . . . .	239
10.5.5 Polymer / water effective medium model (EMT) . . . . .	240
10.5.6 Transducer layer . . . . .	241
<b>11 Conclusion and Outlook</b>	<b>245</b>
<b>Danksagung</b>	<b>247</b>
<b>Eidesstattliche Versicherungen und Erklärungen</b>	<b>249</b>

## List of publications

1. Simple and High Yield Synthesis of Metal-Polymer Nanocomposites: The Role of Theta-Centrifugation as an Essential Purification Step

P. Hummel, A. Lerch, S. M. Goller, M. Karg, M. Retsch, *Polymers* **2017**, 9, 659.

2. Well-defined metal-polymer nanocomposites: The interplay of structure, thermoplasmonics, and elastic mechanical properties

D. Saleta Reig, P. Hummel, Z. Wang, S. Rosenfeldt, B. Graczykowski, M. Retsch, G. Fytas, *Physical Review Materials* **2018**, 2, 123605. (Editors' Suggestion)

3. Anisotropic thermal transport in spray-coated single-phase 2D materials: synthetic clay vs. graphene oxide

A. Philipp<sup>§</sup>, P. Hummel<sup>§</sup>, T. Schilling, P. Feicht, S. Rosenfeldt, M. Ertl, M. Schöttle, A. M. Lechner, Z. Xu, C. Gao, J. Breu, M. Retsch, *ACS Appl Mater Interfaces*, **2020**, 12, 18785-18791.

<sup>§</sup>Authors contributed equally to the work

4. Tunable thermoelastic anisotropy in hybrid Bragg stacks with extreme polymer confinement

Z. Wang, K. Rolle<sup>§</sup>, T. Schilling<sup>§</sup>, P. Hummel<sup>§</sup>, A. Philipp<sup>§</sup>, B. A. F. Kopera, A. Lechner, M. Retsch, J. Breu, G. Fytas, *Angew. Chem. Int. Ed.*, **2020**, 59, 1286-1294.

<sup>§</sup>Authors contributed equally to the work

5. Thermal Transport in Ampholytic Polymers: The Role of Hydrogen Bonding and Water Uptake

P. Hummel, A. M. Lechner, K. Herrmann, P. Biehl, C. Rössel, L. Wiedenhöft, F. H. Schacher, M. Retsch, *Macromolecules* **2020**, 53, 5528-5537.

## List of contributions

1. Poster Presentation: *Thermal transport in polymer nanocomposites*, Polymers: from Structure to Function, **2016**, Halle (Saale).
2. Poster Presentation: *One component silver-polystyrene nanocomposites: The interplay of thermoplasmonics and elastic mechanical properties*, Makromolekulares Kolloquium: Polymers and the Digital Age, **2019**, Freiburg im Breisgau.

## List of abbreviations

<b>AC</b>	alternating current
<b>AFM</b>	atomic force microscopy
<b>AgPS</b>	silver-polystyrene
<b>AOM</b>	acousto-optic modulator
<b>ATR</b>	attenuated total reflection
<b>ATRP</b>	atom transfer radical polymerization
<b>BLS</b>	Brillouin light scattering
<b>CNT</b>	carbon nanotubes
<b>CV</b>	coefficient of variation
<b>CPDTTC</b>	2-cyano-propyl dodecyl trithiocarbonate
<b>CTA</b>	chain transfer agent
<b>DC</b>	direct current
<b>DLS</b>	dynamic light scattering
<b>DMSO</b>	dimethyl sulfoxide
<b>DSC</b>	differential scanning calorimetry
<b>DTGA</b>	differential thermal gravimetric analysis
<b>EMA</b>	effective medium approximation
<b>EMT</b>	effective medium theory
<b>EOM</b>	electro-optic modulator
<b>FDTR</b>	frequency-domain thermoreflectance
<b>FEM</b>	finite element method
<b>FR</b>	free radical
<b>FSD</b>	Fourier self-deconvolution
<b>FWHM</b>	full width at half maximum

<b>GO</b>	graphene oxide
<b>hBN</b>	hexagonal boron nitride
<b>H-bond</b>	hydrogen bond
<b>HOMO</b>	highest occupied molecular orbital
<b>IPD</b>	interparticle distance
<b>IR</b>	infrared
<b>LIT</b>	lock-in thermography
<b>LSPR</b>	localized surface plasmon resonance
<b>LUMO</b>	lowest unoccupied molecular orbital
<b>MFP</b>	mean free path
<b>MMA</b>	methyl methacrylate
<b>MWCNT</b>	multi-walled carbon nanotubes
<b>MWD</b>	molecular weight distribution
<b>NMR</b>	nuclear magnetic resonance
<b>NP</b>	nanoparticle
<b>PA</b>	photoacoustic
<b>PAA</b>	poly(acrylic acid)
<b>PAGA</b>	poly(2-acrylamido glycolic acid)
<b>PCM</b>	phase change material
<b>PDha</b>	polydehydroalanine
<b>PDI</b>	polydispersity index
<b>PET</b>	polyethylene terephthalate
<b>PImAA</b>	poly(2-(imidazol-1-yl)acrylic acid)
<b>PMeImAA</b>	poly(2-(methyl imidazolium-1-yl)acrylic acid)
<b>PMMA</b>	poly(methyl methacrylate)

<b>PNC</b>	polymer nanocomposite
<b>PS</b>	polystyrene
<b>PVP</b>	polyvinylpyrrolidone
<b>RAFT</b>	reversible addition-fragmentation chain transfer
<b>rcf</b>	relative centrifugal force
<b>ROMP</b>	ring-opening metathesis polymerization
<b>SAXS</b>	small-angle X-ray scattering
<b>SAM</b>	self-assembled monolayer
<b>SEC</b>	size exclusion chromatography
<b>SEM</b>	scanning electron microscopy
<b>SERS</b>	surface-enhanced Raman scattering
<b>SRM</b>	series resistance model
<b>SWCNT</b>	single-wall carbon nanotubes
<b>TDTR</b>	time-domain thermoreflectance
<b>TEM</b>	transmission electron microscopy
<b>T<sub>g</sub></b>	glass transition temperature
<b>TGA</b>	thermal gravimetric analysis
<b>THF</b>	tetrahydrofuran
<b>TIM</b>	thermal interface material
<b>UV/Vis</b>	ultraviolet and visible light
<b>XFA</b>	xenon flash analysis
<b>XRD</b>	X-ray diffraction



## Summary

The technological progress of electronic devices is still enormous. Modern electronic devices already reached nanometer dimensions. Simultaneously, the computing power of these devices increases. This development implies enhancing power and heat densities. The cooling of these nanostructured devices is a challenging task of great interest. A fundamental understanding of heat transport on the nanoscale is necessary for optimizing thermal management. For a better understanding of thermal transport on the nanoscale, systematic investigations of structure-property relationships are required. For this purpose, model systems with precise structural and chemical control are essential.

However, such nanostructured materials usually provide only small sample geometries. The small dimensions make thermal conductivity characterization quite challenging. For this work, a photoacoustic (PA) setup was implemented. With this method, it is possible to characterize thin films of a sample, which is supported by a substrate. Thus, small amounts of brittle samples that cannot be processed into free-standing films can be characterized. The capability of the PA method to determine the thermal properties of thin films was demonstrated by the investigation of three different polymer-based materials.

The first two materials present the class of polymer nanocomposites (PNCs). Due to the miscibility on the molecular level, these can be also referred to as hybrid materials. The investigated PNCs can be divided by their filler geometry. First, the most straightforward filler geometry is investigated. Spherical Ag nanoparticles (NPs) are functionalized by polystyrene (PS) brushes of different molecular weights. The steric repulsion allows the adjustment of the interparticle distance (IPD) from 2 nm to 16 nm in the resulting PNC material. The ligand exchange used for this purpose is designed to be flexible. Thus, also different material combinations are viable with the presented procedure. Additionally, a new purification method is introduced, the centrifugation at  $\theta$ -conditions of the ligand.

The AgPS PNCs were processed into thin films and characterized regarding optical, mechanical and thermal properties. The individual distribution of the Ag NPs preserves the localized surface plasmon resonance (LSPR). Therefore, a laser can be used to locally heat up the sample within the laser spot. The higher the Ag volume fraction, the more significant the thermoplasmonic effect. Also the mechanical properties, determined by Brillouin light scattering (BLS) measurements, and the thermal conductivity depend on the Ag ratio. However, thermal conductivity could not be predicted by effective medium models without an finite interfacial thermal conductance. Accordingly, our findings suggest, that interfaces have an impact on

thermal conductivity in this nanostructured material.

The second filler type is characterized by two-dimensional extensions. The in-plane dimensions of these sheets are in the micrometer regime, while their thickness in cross-plane direction is only a few nanometers. When such nanoplatelets are aligned in stacks, their properties are strongly anisotropic, hence, direction-dependent. In a first study, different sizes of graphene oxide (GO) and sodium fluorohectorite platelets were compared regarding their in-plane and cross-plane thermal conductivity. The anisotropy ratio of the synthetic clay was found to be higher, due to the significant higher in-plane thermal conductivity.

In a consecutive work, the sodium hectorite was processed into a layered hybrid material with perfect periodicity. The high anisotropy ratio could be further increased, by the enormous drop in cross-plane thermal conductivity. This drop is caused by the tremendous number of hard-soft interfaces in this direction. The measured cross-plane thermal conductivity of  $0.09 \text{ Wm}^{-1}\text{K}^{-1}$  is extremely low for a completely dense material. The low cross-plane thermal conductivity was observed for all hybrid samples, regardless of the individual basal spacing, which varied from 1.9 nm to 3.8 nm. Despite the extreme polymer confinement and the nanolaminate structure, the density, specific heat, and in-plane thermal conductivity can be described by a classical parallel mixing model.

The last material in this work handles the unique class of ampholytic polymers. The implementation of functional groups in a polymer can enhance interchain thermal transport. The investigated ampholytic polymers provide a hydrogen bond (H-bond) donor and acceptor group per repetition unit. The high amount of functional groups ensures a high density of intermolecular H-bonds. These bonds were characterized by infrared (IR) spectroscopy. The carbonyl stretching vibration around  $1700 \text{ cm}^{-1}$  was used to deduce the local H-bond environment. For a better resolution, Fourier self-deconvolution (FSD) was applied to this absorption peak. Within the ampholytic polymers, a correlation between the H-bond strength and thermal conductivity was observed.

In summary, the results of this thesis underline the impact of interfaces and surface chemistry in polymers and polymer-based hybrid materials on the thermal transport properties. In polymer hybrids, the organic-inorganic interfaces provide significant thermal resistance. In polymers, the bonding strength of interchain interactions can improve thermal transport. Because of the great industrial importance of polymer-based materials, the results of this work are of great interest in the future development of thermal management applications.

## Zusammenfassung

Der technologische Fortschritt im Bereich elektronischer Bauteile ist heute immer noch enorm. Die Entwicklung kleinerer Schaltkreise im Nanometerbereich, bei gleichzeitiger Verbesserung der Rechenleistung, sorgt für immer höhere Energiedichten in den Bauteilen. Die Folge ist eine stetig steigende lokale Wärmeentwicklung. Das Wärmemanagement in diesen nanostrukturierten Bauteilen stellt demnach eine besondere Herausforderung dar. Um diese Aufgabe bewältigen zu können, benötigt man ein grundlegendes Verständnis des Wärmetransports auf der Nanometerebene. Dieses Verständnis kann man durch systematische Untersuchungen von Struktur-Eigenschafts-Beziehungen aufbauen. Die Grundlage dafür bilden Modellsysteme Modellsysteme mit präziser Kontrolle der räumlichen und chemischen Struktur.

Nanostrukturierte Materialien sind jedoch meistens nur in kleinen Probengeometrien herstellbar. Die Bestimmung der Wärmeleitfähigkeit in solchen kleinen Proben ist sehr schwierig. Daher wurde in dieser Arbeit eine Messmethode aufgebaut, die auf dem photoakustischen Effekt basiert. Diese Methode erlaubt es dünne Filme auf einem Substrat zu charakterisieren. Auf diese Weise können selbst spröde Proben, die nicht als freistehende Filme hergestellt werden können, untersucht werden. Die Leistungsfähigkeit der photoakustischen Methode die thermischen Eigenschaften von dünnen Filmen zu bestimmen wurde anhand von drei verschiedenen polymerbasierten Materialien demonstriert.

Die ersten beiden Materialien gehören der Klasse der Polymernanokompositen (PNCs) an. Da die hier verwendeten Systeme eine Durchmischung auf molekularer Ebene aufweisen, ist auch von Hybridmaterialien die Rede. Die untersuchten PNCs können durch die Geometrie des Füllermaterials unterschieden werden. Im ersten Schritt wurde ein Material mit der einfachsten Füllergeometrie untersucht. Kugelförmige Silbernanopartikel (AgNP) wurden mit linearen, kurzkettigen Polystyrol (PS) Liganden mit unterschiedlichen Molekulargewichten funktionalisiert. Die sterische Abstoßung der entstehenden Polymerbürsten erlaubt, je nach Molekulargewicht, die Variation des Abstandes zwischen den Partikeln im entstehenden PNC. Der für die Funktionalisierung verwendete Ligandenaustausch ist sehr variabel und erlaubt darum die Übertragung des Konzepts auf verschiedenste Materialkombinationen. Darüberhinaus wurde eine neue Aufreinigungsmethode für die PNCs entwickelt, die Zentrifugation bei  $\theta$ -Bedingungen des Ligandes.

Dünne Filme der AgPS PNCs wurden hinsichtlich ihrer optischen, mechanischen und thermischen Eigenschaften untersucht. Die gleichmäßige Verteilung der Ag-NPs erhält die plasmonischen Eigenschaften, sodass das Material mit einem Laser lokal erhitzt werden kann. Je höher der Ag Anteil ist, desto größer der thermoplas-

monische Effekt. Ebenso hängen die mechanischen Eigenschaften, untersucht mit Brillouin Lichtstreuung (BLS), sowie die Wärmeleitfähigkeit vom Ag Anteil ab. Die Wärmeleitfähigkeit wurde mit einem Effektiv-Medium-Theorie Modell verglichen. Dabei zeigte sich, dass ein Modell ohne endliche Grenzflächen Wärmeleitfähigkeit die gemessene Wärmeleitfähigkeit überschätzt. Dementsprechend legen die Ergebnisse nahe, dass Grenzflächen eine Rolle beim Wärmetransport in nanostrukturierten Materialien spielen.

Neben den sphärische NP wurden als zweite Füllmaterialgeometrie zweidimensionale Plättchen untersucht. Die Ausdehnung in der Ebene ist dabei im Mikrometerbereich, während die Dicke nur einige Nanometer beträgt. Wenn solche Plättchen in Stapeln angeordnet werden, sind ihre Eigenschaften anisotrop, also richtungsabhängig. Zunächst wurden verschiedene Größen von Graphenoxid (GO) und Natriumhektorit Plättchen hinsichtlich ihrer Wärmeleitfähigkeit in der Ebene und senkrecht zur Ebene verglichen. Der Vergleich zeigte ein höheres Anisotropieverhältnis der synthetischen Tonmineralien. Der Hauptgrund lag bei der signifikant höheren Wärmeleitfähigkeit in der Ebene.

In der anschließenden Studie wurde aus dem Natriumhektorit und Polyvinylpyrrolidon (PVP) ein Schichtmaterial mit perfekter Periodizität hergestellt. Das Anisotropie-

verhältnis konnte durch die enorme Reduktion der Wärmeleitfähigkeit senkrecht zur Ebene weiter erhöht werden. Die Ursache dafür liegt in der großen Anzahl an hart-weich Grenzflächen senkrecht zu den Ebenen in diesem Material. Die Wärmeleitfähigkeit senkrecht zur Ebene beträgt ungefähr  $0.09 \text{ Wm}^{-1}\text{K}^{-1}$  und ist sehr niedrig für ein Material ohne Porosität. Unabhängig vom basalen Abstand konnte die niedrige Wärmeleitfähigkeit senkrecht zur Ebene für alle Proben des Hybridmaterials beobachtet werden. Trotz der extremen Einschränkung der Polymerketten zwischen den Schichtsilikaten konnten die Dichte, die spezifische Wärmekapazität und die Wärmeleitfähigkeit in der Ebene mit einem klassischen parallelen Mischungsmodell berechnet werden.

Abschließend wird in dieser Arbeit die einzigartige Materialklasse der ampholyten Polymere behandelt. Das Einbringen von funktionellen Gruppen kann den Wärmetransport zwischen den einzelnen Polymerketten erhöhen. Die untersuchten ampholyten Polymere besitzen sowohl Donor- als auch Akzeptor-Gruppen für Wasserstoffbrücken innerhalb jeder Wiederholeinheit. Die hohe Dichte an funktionellen Gruppen stellt eine hohe Dichte an intermolekularen Wasserstoffbrücken sicher. Die Wasserstoffbrücken wurden mittels Infrarotspektroskopie charakterisiert. Im speziellen wurde die Carbonyl Streckschwingung bei ungefähr  $1700 \text{ cm}^{-1}$  dazu verwendet. Um eine bessere Auflösung dieser Bande zu erhalten, wurde die Fourier

Selbstentfaltung (FSD) angewandt. Innerhalb der ampholyten Polymere konnte eine Korrelation zwischen der Stärke der Wasserstoffbrückenbindung und der Wärmeleitfähigkeit festgestellt werden.

Zusammengefasst zeigen die Ergebnisse dieser Arbeit den Einfluss von Grenzflächen und Oberflächenchemie auf den Wärmetransport in Polymeren und polymerbasierten Hybridmaterialien. In letzterer Gruppe stellen die Grenzflächen zwischen harten und weichen Materialien einen signifikanten thermischen Widerstand dar. In Polymeren kann die Bindungsstärke von intermolekularen Wechselwirkungen den Wärmetransport begünstigen. Wegen des großen industriellen Interesses an polymerbasierten Materialien sind diese Ergebnisse von großer Bedeutung für die zukünftige Entwicklung von Anwendungen für das Wärmemanagement.



# 1 Introduction

When the first computers were invented, they filled whole rooms. Since then, the dimensions of electronic devices were drastically reduced. Today, we face powerful computers everywhere in our daily life. It was Gordon E. Moore, who first found the linear correlation of the number of components per integrated circuit over time.<sup>[1]</sup> According to the so-called Moore's law, the number of transistors in integrated circuits doubles about every second year.<sup>[2]</sup> Due to this development, devices become faster, cheaper, and more powerful. At the same time, the dimensions of devices decreased permanently. Today, modern electronics work with dimensions in the nanometer regime. As an effect, the energy density, and consequently, the heat density drastically enhanced.<sup>[3]</sup> The high power density and the non-uniform power dissipation in modern chips can lead to hot spots. At these spots, the local temperatures are significantly higher than the average device temperature.<sup>[4]</sup> Therefore, thermal management is an essential factor in preventing a reduction in performance or even the destruction of the device.

One goal of thermal management is to ensure a sufficient heat flux to prevent overheating. For this reason, a high thermal conductivity between the heat source and the heat sink is essential. Additionally, it is necessary to minimize the contact resistance to the heat sink, which is usually achieved by thermal interface materials (TIMs).<sup>[5]</sup> In other scenarios, thermal management can also refer to very low thermal conductivities, like in isolation materials or thermoelectric devices.<sup>[2]</sup> Moreover, thermal conductivity is a crucial property in materials where the primary goal is non-thermal. Examples are phase change materials (PCMs)<sup>[6,7]</sup>, heat-assisted magnetic recording<sup>[8,9]</sup>, and nanoscale (opto-)electronic devices.<sup>[10]</sup>

Due to their enormous variety, easy processability, and availability polymers are of great interest for new thermal management applications. Their lack of a high intrinsic thermal conductivity can be overcome by the addition of high conducting filler materials, or structural engineering. Here, nanoscale fillers offer novel possibilities for thermal management. Not only the filler content but rather the interface density<sup>[11,12]</sup> and surface chemistry<sup>[13]</sup> influence the composite properties. When it comes to structural engineering, besides the polymer design<sup>[14-17]</sup>, and the conformational structure<sup>[18]</sup>, polymer blends with interpenetrating networks of thermal pathways lead to promising results.<sup>[19]</sup>

Moreover, the low intrinsic thermal conductivity makes them a promising candidate for thermoelectric applications. Foaming polymers can even lower thermal conductivity. Polymer foams are state-of-the-art isolation materials.<sup>[20]</sup> They may also be seen as composites of polymer and air (or gas in general). The performance

can be further increased when lowering the dimensions. So the Knudsen effect takes place when the pores are smaller than the mean free path (MFP) of the heat-carrying phonons.<sup>[21]</sup> However, also solid polymer-based insulating materials are imaginable in nanolaminates with suitable interface density.<sup>[12]</sup>

Nevertheless, only a small number of studies exist. Further on, some studies did not use polymers but small organic molecules. These molecules are readily available and mostly better defined in comparison to polymers, where the molecular weight is usually distributed to some extent. In contrast, polymers show superior physical and mechanical properties and are, therefore, more relevant for applications.

An additional challenge is the determination of the thermal conductivity. Usually, the preparation of materials with a well-controlled nanostructure is coupled with enormous scientific effort. Hence, only small sample amounts are obtained. The characterization of such small samples is a demanding task. Thus, not only new materials have to be developed but also advanced measurement methods.

Although enormous progress was achieved in this field, most measurement techniques are complicated to set-up. For this reason, this thesis not only focuses on the investigation of different polymer and polymer-based hybrid materials but also on the implementation of the relatively simple photoacoustic (PA) method. With this method, the thermal conductivity of thin substrated films can be determined. Before the PA effect and the method are discussed in Chapter 2.2, first the principles of thermal transport in polymers and hybrid structures are introduced in Chapter 2.1.

In the following parts, the thesis presents various concepts to control the thermal conductivity of polymers and polymer-based hybrid materials. It begins with the description of the synthesis of a one-component PNC in Chapter 6. The characteristic of this material consisting of silver cores and polymer ligands is the adjustable interparticle distance (IPD). It is further characterized in Chapter 7, which ends with the investigation of the thermal conductivity of polymer nanocomposites (PNCs) with different IPDs.

The following part of the thesis focuses on two-dimensional filler materials in the form of platelets. Two types of fillers, namely graphene oxide (GO) and Hectorite are compared in Chapter 8. Furthermore, a hybrid material with exceptional low cross-plane and tremendous anisotropic thermal conductivity is presented in Chapter 9.

In Chapter 10, functional polymers are addressed. The investigated polymers have at least two functional moieties per repetition unit. The functional groups form hydrogen bonds (H-bonds) and the strength and the influence of these on the thermal conductivity is investigated. Furthermore, the effect of water absorption on the

Hydrogen-bonding and on the thermal conductivity were studied. The thesis closes with the conclusion and the outlook on future perspectives in the research field of thermal transport in polymers and polymer-based hybrid materials.



## 2 Theoretical overview

### 2.1 Heat transfer

#### 2.1.1 Macroscopic Heat transfer

Energy transfer due to a temperature gradient is called heat. According to the First Law of Thermodynamics, heat always flows from hot to cold. In general, three modes of heat transfer exist, namely heat conduction, convection, and radiation. These will be described in this section.

Heat conduction occurs through physical contact of two bodies, one with a higher and one with a lower temperature. This process takes place at the molecular level. In a gas or a liquid, for example, the average kinetic energy of molecules on the hot side of the temperature gradient is higher than of the molecules on the cold side. Due to the random collision of molecules, those with a higher energetic level transfer the energy to those with a lower level of energy. Hence, heat conduction takes place. In electrically conducting solids, the free electrons behave gas like and carry the heat. In comparison, the heat transfer in electrically nonconducting solids occurs by lattice waves caused by random atomic vibrations. These lattice waves also exist in electrical conductors, but the contribution is only small compared to the transfer by electrons.<sup>[22]</sup>

At the macroscopic level, the conduction of heat is described by Fourier's Law.<sup>[23]</sup>

$$q = -\kappa \cdot \frac{dT}{dx} \quad (2.1)$$

Equation 2.1 describes the one-dimensional heat flux,  $q$  ( $W/m^2$ ), i.e., the heat transfer rate per  $m^2$  in the direction of the temperature gradient. As already mentioned, the heat flow always occurs from hot to cold. Therefore,  $q$  is opposite in sign to  $\frac{dT}{dx}$ . The proportionality constant,  $\kappa$ , is the thermal conductivity and has the dimension  $W/mK$ . The more general, three-dimensional form of the Fourier's Law is written in Equation 2.2.<sup>[24]</sup>

$$\vec{q} = -\kappa \cdot \nabla T \quad (2.2)$$

By the combination of the Fourier's Law and the First Law of Thermodynamics, the one-dimensional heat conduction equation can be formed.<sup>[24]</sup>

$$\frac{\partial^2 T}{\partial x^2} = \frac{1}{\alpha} \frac{\partial T}{\partial t} \quad (2.3)$$

Here, the thermal diffusivity,  $\alpha$  ( $\text{m}^2/\text{s}$ ), is introduced. In comparison to  $\kappa$ , which is a measure of the energy transfer per unit time due to a steady-state temperature gradient,  $\alpha$  describes how fast the temperature distribution changes in a material. Both dimensions are connected through the density,  $\rho$ , and the specific heat capacity,  $c_p$ , by Equation 2.4.<sup>[24]</sup>

$$\kappa = \alpha \cdot \rho \cdot c_p \quad (2.4)$$

The one-dimensional heat conduction equation (Equation 2.3) is of great practical importance. By the elimination of the unknown heat transfer rate, a differential equation is obtained. Hence, it can be solved for the temperature distribution,  $T(x,t)$ , and is the basis of heat conduction theory.<sup>[24]</sup>

Convective heat transfer describes the heat exchange between a body and a fluid flowing past the body. It is divided into natural convection and forced convection. In the case of natural convection, the density difference caused by the temperature gradient induces the motion of the fluid. Forced convection, by contrast, occurs when the flow is induced by an external force, like a pump or a blower. Regardless of which of both cases takes place, heat is convected in form of internal energy. Hence, the heat transfer mechanism is technically still conduction. Nevertheless, the Newtons' law of cooling (Equation 2.5) describes the convective heat transfer from a body to a fluid.<sup>[22]</sup>

$$q = \bar{h} \cdot (T_{body} - T_{fluid}) \quad (2.5)$$

Here,  $T_{body}$  and  $T_{fluid}$  are the temperatures of the body and the fluid, respectively. The constant in this equation is the heat transfer coefficient,  $\bar{h}$  ( $\text{W}/\text{m}^2\text{K}$ ). The bar specifies that it is averaged over the surface of the body.<sup>[24]</sup>

The last general heat transfer mechanism is thermal radiation. Herein, the energy transfer occurs by electromagnetic radiation. Therefore, in comparison to the two former mechanisms, it does not need a medium for heat transfer. Thermal radiation is most efficient in a vacuum when conduction and convection are absent. Another factor influencing thermal radiation is the temperature. All bodies emit thermal radiation. However, often, it can be neglected compared to heat conduction and convection. Nevertheless, its intensity scales with the temperature to the power of four, and therefore, it becomes relevant at higher temperatures. The radiation

energy,  $e(T)$  ( $\text{W}/\text{m}^2$ ), is described by the Stefan-Boltzmann law in Equation 2.6.<sup>[22,24]</sup>

$$e_b(T) = \sigma \cdot T^4 \quad (2.6)$$

The Stefan-Boltzmann law, with  $\sigma$  as the Stefan-Boltzmann constant, assumes a perfect thermal radiator. Such radiators are called black bodies. A black body ideally absorbs all energy that reaches it. Indeed, most real systems do not behave like a black body. Therefore, the emissivity,  $\varepsilon$ , is introduced to characterize the ability of a surface to emit thermal radiation.<sup>[22,25]</sup>

$$e_b(T) = \varepsilon \cdot \sigma \cdot T^4 \quad (2.7)$$

### 2.1.2 Microscopic heat transfer

Within solids, thermal conduction is the dominant heat transfer mechanism. The microscale conduction mechanism depends on the material class. While in metals, electrons are the leading heat carriers, collective lattice vibrations dominate the energy transfer in dielectric materials and semiconductors. A quantum of this vibrational energy is called phonon.<sup>[22]</sup> Therefore, the energy of a phonon is an integer of  $h\nu$ , with  $h$  as the Planck's constant ( $6.626 \cdot 10^{-34}$  Js) and  $\nu$  as the frequency of the lattice vibration. Similar to photons, phonons can be treated as quasi-particles, hence the Debye equation (Equation 2.8) describes the thermal conductivity of a dielectric material.

$$\kappa = \frac{1}{3} \cdot c_v \cdot v_g \cdot \Lambda \quad (2.8)$$

Where  $c_v$  is the specific heat capacity at constant volume,  $v_g$  the average phonon group velocity, and  $\Lambda$  the average phonon MFP. Accordingly, heat transport by phonons can be imagined similar to thermal conduction in gases. Like the molecules in the gas, phonons also move around and exchange energy by colliding. The distance between consecutive collisions is the MFP. Since the lattice vibrations occur at different frequencies and directions, phonons also have a broad dispersion of frequencies, velocities, relaxation times, and, consequently, MFPs.<sup>[26]</sup>

The MFP not only depends on the elemental composition of a material. Different scattering mechanisms strongly influence the phonon MFP. These mechanisms are illustrated in Figure 2.1. The main mechanisms are phonon-phonon scattering, phonon-defect scattering, and phonon-boundary scattering.<sup>[27]</sup>

Creation and annihilation are two types of phonon-phonon scattering. Creation de-

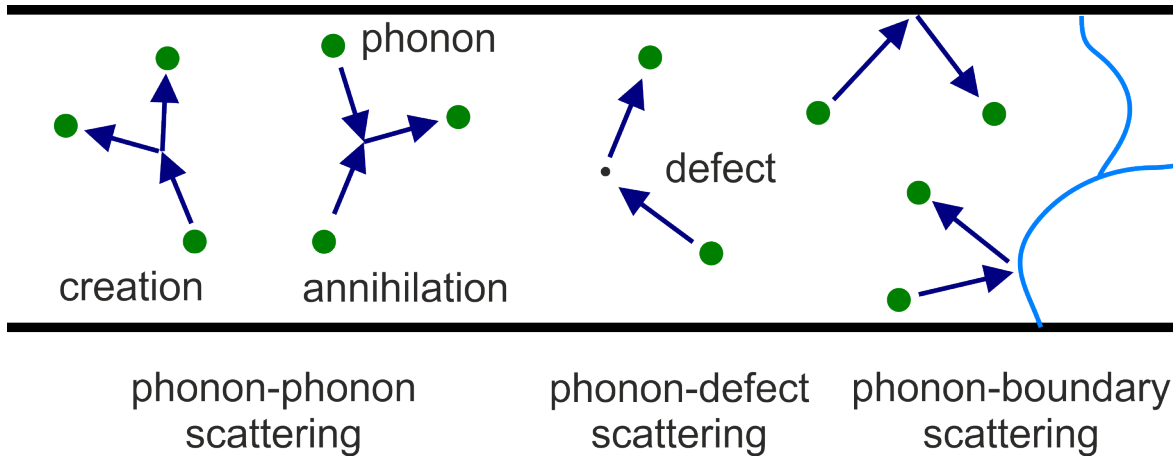


Figure 2.1: Different mechanisms of phonon scattering. From left to right, phonon-phonon scattering, phonon-defect scattering, and phonon-boundary-scattering. Defects can exist as point defects and impurities. Boundary-scattering occurs at the edges of the samples as well as at grain boundaries. Adapted from Asheghi et al.<sup>[27]</sup>, with permission of AIP Publishing.

describes one phonon that splits into two, while during the annihilation two phonons merge into one.<sup>[25]</sup> In metals phonons can also be scattered at electrons. Further, it is divided into normal and Umklapp scattering. The normal process retains energy and momentum, while the Umklapp process only conserves energy, but the momentum changes. Phonon-defect scattering occurs at atom defects or impurities. These effects are dominant in bulk material.<sup>[22]</sup>

Scattering at boundaries is only relevant in materials with microscopic scales in the range of the phonon MFP. Examples are thin films, polycrystalline samples, and nanostructured materials. Besides the crystallographical orientation, interface roughness, and structural defects at the interface, the boundary scattering depends on the acoustic impedance mismatch. The acoustic impedance,  $Z$ , is defined as the product of material density and the speed of sound ( $Z = \rho c$ ). Like the scattering of a light beam at an interface depends on the refractive indices of the two media connected at the interface, the phonon-boundary scattering depends on the difference of  $Z$ . Hence, the higher the difference in  $Z$ , the higher is the chance that the interface reflects the phonon. Consequently, the phonon MFP, and therefore, the thermal conductivity, is negatively affected by a high interface density and a high difference in  $Z$ .<sup>[26]</sup>

Temperature dependent thermal conductivity strongly depends on which scattering mechanism dominates. For the classification of the temperature regimes, the Debye temperature,  $\theta_D$ , is introduced. It is a notional temperature defined as<sup>[22]</sup>:

$$\theta_D = \frac{\hbar \cdot \omega_D}{k_B} \quad (2.9)$$

With  $\omega_D$  as the upper phonon frequency cutoff,  $\hbar$  as the reduced Planck's constant and  $k_B$  the Boltzmann constant. At low temperatures, phonon-phonon scattering can be neglected. Thus, the phonon MFP is of considerable length and much larger than defects and grain boundaries. Hence, the MFP is temperature independent in this region. Consequently, the temperature dependence of the thermal conductivity follows only the temperature dependence of the specific heat capacity, which scales with  $T^3$ . The only present scattering is boundary-scattering at the edges of the sample.<sup>[28]</sup> If the phonon MFP is on the order of the defect size of the material, defect scattering will dominate the heat transport. Defect-scattering is temperature independent.

With increasing temperature, the amount of phonon-phonon scattering rises. Although normal scattering retains energy and momentum, and thus, pose no resistance, it distributes the phonon energy to higher frequencies. Above  $T = \theta_D/10$ , Umklapp scattering dominates because of large wave vectors and the elevated phonon density at high frequencies. As a consequence, the phonon MFP drastically decreases with temperature, and therefore, also the thermal conductivity goes down.<sup>[22]</sup>

Figure 2.2 schematically illustrates the temperature dependent thermal conductivity of dielectric materials. As described above, the thermal conductivity of crystalline dielectric materials increases with a  $T^3$ -dependence. After a peak at around  $\theta_D/10$ , the thermal conductivity falls off with  $T^{-1}$ , due to increased phonon-phonon scattering. In comparison, the thermal conductivity of amorphous solids increases monotonically. The proportionality factors vary but are always positive. As an example, some amorphous polymer blends show values between  $T^{0.1}$  to  $T^{0.4}$ .<sup>[19]</sup> It becomes clear that the above-described heat transfer by phonons is only valid for crystalline dielectric materials. In conclusion, heat transfer must occur differently in amorphous materials.

Amorphous materials possess no translational symmetry. Due to this lack of order, the phonon MFP is very short in amorphous structures. Therefore, the thermal conductivity of amorphous materials is, in general, lower than in crystals.<sup>[29,30]</sup> The amorphous structure can be interpreted as crystal with extremely high defect density, meaning every atom is displaced from its lattice site. Vibrational modes still carry the heat, but they cannot be described as phonons anymore. These circumstances lead to the different dependence of the thermal conductivity on the temperature. Allen and Feldman developed a new concept to describe the vibrational

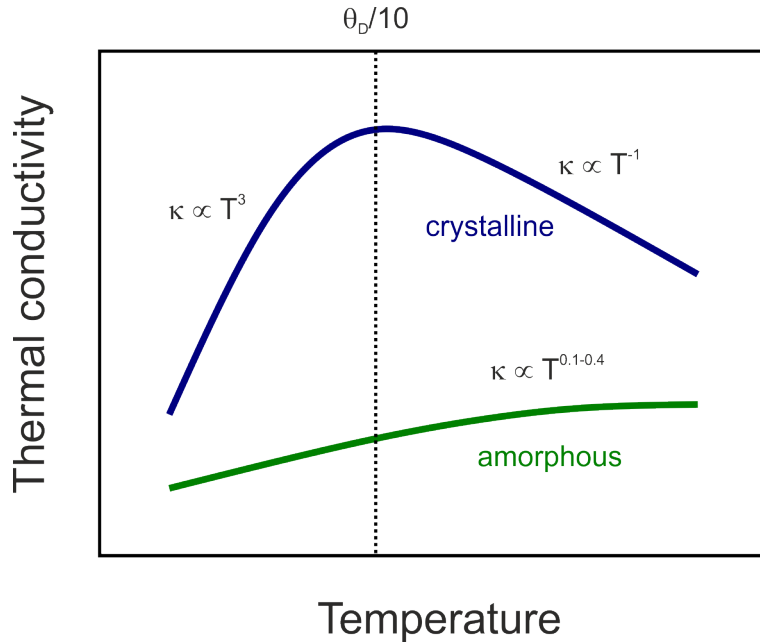


Figure 2.2: Temperature dependence of the thermal conductivity in dielectric materials. The different behavior between crystalline and amorphous materials indicates different heat transfer mechanisms.

modes in amorphous materials and called them vibrons.<sup>[31,32]</sup>

Vibrons are classified in extendons and locons, whereas extendons are again distinguished in propagons and diffusons.

Locons are localized and non-propagating vibrational modes. They usually exist in the high-frequency range. In contrast to locons, extendons are delocalized. Propagons are propagating and typically found in the low-frequency range. Diffusons are non-propagating and found in the middle-frequency range of the vibrational spectrum.

While Allen and Feldman only consider harmonic normal modes, it was shown, that this is only applicable for materials with one type of atom, where anharmonicity does not play an important role. In complex structures with more than one type of element, anharmonic coupling dominates the heat transfer. Moreover, this positive contribution to thermal conductivity is increasing with temperature.<sup>[33]</sup> Together with the increase in specific heat, this leads to the monotonic increase of the thermal conductivity in amorphous dielectric materials.<sup>[33–35]</sup>

### 2.1.3 Thermal transport in hybrid structures

In a heterogeneous material, i.e., a material that comprises two or more different constituents, the effective properties depend on the properties of the individual

components. Such materials are being referred to as composites. Composites allow combining the favorable properties of two individual components in one material. For example, polymers are filled with glass fibers to reinforce mechanical properties like the tensile strength and the flexural strength at a comparatively low density.<sup>[36]</sup> Nanocomposites are a particular class of composite materials. Here, at least one dimension of the filler material has nanoscale dimensions. This phenomenon is in principle based on the high surface to volume ratio and the associated high amount of surface atoms.<sup>[37]</sup> Properties that can be influenced by nanomaterials cover optical, electrical, mechanical, thermal, and fire-retardant characteristics.<sup>[38]</sup> Besides the classical mechanical improvements, NP integration can lead to changes in the nucleation behavior or the glass transition temperature ( $T_g$ ).<sup>[39]</sup> However, a great issue is the usually occurring aggregation of the NPs with the loss of any nanoscale benefits. Therefore, methods to stabilize the NPs in the polymer matrix have been developed.<sup>[40]</sup> Important fillers are nanoclays<sup>[39,41]</sup>, carbon nanotubes<sup>[41,42]</sup> but also spherical inorganic NPs<sup>[41,43]</sup> are used. The improvement of mechanical properties surely is best investigated, but while devices are getting smaller and smaller, also the interest in influencing and understanding of energy transport phenomena, e.g., thermal transport, in nanostructures has emerged.

One approach to increase the thermal conductivity is to mix additives with a higher thermal conductivity, e.g., carbon nanotubes<sup>[42]</sup>, in a polymer. Various mixing models can predict the effective thermal conductivity of such composite materials.<sup>[44,45]</sup> The principal mixing models are schematically illustrated in Figure 2.3 and consist of the series model, the parallel model, the Maxwell model, and the effective medium theory (EMT).

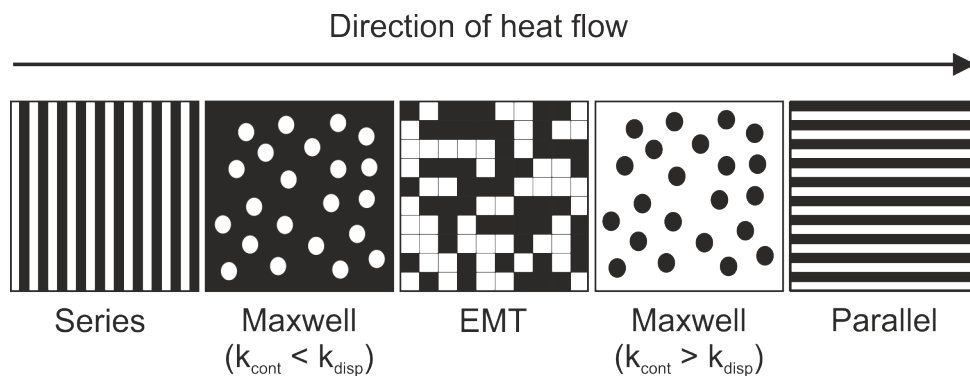


Figure 2.3: Five basic mixing models to predict the effective thermal conductivity of a two-phase composite material. Adapted from Wang et al.<sup>[45]</sup>, with permission from Elsevier.

For the series and the parallel model, a layered system of two different materials is assumed, which is aligned perpendicular or parallel to the heat flow. In the Maxwell model, one phase is dispersed in the other (continuous phase) without any contact

between the single dispersed domains. Two cases are distinguished according to which phase has the lower, respectively higher thermal conductivity. As the dispersed phase never forms continuous conduction pathways, this model has a bias to the continuous phase. In contrast, the EMT is unbiased to its components because they distribute randomly in space.<sup>[44]</sup>

The series and parallel model depict the boundary conditions of the effective thermal conductivity of a composite material. They are mathematically described by Equations 2.10 and 2.11, respectively.<sup>[44]</sup>

$$\kappa_{eff}(series) = \frac{1}{\frac{\phi_1}{\kappa_1} + \frac{(1 - \phi_1)}{\kappa_2}} \quad (2.10)$$

$$\kappa_{eff}(parallel) = \phi_1 \cdot \kappa_1 + (1 - \phi_1) \cdot \kappa_2 \quad (2.11)$$

Here  $\kappa_{eff}$  is the effective thermal conductivity,  $\kappa_{1/2}$  are the thermal conductivities of phase 1, and phase 2, respectively, and  $\phi_1$  is the volume ratio of phase 1. For the case of lattice thermal conduction as the only mechanism of heat transport, the effective thermal conductivity of any heterogeneous material, should lie between these boundaries.<sup>[45]</sup> In Figure 2.4, the relative effective thermal conductivity is plotted over the full range of composition of a heterogeneous two-phase system. All other models lie between the series case as the lower limit and the parallel case as the upper boundary.

Hashin and Shtrikman<sup>[46]</sup> presented even narrower boundaries in which the thermal conductivity of a composite should lie. This model is valid for a macroscopically homogeneous and isotropic two-phase material, where no information about the spatial distribution of the components has to be known. Their approach coincides mathematically with the Maxwell model.

However, the models introduced here are most appropriate for materials with macroscopic phases. When going to the nanoscale, interfacial phenomena play an essential role<sup>[10]</sup>, which are not covered by these models. Ong et al.<sup>[11]</sup> emphasized this by investigation of the thermal conductivity in three-dimensional nanocrystal arrays. The explored structure is shown in Figure 2.5 A. The organic ligands used to stabilize the NPs function as the matrix with the effect that the NPs form a defined array. In Figure 2.5 B, the measured values of an array of PbS NPs with oleate ligands (PbS@Oleate) are shown (green squares). They show a higher thermal conductivity than a PbS-oleate film without NPs (yellow line).

Additionally, calculated values for different models are plotted. The EMT, the

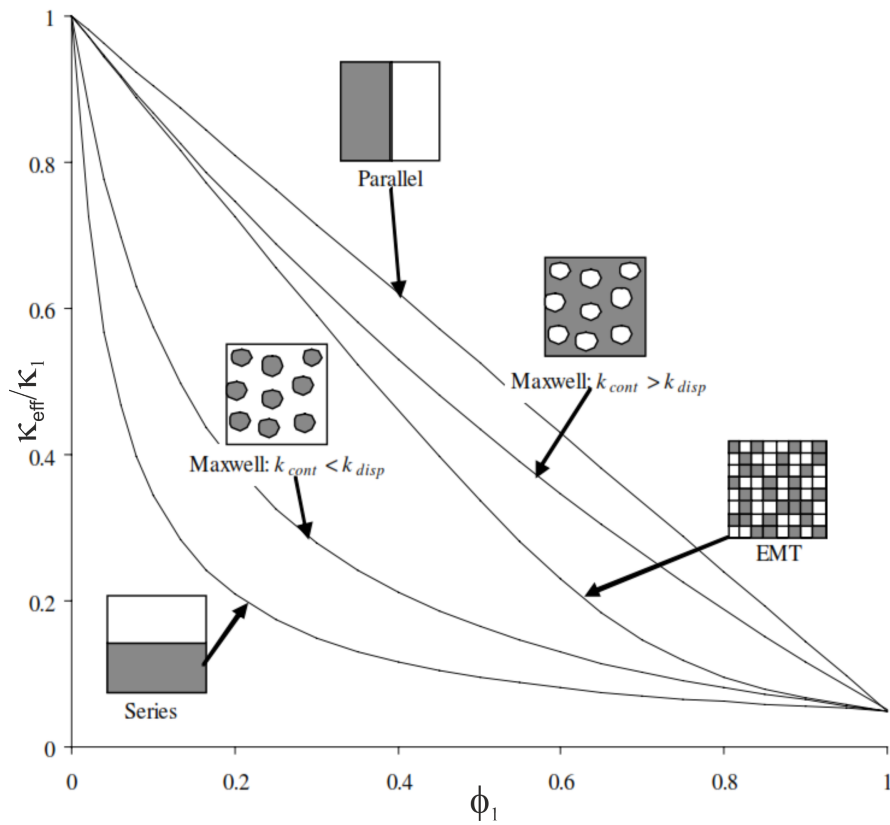


Figure 2.4: Diagram of the relative effective thermal conductivity versus the volume ratio for the series model, the parallel model, EMT model, and two forms of the Maxwell model reprinted from Carson et al.<sup>[44]</sup>, with permission from Elsevier.

Maxwell and the Hashin model all overestimate the thermal conductivity. In comparison to the named models, those involving a finite thermal interface conductance show better accordance. They adapted a modified effective medium approximation (EMA) model from Minnich and Chen<sup>[47]</sup> (solid green line). Nevertheless, Ong et al.<sup>[11]</sup> had to modify the model because the phonon group velocity and the bulk mean free path were not available. These values are used to estimate the thermal conductivity reduction of the PbS cores and the oleate matrix due to boundary scattering. As an approximation, the thermal conductivity accumulation function of bulk PbTe was used to estimate the relative reduction of the thermal conductivity in the PbS cores. The relative reduction in the oleate matrix was ignored because the thermal conductivity is already low.

The other model which agrees well with the experimental data is the model by Hasselman and Johnson<sup>[48]</sup> (dotted red line). They also introduced a finite thermal interface conductance. In comparison to the Minich and Chen, they based their calculations on the Maxwell model. In both cases, the finite thermal interface conductance was used as a fitting parameter, leading to values between 60 and 310 MW m<sup>-2</sup> K<sup>-1</sup>.<sup>[11]</sup>

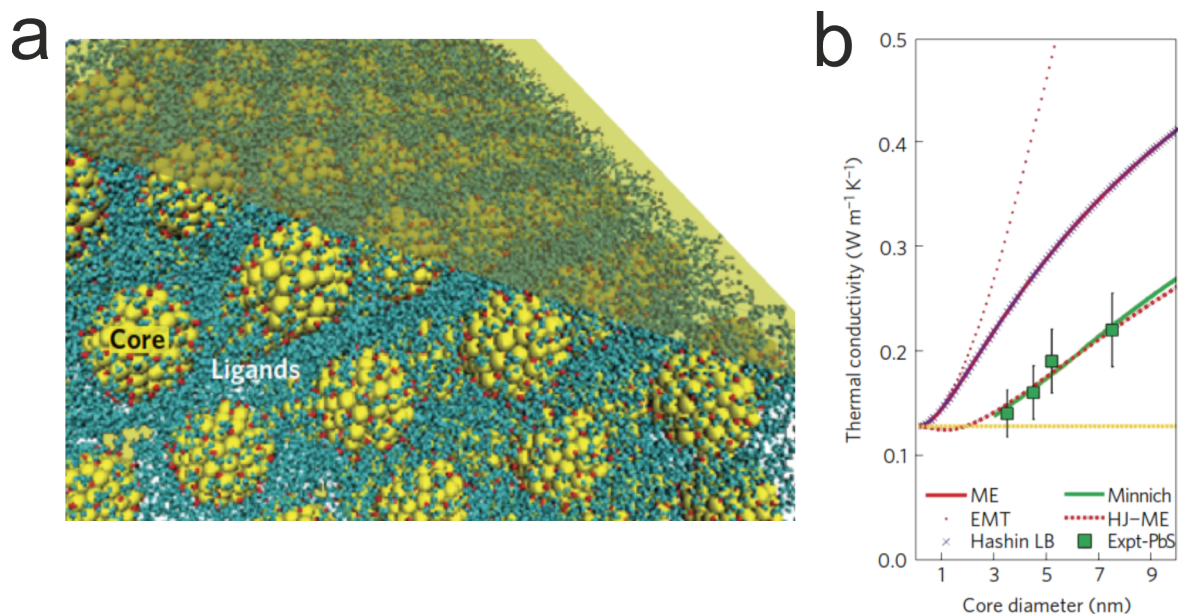


Figure 2.5: (a) Structure of the material measured by Ong et al. The NPs are arranged in the matrix provided by the ligands. (b) Plot of the particle size against the thermal conductivity for different models as well as the measured values of the PbS@oleate series. Models, not using a finite thermal interface conductance, like the EMT, the Maxwell (ME), and the Hashin model, cannot explain the results. In contrast, the Minnich and Hasselman-Johnson (HJ-ME) models fit well with the data by using a finite thermal interface conductance at the core/ligand interface. The yellow line is the thermal conductivity of bulk Pb-oleate at 300 K. Adapted by permission from Springer Nature: Nature Materials Ref. [11], Copyright 2013.

The necessity to introduce a thermal interface conductance implies that the increase of the effective thermal conductivity with increasing core diameter shown in Figure 2.5 B is not only ascribed to the increase of the volume fraction of PbS cores compared to the ligand but also the decrease in interface density.

Consequently, new opportunities open up to adjust the thermal conductivity by the implementation of interfaces. Nanostructured materials comprise an enormous amount of interfaces. The investigation of the thermal conductivity in nanolaminates also showed the influence of interfaces on the thermal conductivity.<sup>[49]</sup> The raw nanolaminates have one interface per unit cell, consisting of two sheets. When arranging organic molecules between the clay sheets, two interfaces per unit cell arise. The structures of both unmodified clay and organoclay are shown in Figure 2.6 A. The increase of interfaces leads to a decrease of thermal conductivity by a factor of  $\sim 5$ , from  $0.48 \text{ W} \cdot \text{m}^{-1} \cdot \text{K}^{-1}$  to  $0.09 \text{ W} \cdot \text{m}^{-1} \cdot \text{K}^{-1}$ .

In this way, the lower limit from the series model is not valid anymore. Due to phonon-boundary scattering, the thermal conductivity perpendicular to the layers is decreased even below the value of the lower conducting component. At the same

time, the in-plane thermal conductivity is unaffected. Hence, high anisotropy ratios are achievable with such structures.

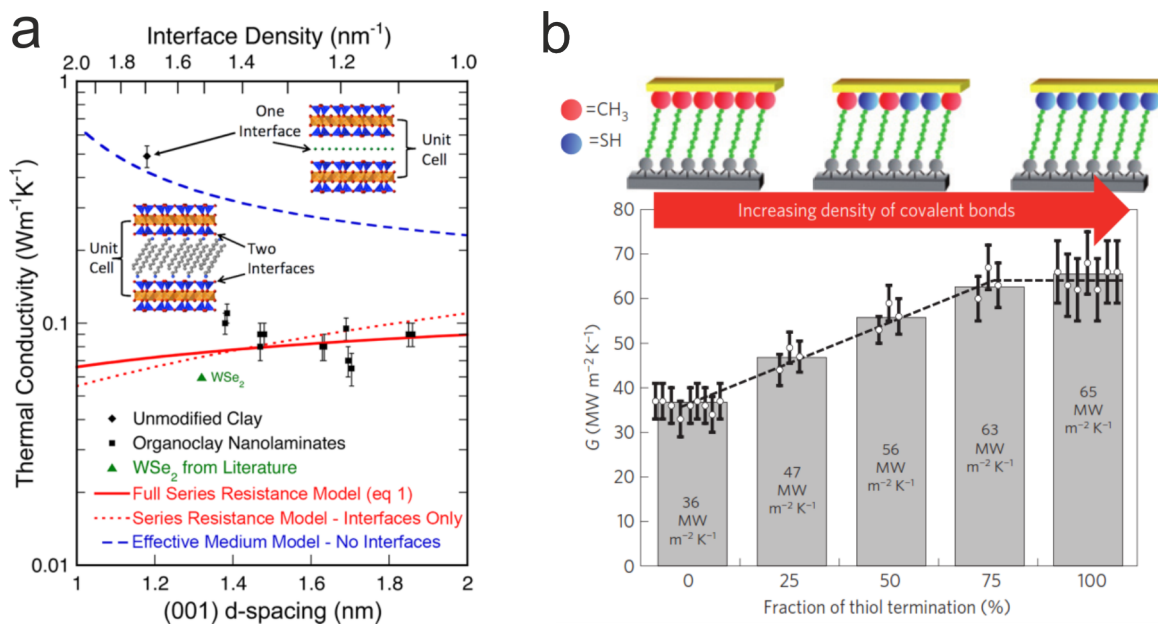


Figure 2.6: Picture (a) depicts the data of the thermal conductivity measurements of nanolaminates. The thermal conductivity decreases by a factor of 5, from  $0.48 \text{ W}\cdot\text{m}^{-1}\cdot\text{K}^{-1}$  to  $0.09 \text{ W}\cdot\text{m}^{-1}\cdot\text{K}^{-1}$ , upon implementation of a second interface per unit cell by modification of the clay with organic molecules. Reprinted with permission from Ref. [49]. Copyright 2013 American Chemical Society. Picture (b) shows the interfacial thermal conductance as a function of the thiol:methyl end group ratio, which increases with a higher ratio of thiol groups. Reprinted by permission from Springer Nature: Nature Materials Ref. [13], Copyright 2012.

Besides the number of interfaces, also the surface chemistry at the interface affects the thermal conductivity. Losego et al.<sup>[13]</sup> demonstrated the influence of the surface chemistry by investigating the thermal conductivity of self-assembled monolayer (SAM) structures. The sandwich structure consisted of the SAM between a quartz glass substrate and a gold layer. Thereby, the SAM is covalently bonded to the quartz glass, while the functional group, oriented to the gold layer, can be varied. In Figure 2.6 B on top, the simplified structure of the investigated system is illustrated. The plot shows the interfacial thermal conductance as a function of the thiol:methyl end group ratio. A trend is observed in the data showing an increase of interfacial thermal conductance with increasing ratio of thiol groups. This trend is ascribed to the bonding strength, which can be seen as covalent for the thiol gold surface, while at the methyl gold surface, only Van der Waals forces are active.

Recapitulating, the thermal conductivity in nanostructured composite materials depends on not only classic aspects like the composition ratio and the dispersion of the components but also the interface density plays an important role.<sup>[11,49]</sup> Addition-

ally, it is possible to manipulate the interfacial thermal conductance by controlling the surface chemistry, i.e., the bonding strength at the interface.<sup>[13]</sup>

Hybrid materials are heterogeneous structures, that bring both a tremendous number of interfaces and the opportunity to control the surface chemistry. The IUPAC defines the term hybrid material as "Material composed of an intimate mixture of inorganic components, organic components, or both types of component."<sup>[50]</sup>, which is a broad definition. Here, we want to use a more specified definition. "A hybrid material consists of at least two components – usually an inorganic and an organic component – that are molecularly dispersed in the material."<sup>[51]</sup> This definition is also fulfilled by all mentioned examples, showing the high interest of hybrid materials in the research field of nanoscale thermal transport. The reason is simple. Hybrid nanostructures have access to a vast amount of hard-soft interfaces. The reasonable structural control allows engineering these interfaces to achieve new transport properties in hybrid nanomaterials.<sup>[52]</sup>

## 2.2 Photoacoustic method

### 2.2.1 Solving the heat equation

In 1880, Alexander Graham Bell was the first one to describe the PA effect. He conducted experiments with solids situated in closed cells. When illuminated by an intermittent beam of sunlight, a musical sound emerged.<sup>[53]</sup>

Over 90 years, no satisfactory theoretical explanation appeared in the literature. Then Rosencwaig and Gersho described the acoustic wave as a result of the pressure change induced by two parallel effects.<sup>[54]</sup> When the modulated laser beam heats the specimen the following occurs. On the one hand, the pressure change caused by the alternating thermal expansion and contraction of the material results in a mechanical wave (mechanical piston). On the other hand, a pressure change is induced by the periodic heat flux from the surface of the solid to the surrounding gas phase. The heated gas at the surface pushes away the rest of the gas in the closed-cell, which is usually described as a thermal piston effect.

A generalized theory of the PA effect in a multilayer material was derived from Hu et al.<sup>[55]</sup> A cross-sectional view of their multilayer model is shown in Figure 2.7. The model consists of the backing material 0, multiple layers from 1 to  $N$ , and the gas volume  $N+1$ .

As a light source, a sinusoidally modulated monochromatic laser beam of wavelength  $\lambda$  is assumed. The intensity  $I$  at time  $t$  is therefore

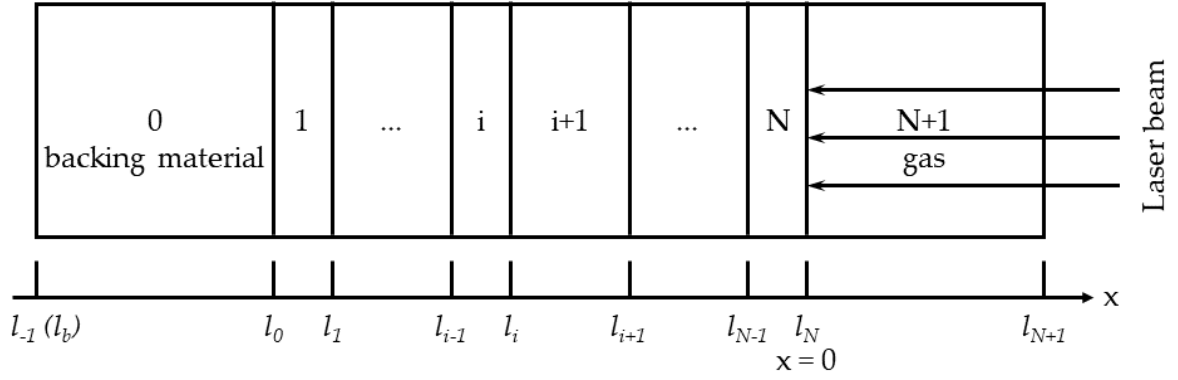


Figure 2.7: Schematic cross-section of the multilayer model used for solving the thermal diffusion equation. Adapted from Ref. [55], with permission of AIP Publishing.

$$I(t) = I_0(1 + \cos(\omega t))/2, \quad (2.12)$$

where  $I_0$  is the incident laser flux,  $\omega$  is the modulated angular frequency ( $= 2\pi f$ ) of the incident laser beam. A one-dimensional heat transfer model is assumed. This is a suitable assumption if the thermal diffusion lengths in the gas and the solid are much smaller than the diameter of the laser beam. The thermal diffusion length can be calculated as  $l_\alpha = \sqrt{2\alpha/\omega}$ , where  $\alpha$  is the thermal diffusivity. Consequently, the thermal diffusion equation in layer  $i$  can be expressed as

$$\frac{\partial^2 \theta_i}{\partial x^2} = \frac{1}{\alpha_i} \frac{\partial \theta_i}{\partial t} - \frac{\beta_i I_0}{2k_i} \exp\left(\sum_{m=i+1}^N -\beta_m L_m\right) \cdot e^{\beta_i(x-l_i)}(1 + e^{j\omega t}), \quad (2.13)$$

with  $\theta_i = T_i - T_{amb}$  as the modified temperature in layer  $i$ , where  $T_{amb}$  is the ambient temperature,  $k_i$  the thermal conductivity,  $\beta_i$  the optical absorption coefficient,  $j = \sqrt{-1}$  and the layer thickness  $L$ .  $x$  takes values from  $l_N$  ( $x = 0$ ) to  $l_0$  with the light incident at  $l_N$ , as marked in Figure 2.7. The solution of this equation consists of three parts, as can be seen in Equation 2.14. The transient component  $\theta_{i,t}$ , which considers the early stage temperature variation, the direct current (DC) component  $\bar{\theta}_{i,s}$ , which describes the steady-state temperature rise by the laser heating and the alternating current (AC) component  $\tilde{\theta}_{i,s}$ , which fluctuates periodically with the modulation of the laser beam.

$$\theta_i = \theta_{i,t} + \bar{\theta}_{i,s} + \tilde{\theta}_{i,s} \quad (2.14)$$

In a PA measurement, usually, a lock-in amplifier is used. Therefore, only the periodic component is measured. Hence, only the ac component needs to be eval-

uated. The respective term is  $-\frac{\beta_i I_0}{2k_i} \exp\left(\sum_{m=i+1}^N -\beta_m L_m\right) \cdot e^{\beta_i(x-l_i)}(1 + e^{j\omega t})$  (last term of Equation 2.13). Equation 2.13 now has a particular solution in the form of  $-E_i e^{\beta_i(x-l_i)} e^{j\omega t}$ , with  $E_i = G_i / (\beta_i^2 - \sigma_i^2)$ ,  $G_i = \beta_i I_0 / (2k_i) \exp\left(-\sum_{m=i+1}^N \beta_m L_m\right)$  for  $i < N$ ,  $G_N = \beta_N I_0 / 2k_N$ , and  $G_{N+1} = 0$ .  $\sigma_i$  is defined as  $(1 + j)a_i$  with  $j = \sqrt{-1}$ . The general solution of  $\tilde{\theta}_{i,s}$  is given by

$$\tilde{\theta}_{i,s} = \left[ A_i e^{\sigma_i(x-h_i)} + B_i e^{-\sigma_i(x-h_i)} - E_i e^{\beta_i(x-h_i)} \right] \cdot e^{j\omega t} \quad (2.15)$$

Here,  $h_i$  is calculated as  $h_i = l_i$ , for  $i = 0, 1, \dots, N$ , and  $h_{N+1} = 0$ . If working with a thermally thick substrate and gas layer, the coefficients  $A_{N+1}$  and  $B_0$  are virtually zero, because  $|\sigma_0 L_0| \gg 1$  and  $|\sigma_{N+1} L_{N+1}| \gg 1$ . The other coefficients  $A_i$  and  $B_i$  can be defined by using the interfacial conditions at  $x = l_i$ . It indicates a continuous heat flux at the boundaries between the layers, while the temperatures differ in the presence of thermal contact resistance, and is expressed as

$$k_i \frac{\partial \tilde{\theta}_{i,s}}{\partial x} - k_{i+1} \frac{\partial \tilde{\theta}_{i+1,s}}{\partial x} = 0 \quad (2.16)$$

$$k_i \frac{\partial \tilde{\theta}_{i,s}}{\partial x} + \frac{1}{R_{i,i+1}} (\tilde{\theta}_{i,s} - \tilde{\theta}_{i+1,s}) = 0 \quad (2.17)$$

Within these conditions, the recursive formula of both coefficients,  $A_i$  and  $B_i$ , is obtained as a matrix

$$\begin{bmatrix} A_i \\ B_i \end{bmatrix} = U_i \begin{bmatrix} A_{i+1} \\ B_{i+1} \end{bmatrix} + V_i \begin{bmatrix} E_i \\ E_{i+1} \end{bmatrix}, \quad (2.18)$$

$U_i$  describes the transmission of heat from layer (i+1) to i and is given by

$$U_i = \frac{1}{2} \begin{bmatrix} u_{11,i} & u_{12,i} \\ u_{21,i} & u_{22,i} \end{bmatrix} \quad (2.19)$$

with

$$u_{11,i} = (1 + k_{i+1}\sigma_{i+1}/k_i\sigma_i - k_{i+1}\sigma_{i+1}R_{i,i+1}) \cdot \exp[-\sigma_{i+1}(h_{i+1} - h_i)], \quad (2.20)$$

$$u_{12,i} = (1 - k_{i+1}\sigma_{i+1}/k_i\sigma_i + k_{i+1}\sigma_{i+1}R_{i,i+1}) \cdot \exp[+\sigma_{i+1}(h_{i+1} - h_i)], \quad (2.21)$$

$$u_{21,i} = (1 - k_{i+1}\sigma_{i+1}/k_i\sigma_i - k_{i+1}\sigma_{i+1}R_{i,i+1}) \cdot \exp[-\sigma_{i+1}(h_{i+1} - h_i)], \quad (2.22)$$

and

$$u_{22,i} = (1 + k_{i+1}\sigma_{i+1}/k_i\sigma_i + k_{i+1}\sigma_{i+1}R_{i,i+1}) \cdot \exp[+\sigma_{i+1}(h_{i+1} - h_i)]. \quad (2.23)$$

$V_i$  expresses the absorption of light.

$$V_i = \frac{1}{2} \begin{bmatrix} v_{11,i} & v_{12,i} \\ v_{21,i} & v_{22,i} \end{bmatrix} \quad (2.24)$$

with

$$v_{11,i} = 1 + \beta_i/\sigma_i, \quad (2.25)$$

$$v_{12,i} = (-1 - k_{i+1}\beta_{i+1}/k_i\sigma_i + k_{i+1}\beta_{i+1}R_{i,i+1}) \cdot \exp[-\beta_{i+1}(h_{i+1} - h_i)], \quad (2.26)$$

$$v_{21,i} = 1 - \beta_i/\sigma_i, \quad (2.27)$$

and

$$v_{22,i} = (-1 + k_{i+1}\beta_{i+1}/k_i\sigma_i + k_{i+1}\beta_{i+1}R_{i,i+1}) \cdot \exp[-\beta_{i+1}(h_{i+1} - h_i)]. \quad (2.28)$$

With  $A_{N+1} = 0$ ,  $B_0 = 0$  and

$$B_{N+1} = - \frac{\begin{bmatrix} 0 & 1 \end{bmatrix} \sum_{m=0}^N (\prod_{i=0}^{m-1} U_i) V_m \begin{bmatrix} E_m \\ E_{m+1} \end{bmatrix}}{\begin{bmatrix} 0 & 1 \end{bmatrix} (\prod_{i=0}^N U_i) \begin{bmatrix} 0 \\ 1 \end{bmatrix}}, \quad (2.29)$$

the coefficients  $A_i$  and  $B_i$  can be expressed as

$$\begin{bmatrix} A_i \\ B_i \end{bmatrix} = (\prod_{m=i}^N U_m) \begin{bmatrix} 0 \\ B_{N+1} \end{bmatrix} + \sum_{m=i}^N (\prod_{k=i}^{m-1} U_k) \begin{bmatrix} E_m \\ E_{m+1} \end{bmatrix} \quad (2.30)$$

where  $\prod_{k=i}^{m-1} U_k$  is taken as  $\begin{bmatrix} 1 & 0 \\ 0 & 1 \end{bmatrix}$ .

The final expression of the ac temperature distribution in the gas phase ( $i = N + 1$ ), where the PA signal emerges, is found by substituting Equation 2.30 into Equation 2.15. The obtained formula is

$$\tilde{\theta}_{N+1,s} = B_{N+1} e^{-\sigma_{N+1}x} e^{j\omega t}. \quad (2.31)$$

### 2.2.2 The photoacoustic signal

After looking at the temperature distribution in the gas phase, the next step is to study the thermoacoustic response. As described before, the PA effect has two origins. On the one hand, the thermal piston effect caused by the thermal expansion of the gas near the sample is causing a compression of the rest of the gas phase. On the other hand, there is the mechanical piston effect, initiated by mechanical vibrations of the sample surface, which results in an additional temperature change  $\delta\tilde{\theta}_{i,s}$ . However, it was shown that the influence of the resulting pressure change is negligible small for solid samples. At modulation frequencies below 20 kHz, which is the resolution limit of most microphones, the ratio between the pressure change by the mechanical piston effect and the thermal piston effect is less than 1 %.<sup>[55]</sup> Therefore, only the thermal piston effect will be discussed hereafter.

The pressure change  $dp$  in the measurement cell generates the acoustic signal. It can be expressed in terms of temperature  $T$  and volume  $V$  as

$$dp = \left( \frac{\partial p}{\partial T} \right)_V dT + \left( \frac{\partial p}{\partial V} \right)_T dV \quad (2.32)$$

assuming an ideal gas one has

$$\left( \frac{\partial p}{\partial T} \right)_V = \frac{p}{T}, \quad \left( \frac{\partial p}{\partial V} \right)_T = -\frac{p}{V}. \quad (2.33)$$

The pressure is uniform in the whole measurement cell, if it is designed in a way that  $L_g < \Lambda_S/2$ . This means that the dimension of the cell ( $L_g$ ) is smaller than half of the shortest acoustic wave  $\Lambda_S$ . On the other side, we already know that there is a temperature distribution in the gas. With  $\langle dT \rangle$  as the average temperature distribution and Equation 2.33, Equation 2.32 can be rearranged as

$$dp = \frac{p}{T} \langle dT \rangle - \frac{p}{V} dV. \quad (2.34)$$

Here, we see that the pressure change, responsible for the acoustic signal, depends

on two terms. The first one describes the influence of the periodical temperature variation,  $dT = \tilde{\theta}_{N+1,s}$ . The second one depends on a volumetric change of the sample. As already discussed, the volume change of the sample has a negligible influence on the pressure wave. Therefore, Equation 2.34 can be simplified to

$$dp = \frac{p_{amb}}{T_{amb}} \langle \tilde{\theta}_{N+1,s} \rangle \quad (2.35)$$

with  $p_{amb}$  and  $T_{amb}$  beeing the ambient pressure and temperature, respectively. By inserting Equation 2.31 and averaging over the whole cell the following expression is formed

$$dp = \frac{p_{amb}}{T_{amb}L_g} \int_0^{L_g} B_{N+1} e^{-\sigma_{N+1}x} dx \cdot e^{j\omega t} = \frac{p_{amb}B_{N+1}}{\sqrt{2}T_{amb}L_g a_g} \cdot e^{j(\omega t - \pi/4)}. \quad (2.36)$$

With Equation 2.36, the phase shift and the amplitude signal of the PA wave can be calculated as  $\text{Arg}(B_{N+1}) - \pi/4$  and  $|p_{amb}B_{N+1}/\sqrt{2}T_{amb}L_g a_g|$ , respectively.

It is possible to fit both the phase shift and the amplitude signal. The advantage of the amplitude fit is the possibility to measure thermally thick samples, while the phase shift for such samples is always  $-90^\circ$ . However, the reflectivity has to be determined for every sample, which introduces another variable that has to be investigated by another method and therefore opens an additional potential source of error.<sup>[56]</sup> Moreover, it exists a variety of established and commercial methods to measure the thermal conductivity of thermally thick (bulk) samples<sup>[57]</sup>, whereas the determination of thin samples is still challenging. Because of these two reasons, and the fact that all samples of interest in this thesis are thermally thin, only the phase fitting method is used in this work.

### 2.2.3 The photoacoustic method to determine the thermal properties of a sample

The PA effect can be exploited to determine the thermal properties of a sample. Its versatility has been demonstrated in the literature. It was used to determine the thermal properties of bulk materials<sup>[56]</sup>, liquids<sup>[58]</sup>, gases<sup>[59]</sup>, and thin films<sup>[18,55,56,60–64]</sup>.

Here, especially, the measurement of thin films on substrates is of interest, as there exist only a few techniques that can handle such samples. Besides the PA method, the  $3-\omega$  method, frequency-domain thermoreflectance (FDTR), and time-domain thermoreflectance (TDTR) shall be mentioned. At the same time, the PA method has advantages compared to these methods, as it has a much simpler setup than FDTR

and TDTR. Additionally, these two methods require the determination of the reflectivity of the surface, and are vulnerable to surface roughness effects. Furthermore, the PA method can handle electrical conductive samples, which is not possible for the  $3\text{-}\omega$  method without further effort.<sup>[65,66]</sup>

The setup consists of a gas-tight measurement cell, which is schematically shown in Figure 2.8a. The modulated laser beam enters the cell through a sapphire window. It hits the sample, which is mounted to the cell from the backside. An o-ring ensures a leakage free connection. The microphone and a gas inlet are connected from the side. The latter enables the possibility to put the cell under pressure with a specific gas. Usually, helium is used because it has high thermal conductivity, and therefore, improves the signal to noise ratio. The microphone measures the pressure wave described in Chapter 2.2.2. Then, it transfers the signal to the lock-in amplifier, as shown in the scheme of the PA setup in Figure 2.8b. The lock-in amplifier detects the amplitude and the phase shift of the acoustic signal. The phase shift refers to the incident signal produced by the function generator, which controls the electro-optic modulator (EOM) and thereby the frequency of the modulated laser beam.

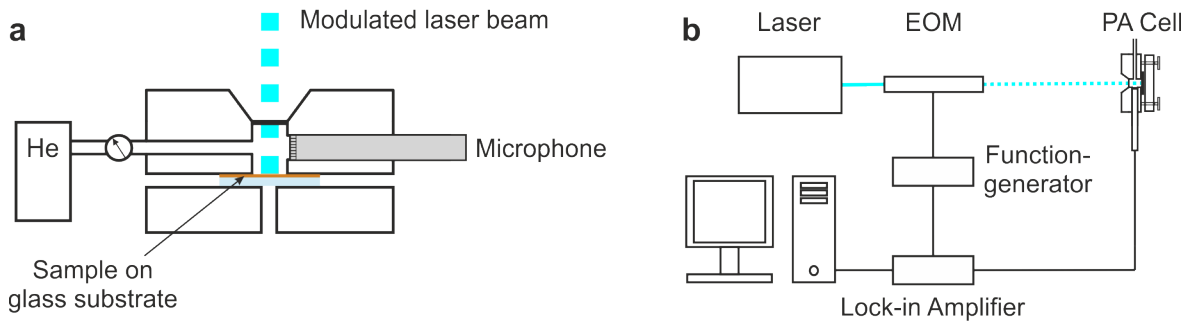


Figure 2.8: Schematic of (a) the PA cell and (b) the complete PA setup.

In a PA measurement, a frequency sweep is performed. The phase shift is measured in dependence on the frequency. Besides the thermal properties of the sample, also the measurement geometry influences the signal. Factors are the dimensions of the measurement cell, the time the acoustic wave needs to reach the microphone, and the delay of the electronic circuit. Measuring a reference sample of known properties eliminates the overlaying signals. For this purpose, a thermally thick glass slide with a metal transducer layer on top can be used. The thermal properties of the glass slide are well known or can be easily determined. Due to the thermal thickness, the phase shift of the reference sample should be  $-90^\circ$  (taking only the PA signal into account). Therefore, the corrected phase shift ( $\Phi$ ) of the sample results from

$$\Phi = \Phi_{sample} - \Phi_{reference} - 90^\circ \quad (2.37)$$

$\Phi$  dependent on the frequency is then compared to the theoretical values, which are described by  $\text{Arg}(B_{N+1}) - \pi/4$ , as discussed in Chapter 2.2.2.  $B_{N+1}$  is a function of the densities, thermal conductivities, specific heats, thicknesses, optical absorption coefficients, and interface resistances in the multilayered sample. Known parameters are directly put into the calculations. Unknown values are used as fitting parameters to approach the theoretical calculations to the experimental data. The accuracy of the fit depends on the number of unknown parameters. For that reason, it is of considerable interest to determine as much properties as possible by other characterizations techniques. The optical absorption coefficient can be neglected, if the sample does not absorb the laser power. In other words, the transducer layer should be not permeable for the laser. Density, specific heat, and thicknesses can be measured by common methods. Accordingly, in a usual PA experiment three parameters are unknown. These parameters are the thermal conductivity, and the two interface resistances adjacent to the sample. One is the contact resistance between transducer layer and sample, and the other is the contact resistance between sample and substrate. Investigations have shown, that the fitting of two unknowns results in an accuracy of 1 % for a one-sided carbon nanotubes (CNT) interface grown on silicon and in dry contact with Ag foil. The accuracy for three unknowns exceeds already 15 %, which is in case of the determination of the thermal conductivity of thin films still acceptable. More unknowns further decrease the accuracy. However, it was also shown, that even if the individual properties are not accurately predicted, the total resistance is determined to an accuracy of 2 %.<sup>[67]</sup> Thus, the determination of the total resistance is a reasonable method for the evaluation of PA measurements. Furthermore, an effective thermal conductivity can be calculated by dividing the thickness by the total resistance.

Nevertheless, for a high sensitivity towards the sample layer thermal conductivity, the contact resistances should be low. Especially a high contact resistance in front of the sample, namely between sample and transducer layer reduces the sensitivity towards the sample layer.<sup>[67]</sup> Small contact resistances are usually achieved by evaporating the transducer layer on the sample, and directly cast the sample layer on the substrate, e.g., by spin-coating.

Overall, the PA method is a useful addition to other characterization techniques, like the  $3-\omega$  method, FDTR, and TDTR. Its drawbacks, like the small accuracy regarding the direct determination of the thermal conductivity are compensated by the simple setup and the almost unrestricted sample selection. For the phase shift evaluation, the sample must be thermally thin in the measured frequency range. This range is limited by the hardware but comprises usually an enormous range between 50 Hz to 20 kHz.



## 3 Materials and Methods

### 3.1 Materials

#### 3.1.1 Nanoparticles

The dimensions of NPs often determine their properties, like melting point, color, catalytic activity, or magnetic properties, compared to the bulk material. The effects can be divided into surface effects and quantum effects. Thereby, surface effects originate from the high surface area compared to the volume. The surface atoms are weaker bound and supply coordination sites in contrast to central atoms, which are entirely surrounded by other atoms of the material. For spherical particles with a radius  $r$ , the surface area ( $A$ ) to volume ( $V$ ) ratio is calculated by Equation 3.1.

$$\frac{A}{V} = \frac{4 \cdot \pi \cdot r^2}{\frac{4 \cdot \pi \cdot r^3}{3}} = \frac{3}{r} \quad (3.1)$$

The equation shows that  $\frac{A}{V}$  is dependent on the inverse radius. For spherical particles, the total number of atoms  $N$  scales linearly with the volume, and hence,  $N^{\frac{1}{3}}$  scales linearly with  $r$ . Consequently, all properties depending on the surface to volume ratio present a linear behavior when plotted against  $r^{-1}$  or  $N^{-\frac{1}{3}}$ .<sup>[37,68]</sup>

By contrast, the quantum effect only occurs in materials with delocalized electron states like metals and semiconductors. Here, the atomic orbitals typically combine to extended band structures. In NPs, the amount of orbitals is drastically decreased, and therefore, the density of states is reduced. As a consequence, the continuous bands are split off into discrete bands leading to the so-called quantum effect. Because the density of states scales with size, the quantum effect is also size-dependent but with another scaling than the surface effect.<sup>[37]</sup>

The range of materials for NPs is numberless and includes polymers<sup>[69]</sup>, metal-oxides<sup>[70]</sup>, semiconductors<sup>[71]</sup> and metals, like gold<sup>[72]</sup> or silver<sup>[73]</sup>. Most common are spherically shaped NPs, but also other shapes like nanorods<sup>[74]</sup>, cubes<sup>[70]</sup>, or stars<sup>[75]</sup> have been realized.

Metal NPs exhibit another effect, which is the localized surface plasmon resonance (LSPR). The LSPR are collective oscillations of the electrons in the conduction band. The size of NPs is usually referred to be between 1 nm and 100 nm. Hence, the wavelength of visible light is much larger than the NP size, and requirements for standing resonance conditions are fulfilled. When the wavelength of the light corresponds to the LSPR, the free-electrons in the metal start to oscillate. This leads to

a polarization of the electron density on the surface of the particles. This polarized electron density oscillates in resonance with the frequency of the light, causing a standing oscillation. It is illustrated in Figure 3.1.<sup>[76]</sup>

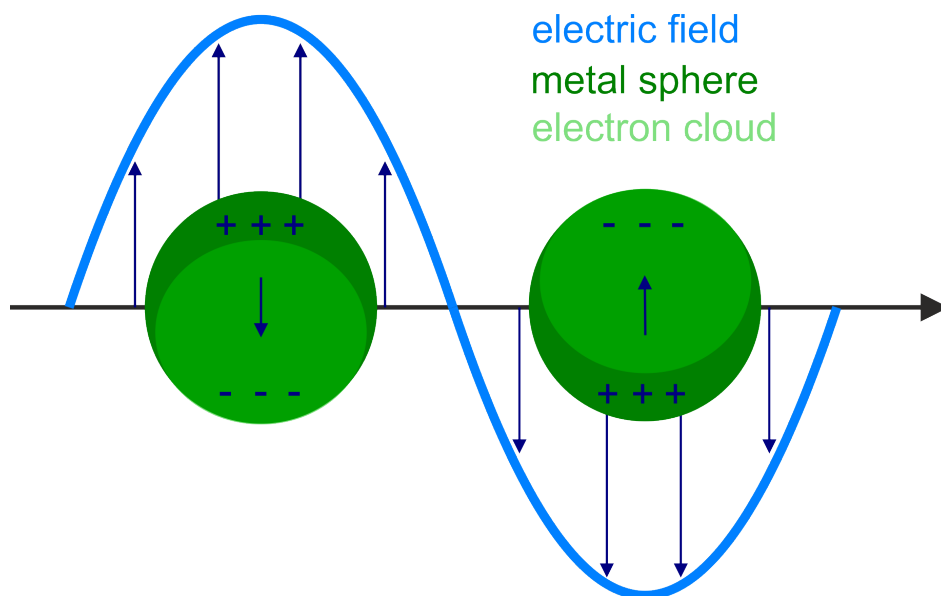


Figure 3.1: Schematic illustration of a localized surface plasmon. An electromagnetic wave induces an electric field, which in turn initiates the oscillation of free electrons from the metal surface. The frequency of this local oscillation is called localized surface plasmon resonance (LSPR). Adapted with permission of Annual Reviews, from Willets et al.<sup>[77]</sup>, Copyright 2007.

The LSPR depends on the size, shape, and dielectric constants of the metal and the surrounding medium. Thereof a vast amount of optical applications emerge. Examples are surface-enhanced Raman scattering (SERS)<sup>[78]</sup>, sensors<sup>[79,80]</sup> and thermo-plasmonic heating<sup>[81]</sup>. The latter exploits the absorbance of the LSPR to use NPs as nano heat sources. Thereby, it is possible to control the temperature at nanoscale by using a light source. Thermo-plasmonics find applications in photothermal cancer therapy. Compared to conventional dyes, the LSPR has a higher absorption coefficient. For this application, NPs are labeled with antibodies, which preferentially bind to cancer cells. The subsequent radiation leads to selective photodamage of the cancer cells.<sup>[82]</sup>

Concerning the strong dependence of NP properties on the size and shape, it is usually desirable to have monodisperse NP samples and, therefore, well-defined properties. The monodispersity of NPs depends strongly on the synthesis conditions. LaMer described a basic concept for growing monodisperse NPs. According to that, all nuclei must be formed homogeneously at the same time and afterward grow without further nucleation.

The LaMer plot in Figure 3.2 depicts the fundamental steps of the concept. Here

the concentration of a precursor is plotted against the time. In the first part of the plot (part I) the concentration of the precursor increases over the point of saturation ( $c_s$ ). However, due to the high energy barrier, the nucleation cannot occur yet. The further increase of the concentration leads to a critical level of supersaturation ( $c_{ss}$ ) above which the energy barrier is crossed, and nuclei are formed. The nucleation takes place in part II of the graph in Figure 3.2, and as a result, the precursor concentration decreases. After the concentration reaches the  $c_{ss}$  again, the nucleation stops because the energy barrier is too high. The growing nuclei consume the precursor and so the concentration of the precursor levels off at  $c_s$  (part III). In this way, the nucleation step is separated from the growth process, which leads to the same growing history of all particles, and in turn, to a good monodispersity.

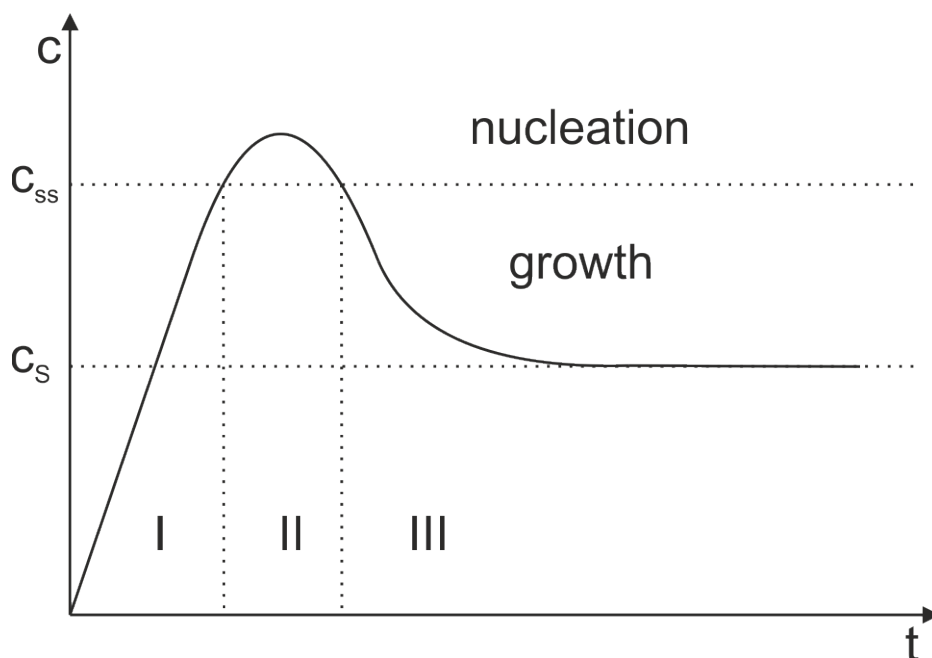


Figure 3.2: LaMer plot of the precursor concentration as a function of time. In the first part of the plot, the concentration increases over the point of saturation ( $c_s$ ). Due to the high energy barrier, no nucleation occurs. When the critical point of supersaturation ( $c_{ss}$ ) is reached (part II), the energy barrier can be overcome, and nuclei are formed. The formation of nuclei leads to a decreasing concentration of the precursor. Finally, the nucleation stops when the concentration of precursor falls below  $c_{ss}$  and, therefore, no more nuclei are formed. The remaining precursor is attached to the nuclei by diffusion in part III until  $c_s$  is reached again. Adapted with permission from Ref. [83]. Copyright 1950 American Chemical Society.

One target of this thesis was the three-dimensional assembly of silver NPs in a polymer matrix. Moreover, the interparticle distance in these assemblies should be controlled. Silver was chosen as core material, due to the high thermal conductivity of the bulk material in contrast to the insulating character of polymers. In order to produce enough material a high-yield synthesis leading to monodisperse particles

was desired.

There are, in principle, two methods for preparing Ag-NPs, either in water or in organic solvents. Thereby, the aqueous approach often only works with low silver-salt concentrations of  $0.1 \text{ mmol}\cdot\text{L}^{-1}$ <sup>[84]</sup> or results in particles with a broad size distribution<sup>[85]</sup>. By contrast, syntheses in organic solvents often lead to narrow size distributions<sup>[73,86–89]</sup>. In order to achieve the necessary colloidal stability in a highly concentrated metal NP dispersion, short-chain ligands have to be used, which form a dense corona around the metallic core. In case of amino-ligands<sup>[87,88]</sup> and especially thiol-ligands<sup>[89]</sup> the possibility to exchange the ligand is limited, because of the strong bonding of the functional group to the metal surface. That is the reason why synthetic routes with carboxy-ligands are preferred when targeting a subsequent ligand exchange.

For this thesis, the synthesis, according to Yamamoto *et al.*<sup>[73]</sup> was selected. The advantage of this synthesis is the possibility to produce large quantities (gram scale) while getting monodisperse particles in a simple one-pot synthesis. At the same time, a carboxylic acid functionalization enables a convenient ligand exchange.

### 3.1.2 Polymer synthesis

Polymer ligands give access to a broader range of distances between the NPs compared to conventional ligands, which often comprise of functional alkanes or other short molecules. Nevertheless, the demands are the same for both types of ligands. In other words the polymer ligands shall consist of linear chains with a functional end-group. Furthermore, it is of great importance to have a narrow molecular weight distribution (MWD), measured as the polydispersity index (PDI). If the MWD is too large, the length of the single polymer ligands will differ significantly. Hence, the control over the IPD in the PNC will be limited. Therefore, a synthesis route with reasonable control over the PDI is needed.

The lowest PDIs are known for polymers from anionic polymerization. However, the reaction requires rigorous conditions. Notably, this means it has to be carried out under the complete exclusion of air and water.<sup>[90]</sup> Consequently, it is accompanied by a high experimental effort.

For this reason, a controlled radical polymerization was chosen as a reasonable compromise between convenience and control. It can be performed under relatively mild conditions with a great variety of monomers but still provides low PDIs. Furthermore, reversible addition-fragmentation chain transfer (RAFT) polymerization offers trithiocarbonates as chain transfer agents (CTAs), which can be easily pro-

cessed into a variety of end-groups.<sup>[91]</sup> Notably, the simple transformation into thiol groups by aminolysis is attractive for subsequent ligand exchange.<sup>[92]</sup>

In a conventional chain-growth polymerization, three steps exist initiation, propagation, and termination. Moreover, in a free radical (FR) polymerization, usually side reactions occur, like chain transfer and termination.<sup>[90]</sup> The aim of a controlled radical polymerization is the elimination of these side reactions. A dynamic equilibrium between active (propagating) chains and inactive (dormant) chains ensures a controlled chain-growth.<sup>[93]</sup>

RAFT polymerization is a controlled radical polymerization. It is based on the principle of FR polymerization but displays characteristics of living polymerizations. In contrast to an FR polymerization, in RAFT polymerizations, a CTA is used to mediate the polymerization process, and thereby, to control the molecular weight and polydispersity. At the same time the RAFT process features an equal versatility, convenience, and applicability to monomers as conventional FR polymerization. Advantageously, polymer chains grown by RAFT polymerization can be reactivated for chain extension or used as precursors. Thus complex architectures such as block copolymers, dendrimers, star or brush polymers can be synthesized via different approaches<sup>[91]</sup> One of the features of RAFT is its tolerance to functional groups, including hydroxy, carboxylic acid, sulfonic acid and primary, secondary, tertiary, and quaternary ammonium.<sup>[94]</sup>

In the beginning, a RAFT polymerization proceeds identically to an FR polymerization via initiation by thermal, photochemical, or redox methods and subsequent propagation. The first line in Figure 3.3 shows the initiation step. In the following step the propagating polymer chain adds to the CTA, which is called chain transfer in Figure 3.3. An intermediate radical is formed before undergoing  $\beta$ -scission to either reform the polymeric radical or separating the leaving group of the CTA (R-group). In this concern, the R-group has to be chosen so that it preferably dissociates from the intermediate radical and subsequently can reinitiate polymerization (cf. Figure 3.3 reinitiation). The aim is to convert the initial CTA as fast as possible into the poly-CTA adduct and the R-group into a polymer chain so that an equilibrium between propagating and dormant species is obtained like it is presented in Figure 3.3. However, as RAFT polymerization involves free radical intermediates, some radical-radical termination cannot be avoided. Finally, a certain amount of dead polymer, determined by the number of chains initiated by initiator-derived radicals, will be formed.

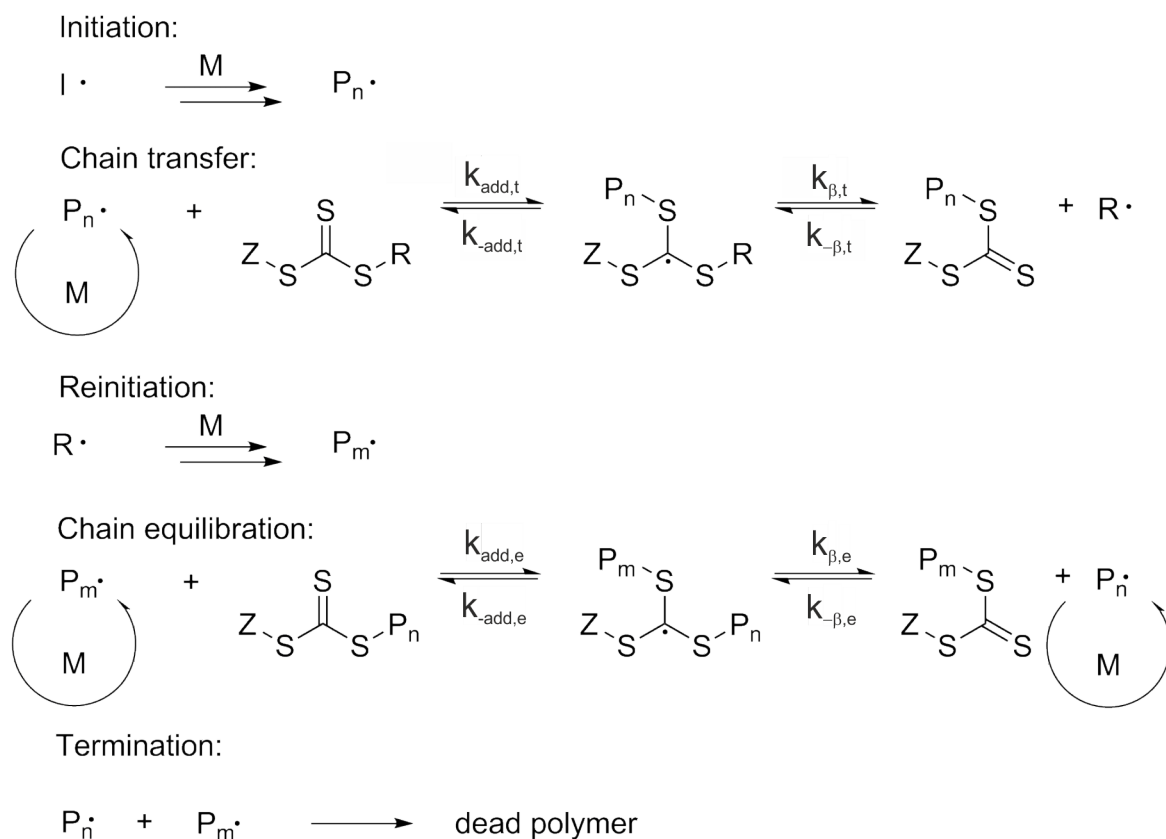


Figure 3.3: Mechanism of RAFT polymerization.

A crucial aspect of obtaining control over the polymerization is to balance the rates of the reactions mentioned above. Thereby, both the ratio between the dormant and the propagating species has to be very high, and the exchange between those two forms has to be fast. In this respect, the CTA has to be tailored to match the reactivity and the stability of the propagating polymer. Commonly used RAFT agents include thiocarbonylthio compounds such as dithioesters, dithiocarbamates, trithiocarbonates, and xanthates.<sup>[95]</sup> Figure 3.4 shows the general structure of a CTA on the left and the structure of 2-cyano-propyl dodecyl trithiocarbonate (CPDTTC), the RAFT agent, used in this work.

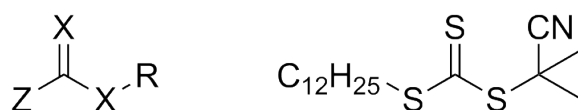


Figure 3.4: General structure of a CTA (left) and the structure of CPDTTC used in this work (right).

The substituents R and Z determine the effectiveness of RAFT agents. The R-group is the leaving group and must be able to reinitiate polymerization. The Z-group controls the reactivity of the CTA by stabilizing or destabilizing the intermediate radical. By this means, Z influences the rate of radical addition and fragmentation.<sup>[94]</sup> For

the polymerization of a particular monomer, both R and Z have to be adjusted in order to achieve minimal retardation and, therefore, a high fraction of living chains. Trithiocarbonates are less active than similar CTAs but still give good control over the polymerization of acrylic and styrene monomers. Moreover, they are less prone to hydrolytic degradation, lead to less retardation, and have better availability.<sup>[95]</sup> Furthermore, the obtained polymers, with a trithiocarbonate end-group, show the tendency to interact with Au-NPs.<sup>[96,97]</sup> As mentioned before, it is also possible to transform the trithiocarbonate groups into thiol groups, which is desirable for the preparation of polymer-metal nanocomposites. A reaction with any nucleophile can achieve the transformation.<sup>[91]</sup> Nevertheless, in this work, only aminolysis is used. Deletre and Levesque described the mechanism of this reaction.<sup>[92]</sup>

The synthesis of the PS ligands was adapted from Mayadunne et al.<sup>[98]</sup> They reported the bulk polymerization of styrene by thermal initiation at a temperature of 110 °C. Their molecular weight data show an excellent correlation to Equation 3.2. Accordingly, a controlled character can be assumed.

$$M_n(\text{calc}) = \frac{[\text{monomer}]}{[\text{CTA}]} \cdot \text{conversion} \cdot M_{\text{monomer}} \quad (3.2)$$

With Equation 3.2, it is possible to predict the molecular weight of the polymer. The prediction of the molecular weight is of great importance because ligands with different molecular weights are needed to adjust the IPD in the nanocomposite. A significant advantage of this synthesis is that only two components are used, styrene as monomer and CPDTTC as CTA. Seven polymer ligands with varying molecular weight were synthesized. The reaction parameters are given in Table 6.1 of Section 6. The ratio [styrene]/[CTA] was chosen in that manner, that they reach the desired molecular weight at a conversion of 80 %. The reason for this precaution is the gel effect. As the polymerization is conducted in bulk, very high conversions would lead to an uncontrolled increase of viscosity. In order to determine the correct time to quit polymerization, the conversion was monitored by nuclear magnetic resonance (NMR) spectroscopy. For this purpose, samples were taken from time to time. The conversion was calculated using Equation 3.3.

$$\text{conversion} = \frac{\int_{6.3}^{7.5} (\text{ppm}) d\text{ppm} - 6 \cdot \int_{5.7}^{5.9} (\text{ppm}) d\text{ppm}}{\int_{6.3}^{7.5} (\text{ppm}) d\text{ppm} - 1} \quad (3.3)$$

The integral between 6.3-7.5 ppm is assigned to the protons of the aromatic ring in the monomer and the polymer (position 1-3) and the proton of the vinyl group of the styrene monomer next to the ring (position a). The other protons of the monomer

(position b) exhibit a doublet at 5.7-5.9 ppm and 5.3-5.4 ppm, respectively. The unambiguous allocation of these signals allows us to use them as references. The integral of one doublet is assigned to precisely one proton. Consequently, the signal was used to normalize the integrals to the number of protons. Six protons have to be subtracted from  $\int_{6.3}^{7.5}(\text{ppm})d\text{ppm}$  to obtain the portion of protons of the polymer. Subsequently, this portion is divided by the amount of all protons of the styrene ring ( $\int_{6.3}^{7.5}(\text{ppm})d\text{ppm} - \text{proton a}$ ). As a consequence, the ratio between the protons of the styrene ring inside the polymer and in the monomer is received and thereby the conversion of monomer into polymer. As an example, the NMR spectrum of the polymerization of PS18k after 22 h is shown in Figure 3.5. All spectra were evaluated accordingly.

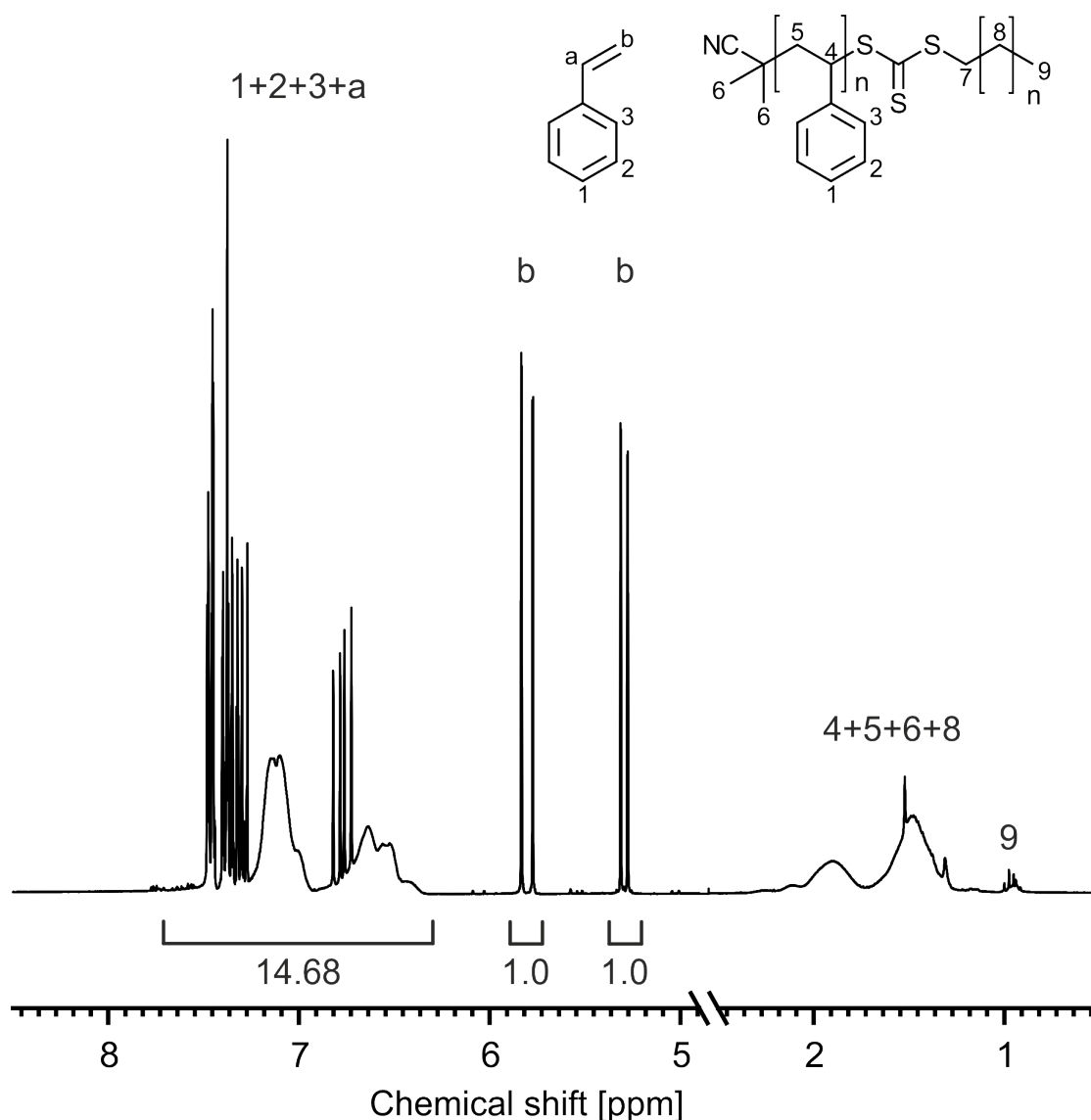


Figure 3.5:  $^1\text{H}$ -NMR spectra of the polystyrene synthesis of the PS18K sample after 22 h. The conversion was determined to be 63.5 %.  $^1\text{H}$ -NMR(300 Mhz,  $\text{CDCl}_3$ ):  $\delta(\text{ppm}) = 6.3-7.5$  (m,  $\text{H}_{1-3,a}$ ), 5.7-5.9 and 5.3-5.4 (d,  $\text{H}_b$ ), 1.3-2.3 (m,  $\text{H}_{4-6,8}$ ), 0.9 (t,  $\text{H}_9$ ).

Since the RAFT polymerization belongs to the controlled/living polymerization techniques, we assume a fast initiation and the absence of termination and transfer reactions. Therefore, Equation 3.4 describes the polymerization rate. The integration of Equation 3.4 leads to Equation 3.5.

$$v_p = -\frac{d[M]}{dt} = k_p \cdot [M] \cdot [P^*] \quad (3.4)$$

$$[M] = [M]_0 \cdot e^{k_p \cdot [P^*] \cdot t} \text{ or } \ln \frac{[M]_0}{[M]} = k_p \cdot [P^*] \cdot t \quad (3.5)$$

From the right side in Equation 3.5, it is apparent that the relation between  $\ln([M]_0/[M]_t)$ , and the reaction time has a linear behavior. In Figure 3.6, all performed polymerization show this behavior. Hence, the controlled character of those is proofed. Moreover, the linear relation was used to calculate the point to terminate the reaction with a conversion of 80 %.

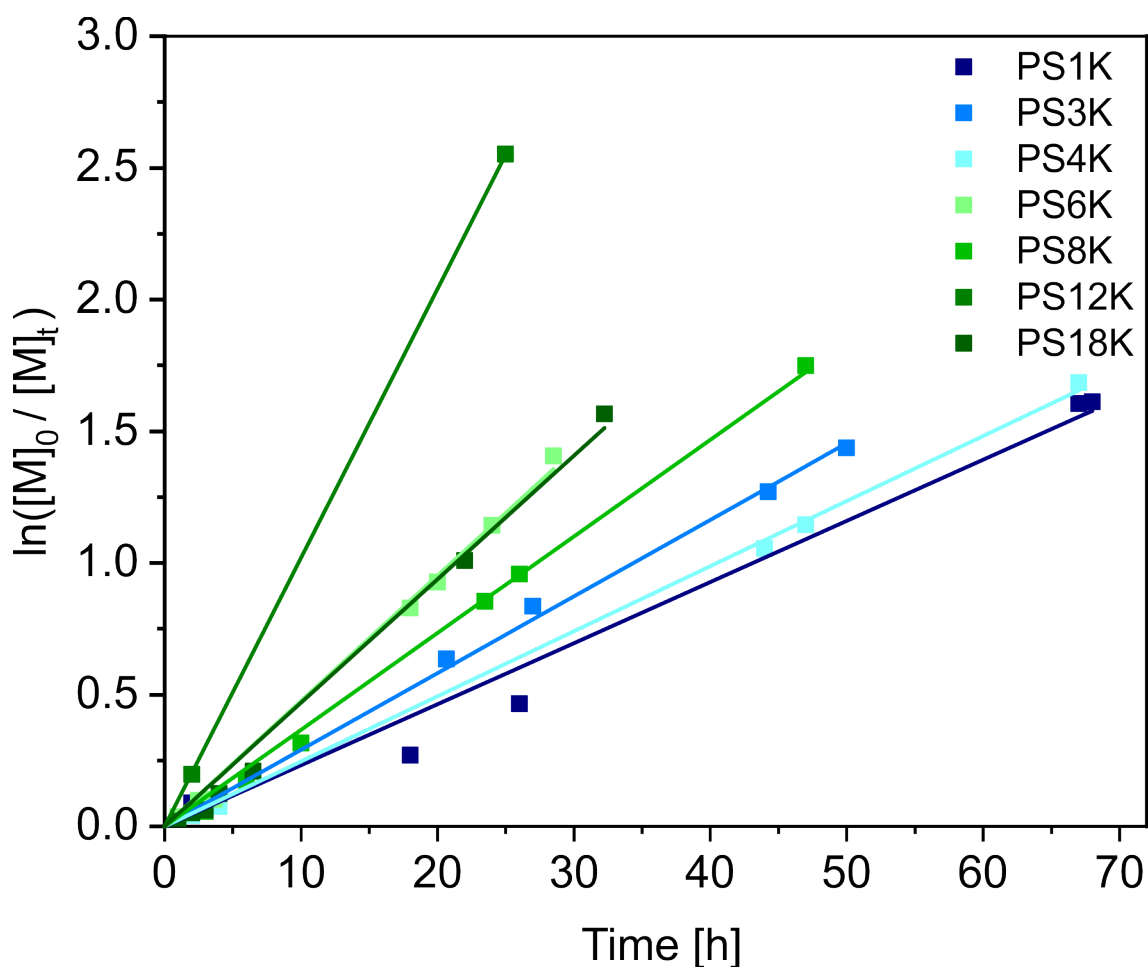


Figure 3.6: The linear behavior of  $\ln([M]_0/[M]_t)$  plotted against the time proves the living character of the RAFT polymerization. The slope increases with increasing monomer concentration.

The slope in the chart above represents  $k_p \cdot [P^*]$ , which directly influences the reaction rate, as it can be seen in Equation 3.4. The slope is steeper for polymerizations achieving higher molecular weights. Thus, the reaction rate is higher for these polymerizations. Two different factors are the reason. First, the higher the targeted molecular weight, the higher  $[M]$ . As the polymerization is self-induced by thermal initiation, a high  $[M]$  equates to a high  $[I]$ . Further on, a high  $[I]$  yields a high  $[P^*]$ . Second, the  $[CTA]$  influences the equilibrium between  $CTA + P^*$  and  $CTA^*-P$ , which is shown in the RAFT mechanism in Figure 3.3. The  $[CTA]$  is low if the targeted molecular weight is high, and vice versa. Thus,  $k_{-add,e}$  is favored, and  $[P^*]$  is higher. In both cases,  $[P^*]$  is increased, which in turn affects the reaction rate.

Overall, it is possible to produce linear polystyrene ligands with thiol end-group by RAFT polymerization. A series of designated molecular weights with a narrow distribution were obtained. For this purpose, the ratio of  $[M]/[CTA]$  was varied. The characterization of the obtained polymers is described in Section 6, Figure 6.2. All polymerizations showed a controlled character, as it is seen in Figure 3.6. The observed increase in reaction rate for polymers with higher targeted molecular weight is attributed to two factors and expected for this kind of reaction.

### 3.1.3 Nanocomposites

When integrating NPs into polymer matrices, one speaks of PNC or hybrid materials. The latter is the case when the mixing occurs at molecular level, as mentioned in Section 2.1.3. The principal target, when engineering composites is to achieve synergistic effects from the properties of both components. Looking at PNC this is usually the combination of the favorable processability of polymers with the properties of the filler material. In hybrid materials it is even possible to produce entirely new material properties by introducing a vast number of interfaces by structures at the nanoscale.<sup>[52]</sup>

However, a big issue is the aggregation of NPs and the related loss of any benefits of the NPs.<sup>[40]</sup> To prevent this, the NPs have to be stabilized. A convenient way of stabilization is a polymer brush attached to the NP surface.<sup>[99]</sup> Polymer brushes are linear polymer molecules that are attached with one end to the surface, and the other end freely stretched away from the surface. Due to the low segment density at their periphery, sufficient conformational freedom for the matrix polymer is provided, and as a result, the NPs become miscible with the matrix. The different routes to prepare polymer brushes are divided into grafting-from and grafting-to processes.<sup>[40]</sup>

Grafting-from processes require an anchoring group to start the polymerization

from the NP surface. For a uniformly thick shell, it is also of interest to use a controlled polymerization technique. One possibility is to polymerize from the surface by immobilization of an initiating group. Skaff et al.<sup>[100]</sup> demonstrated this with a catalyst for ring-opening metathesis polymerization (ROMP) immobilized on the surface of CdSe-NPs. Other systems are based on controlled radical polymerization. Ohno et al.<sup>[101,102]</sup> used atom transfer radical polymerization (ATRP) to grow linear poly(methyl methacrylate) (PMMA) polymer chains from Au-NPs, achieving a grafting density of  $0.3 \text{ nm}^{-2}$  and a distance control by variation of the molecular weight. Li *et al.*<sup>[103,104]</sup> anchored different CTAs on silica-NPs for subsequent RAFT polymerization of methyl methacrylate (MMA). The polymer brushes had a grafting density of up to  $0.54 \text{ nm}^{-2}$ . An advantage of the grafting-from method is the relatively low content of excess polymer<sup>[104]</sup>, which is desirable for an assembly of the nanocomposites in an ordered structure.

In contrast, grafting-to methods couple a preformed polymer to the NP. For this reason, a functional group at the surface of the particle, as well as in the polymer chain, or more usual at the end of the chain, is necessary. Examples of coupling reactions are click-reactions. For instance, azide functionalized PS was coupled to the strained double bonds of C60 fullerene, and single-wall carbon nanotubes (SWCNT)<sup>[105]</sup> or carboxylic acid functionalized PS was linked to epoxy functionalized surfaces.<sup>[106]</sup>

The ligand exchange is another approach counted to the grafting-to methods. Here, the initially used ligands during NP synthesis are substituted by a polymer ligand. Again, the polymer ligand needs at least one functional group. However, at this time, the functional group is not used to form a covalent bond but rather to coordinate with the NP. For polymer brushes, the functional group is typically located at the end of the polymer chain, but also  $\alpha$ - $\omega$  functionalized polymers can be used whereby one group attaches to the NP, and the other introduces a functional group at the outside of the NP shell. Such configurations, for example, provide the possibility to cross-link NPs.<sup>[107]</sup>

A significant advantage of this method is that both the NPs and polymer ligands are synthesized separately. Hence, reaction conditions can be chosen independently regarding solvent, temperature, inert gas, etc. This is of importance when the NPs are sensitive to polymerization conditions.

The functionality of the polymer can be a single functional group, like carboxylic acid, amino, or thiol groups, as well as a whole functional block (e.g., a 2-vinyl pyridine block) of a block-copolymer.<sup>[108]</sup> As mentioned before, there are no restrictions for the ligand synthesis, so theoretically, every polymerization method that can lead to a functional group in the polymer chain can be exploited.

The ligand exchange approach has already been shown for many different NP/ligand combinations<sup>[109–111]</sup>. Accordingly, it has proved its applicability to a vast range of material combinations. This versatility is the main advantage of the ligand exchange process. It is based on the possibility to independently synthesize the individual components and combine them in a second, separated step.

The ligand exchange process and the subsequent purification is shown schematically in Figure 3.7. On the left side, the functionalized polymer ligands are added to the pre-synthesized NPs. Both components are in the same solvent, that is why it is called single-phase ligand exchange. The mixture is incubated for an appropriate time to substitute the initial ligands by the polymer ligand. Because the ligand exchange is an equilibration process, a high excess of polymer ligand is required.

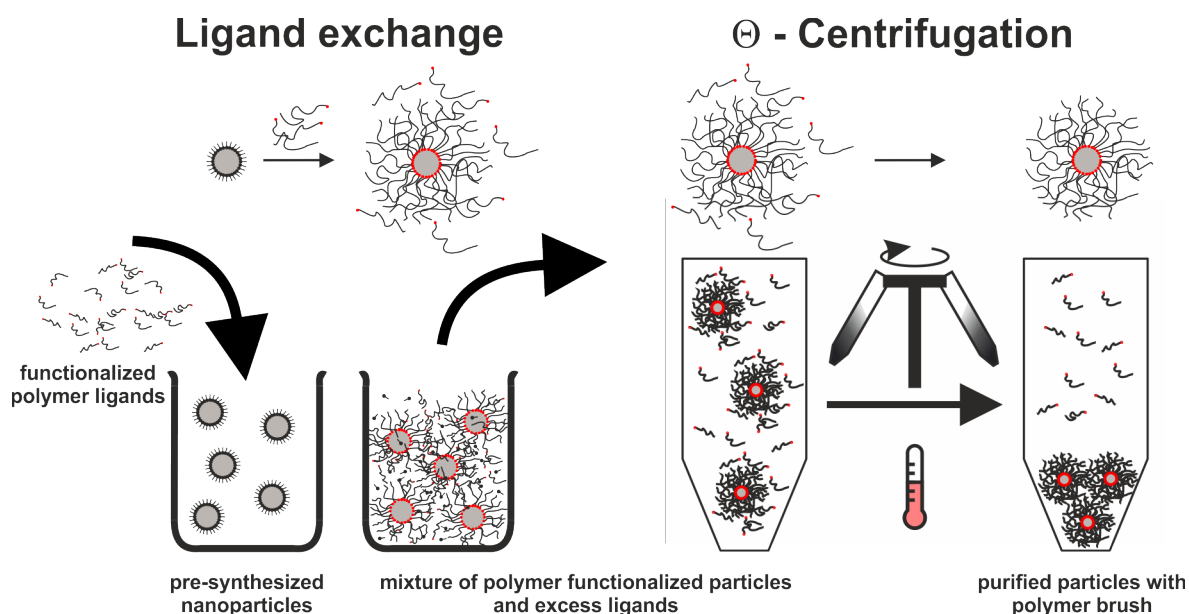


Figure 3.7: Schematic illustration of the ligand exchange and the subsequent purification. In the first step, the functional polymers are added to the pre-synthesized nanoparticles. The mixture of polymer brush functionalized particles, excess ligand, and short alkane ligand is then quantitatively precipitated and centrifuged. A centrifugation step at  $\theta$ -conditions finally removes the remaining excess ligand. The purified, polymer brush functionalized particles are obtained.

However, generally, a high excess alone is not sufficient for complete ligand exchange. The high concentration of the initial ligand at the surface of the NPs is usually hindering a quantitative exchange. By precipitation of both the NPs and the polymer ligand, the concentration of the latter is locally increased at the surface of the NPs. Consequently, the efficiency of the ligand exchange is highly improved.<sup>[111]</sup> This step is also called quantitative precipitation and finishes the ligand exchange.

A drawback of this procedure is the high excess of polymer ligand that needs to be used. It remains as free chains in the sample. A method to remove unbound poly-

mer is the so-called selective precipitation that is described in the literature.<sup>[111]</sup> The selective precipitation is based on the principle that nanocomposite and unbound polymer have different solubilities, due to their different molecular weights. Thus, only a small amount of a nonsolvent is used, just until the nanocomposites begin to precipitate, leaving the free polymer in solution. The precipitate is separated from dissolved free polymer by centrifugation. If necessary, this step is repeated multiple times to achieve a complete separation of the nanocomposites from the free polymer. However, this procedure turned out to be synthetically challenging and very time-consuming.

For this purpose, another procedure was developed, the so-called  $\theta$ -centrifugation. The method is illustrated on the right side of Figure 3.7 and is described in detail in Chapter 6.2.4 and 6.3. It is based on the simple centrifugation at  $\theta$ -conditions of the ligand. In this way, the unbound ligand stays dissolved, while the colloidal stability of the polymer-coated particles is reduced. As a consequence, the particles precipitate during the centrifugation. Instead of numerous selective centrifugation steps, it is sufficient to centrifuge once at  $\theta$ -conditions. Hence, this method presents a considerable advantage compared to the procedures described in the literature.

A material based on the purified nanocomposites presents a distinct interparticle distance (IPD). It depends on the molecular weight of the polymer ligand, which forms the matrix phase in the hybrid material. By variation of the molecular weight of the polymer ligands, a multitude of IPDs can be achieved.<sup>[109,111]</sup> The possibility to adjust the IPD presents another advantage of the ligand exchange method. All the advantages originate from separated synthetic routes for NP and polymer ligands. Therefore, almost an unlimited amount of material combinations is imaginable.

In this thesis, only one material combination was chosen as a model material to investigate the structure-property relationships concerning the IPD. Silver cores with a short alkane carboxylate, described in Chapter 3.1.1, and polystyrene ligands of different molecular weights, described in Chapter 3.1.2, were used as starting material. The ligand exchange was conducted in toluene. The purification, though, in cyclohexane, which fulfills the  $\theta$ -conditions for polystyrene at 35 °C. The total synthesis is described in detail in Chapter 6. The characterization of the resulting material is discussed in Chapters 6 and 7.

### 3.1.4 Sample preparation for PA measurements

The samples for PA measurements were all prepared on 1 mm thick glass substrates, with dimensions of 25 x 25 mm. For the deposition of the materials on the substrates, two different techniques were used. All samples used in Chapters 7 and 10 were spin-cast with an SCS G3 Spin Coater from Specialty Coating Systems (Indianapolis, IN, USA). The samples from Chapters 9 and 8 were spray-coated with a fully automatic spray coating system equipped with a SATA 4000 LAB HVLP 1.0 mm spray gun (SATA GmbH & Co. KG, Germany). The specific coating parameters are given in the respective sections. In principle, films with thicknesses of 200 nm to 2  $\mu\text{m}$  were used for the PA measurements. For the absorption of the laser beam, a 100 nm to 200 nm Au film was evaporated on the samples. Therefore, a Balzers (Liechtenstein) BA360 thermal evaporation chamber was used. For better adhesion of the gold layer, a 3 nm chromium layer was evaporated before the gold deposition. In Section 10, humidity dependent measurements were performed. For this purpose, the samples were stored at different relative humidities, adjusted by saturated salt solutions. The procedure is described in detail in the named section.

## 3.2 Methods

### 3.2.1 Photoacoustic method

A scheme of the PA setup used in this work is shown in Figure 2.8. A continuous-wave laser Coherent Genesis MX488-1000 ( $\lambda = 488 \text{ nm}$ , max. power 1 W) was modulated using a ConOptics M25A EOM. The integrated function generator of a Zurich Instruments lock-in amplifier HF2LI produced the periodical signal. The Au transducer layer (see Figure 3.8 top layer) absorbs the laser beam. A Bruel & Kjaer 4398-A-011 microphone detects the PA signal. A Bruel & Kjaer 2690-0S1 amplifier with 1 V/Pa or 3.16 V/Pa, then amplifies the signal to reach a maximum amplitude between 300 mV and 700 mV. A 10 Hz high-pass filter and a 22.4 kHz low-pass filter were applied.

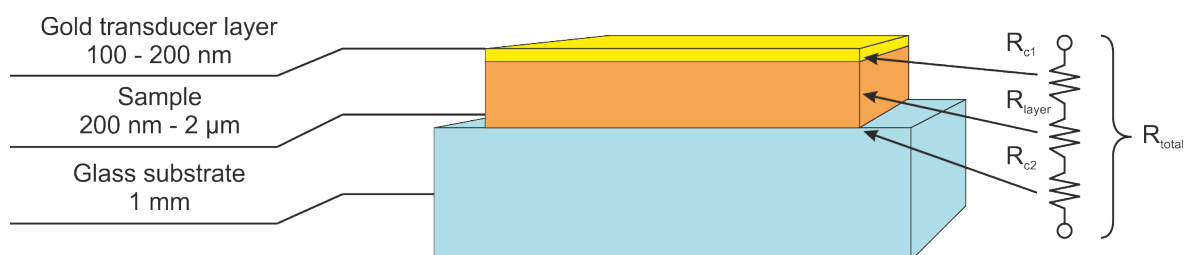


Figure 3.8: Schematic sample structure for PA measurements.

The measurement conditions should be chosen in such a way that the temperature field completely penetrates the sample and advances into the substrate. The penetration depth depends on the thermal diffusion length,  $l_\alpha$ . Measurements performed at a ratio of  $l_\alpha/l = 10$ , where  $l$  is the sample thickness, have shown an uncertainty of 5 %. The uncertainty increases to 15 % when the ratio is increased to 100.<sup>[56]</sup> Because the thermal diffusion length  $l_\alpha$  depends on the frequency ( $l_\alpha = \sqrt{2\alpha/f}$ ), the frequency can be adjusted to reach the desired ratio.

For polymeric samples, where the thermal diffusivity,  $\alpha$  is in the range of  $10^{-7} \text{ m}^2/\text{s}$ <sup>[112]</sup> and thicknesses between 200 nm and 2  $\mu\text{m}$ , a frequency range between 110 Hz and 4000 Hz is appropriate. Only for very thin samples ( $\sim 200 \text{ nm}$ ), the range was extended to 6000 Hz. All measurements were determined in a helium atmosphere at room temperature. The set pressure was 20 psi, corresponding to 1.379 bar.

Data fitting was accomplished by using a MATLAB script provided by the Georgia Institute of Technology, written by Thomas L. Bougher (Photoacoustic Data Fitting, Version 2.3a, June 2012).<sup>[18]</sup> It uses the Levenberg-Marquardt method to fit the unknown parameters. It combines the steepest descent and Hessian methods, which means it takes substantial steps when far away from a minimum and reduces the step width when approaching the minimum - this way, the method prevents the overestimation of the final values. Moreover, the initial guess values are altered to ensure that a global, instead of, a local minimum is found.

Even with this approach, the accuracy of the parameter estimation depends strongly on the selection of reasonable initial guess values and the number of known parameters. As discussed before, the phase shift depends on  $B_{N+1}$ , which consists of the densities, thermal conductivities, specific heat capacities, thicknesses, optical absorption coefficients, and interface resistances of the different layers (transducer, sample, substrate). The properties of the substrate and the transducer layer are listed in the literature. The optical absorption coefficients do not play a role if the laser is only absorbed in the transducer layer. The densities, specific heat capacities, and thicknesses of the samples can be determined by helium pycnometry, differential scanning calorimetry (DSC), and atomic force microscopy (AFM), respectively. Finally, the thermal conductivity of the sample, and the two bordering interface resistances  $R_{c,1}$ , and  $R_{c,2}$  stay unknown. With the PA method, it is possible to fit those parameters. However, the uncertainty is high when fitting three parameters. Moreover, fitting results may differ for the single values, while a satisfactory overall fit is achieved. Fortunately, the total layer resistance,  $R_{total}$ , is relatively independent of the thermal diffusivity (and, therefore, thermal conductivity) of the sample.<sup>[67]</sup> It is the sum of the two interface resistances and the layer resistance of the sample, as it

is illustrated in Figure 3.8, i.e., it unites the three fitting parameters. Consequently, the measurements are only evaluated in terms of  $R_{total}$ , leading to reliable results. Additionally,  $R_{total}$  can be converted into the effective thermal conductivity of the sample layer. Therefore, the layer thickness is divided by  $R_{total}$ .

$$\kappa_{eff} = \frac{l}{R_{total}} \quad (3.6)$$

In comparison to the literature, the lens usually placed in front of the cell, to focus the laser beam on the sample was dismissed in the used setup (Figure 2.8). Experiments showed that it is not necessary to focus the laser for the conducted experiments. It can be even unfavorable to focus the laser on a small area of the sample, due to thermal losses, or beam damage. Figure 3.9 shows the results of different PA measurements. The samples were a 107  $\mu\text{m}$  brass plate pressed on a glass substrate and a 2.3  $\mu\text{m}$  PS film spin-cast on a glass substrate. The spot size of the laser was varied with a lens in front of the glass cell. In Figure 3.9a and b, it can be seen, that the signal changes from a spot size of 500  $\mu\text{m}$  to 1200  $\mu\text{m}$ , but the measurement curves are overlaying for a spot size of 1800  $\mu\text{m}$  and 2500  $\mu\text{m}$ . When evaluating the data, it becomes clear that at smaller spot sizes, the thermal conductivity is underestimated for the PS sample (Figure 3.9d). This is explained by thermal losses perpendicular to the laser beam. Consequently, a two-dimensional heat flow occurs, whereas the model from Hu et al.<sup>[55]</sup> assumes a one-dimensional heat flow. Therefore, the data will only be appropriately fitted as long as the thermal losses can be neglected. This is the case when the spot size reaches a specific size. Especially for samples with low thermal conductivity, two-dimensional heat flow can be an issue. That is why the effect is not present for the brass sample, which thermal conductivity scatters around the expected value. For the PS sample the effective thermal conductivity increases steadily from 0.087 W/mK at a spot size of 500  $\mu\text{m}$  to 0.124 W/mK at a spot size of 1800  $\mu\text{m}$ . At this spot size the effective thermal conductivity levels off. The determined value is still lower compared to literature values of 0.139 W/mK<sup>[113]</sup>, determined by xenon flash analysis (XFA) measurements. However, this can be explained by the fact that the effective thermal conductivity was determined, which is affected by the thermal resistances between transducer and sample, as well as sample and substrate.

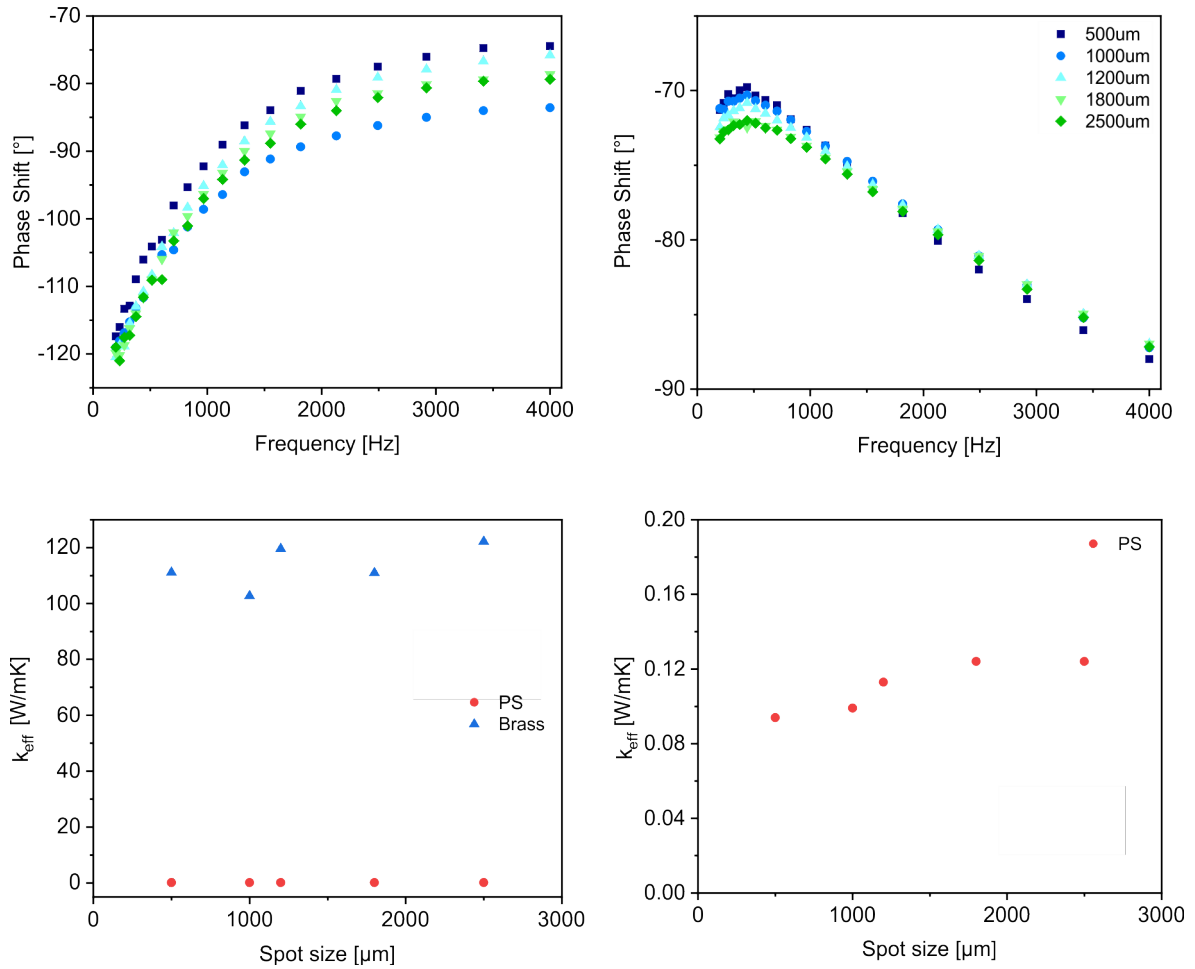


Figure 3.9: PA measurements performed on a PS sample (a) and a brass sample (b). The laser spot size was varied throughout the measurements. The evaluated effective thermal conductivities are shown in (c) and (d). In (d), the Y-axis is zoomed in to see the variation of the thermal conductivity with spot size. At a spot size lower than  $1800 \mu\text{m}$  heat losses cannot be neglected anymore for samples with low thermal conductivity like PS. Therefore, the thermal conductivity is underestimated. The thermal conductivity of brass is high enough so that the thermal losses can be neglected over the full range of spot sizes.

### 3.2.2 Further methods

#### Transmission electron microscopy

Transmission electron microscopy (TEM) is a powerful method to image small structures. Due to the short wavelength of electrons, very high resolutions in the nanometer regime can be achieved. The electron gun produces an electron beam. The accelerating voltage usually lies between 80 kV and 300 kV. After passing the anode at high velocity, the electrons enter the illumination system. There, the beam is focused

by the condenser lenses. When passing through the specimen, the electrons are scattered. For a projection of the sample, the scattered electrons have to be focused by electromagnetic lenses in the imaging-forming system.<sup>[114]</sup>

The image contrast occurs by interactions of the incident electrons of the beam with the atoms of the sample. Two fundamental scattering mechanisms are distinguished, elastic, and inelastic scattering. Elastic scattering can be considered as an electron-nucleus interaction with a negligible energy loss but a change of direction. This kind of scattering increases with the atomic number of an element. Inelastic scattering is an electron-electron interaction and is therefore dependent on the electron density. Here not only the direction of the electron is changed, but also a partial energy loss occurs.<sup>[115]</sup> As a result of scattering, a fewer amount of electrons will reach the detector, and the sample appears darker in regions with strong scattering.

Due to the higher electron density of atoms with a higher atomic number, there is a contrast between metal NP and the polymer matrix. Therefore, transmission electron microscopy (TEM) can be used to determine the size of the metal NP, but also, the IPD in the nanocomposites can be measured.

In this work, a Zeiss (Jena, Germany) EM922 Omega TEM and a JEOL (Akishima, Japan) JEM-2200FS TEM, both with an acceleration voltage of 200 kV, were used.

Samples were prepared by drop-casting and spin-coating. For the drop-cast samples 5  $\mu\text{L}$  of a diluted dispersion of the NP or nanocomposite sample were deposited on a TEM grid with a thin carbon layer on it and blotted with filter paper. The film samples were spin-cast on glass substrates. Subsequently, the samples were immersed in a dish of water. The films peeled off the glass and floated on the water surface. From there, the films were transferred to TEM grids. However, this procedure did not apply to the thermally annealed films in Section 7. The thermal annealing led to an increased adhesion between PNC film and glass substrate.

For this reason, a sacrificial layer of ZnO was coated in between. The ZnO layer was prepared by spin-coating a zinc acetate solution (110 mg zinc acetate in 30  $\mu\text{L}$  2-amino ethanol and 1 mL 2-methoxy ethanol) at 3000 rpm for 50 s. Afterward, the substrates were baked for 5 min at 150 °. The nanocomposite films were spin-coated on top of the ZnO layers. After thermal annealing of the samples, the ZnO layers were dissolved in 1 M HCl. The hydrophobic PNC films were unaffected by the acid and floated on the liquid surface. As before, the films were transferred to TEM grids.

## Differential scanning calorimetry

The specific heat capacity at constant pressure,  $c_p$ , was determined by DSC measurements. In principle, in a DSC measurement, a sample and a reference (usually an empty pan) are heated with a constant heating rate. At a phase change, the enthalpy of the sample changes. Therefore, the heat flow changes compared to the reference. The change of the heat flow is related to  $c_p$ , which is shown in Equation 3.7.

$$c_p = \frac{C_p}{m} = \frac{1}{m} \cdot \frac{dH}{dT} = \frac{1}{m} \cdot \frac{\dot{Q}_p}{\dot{T}} = \frac{\dot{q}_p}{\dot{T}} \quad (3.7)$$

Where  $C_p$  is the heat capacity,  $dH$  the change in enthalpy,  $\dot{Q}_p$  the heat flux,  $\dot{q}_p$  the specific heat flux, and  $\dot{T}$  the rate of change of temperature. For the determination of the  $c_p$ , the heating rate has to be calibrated. This is done with a sapphire ( $\text{Al}_2\text{O}_3$ ) standard sample.

DSC measurements were accomplished on a TA Instruments (New Castle, DE, USA) Discovery DSC 2500. Besides the  $c_p$  measurements in Chapters 7, 9, 8, and 10, DSC was also used to determine the  $T_g$  in Chapter 7 and to proof the lack of crystallinity in the ampholytic polymer samples in Chapter 10. The exact conditions are described in the respective section.

## Thermal gravimetric analysis

In thermal gravimetric analysis (TGA), the mass change of a sample, dependent on temperature and time, is measured. Therefore, degradation steps of different components can be differentiated. With the knowledge of the degradation temperature of an individual component, the mass fraction can be calculated by employing the relative mass loss.

For the measurement, the sample is stored in an inert sample holder and heated with a constant heating rate. The mass loss is detected dependent on temperature and time. On the one hand, mass losses can occur through evaporation or decomposition. On the other hand, the mass can increase by chemical reactions (e.g., oxidation) with molecules of the surrounding atmosphere. The measurement chamber is purged with an inert gas like  $\text{N}_2$ , to prevent oxidation of the sample. For polymers, usually the thermal stability and decomposition are of interest.

For the evaluation, the relative mass loss is plotted versus the temperature. Due to the mass loss of degradation, a step is observed in the diagram. The position of the step depends on the experimental conditions, like the heating rate or the atmosphere, and therefore has no absolute significance. Sometimes two or more decomposition steps are superimposed, which can be distinguished more clearly by the derivative of the relative mass loss (differential thermal gravimetric analy-

sis (DTGA)). At the position of the highest mass loss a peak occurs in the DTGA diagram. By that, two peaks might be easier to distinguish than two inflection points.<sup>[116]</sup>

In the case of ligand stabilized NPs, where the NPs are temperature stable, TGA can be used to detect the weight fractions of the individual components. Therefore, the mass loss, which can be ascribed to the ligand, is determined. In turn, the residual mass belongs to the NPs. With the information of the weight fraction of the NPs ( $X_{np}$ ) and the information of the size (radius  $r$  respectively diameter  $d$ ) of the NPs, the molecular weight of the polymer  $M$  and the bulk density of the NP material  $\rho_{np}$  the grafting density  $D$  can be calculated with equation 3.8, where  $N_A$  is the Avogadro constant.<sup>[117]</sup>

$$D = \frac{4 \cdot r^3 \cdot \rho_{np} \cdot N_A \cdot (100 - X_{np})}{3 \cdot d^2 \cdot M \cdot X_{np}} \quad (3.8)$$

The TGA measurements were conducted on a Mettler Toledo (Columbus, OH, USA) TGA/STDA 851e Star System at a heating rate of  $10 \text{ K} \cdot \text{min}^{-1}$  in a temperature range between  $30 \text{ }^\circ\text{C}$  and  $700 \text{ }^\circ\text{C}$  and under a nitrogen flow of  $50 \text{ mL} \cdot \text{min}^{-1}$ .

### UV/Vis spectroscopy

Ultraviolet and visible light (UV/Vis) spectroscopy observes the interaction of electromagnetic radiation and matter in the wavelength range between 200 nm and 750 nm. In molecules, this often corresponds to the excitation of an electron of the highest occupied molecular orbital (HOMO) to the lowest unoccupied molecular orbital (LUMO). In metal NP like gold and silver, the electromagnetic radiation excites the band electrons to a collective oscillation, which is called plasmon. This oscillation leads to an absorption peak in the extinction spectrum. At the same time, the sample appears in the complementary color of the absorption peak. The plasmon resonance depends on material, size and shape of the NPs. The extinction  $E$  (or absorbance) describes the reduction of the initial light intensity by absorption, scattering, and reflection. It is defined as the negative logarithmic ratio of the light intensity after passing the sample  $I$  to the initial intensity  $I_0$ .

$$E = -\log \frac{I}{I_0} = \varepsilon \cdot c \cdot d \quad (3.9)$$

In the Lambert-Beer law (Equation 3.9), extinction is also related to the concentration  $c$ , while  $\varepsilon$  is the wavelength-dependent extinction coefficient, and  $d$  is the path length through the sample.

An Analytik Jena (Jena, Germany) SPECORD 250 Plus spectrophotometer was used

to measure the ultraviolet and visible light (UV/Vis) spectra. For the measurement of liquid samples, high-precision quartz glass cuvettes 110-QS of *Hellma*, with a thickness of 10 mm, were used. Solid samples were measured on glass substrates.

### IR spectroscopy

Like in UV/Vis spectroscopy, in IR spectroscopy, the interaction of electromagnetic radiation with matter is investigated. The difference, however, is the wavelength of the radiation. The range of IR radiation comprises the wavelength range between 750 nm to 1 mm. Hence, it connects seamlessly to the upper end of the UV/Vis spectrum. The IR region is further divided into Near-Infrared (NIR), Mid-Infrared (MIR), and Far-Infrared (FIR). In conventional IR spectroscopy, only the MIR region is of interest. The typical wavelength range is from 2.5  $\mu\text{m}$  to 25  $\mu\text{m}$ . In terms of IR spectroscopy, it is more familiar to use the wavenumber,  $\bar{\nu}$  instead of the wavelength. The wavenumber is the inverse wavelength ( $\bar{\nu} = 1/\lambda$ ) and describes the number of waves within a certain length. Usually, it is given in [ $\text{cm}^{-1}$ ] and has the advantage that it scales linearly with energy. Consequently, the respective wavenumber region is 4000  $\text{cm}^{-1}$  to 400  $\text{cm}^{-1}$ .<sup>[118]</sup>

When a molecule absorbs IR radiation, it induces molecular vibrations and rotations. The vibrations are classified into stretching and bending vibrations. The different vibrational modes are illustrated schematically in Figure 3.10 for a three-atomic molecule. Stretching vibrations can be symmetric and asymmetric, whether the green atoms stretch in the same direction or not. Bending vibrations are divided into deformation, rocking, twisting and wagging vibrations. While the first two occur in-plane, the latter two bend out-of-plane.<sup>[118]</sup>

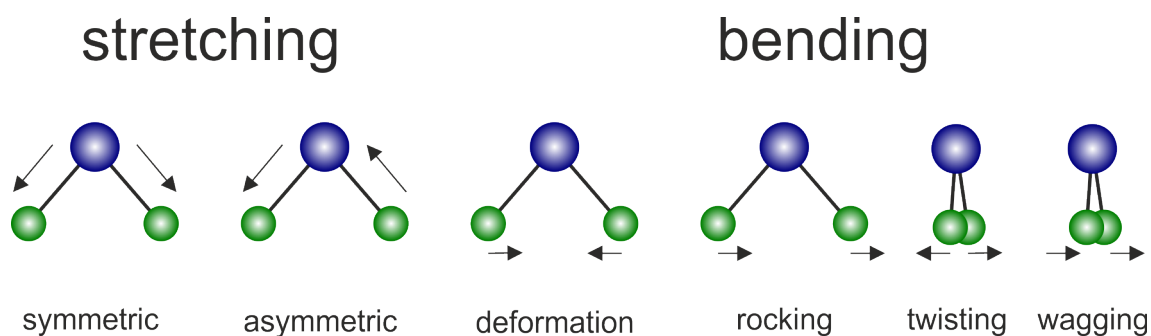


Figure 3.10: Schematic illustration of different molecular vibrations. In general, they are divided into stretching and bending vibrations. Depending on the green atom stretch simultaneously to the blue atom or not, it is differentiated between symmetric and asymmetric stretching vibrations. For bending vibrations exist even more possibilities. The green atoms can bend in-plane (deformation and rocking) or out-of-plane (twisting and wagging). The latter is displayed by turning the molecule around 90°.

A vibration must change the dipole moment of the molecule, to show IR absorption. The intensity of the absorption band depends on the magnitude of the change. Therefore, bonds between atoms with a tremendous difference in electronegativity usually have an intense peak in the IR spectrum. Such bonds already have a significant dipole moment in the ground state, stretching further increases this dipole and consequently leads to an intense band.<sup>[118]</sup>

One example of such a bond is the carbonyl group, which shows an intense stretching vibration peak in the range between 1600-1800  $\text{cm}^{-1}$ . Due to the already mentioned dipole moment, carbonyl groups are also available for H-bonds. The formation of H-bonds affects the bond length and consequently, the absorption frequency of the IR band. The stronger the H-bond, the longer the carbonyl bond, and consequently, the lower the frequency of the absorption.<sup>[118]</sup> This makes IR spectroscopy a powerful tool to analyze H-bonds, for example, in polymers<sup>[119-123]</sup> and polymer blends<sup>[19,124,125]</sup>.

In this context, the carbonyl group is superior to the OH-group. On the one hand, the OH-group has a lot of overtones and combination vibrations, which make the spectrum quite complicated. On the other hand, Coleman et al. showed that the absorption coefficient of the OH-group strongly varies with the strength of H-bond, while it is relatively constant for the carbonyl group.<sup>[121]</sup>

Nevertheless, in more complex structures, like proteins, the carbonyl peak will also have overlaying absorption bands, due to different H-bond configurations. Fortunately, Fourier self-deconvolution (FSD) was developed. This mathematic method increases the spectral resolution, leading to the separation of overlapping bands.<sup>[126]</sup>

For this purpose, an inverse Fourier transform is applied to the spectrum. Subsequently, the damped circular function is multiplied with a rising exponential. This deconvolves the transform and removes the profile determining the bandwidth. The received circular function has a constant amplitude. When Fourier transforming this function, a single line would be obtained, if the data set would be infinite. In reality, infinite data sets are not available, and the transformation leads to a spectrum with peaks much narrower than before. However, the peaks will have sinusoidal side-lobes. The circular function is scaled with an apodisation function before transformation to eliminate these artifacts.<sup>[127]</sup>

FSD has been widely used to investigate IR spectra. Especially, proteins were the objectives of researchers. H-bonds formed between different amino acids define the secondary structure of proteins. Therefore, the carbonyl band comprises a lot of different peaks. FSD has proven the ability to resolve different secondary structures of proteins.<sup>[128-131]</sup> Here, FSD was used to characterize different H-bonds in polymers with multiple functional groups (Section 10).

A Bruker (Billerica, MA, USA) Vertex 70 IR spectrometer equipped with attenuated total reflection (ATR) measurement unit was used for IR measurements. The samples were identically prepared like the samples used for PA measurements but without the transducer layer. The coated side of the sample was pressed on the ATR crystal. The measurements were performed from  $380\text{ cm}^{-1}$  to  $4000\text{ cm}^{-1}$  with a resolution of  $4\text{ cm}^{-1}$  and 128 scans.

IR spectra evaluation was performed with OPUS 7.5 from Bruker (Billerica, MA, USA). For the FSD evaluation, the spectrum was first cut-off between  $1800\text{ cm}^{-1}$  and  $1540\text{ cm}^{-1}$  to solely obtain the carbonyl region. Then a baseline correction with one iteration was performed, and the spectrum was smoothed by 5-9 points. The next step was the FSD with a Lorentzian shape with a half-bandwidth of 25, and a noise reduction of 0.30. Afterward, another baseline correction was performed. The peaks were selected according to the minima from the secondary derivation. All recognized peaks were fitted with Gaussian profile with the Levenberg-Marquardt method.

### **Size exclusion chromatography**

Size exclusion chromatography (SEC) is a method to determine the molecular weight distribution of a polymer sample. A dilute polymer sample is pumped through several columns, which contain a macroporous gel. Due to the different accessibility of the pores for molecules of different sizes, smaller molecules permeate into the pores and therefore have a longer elution time than bigger molecules that cannot or only partially permeate into the pores. This leads to a separation of the polymer chains by their hydrodynamic volume. By using several columns with different pore sizes a good separation is achieved.

Because the elution time strongly depends on the system, i.e., polymer, solvent, and columns, a calibration curve has to be used for the determination of the molecular weight distribution. From the molecular weight distribution the mass average and the number average molecular weight can be determined. The ratio of those is called PDI and gives information about the width of the distribution.

The measurement setup is described in Chapter 6 in Section 6.2.5.

## Helium pycnometry

Helium pycnometry is a measurement method to determine the density of a substance. More specifically, the volume of the sample is measured. For this, the sample is weighed into a measurement cell. This is pressurized with helium to a target pressure. After the pressure is stabilized, the gas is lead into a reference cell of known volume, and the pressure drop is detected. Before the measurement, a reference sphere of known volume calibrates the pressure drop. The sample volume is determined by the comparison of the pressure drops of both measurements. This volume can be seen as the true volume because helium penetrates all pores. Thus, also the true density is obtained by dividing the volume by the mass.<sup>[132]</sup>

For the measurements an Ultrapyc 1200e (Quantachrome Instruments, Boynton Beach, FL, USA) was used. Depending on the sample size, three different measurement cells were available, small (0.25 cm<sup>3</sup>), middle (1.8 cm<sup>3</sup>), and large(4.25 cm<sup>3</sup>). Every measurement was repeated 100 times to ensure statistical accuracy.

## 4 References

- [1] G. E. Moore, *Electronics* **1965**, *38*, 114–117.
- [2] D. G. Cahill, W. K. Ford, K. E. Goodson, G. D. Mahan, A. Majumdar, H. J. Maris, R. Merlin, S. R. Phillpot, *Journal of Applied Physics* **2003**, *93*, 793–818.
- [3] A. L. Moore, L. Shi, *Materials Today* **2014**, *17*, 163–174.
- [4] H. F. Hamann, A. Weger, J. A. Lacey, Z. Hu, P. Bose, E. Cohen, J. Wakil, *IEEE Journal of Solid-State Circuits* **2007**, *42*, 56–65.
- [5] R. Prasher, *Proceedings of the IEEE* **2006**, *94*, 1571–1586.
- [6] F. L. Tan, C. P. Tso, *Applied Thermal Engineering* **2004**, *24*, 159–169.
- [7] M. Liu, Y. Ma, H. Wu, R. Y. Wang, *ACS Nano* **2015**, *9*, 1341–1351.
- [8] M. H. Kryder, E. C. Gage, T. W. McDaniel, W. A. Challener, R. E. Rottmayer, G. Ju, Y. Hsia, M. F. Erden, *Proceedings of the IEEE* **2008**, *96*, 1810–1835.
- [9] A. Datta, Z. Zeng, X. Xu, *Optics Express* **2019**, *27*, 28264–28278.
- [10] D. G. Cahill, P. V. Braun, G. Chen, D. R. Clarke, S. Fan, K. E. Goodson, P. Keblinski, W. P. King, G. D. Mahan, A. Majumdar, H. J. Maris, S. R. Phillpot, E. Pop, L. Shi, *Applied Physics Reviews* **2014**, *1*, 011305.
- [11] W. L. Ong, S. M. Rupich, D. V. Talapin, A. J. McGaughey, J. A. Malen, *Nat. Mater.* **2013**, *12*, 410–5.
- [12] M. D. Losego, I. P. Blitz, R. A. Vaia, D. G. Cahill, P. V. Braun, *Nano Lett* **2013**, *13*, 2215–9.
- [13] M. D. Losego, M. E. Grady, N. R. Sottos, D. G. Cahill, P. V. Braun, *Nat. Mater.* **2012**, *11*, 502–6.
- [14] X. J. Wang, V. Ho, R. A. Segalman, D. G. Cahill, *Macromolecules* **2013**, *46*, 4937–4943.
- [15] X. Xie, D. Y. Li, T. H. Tsai, J. Liu, P. V. Braun, D. G. Cahill, *Macromolecules* **2016**, *49*, 972–978.
- [16] X. Xie, K. Yang, D. Li, T.-H. Tsai, J. Shin, P. V. Braun, D. G. Cahill, *Physical Review B* **2017**, *95*, 035406.
- [17] A. Shanker, C. Li, G.-H. Kim, D. Gidley, K. P. Pipe, J. Kim, *Science Advances* **2017**, *3*, e1700342.
- [18] V. Singh, T. L. Bougher, A. Weathers, Y. Cai, K. Bi, M. T. Pettes, S. A. McMenamin, W. Lv, D. P. Resler, T. R. Gattuso, D. H. Altman, K. H. Sandhage, L. Shi, A. Henry, B. A. Cola, *Nat Nanotechnol* **2014**, *9*, 384–90.

- [19] G. H. Kim, D. Lee, A. Shanker, L. Shao, M. S. Kwon, D. Gidley, J. Kim, K. P. Pipe, *Nat Mater* **2015**, *14*, 295–300.
- [20] K. W. Suh, C. P. Park, M. J. Maurer, M. H. Tusim, R. D. Genova, R. Broos, D. P. Sophiaea, *Advanced Materials* **2000**, *12*, 1779–1789.
- [21] M. Knudsen, *Annalen der Physik* **1909**, *333*, 75–130.
- [22] W. Rohsenow, J. Hartnett, Y. Cho, *Handbook of heat transfer*, McGraw-Hill, **1998**.
- [23] J. Fourier, *The Analytical Theory of Heat*, Cosimo Classics, **2007**.
- [24] J. Lienhard, IV, J. Lienhard, V, *A Heat Transfer Textbook*, 5th, Phlogiston Press, Cambridge, MA, **2019**, 784 pp.
- [25] G. Chen, *Nanoscale Energy Transport and Conversion: A Parallel Treatment of Electrons, Molecules, Phonons, and Photons*, Oxford University Press, **2005**.
- [26] X. Wang, *Experimental Micro/Nanoscale Thermal Transport*, **2012**.
- [27] M. Asheghi, K. Kurabayashi, R. Kasnavi, K. E. Goodson, *Journal of Applied Physics* **2002**, *91*, 5079–5088.
- [28] R. Berman, E. L. Foster, J. M. Ziman, F. E. Simon, *Proceedings of the Royal Society of London. Series A. Mathematical and Physical Sciences* **1955**, *231*, 130–144.
- [29] R. C. Zeller, R. O. Pohl, *Physical Review B* **1971**, *4*, 2029–2041.
- [30] D. G. Cahill, R. O. Pohl, *Annual Review of Physical Chemistry* **1988**, *39*, 93–121.
- [31] P. B. Allen, J. L. Feldman, *Physical Review B* **1993**, *48*, 12581–12588.
- [32] P. B. Allen, J. L. Feldman, J. Fabian, F. Wooten, *Philosophical Magazine B* **1999**, *79*, 1715–1731.
- [33] S. Shenogin, A. Bodapati, P. Keblinski, A. J. H. McGaughey, *Journal of Applied Physics* **2009**, *105*, 034906.
- [34] C. Kittel, *Physical Review* **1949**, *75*, 972–974.
- [35] S. Alexander, O. Entin-Wohlman, R. Orbach, *Physical Review B* **1986**, *34*, 2726–2734.
- [36] S.-H. Wu, F.-Y. Wang, C.-C. Ma, W.-C. Chang, C.-T. Kuo, H.-C. Kuan, W.-J. Chen, *Materials Letters* **2001**, *49*, 327–333.
- [37] E. Roduner, *Chemical Society Reviews* **2006**, *35*, 583–592.
- [38] J. Cuppoletti, *Nanocomposites and Polymers with Analytical Methods*, InTech, **2011**.
- [39] D. R. Paul, L. M. Robeson, *Polymer* **2008**, *49*, 3187–3204.

- [40] A. C. Balazs, T. Emrick, T. P. Russell, *Science* **2006**, *314*, 1107–10.
- [41] L. S. Schadler in *Nanocomposite Science and Technology*, Wiley-VCH Verlag GmbH & Co. KGaA, **2004**, pp. 77–153.
- [42] M. Moniruzzaman, K. I. Winey, *Macromolecules* **2006**, *39*, 5194–5205.
- [43] S.-Y. Fu, X.-Q. Feng, B. Lauke, Y.-W. Mai, *Composites Part B: Engineering* **2008**, *39*, 933–961.
- [44] J. K. Carson, S. J. Lovatt, D. J. Tanner, A. C. Cleland, *International Journal of Heat and Mass Transfer* **2005**, *48*, 2150–2158.
- [45] J. F. Wang, J. K. Carson, M. F. North, D. J. Cleland, *International Journal of Heat and Mass Transfer* **2006**, *49*, 3075–3083.
- [46] Z. Hashin, S. Shtrikman, *Journal of Applied Physics* **1962**, *33*, 3125–3131.
- [47] A. Minnich, G. Chen, *Applied Physics Letters* **2007**, *91*, 073105.
- [48] D. P. H. Hasselman, L. F. Johnson, *Journal of Composite Materials* **1987**, *21*, 508–515.
- [49] M. D. Losego, D. G. Cahill, *Nature Materials* **2013**, *12*, 382–384.
- [50] A. D. McNaught, A. Wilkinson, *IUPAC. Compendium of Chemical Terminology*, 2nd ed. (the "Gold Book"), Blackwell Scientific Publications, Oxford, **1997**.
- [51] G. Kickelbick, *Hybrid Materials* **2014**, *1*, 39–51.
- [52] E. S. Cho, N. E. Coates, J. D. Forster, A. M. Ruminski, B. Russ, A. Sahu, N. C. Su, F. Yang, J. J. Urban, *Adv Mater* **2015**, *27*, 5744–52.
- [53] A. G. Bell, *American Journal of Science* **1880**, *s3-20*, 305–324.
- [54] A. Rosencwaig, A. Gersho, *Journal of Applied Physics* **1976**, *47*, 64–69.
- [55] H. P. Hu, X. W. Wang, X. F. Xu, *Journal of Applied Physics* **1999**, *86*, 3953–3958.
- [56] X. Wang, H. Hu, X. Xu, *Journal of Heat Transfer* **2001**, *123*, 138–144.
- [57] D. L. Zhao, X. Qian, X. K. Gu, S. A. Jajja, R. G. Yang, *Journal of Electronic Packaging* **2016**, *138*, 040802-040802–19.
- [58] M. A. Zambrano-Arjona, F. Penunuri, M. Acosta, I. Riech, R. A. Medina-Esquivel, P. Martinez-Torres, J. J. Alvarado-Gil, *Rev Sci Instrum* **2013**, *84*, 024903.
- [59] B. Bonno, J. L. Laporte, R. T. D'Leon, *Review of Scientific Instruments* **2005**, *76*, 096104.
- [60] A. Lachaine, P. Poulet, *Applied Physics Letters* **1984**, *45*, 953–954.
- [61] B. A. Cola, J. Xu, C. R. Cheng, X. F. Xu, T. S. Fisher, H. P. Hu, *Journal of Applied Physics* **2007**, *101*, 054313.

- [62] J. H. Taphouse, T. L. Bougher, V. Singh, P. P. S. S. Abadi, S. Graham, B. A. Cola, *Nanotechnology* **2013**, *24*, 105401.
- [63] M. K. Smith, D. X. Luong, T. L. Bougher, K. Kalaitzidou, J. M. Tour, B. A. Cola, *Applied Physics Letters* **2016**, *109*, 253107.
- [64] M. K. Smith, T. L. Bougher, K. Kalaitzidou, B. A. Cola, *MRS Advances* **2017**, *2*, 3619–3626.
- [65] S. R. Choi, J. Kim, D. Kim, *Review of Scientific Instruments* **2007**, *78*, 084902.
- [66] P. B. Kaul, K. A. Day, A. R. Abramson, *Journal of Applied Physics* **2007**, *101*, 083507.
- [67] X. Wang, B. A. Cola, T. L. Bougher, S. L. Hodson, T. S. Fisher, X. Xu in *Annual Review of Heat Transfer*, **2013**, pp. 135–157.
- [68] E. Roduner, *Nanoscope Materials, Size-Dependent Phenomena*, The Royal Society of Chemistry, **2006**.
- [69] J. P. Rao, K. E. Geckeler, *Progress in Polymer Science* **2011**, *36*, 887–913.
- [70] J. Park, K. An, Y. Hwang, J.-G. Park, H.-J. Noh, J.-Y. Kim, J.-H. Park, N.-M. Hwang, T. Hyeon, *Nature Materials* **2004**, *3*, 891–895.
- [71] R. Yang, G. Chen, M. S. Dresselhaus, *Nano Letters* **2005**, *5*, 1111–1115.
- [72] J. Turkevich, P. C. Stevenson, J. Hillier, *Discussions of the Faraday Society* **1951**, *11*, 55–75.
- [73] M. Yamamoto, Y. Kashiwagi, M. Nakamoto, *Langmuir* **2006**, *22*, 8581–6.
- [74] B. Nikoobakht, M. A. El-Sayed, *Chemistry of Materials* **2003**, *15*, 1957–1962.
- [75] C. L. Nehl, H. Liao, J. H. Hafner, *Nano Letters* **2006**, *6*, 683–688.
- [76] S. Eustis, M. A. El-Sayed, *Chemical Society Reviews* **2006**, *35*, 209–217.
- [77] K. A. Willets, R. P. V. Duyne, *Annual Review of Physical Chemistry* **2007**, *58*, 267–297.
- [78] G. Santoro, S. Yu, M. Schwartzkopf, P. Zhang, S. Koyiloth Vayalil, J. F. H. Risch, M. A. Rübhausen, M. Hernández, C. Domingo, S. V. Roth, *Applied Physics Letters* **2014**, *104*, 243107.
- [79] M. D. Malinsky, K. L. Kelly, G. C. Schatz, R. P. Van Duyne, *Journal of the American Chemical Society* **2001**, *123*, 1471–1482.
- [80] A. D. McFarland, R. P. Van Duyne, *Nano Letters* **2003**, *3*, 1057–1062.
- [81] G. Baffou, R. Quidant, *Laser Photonics Rev.* **2013**, *7*, 171–187.
- [82] X. Huang, P. K. Jain, I. H. El-Sayed, M. A. El-Sayed, *Lasers in Medical Science* **2007**, *23*, 217.

- [83] V. K. LaMer, R. H. Dinegar, *Journal of the American Chemical Society* **1950**, *72*, 4847–4854.
- [84] H. S. Al-Ghamdi, W. E. Mahmoud, *Journal of Luminescence* **2014**, *145*, 880–883.
- [85] M. Popa, T. Pradell, D. Crespo, J. M. Calderon-Moreno, *Colloids and Surfaces A: Physicochemical and Engineering Aspects* **2007**, *303*, 184–190.
- [86] Z. Xu, G. Hu, *RSC Advances* **2012**, *2*, 11404–11409.
- [87] S. D. Bunge, T. J. Boyle, T. J. Headley, *Nano Letters* **2003**, *3*, 901–905.
- [88] J. Wei, N. Schaeffer, M. P. Pileni, *J Phys Chem B* **2014**, *118*, 14070–5.
- [89] S. A. Harfenist, Z. L. Wang, M. M. Alvarez, I. Vezmar, R. L. Whetten, *The Journal of Physical Chemistry* **1996**, *100*, 13904–13910.
- [90] M. D. Lechner, K. Gehrke, E. H. Nordmeier, *Makromolekulare Chemie: Ein Lehrbuch für Chemiker, Physiker, Materialwissenschaftler und Verfahrenstechniker*, 4. ueberarbeitete und erweiterte Auflage, Birkhäuser Basel, Basel, **2010**.
- [91] G. Moad, E. Rizzardo, S. H. Thang, *Polymer International* **2011**, *60*, 9–25.
- [92] M. Deletre, G. Levesque, *Macromolecules* **1990**, *23*, 4733–4741.
- [93] W. A. Braunecker, K. Matyjaszewski, *Progress in Polymer Science* **2007**, *32*, 93–146.
- [94] D. J. Keddie, G. Moad, E. Rizzardo, S. H. Thang, *Macromolecules* **2012**, *45*, 5321–5342.
- [95] G. Moad, E. Rizzardo, S. H. Thang, *Polymer* **2008**, *49*, 1079–1131.
- [96] C.-A. Fustin, A.-S. Duwez, *Journal of Electron Spectroscopy and Related Phenomena* **2009**, *172*, 104–106.
- [97] B. Ebeling, P. Vana, *Macromolecules* **2013**, *46*, 4862–4871.
- [98] R. T. A. Mayadunne, E. Rizzardo, J. Chiefari, J. Krstina, G. Moad, A. Postma, S. H. Thang, *Macromolecules* **2000**, *33*, 243–245.
- [99] S. T. Milner, *Science* **1991**, *251*, 905–914.
- [100] H. Skaff, M. F. Ilker, E. B. Coughlin, T. Emrick, *Journal of the American Chemical Society* **2002**, *124*, 5729–5733.
- [101] K. Ohno, K.-m. Koh, Y. Tsujii, T. Fukuda, *Macromolecules* **2002**, *35*, 8989–8993.
- [102] K. Ohno, K. Koh, Y. Tsujii, T. Fukuda, *Angewandte Chemie International Edition* **2003**, *42*, 2751–2754.
- [103] C. Li, B. C. Benicewicz, *Macromolecules* **2005**, *38*, 5929–5936.
- [104] C. Li, J. Han, C. Y. Ryu, B. C. Benicewicz, *Macromolecules* **2006**, *39*, 3175–3183.

- [105] S. Qin, D. Qin, W. T. Ford, D. E. Resasco, J. E. Herrera, *Macromolecules* **2004**, *37*, 752–757.
- [106] I. Luzinov, D. Julthongpiput, H. Malz, J. Pionteck, V. V. Tsukruk, *Macromolecules* **2000**, *33*, 1043–1048.
- [107] M. Wang, C. Wang, K. L. Young, L. Hao, M. Medved, T. Rajh, H. C. Fry, L. Zhu, G. S. Karczmar, C. Watson, J. S. Jiang, N. M. Markovic, V. R. Stamenkovic, *Chemistry of Materials* **2012**, *24*, 2423–2425.
- [108] N. Jouault, D. Lee, D. Zhao, S. K. Kumar, *Advanced Materials* **2014**, *26*, 4031–4036.
- [109] S. Fischer, A. Salcher, A. Kornowski, H. Weller, S. Forster, *Angew. Chem. Int. Ed.* **2011**, *50*, 7811–4.
- [110] M. Bieligmeyer, S. M. Taheri, I. German, C. Boisson, C. Probst, W. Milius, V. Altstadt, J. Breu, H. W. Schmidt, F. D’Agosto, S. Forster, *J Am Chem Soc* **2012**, *134*, 18157–60.
- [111] S. Ehlert, S. M. Taheri, D. Pirner, M. Drechsler, H. W. Schmidt, S. Forster, *ACS Nano* **2014**, *8*, 6114–22.
- [112] W. Nunes dos Santos, P. Mummery, A. Wallwork, *Polymer Testing* **2005**, *24*, 628–634.
- [113] F. A. Nutz, P. Ruckdeschel, M. Retsch, *J Colloid Interface Sci* **2015**, *457*, 96–101.
- [114] B. Fultz, J. Howe, *Transmission Electron Microscopy and Diffractometry of Materials*, Springer Berlin Heidelberg, Berlin and Heidelberg, **2013**.
- [115] G. Michler, *Electron Microscopy of Polymers*, Springer, **2008**.
- [116] T. Hatakeyama, F. Quinn, *Thermal analysis: fundamentals and applications to polymer science*, Wiley, **1999**.
- [117] S. Ehlert, T. Lunkenbein, J. Breu, S. Forster, *Colloids and Surfaces a-Physicochemical and Engineering Aspects* **2014**, *444*, 76–80.
- [118] B. H. Stuart, *Infrared Spectroscopy: Fundamentals and Applications*, **2004**.
- [119] D. J. Skrovanek, S. E. Howe, P. C. Painter, M. M. Coleman, *Macromolecules* **1985**, *18*, 1676–1683.
- [120] D. J. Skrovanek, P. C. Painter, M. M. Coleman, *Macromolecules* **1986**, *19*, 699–705.
- [121] M. M. Coleman, D. J. Skrovanek, S. E. Howe, P. C. Painter, *Macromolecules* **1985**, *18*, 299–301.
- [122] M. M. Coleman, M. Sobkowiak, G. J. Pehlert, P. C. Painter, T. Iqbal, *Macromolecular Chemistry and Physics* **1997**, *198*, 117–136.

- [123] J. Dong, Y. Ozaki, K. Nakashima, *Macromolecules* **1997**, *30*, 1111–1117.
- [124] M. M. Coleman, D. J. Skrovanek, J. Hu, P. C. Painter, *Macromolecules* **1988**, *21*, 59–65.
- [125] A. Bozkurt, W. H. Meyer, G. Wegner, *Journal of Power Sources* **2003**, *123*, 126–131.
- [126] J. K. Kauppinen, D. J. Moffatt, H. H. Mantsch, D. G. Cameron, *Applied Spectroscopy* **1981**, *35*, 271–276.
- [127] P. B. Tooke, *TrAC Trends in Analytical Chemistry* **1988**, *7*, 130–136.
- [128] E. Goormaghtigh, V. Cabiaux, J. M. Ruyschaert, *Eur J Biochem* **1990**, *193*, 409–20.
- [129] C. Mouro, C. Jung, A. Bondon, G. Simonneaux, *Biochemistry* **1997**, *36*, 8125–8134.
- [130] C. Jung, *Journal of Molecular Recognition* **2000**, *13*, 325–351.
- [131] X. Hu, D. Kaplan, P. Cebe, *Macromolecules* **2006**, *39*, 6161–6170.
- [132] S. Lowell, J. E. Shields, M. A. Thomas, M. Thommes, *Characterization of Porous Solids and Powders: Surface Area, Pore Size and Density*, Springer Netherlands, **2004**.



## 5 Thesis overview

### 5.1 Synopsis

This thesis explores the structure-property-relations in polymers and hybrid materials. More specifically, the influence of interfaces and chemical bonds on thermal conductivity is investigated. The work is divided into three topics. Each topic deals with a particular class of material.

The first material consists of spherical Ag nanoparticles (NPs) with a polystyrene (PS) brush. In Chapters 6 and 7, the synthesis and characterization of this one-component polymer nanocomposite (PNC) are described. The brush functionalization allows the investigation of structure-property relationships regarding the adjustable interparticle distance (IPD).

In the next part, 2D materials are the superordinated topic. In Chapter 8, the thermal conductivity of graphene oxide is compared to synthetic hectorite. The next chapter (Chapter 9) treats the thermal and mechanical properties of a layered hybrid material dependent on the composition ratio.

The last contribution is devoted to the thermal conductivity in ampholytic polymers. Here, the different intermolecular interactions and the influence of water absorption are investigated.

Figure 5.1 provides a graphical overview of the topics of this thesis. The photoacoustic (PA) method was set-up for this thesis and took a key role in the work. The principles and set-up are discussed in Chapters 2.2 and 3.2.1. Without implementing the PA method, it would not have been possible to realize these studies.

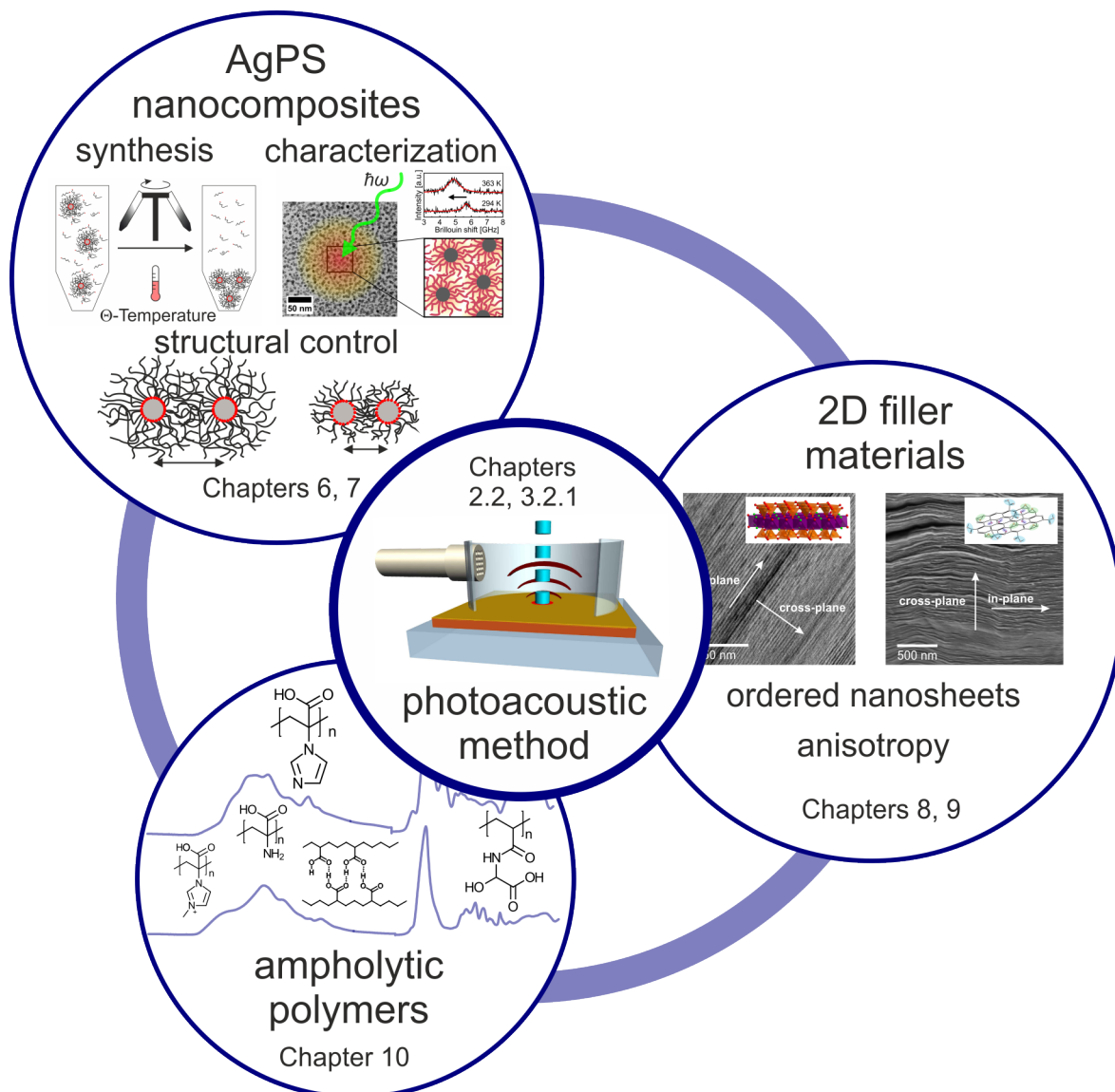


Figure 5.1: Graphical overview of this thesis.

Adding fillers to polymers for improved properties is a widely used concept. The properties of such composites can, usually, be described by effective medium approximations. Thus, the composite properties lie in between the properties of the two bulk materials. However, breaking down the fillers' dimensions to the nanoscale opens up new opportunities to change the composite properties beyond these limits.

The most straightforward filler geometry is a sphere. In the literature, one finds almost endless reports for NP syntheses. Considerable differences exist in the synthetic effort, dispersity, yield, ligands, reaction medium, and conditions. Once synthesized, a considerable challenge is to disperse the NPs within a polymer matrix uniformly. Due to the large surface to volume ratio, they tend to aggregate. A solution for this issue is the functionalization of the NPs surface.

In Chapter 6, a synthesis route for Ag NPs functionalized with a PS brush is de-

scribed. For this purpose, Ag NPs of  $\sim 6$  nm in diameter are synthesized from an Ag-myristate precursor in a one-pot synthesis. In a separate process, the PS ligands are prepared by reversible addition-fragmentation chain transfer (RAFT) polymerization. Afterward, the chain transfer agent (CTA), a trithiocarbonate, is cleaved off by aminolysis. Consequently, a thiol moiety is achieved at the end of every PS chain. RAFT polymerization allows control over the molecular weight and narrow molecular weight distribution (MWD). This aspect is used to produce seven different PS ligands with molecular weights of 1.000 g/mol, 3.000 g/mol, 4.000 g/mol, 6.000 g/mol, 8.000 g/mol, 12.000 g/mol, and 16.000 g/mol. The molecular weight defines the IPD in the final PNC.

The PS ligands are added to the Ag NPs in toluene. Subsequently, the polymer ligands exchange the initial carboxylate ligands. Three driving forces are leading to the exchange. First, the thiol group forms a stronger bond to the Ag NP than the carboxylate. Second, the polymer is added in large excess. Third, the addition of non-solvent precipitates the polymer and the particles. In this way, the local concentration of polymer is tremendously increased at the particle surface.

Afterward, a mixture of polymer-brush functionalized particles and free PS ligands is achieved. The  $\theta$ -centrifugation method was developed to separate this mixture. At  $\theta$ -conditions of the polymer ligands, the colloidal stability of the polymer-brush functionalized particles is weakened. As a result, the centrifugation at  $\theta$ -conditions leads to a precipitation of the PNCs, while the free ligands remain dissolved. For this purpose, the mixture was dissolved in cyclohexane and centrifuged at 34 °C. The decrease of the colloidal stability was proved by dynamic light scattering (DLS) measurements at different temperatures. The  $\theta$ -centrifugation presents a superior way of purification compared to the methods reported in the literature.

The successful purification was verified by thermal gravimetric analysis (TGA) measurements, seen in Figure 5.2a. As expected, the residual mass decreases with increasing molecular weight of the ligand. The dependence of the IPD on the molecular weight also indicates the successful purification. The achieved IPD range lies between 2.1 nm and 16.1 nm. The PS height, half of the IPD, is plotted against the degree of polymerization in Figure 5.2b. The scaling with  $N^{0.67}$  proves the extended brush-structure of the polymer ligands.

It should be noted that this approach is not exclusively valid for the used material combination. Due to the separation of the particle and ligand synthesis, an almost endless number of material combinations is imaginable. Furthermore, it was shown that it is not implicitly necessary to use living polymerization techniques for proper distance control. Controlled radical polymerization leads to acceptable results, too.

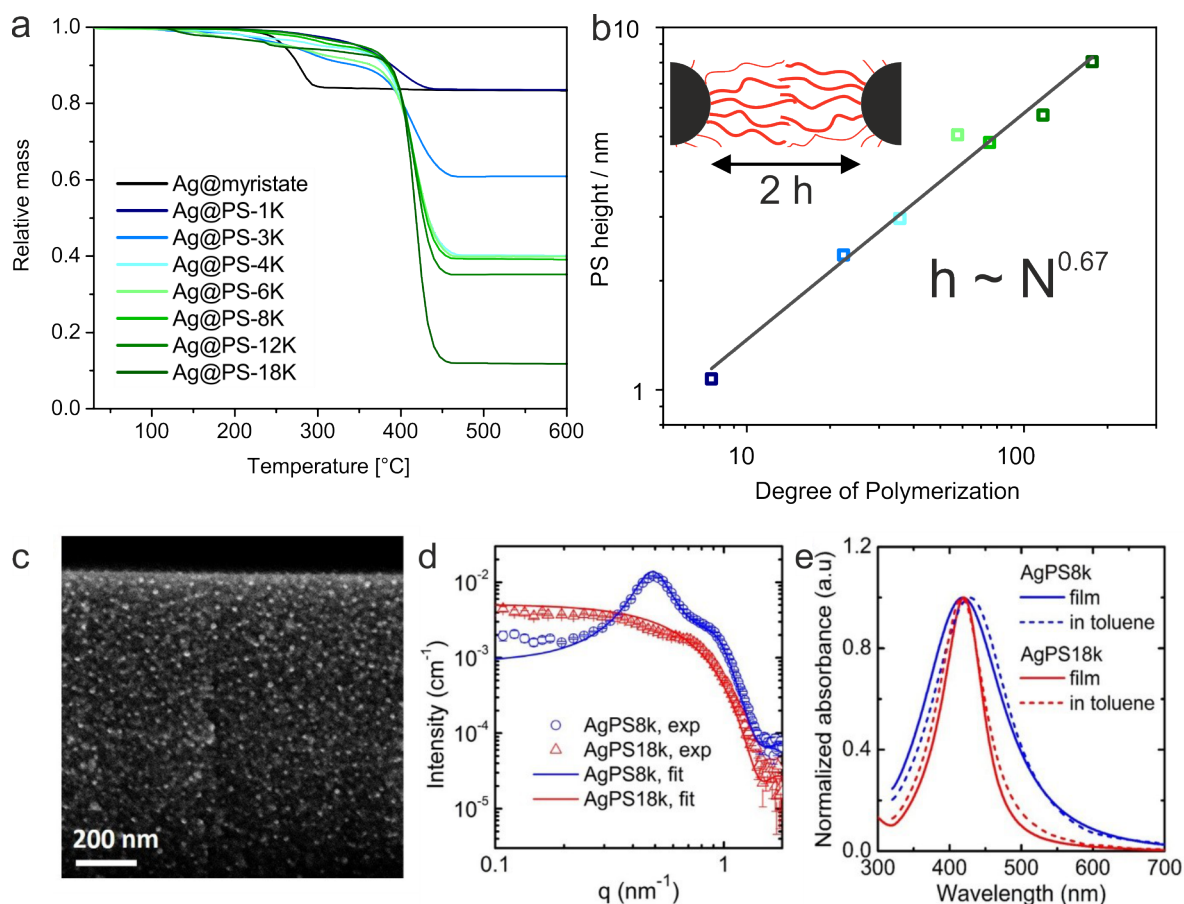


Figure 5.2: (a) TGA curves of the nanocomposites and pure silver particles with myristate ligand as a reference.<sup>[1]</sup> (b) The polymer height determined from the TEM images is plotted as a function of the degree of polymerization, which shows linear relation in the double logarithmic plot. (c) SEM side view image of the AgPS18k film. (d) SAXS patterns of the AgPS8k and AgPS18k films (symbols) and theoretical descriptions (lines) (e) UV/Vis spectra of the AgPS8k and AgPS18k samples measured in solid films (solid lines) and toluene (dashed lines).

The purified PNCs were spin-coated. The characterization of the produced films is the topic of Chapter 7. The polymer-brushes prevent agglomeration as it can be seen on the scanning electron microscopy (SEM) image in Figure 5.2c. The homogeneous dispersion of the particles is also proven by small-angle X-ray scattering (SAXS) experiments. In Figure 5.2d, the patterns of AgPS8k and AgPS18k are depicted. The peak in the measurement curve of AgPS8k presents the distance between the NPs. However, the NPs are not assembled in a crystalline structure but have a glasslike order. In AgPS18k this feature is less pronounced. This result presents the influence of the increasing shell thickness, which leads to a weaker particle-particle interaction.

Nevertheless, the essential point is that the particles are well dispersed in the matrix without significant aggregates. The overlaying ultraviolet and visible light (UV/Vis)

spectra of the films and the PNCs in solution in Figure 5.2e demonstrate the homogeneity of the PNC films, once more. The similarity of the spectra excludes the presence of significant aggregates in the film.

The films were further characterized by Brillouin light scattering (BLS) measurements. BLS allows the determination of the speed of sound in a material, and thus, grants to derive the mechanical properties. Figure 5.3a shows the longitudinal speed of sound plotted against the temperature. The sound velocities of the PNC are smaller than those of the pure polymer. Moreover, it decreases with increasing Ag content. These findings are in good agreement with Wood's Law, as seen in Figure 5.3b. In contrast, the modulus could not be predicted by Woods's Law.

The change of slope, shown in Figure 5.3a, depicts the glass transition of the polymer. The shaded area highlights this region. Furthermore, the inset demonstrates the reversibility. It shows that the frequency is the same before and after the measurement at 363 K. However,  $T_g$ 's of the PNC samples determined by BLS are much smaller compared to differential scanning calorimetry (DSC) measurements on the same sample, which are illustrated by the two vertical lines. The reduced  $T_g$  is attributed to plasmonic heating. The plasmon absorption of the NPs leads to local heating in the film. Hence, the transition occurs, although the ambient temperature is below the  $T_g$ . As expected, this effect is more pronounced in AgPS8k, the sample with a higher Ag concentration.

Moreover, the dependency of the longitudinal sound velocity on the laser power is not linear but shows a stronger dependence at high power levels. The temperature increase dependent on the laser power was evaluated in Figure 5.3c. The nonlinear behavior is confirmed. The horizontal lines depict the  $T_g$ 's from the differential scanning calorimetry (DSC) measurements. At these respective temperatures, the slope changes. Independent thermometry measurements with an infrared (IR) camera verified these findings.

Besides the modulus, sound velocity, and plasmonic heating, also the thermal conductivity depends on the silver content in the PNCs. The values of the effective thermal conductivity are shown in Figure 5.3d dependent on the Ag vol%. The graph depicts the increase in thermal conductivity with increasing Ag content. This result is not unexpected. The Maxwell model is designed to predict the properties of composite materials consisting of a matrix and spherical inclusions. Therefore, it should be valid for our PNC material. Indeed, the blue line shows the increasing trend for increasing Ag content. However, the increase is drastically overestimated. The silver content and the IPD interrelate inversely. Therefore, increasing Ag content means decreasing IPD. The smaller the IPD, the higher the number of interfaces in the material. The enormous number of interfaces in the material contributes to

the thermal resistance of the material. When a finite thermal resistance at the Ag PS interface is added to the Maxwell model, like in the Hasselman-Johnson model (green line), the data is fitted much better. Here, an interfacial thermal conductance of  $300 \text{ MW m}^{-2} \text{ K}^{-1}$  was used. Consequently, the influence of the number of interfaces on thermal conductivity is claimed. Notably, this influence decreases with increasing IPD (or decreasing Ag content), where the Maxwell model is also in good agreement with the data.

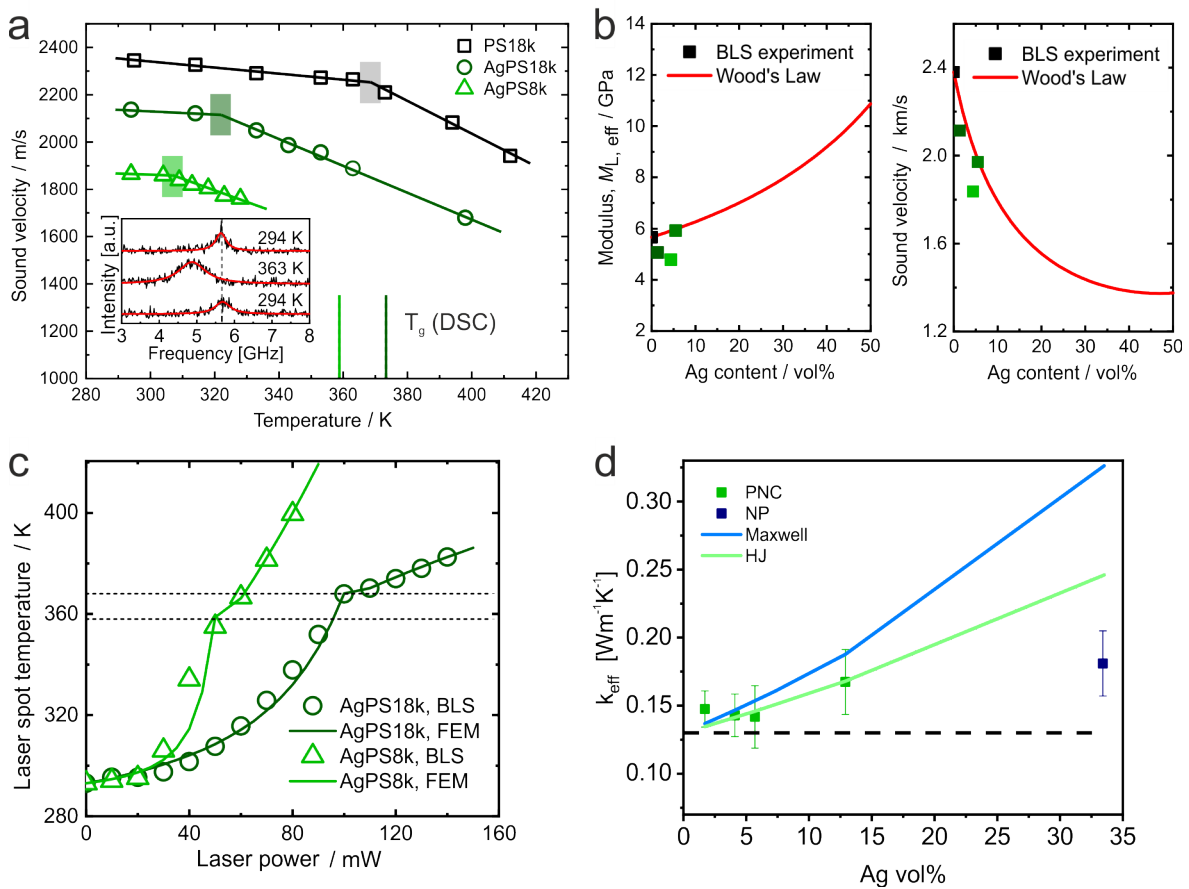


Figure 5.3: (a) Longitudinal sound velocities in the AgPS8k and AgPS18k PNC films, and the bulk PS18k film as a function of temperature. The shaded areas indicate the glass transition temperatures. The vertical lines denote the  $T_g$  obtained from DSC. The inset shows Anti-Stokes BLS spectra of AgPS18k at three different temperatures. The lowest spectrum was recorded at the end of the temperature scan to demonstrate the reversibility. For the AgPS8k and AgPS18k films, the BLS spectra were recorded with laser powers of 45 mW and 60 mW, respectively. (b) Effective longitudinal sound velocity vs. Ag volume fraction and computed effective longitudinal modulus as a function of Ag volume fraction. (c) The local temperature in the laser spot as a function of the laser power. BLS experiments estimated the data. (d) Effective thermal conductivity estimated by PA measurements vs. the Ag volume fraction. The solid lines depict two different effective medium models to estimate thermal conductivity. The dashed line presents the effective thermal conductivity of bulk PS.

The presented PNC films exhibit another exciting feature. When thermally annealed, well above the  $T_g$ , the structure of the film changes. This structural change leads macroscopically to a color change from yellow to reddish-brown and back to yellow (Figure 5.4a). When looking at the UV/Vis spectra in Figure 5.4b, one can observe that the plasmon peak is even more pronounced after turning back to yellow. The TEM images in Figure 5.4c reveal what happens in the films. The initial image shows homogeneously dispersed NPs. After 10 s at 200 °C, a small amount of bigger particles can be observed. The images after 30 s, 1 min, and 5 min then expose significant clusters, which lead to the broadening and redshift of the plasmon absorption and hence, to the change of the color. Between 5 min and 30 min, the NPs redisperse again. However, the size is slightly increased, which results in a stronger plasmonic peak. This unusual aggregation/redispersion effect was observed for all PNC samples. It is attributed to the fast relaxation of the PS chains when heating well above the  $T_g$ . Prolonged annealing, however, leads to a further increase in particle size and a coarsening of the nanostructure.

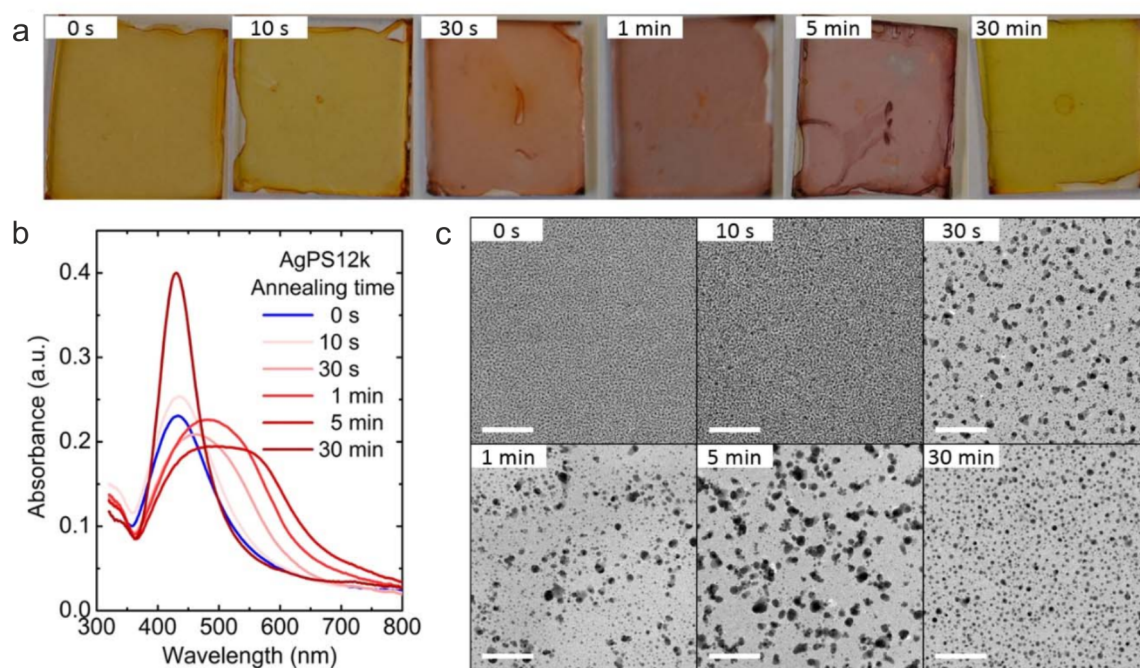


Figure 5.4: Thermal annealing series of the AgPS12k sample at 200°C. Shown are (a) Photographs, (b) UV/Vis spectra, and (c) TEM images after 0 s, 10 s, 30 s, 1 min, 5 min, and 30 min, respectively.

In Chapters 8 and 9, the focus turns from spherical particles to platelets. So-called 2D filler materials have spatial extensions like a piece of paper. Accordingly, nanosheets have large extensions in the x- and y-axis, while the z-axis is in the range of nanometers. In Chapter 8, two such materials are compared. The electron microscope pictures in Figure 5.5a and b reveal the anisotropic structure of the two materials. The

synthetic clay sodium hectorite and graphene oxide (GO) are schematically illustrated in the insets, respectively. Different types of these materials were compared and characterized regarding structure, dimensions, and thermal properties.

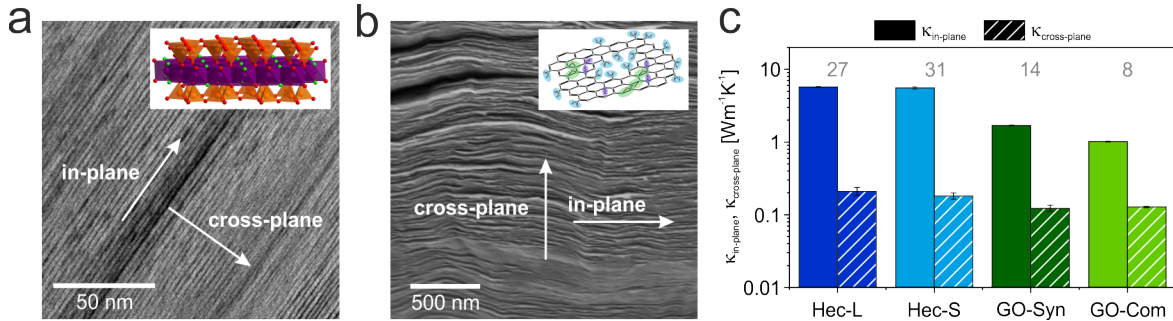


Figure 5.5: (a) TEM image of an aligned sodium fluorohectorite (Hec) film. The inset shows a schematic of the Hec crystal structure. (b) SEM image of an aligned GO sample. The inset shows the exemplary structure of GO with different types of functional groups. The white arrows define the in-plane and cross-plane direction for both materials. (c) In-plane and cross-plane thermal conductivity of the investigated Hec and GO samples. The unicolor bars belong to the in-plane values, while the striped bars represent the cross-plane thermal conductivity. The numbers above express the anisotropy ratio ( $\kappa_{in-plane} / \kappa_{cross-plane}$ ) of each sample.

All samples were spray-coated. This process favors platelet alignment, as shown on the electron microscopy images in Figure 5.5. The number of spraying cycles determines the film thickness. With a sufficient film thickness, even free-standing films can be prepared by peeling them off the substrate.

The thermal conductivity was determined concerning the axial direction, meaning in-plane of the platelets, and cross-plane to them. The determined values are shown in Figure 5.5c. Here, the hectorite samples exhibited a higher in-plane thermal conductivity than the GO samples. Also, the anisotropy ratio, the in-plane thermal conductivity divided by the cross-plane thermal conductivity, is twice as high in the case of the hectorites. Admittedly, the cross-plane thermal conductivity of the GO samples is lower, but it cannot compensate for the lower in-plane thermal conductivity.

For the hectorite, two samples were investigated that featured strongly different platelet sizes. The size of the large platelets (Hec-L) was up to  $800 \mu m^2$ . The small sample (Hec-S) was produced by ultrasonic treatment of the large sample. This treatment reduced the platelet size below  $0.4 \mu m^2$ . Regarding the thermal conductivity, the results suggest that the impact of platelet size is not relevant within the lateral dimensions under investigation.

The GO samples were both prepared by the Hummers method. However, the GO-syn sample was synthesized at the University of Bayreuth, while the GO-com is

commercially available. Despite the same synthesis route, the samples differ in size and degree of oxidation. Since we found that the thermal conductivity is not sensitive to the platelet size, we conclude that the degree of oxidation dominates the in-plane thermal transport. A higher degree of oxidation is associated with a higher degree of defects in the structure, and hence, leads to a decrease in thermal conductivity.

In conclusion, the synthetic hectorite samples are found superior in in-plane thermal conductivity, as well as anisotropy ratio. Moreover, the structure is more defined, provides a better assembly, and is less vulnerable to chemical and structural changes.

In Chapter 9, the hectorite is utilized as a filler in a hybrid material. Therefore, a suspension with the delaminated clay is mixed with a polyvinylpyrrolidone (PVP) solution, and subsequently sprayed-coated. The two phases of the self-assembled nanolaminate are strictly alternating and exhibit a long-range periodicity. Dependent on the PVP volume fraction in the solution, the periodicity is tunable with angstrom precision. The transmission electron microscopy (TEM) images of the Hec40/PVP60 and Hec51/PVP49 samples in Figure 5.6a and b are examples for layered structure with different periodicities.

The basal spacing was determined from the 001 peaks in the X-ray diffraction (XRD) spectra. The spacing expands from 19 to 38 Å. Therefore, the thickness of the PVP layer (9 to 28 Å) is significantly smaller than the radius of gyration ( $R_{g,PVP} \approx 15$  nm), implying strong polymer confinement. Because the gallery height is on the order of the size of an individual polymer chain, only discrete polymer volume fractions lead to essentially defect-free Bragg stacks. For the samples Hec40/PVP60 and Hec31/PVP69, the gallery height corresponds to monolayer and a bilayer, respectively. In the other cases, the PVP layer thickness is the average of two gallery heights, which is exposed by the increased coefficient of variation, and the less discrete peaks in the XRD spectra, as seen in Figure 5.6b.

The perfectly layered samples were characterized by lock-in thermography, photoacoustic (PA) measurements, and BLS, regarding their orientation-dependent thermal conductivities and mechanical properties. As expected, the thermal characterization revealed an anisotropic thermal conductivity for the hybrid samples, as depicted in Figure 5.6e. The hybrid sample with the lowest PVP content offers, with 38, the highest anisotropy ratio of all samples. The reason is simple. The in-plane thermal conductivity follows the linear trend of the parallel mixing model (Figure 5.6c), whereas the cross-plane thermal conductivity is on the same level for all hybrid samples (Figure 5.6d). Hence, the anisotropy ratio is governed by the large in-plane thermal conductivity of the clay.

The broad minimum of the cross-plane thermal conductivity results from the tremendous number of interfaces along this direction. The interface resistance leads to an ultralow thermal conductivity, which is even less than the cross-plane thermal conductivity of the two constituent materials. Hence, the cross-plane thermal conductivity of the Hec/PVP deviates from an effective medium behavior.

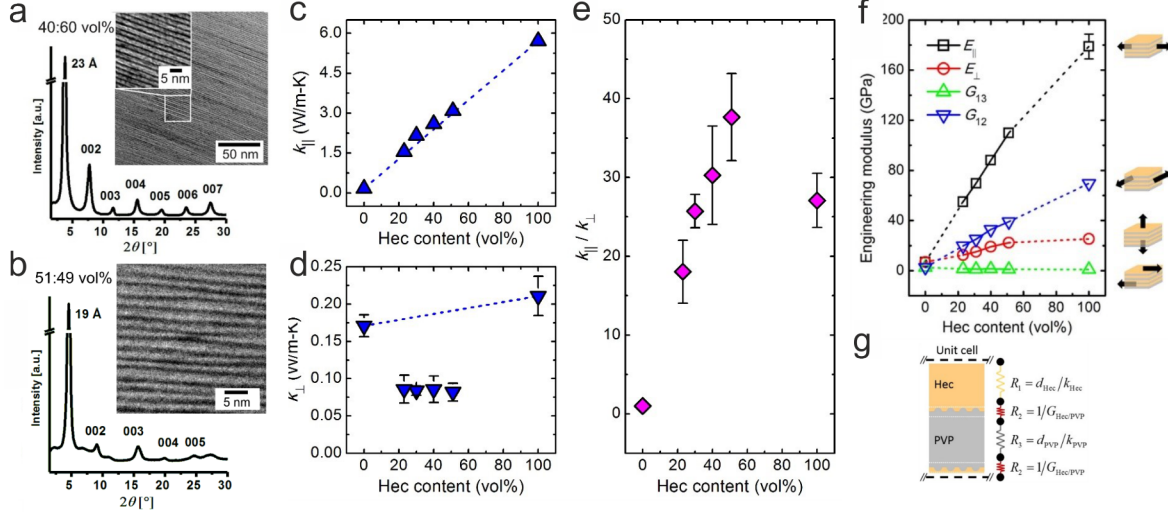


Figure 5.6: (a) and (b) show XRD patterns and microscopic images of two samples of strictly alternating Hec/PVP Bragg stacks with extreme polymer confinement. The Hec/PVP volume ratios are 40:60 vol%, and 51:49 vol%, respectively. (c) In-plane thermal conductivity, (d) Cross-plane thermal conductivity, and (e) anisotropic ratio as a function of the Hec volume fraction. The blue dashed lines show a linear trend based on simple parallel and series mixing models. (f) Composition dependence of Young's moduli,  $E_{\parallel}$  and  $E_{\perp}$ , the torsional shear modulus,  $G_{12}$ , and the sliding shear modulus  $G_{13}$ . The moduli of the hybrids are extrapolated to those of the pure materials, as shown by the dashed lines. The four schematics beside visualize the physical meanings of the corresponding moduli. (g) Series resistance model in the cross-plane direction of the Hec/PVP stacks.

Because of the macroscopic orientation of the hybrid Bragg stacks, it was possible to determine the direction-dependent mechanical properties by BLS. It is the first time, the direction-dependent Young's and shear moduli are reported for hybrid Bragg stacks in general, and clay/polymer nanocomposites in particular. The moduli are plotted in Figure 5.6f. Again, a strong anisotropic behavior is observed. Moreover, Young's moduli,  $E_{\parallel}$  and  $E_{\perp}$ , and the torsional shear modulus,  $G_{12}$ , rise with increasing Hec content. The sliding shear modulus,  $G_{13}$ , decreases. A reason could be the reduction in polymer chain entanglement upon confinement. However, it would require further computer simulations to confirm this, since the elastic moduli of PNCs depend on specific filler-polymer and polymer-polymer interactions.

Analogous to the in-plane thermal conductivity, all mechanical moduli display an effective medium behavior. Consequently, the values range between those of the

two base materials. Although the polymer chains are strongly confined, the bulk properties of the two components are sufficient to describe the hybrid mechanical properties. Therefore, these results corroborate the validity of continuum mechanics at nanometer length scales.

The last part of Chapter 9 refers to the insights into the anisotropic thermoelasticity. Therefore, the direction-dependent sound velocities, the mechanical moduli, and the thermal conductivities are correlated. First, the average phonon mean free path  $\bar{\Lambda}$  is estimated by a kinetic theory model,  $k = c_V \bar{v}_g \bar{\Lambda} / 3$ . The specific heat capacity at constant volume  $c_V$  is substituted by the specific heat capacity at constant pressure  $c_p$  and as phonon group velocity  $\bar{v}_g$ ,  $\bar{v}_{S,\parallel}$ , and  $\bar{v}_{S,\perp}$  are used, respectively. The in-plane  $\bar{\Lambda}$  depends on the hybrid composition, comparable to the in-plane thermal conductivity. The lateral size of the Hec nanosheets exceeds  $\bar{\Lambda}$ . Hence, grain boundaries are not significant for the in-plane thermal conductivity.

In the cross-plane direction,  $\bar{\Lambda}$  is sharply reduced. The periodicity in the Å regime leads to a tremendous number of interfaces in this direction. Thus, interfacial effects dominate the cross-plane thermal transport. This structure is better analyzed using a series resistance model (SRM), as illustrated in Figure 5.6g. The interfacial conductance at the Hec/PVP interface  $G_{Hec/PVP} = 89 \pm 8 \text{ MW m}^{-2} \text{ K}^{-1}$  is lower than the interfacial conductance in the pure Hec  $G_{Hec/Hec} = 219 \pm 28 \text{ MW m}^{-2} \text{ K}^{-1}$ . As a consequence, the intercalation of PVP drastically decreases the cross-plane thermal conductivity.

In summary, platelet filler materials demonstrate direction-dependent properties. This anisotropy is not only expressed in the thermal conductivity but also mechanical moduli. The intercalation of polymers can increase the already significant anisotropy in highly ordered synthetic clays. In this scenario, the cross-plane thermal conductivity is significantly lowered by the interfacial resistance of the vast number of hard/soft interfaces between Hec and PVP. Moreover, the basal spacing in this hybrid material can be adjusted in the Å regime. Due to the small distances, the polymer chains are extremely confined. The in-plane thermal conductivity, as well as mechanical properties strongly depend on the composition, while the interface-driven cross-plane thermal conductivity is unaffected.

The last part of the thesis concentrates on pure polymers, more specifically, highly functional, ampholytic polymers. As already mentioned, interfacial conductance can significantly influence the thermal conductivity. It depends on surface chemistry. In polymers, the intermolecular thermal transport can be seen as transfer across interfaces. Hence, polymers with functional groups that guide the intermolecular transfer present higher thermal conductivity than those without functional groups.

In Chapter 10, we investigate a variety of polymers with more than one functional moiety per repetition unit. The polymers under research provide hydrogen bond (H-bond) donor and acceptor groups at the same time. The structure of the ampholytic polymers is depicted in Figure 5.7c. Beside the ampholytic polymers polydehydroalanine (PDha), poly(2-acrylamido glycolic acid) (PAGA), poly(2-(imidazol-1-yl)acrylic acid) (PImAA), and poly(2-(methyl imidazolium-1-yl)acrylic acid) (PMeImAA), as references, poly(methyl methacrylate) (PMMA) and poly(acrylic acid) (PAA) were involved in the study.

The H-bond strength was analyzed by IR spectroscopy. The IR spectra of all investigated polymers are shown in Figure 5.7a. The H-bond strength was determined from the peak position of the carbonyl absorption around  $1700\text{ cm}^{-1}$ . The lower the wavenumber, the stronger the H-bonds. For the ampholytic polymers, the H-bond strength correlates with the thermal conductivity. Overall, the thermal conductivity of the ampholytic polymers is in a reasonable range for functional polymers, which is illustrated by the two dashed horizontal lines in Figure 5.7b. However, the PAA sample, which carries only one functional group per repetition unit, has a thermal conductivity comparable to the best conducting ampholytic polymer.

For further insight, Fourier self-deconvolution (FSD) was applied to the signal of the carbonyl vibration between  $1600\text{ cm}^{-1}$  and  $1750\text{ cm}^{-1}$ . The deconvoluted spectra are shown in Figure 5.7c. The resolved peaks could be attributed to different forms of interactions. However, the drop in thermal conductivity between PAA and PDha could not be unambiguously resolved by the IR study. Other factors, like the side-chain structure and the influence of the side-chains on the polymer morphology, also contribute to the thermal conductivity. Nevertheless, the monotonic increase of other H-bonds (other than between two carboxylic acid groups) from PDha to PAGA to PImAA and poly(2-(methyl imidazolium-1-yl)acrylic acid) (PMeImAA) follows the general trend of the increased thermal conductivity.

Humidity has an enormous influence on the ampholytic polymers and PAA. Therefore, its effect on the effective thermal conductivity was investigated. The determined values are plotted in Figure 5.7d for four different humidities. All samples, but PMMA, exhibit a considerable water uptake. Nevertheless, dependent on the H-bond nature, water absorption is different. In PAA, for example, water molecules seem to bind directly to the carboxylic acid groups. This bound water does not seem to affect the interchain thermal transport. In PImAA, however, the water seems to be less bound. Consequently, the thermal conductivity measurements indicate a composite like behavior, and an effective medium mixing model adequately describes the increase in thermal conductivity.

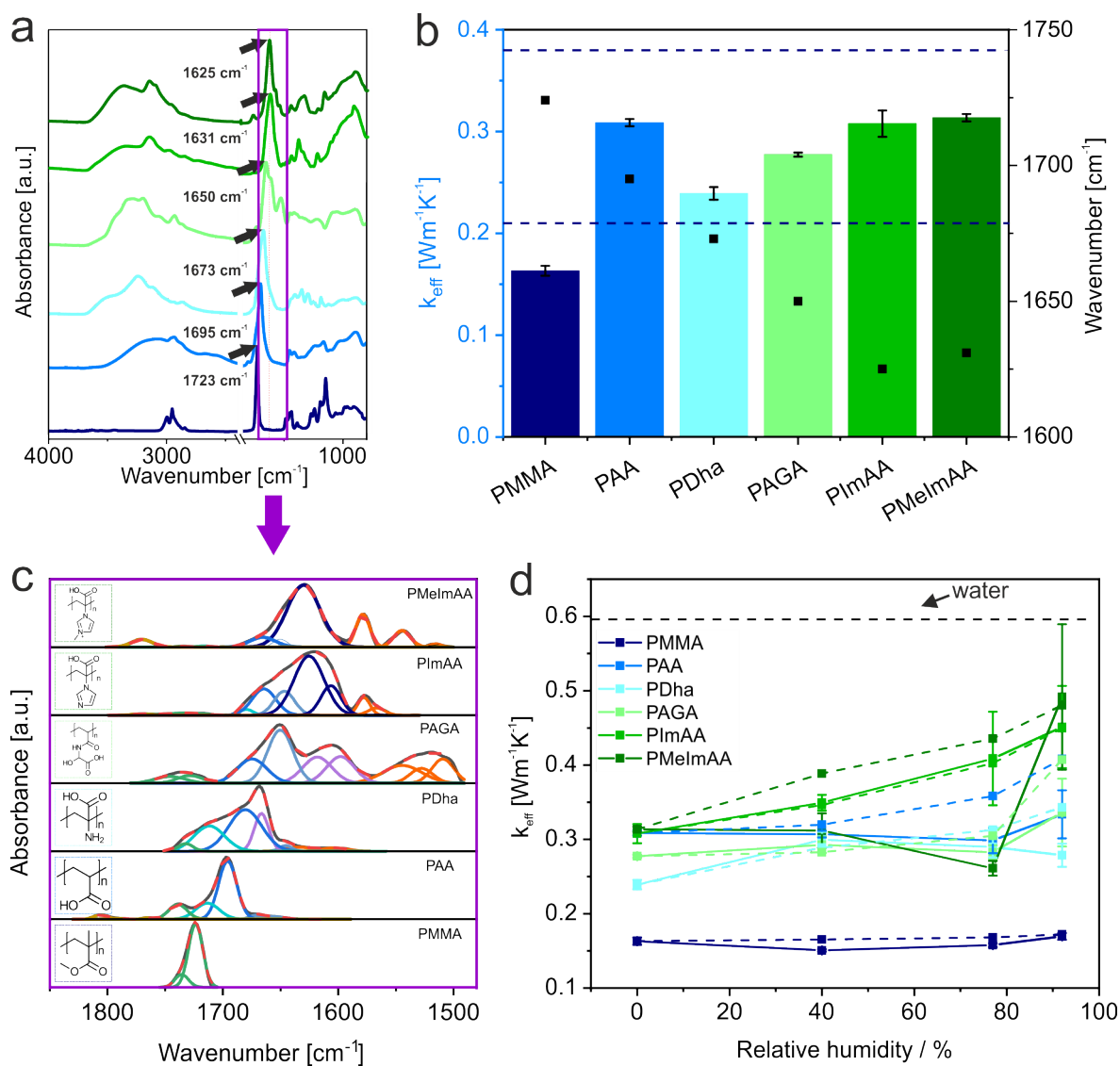


Figure 5.7: (a) IR spectra of the dry polymer samples. The wavenumber plotted in (b) is marked by the black arrows. (b) Effective thermal conductivity (columns) and Wavenumber of the carbonyl-peak of the dry polymers. (c) Deconvoluted IR spectra of the dry polymers. The resolved peaks are attributed to distinct H-bond interactions. On the left, the structure of the respective polymers is illustrated. (d) Effective thermal conductivity plotted dependent on the relative humidity. The solid lines represent the experimental values, while the dashed lines were determined from a simple mixing model.

Overall, we show through the investigation of ampholytic polymers that the thermal transport across interpolymer interactions depends on the bonding strength. However, the number of factors makes it difficult to understand the thermal transport in ampholytic polymers fully. The water uptake also depends on the nature of the different functional groups. Generally, water is absorbed directly bound at a functional group or in an unbound state. Incidence for a composite like behavior was found for samples, which absorb unbound water clusters.

In conclusion, this thesis elaborates the thermal transport in polymers and polymeric hybrid materials. Therefore, the PA method for determining the cross-plane thermal conductivity in thin films on substrates was implemented. The crucial impact of interfaces could be demonstrated based on structurally controlled PNCs. Furthermore, the effect of different filler geometries was investigated. With spherical fillers, isotropic thermal conductivity is expected, while oriented platelets lead to a large anisotropy of the PNC properties. Last, the influence of interchain chemical bonds on the thermal conductivity of polymers was researched. Here, the inter- and intramolecular H-bond strength could be correlated to the thermal conductivity. The results also indicate that some polymers behave like composites when absorbing water.

## 5.2 Individual contributions to joint publications

The results presented in this work were prepared in cooperation with other colleagues. The individual contributions of all authors are designated below.

### **Chapter 6: Simple and High Yield Synthesis of Metal-Polymer Nanocomposites: The Role of Theta-Centrifugation as an Essential Purification Step**

This work was published in *Polymers*, **2017**, *9*, 659.

by *Patrick Hummel, Arne Lerch, Sebastian M. Goller, Matthias Karg and Markus Retsch*

I designed and planned the experiments, synthesized and characterized the polymer nanocomposites, and contributed to the manuscript. Arne Lerch performed and evaluated the dynamic light scattering experiments. Sebastian M. Goller synthesized and characterized parts of the polymer nanocomposite samples during his Bachelor thesis under my supervision. Matthias Karg supervised and analyzed the dynamic light scattering measurements and proofread the manuscript. Markus Retsch supervised the project and corrected the manuscript.

### **Chapter 7: Well-defined metal-polymer nanocomposites: The interplay of structure, thermoplasmonics, and elastic mechanical properties**

This work was published in *Physical Review Materials* **2018**, *2*, 123605.

by *David Saleta Reig, Patrick Hummel, Zuyuan Wang, Sabine Rosenfeldt, Bartłomiej Graczykowski, Markus Retsch and George Fytas*

David Saleta Reig conducted and evaluated the Brillouin light scattering measurements. I prepared the polymer nanocomposite samples and discovered the thermal annealing effect. Zuyuan Wang performed the COMSOL calculations. Sabine Rosenfeldt performed and analyzed the small-angle X-ray scattering experiments. Bartłomiej Graczykowski supervised the Brillouin light scattering measurements. Markus Retsch and George Fytas supervised the project. All authors discussed the results and jointly wrote the manuscript. The Appendix of this chapter was not published, and was solely written by me.

## **Chapter 8: Anisotropic thermal transport in spray-coated single-phase 2D materials: synthetic clay vs. graphene oxide**

This work was published in *ACS Appl Mater Interfaces*, **2020**, *12*, 18785-18791.

by Alexandra Philipp<sup>‡</sup>, Patrick Hummel<sup>‡</sup>, Theresa Schilling, Patrick Feicht, Sabine Rosenfeldt, Michael Ertl, Marius Schöttle, Anna M. Lechner, Zhen Xu, Chao Gao, Josef Breu and Markus Retsch

<sup>‡</sup> These authors contributed equally to this work.

Alexandra Philipp measured the in-plane thermal diffusivity with lock-in thermography and contributed to the manuscript. I measured the cross-plane thermal conductivity with the photo-acoustic method and contributed to the manuscript. Theresa Schilling prepared Hec and GO samples and contributed to the manuscript. Patrick Feicht synthesized the GO-syn sample. Sabine Rosenfeldt performed the small-angle X-ray scattering measurements. Michael Ertl performed the X-ray photoelectron spectroscopy experiments. Marius Schöttle conducted Raman measurements. Anna M. Lechner conducted differential scanning calorimetry measurements to obtain the specific heat. Zhen Xu provided the commercial GO material. Chao Gao proofread the manuscript. Josef Breu was involved in scientific discussion, supervised the project and corrected the manuscript. Markus Retsch was involved in scientific discussion, supervised the project and corrected the manuscript.

## **Chapter 9: Tunable thermoelastic anisotropy in hybrid Bragg stacks with extreme polymer confinement**

This work was published in *Angew. Chem. Int. Ed.*, **2020**, *59*, 1286-1294.

by Zuyuan Wang, Konrad Rolle<sup>‡</sup>, Theresa Schilling<sup>‡</sup>, Patrick Hummel<sup>‡</sup>, Alexandra Philipp<sup>‡</sup>, Bernd A.F. Kopera, Anna M. Lechner, Markus Retsch, Josef Breu and George Fytas

<sup>‡</sup> These authors contributed equally to this work.

Zuyuan Wang and Konrad Rolle performed the mechanical characterization with Brillouin light scattering. Theresa Schilling prepared the composite Hectorite samples. I measured the cross-plane thermal conductivity with the photo-acoustic method. Alexandra Philipp measured the in-plane thermal diffusivity with lock-in thermography. Alexandra Philipp and Bernd A.F. Kopera implemented and built the lock-in thermography setup. Anna Lechner measured differential scanning calorimetry. Markus Retsch, Josef Breu, and George Fytas supervised the work and corrected the manuscript.

## Chapter 10: Thermal Transport in Ampholytic Polymers: The Role of Hydrogen Bonding and Water Uptake

This work was published in *Macromolecules* **2020**, 53, 5528-5537.

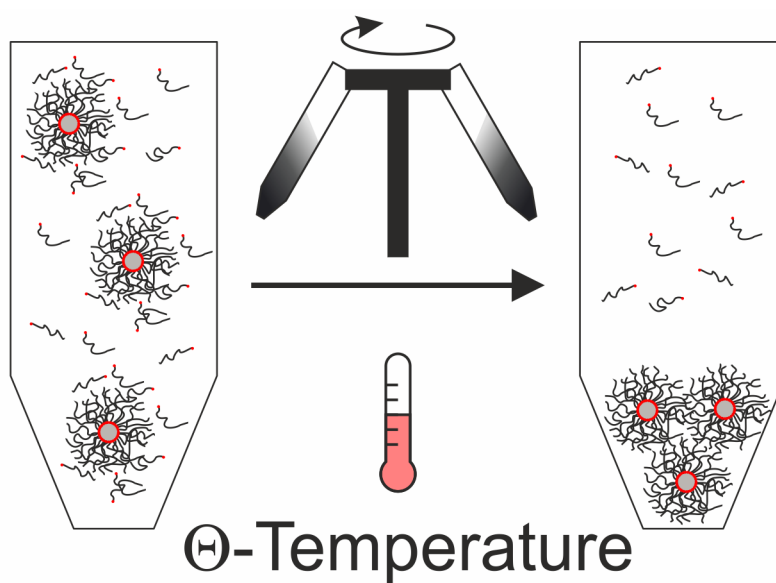
by *Patrick Hummel, Anna M. Lechner, Kai Herrmann, Philip Biehl, Carsten Rössel, Lisa Wiedenhöft, Felix H. Schacher and Markus Retsch*

I prepared the samples, performed the photoacoustic measurements, the density determination, the IR measurements, the humidity experiments and worked on the manuscript. Anna M. Lechner performed standard and modulated differential scanning calorimetry measurements. Kai Herrmann conducted additional photoacoustic and density measurements. Philip Biehl, Carsten Rössel and Lisa Wiedenhöft synthesized and characterized the ampholytic polymers PDha, PAGA, PImAA and PMeImAA. Felix H. Schacher supervised to the polymer synthesis and contributed to the manuscript. Markus Retsch supervised the project and worked on the manuscript.



## 6 Simple and High Yield Synthesis of Metal-Polymer Nanocomposites: The Role of Theta-Centrifugation as an Essential Purification Step

*Patrick Hummel, Arne Lerch, Sebastian M. Goller, Matthias Karg and Markus Retsch*



Reprinted with permission from Hummel et al., *Polymers*, **2017**, 9, 659.

**Abstract:** Nanocomposites are an important materials class, which strives to foster synergistic effects from the intimate mixture of two vastly different materials. Inorganic nanoparticles decorated with polymer ligands, for instance, aim to combine the processing flexibility of polymers with the mechanical robustness of solid state materials. The fabrication and purification of such composite nanoparticles, however, still presents a synthetic challenge. Here, we present a simple synthesis of silver polystyrene nanocomposites with a controllable interparticle distance. The interparticle distance can be well-controlled with a few nanometer precision using polystyrene ligands with various molecular weights. The nanoparticle and polymer ligand synthesis yield both materials on gram scales. Consequently, the polymer nanocomposites can also be fabricated in such large amounts. Most importantly, we introduce  $\theta$ -centrifugation as a purification method, which is capable of purifying large nanocomposite batches in a reproducible manner. We employ a range of characterization methods to prove the successful purification procedure, such as transmission electron microscopy, thermogravimetric analysis, and dynamic light scattering. Our contribution will be of high interest for many groups working on nanocomposite materials, where the sample purification has been a challenge up to now.

## 6.1 Introduction

Polymer nanocomposites (PNC) are a material class of high interest. Superior material properties can be achieved by the synergistic combination of the soft polymer coating and the rigid inorganic core. Depending on the combination of polymer and core material a range of properties can be varied. As an example, the incorporation of nanoclay sheets reinforces the mechanical properties, improves barrier properties and flame retardation<sup>[1]</sup>. PNCs filled with semiconductor nanocrystals have the potential for light conversion applications<sup>[2]</sup>, such as light emitting diodes<sup>[3,4]</sup>. In addition to inorganic fillers, also organic fillers like graphene<sup>[5-8]</sup>, graphene-oxide<sup>[9]</sup>, (modified) carbon fibers<sup>[10]</sup> and multi-walled carbon nanotubes (MWCNT)<sup>[11,12]</sup>, can be used and increase the multifunctionality of PNCs further. Due to the improved mechanical, thermal, and electrical properties they show potential in many applications. For example, graphene-filled thermoplastic elastomers can be used as piezoresistive sensors<sup>[5]</sup>, strain sensors<sup>[6,8]</sup>, and organic vapor sensors<sup>[7]</sup>.

PNCs can be also produced by sputter deposition of metals on a polymer film. The deposition rate controls the cluster growth and therefore the size, shape and morphology of the metal clusters. Hence, the structure and consequently the effective properties can be tailored in a very controlled manner by the variation of the deposition rate<sup>[13-15]</sup>. However, only 2D arrangements are possible with this method. In this paper we focus on systems with the potential to form 3D arrangements of PNCs. A paramount precondition for the fabrication of high-performance polymer nanocomposites is the strict exclusion of nanoparticle aggregation or demixing with the polymer matrix<sup>[16]</sup>. Therefore, it is of great importance to ensure a good stability of the nanoparticles. A conventional method is to coat the nanoparticles with the same polymer as the matrix. Polymer brushes are often used for this purpose.

There exist two main approaches to form a polymer brush around a nanoparticle, grafting-from and grafting-to. In the grafting-from approach molecules, like initiators for ATRP<sup>[17]</sup> or CTAs for RAFT polymerizations<sup>[18]</sup>, are immobilized on the particle surface. The drawbacks of this method are the development of new initiator coupling reactions. Furthermore, the particles have to be colloidally stable under the polymerization conditions. The grafting-to method is more flexible with respect to polymerization conditions because the polymers are synthesized separately. Afterwards they are attached to the particle surface by a chemical reaction or physisorption. One drawback of grafting-to is the usually lower grafting density, due to the steric repulsion of the coiled polymer chains during attachment to the particle surface. A common grafting-to approach is the ligand exchange method. Here, the surfactants used during nanoparticle synthesis are exchanged by functional poly-

mer ligands. Already a wide range of particles, functional groups and polymers was demonstrated by this method<sup>[19–22]</sup>. The biggest advantage is the complete segregation of nanoparticle and polymer synthesis. Thus, on the one hand, high yield nanoparticle synthesis routes can be exploited. On the other hand, the polymerization technique can be freely chosen. Here RAFT synthesis has excelled due to a large variety of monomers and easy functionalization<sup>[23,24]</sup>. The CTA can be readily used as functional group itself<sup>[24]</sup>, a functionalized CTA can be used or the polymer chains can be post-functionalized<sup>[25]</sup>. All grafting-to methods suffer from the drawback that a rigorous workup is necessary to remove the excess of free ligand from the functionalized nanocomposite particle. This is typically achieved by selective precipitation and centrifugation. The selective precipitation is a challenging task and needs high experimental skills.

In this work we present a polymer nanocomposite synthesis based on silver cores stabilized by thiol functionalized polystyrene ligands. We combine well known and simple synthesis routes with access to high yields of silver nanoparticles and end-group functionalized polystyrene. Furthermore, we use a ligand exchange process to obtain densely grafted silver polystyrene nanocomposites and demonstrate a new alternative, and in our opinion superior, purification route based on  $\theta$ -condition centrifugation. Finally, we demonstrate a high control of the edge-to-edge particle distance in our polymer nanocomposites, due to the systematic dependency of the interparticle distance on the molecular weight of the ligands. This tailoring of the interparticle distance is a prerequisite for applications, like efficient SERS sensors<sup>[26]</sup>.

## 6.2 Materials and Methods

### 6.2.1 Materials

All solvents used were pro analysi (p.a.) grade. Prior to polymerization the inhibitor of the styrene (Sigma, St. Louis, MO, USA,  $\geq 99\%$ ) was removed by an aluminum oxide column. CPDTC (Sigma, St. Louis, MO, USA, 97%), 1-butylamine (Alfa Aesar, Ward Hill, MA, USA, 99%), silver nitrate (Alfa Aesar, Ward Hill, MA, USA, 99.9995%), triethylamine (Alfa Aesar, Ward Hill, MA, USA, 99%), and sodium myristate (Sigma, St. Louis, MO, USA,  $\geq 99\%$ ) were all used as received.

### 6.2.2 RAFT synthesis

Our RAFT polymerization was conducted according to the work of Mayadunne et al.<sup>[27]</sup>. The desired ratio of 2-cyano-propyl dodecyl trithiocarbonate and styrene

were weighed in a single-neck flask equipped with a stirrer bar. The flask was sealed with a septum and degassed with argon for 30 min. Afterwards, the reaction was started by heating the flask to 110 °C. The conversion was monitored by <sup>1</sup>H-NMR measurements. When the desired conversion was reached, the reaction was stopped by cooling the flask in an ice bath. Then the reaction mixture was dissolved in tetrahydrofuran (THF) and separated from remaining styrene by precipitation in cold methanol. For the shortest polymer (1000 g/mol) a methanol:water 3:2 mixture was used. The reaction conditions of all polymerizations are summarized in Table 6.1.

Table 6.1: Summary of the reaction conditions of the different polystyrene ligands.

Sample name	[Styrene]/[CTA]	Conversion	Reaction time	M <sub>n</sub>	M <sub>n</sub> (calc)	PDI
		%	h	g/mol	g/mol	
PS1K	12	80.4	68	996	1000	1.05
PS3K	38	76.2	50	2560	3080	1.05
PS4K	48	81.5	67	3940	4070	1.05
PS6K	96	75.5	28.5	6030	7660	1.04
PS8K	96	82.6	47	7940	8260	1.04
PS12K	154	92.2	25	11,380	14,770	1.04
PS18K	288	79.1	32	18,850	23,730	1.04

For the aminolysis the polymers were dissolved in toluene and a 25-fold excess of butylamine was added. The solution was stirred for 24 h. Afterwards the solution was extracted three times with brine and precipitated in cold methanol.

### 6.2.3 Nanoparticle synthesis

The nanoparticle synthesis was performed according to Yamamoto et al.<sup>[28]</sup>. The precursor for the silver nanoparticle synthesis, silver myristate, was received by mixing equal molarities of sodium myristate and silver nitrate. The white precipitate was filtered and dried overnight in a vacuum oven. For a standard formulation of the nanoparticle synthesis 1 g silver myristate and 22 mL triethylamine were used. Additionally, reactions with up to 10 g silver myristate and 220 mL trimethylamine were performed. Both reactants were mixed in a Schlenk flask connected to a reflux condenser. The flask was then purged with argon for 30 min. Hereafter, the reaction mixture was heated to 80 °C and held at this temperature for 4 h. After around

15 min the white dispersion slowly becomes yellow and brown. Finally, a homogeneous black solution is formed. The nanoparticles were purified by precipitation with acetone with subsequent centrifugation at 5095 relative centrifugal force (rcf) for 30 min. They were dissolved in toluene and the purification step was repeated two times.

#### 6.2.4 Ligand exchange

An excess of polymer ligand was used for the ligand exchange. The excess was calculated based on the amount of ligand needed for a potential grafting density of  $10 \text{ nm}^{-2}$ . The required amount of polystyrene was dissolved in toluene and the corresponding nanoparticle dispersion was added dropwise. This mixture was stirred for 65 h. In the next step, the nanocomposites were quantitatively precipitated with ethanol. The precipitate was separated by centrifugation at 5095 rcf for 30 min and redispersed in toluene. This procedure was repeated two times, but after the last centrifugation the precipitate was redispersed in cyclohexane instead of toluene. Subsequently the nanocomposites were centrifuged at 10,000–50,000 rcf at the  $\Theta$ -temperature of styrene in cyclohexane,  $34 \text{ }^\circ\text{C}$ . We want to mention that a centrifugal force of 10,000–15,000 rcf was already sufficient to sediment the nanocomposite particles. Higher centrifugation forces speed up the work up procedure. The centrifugations were usually proceeded overnight. We note that compatibility of centrifugal tubes with elevated temperatures and solvents should be tested prior to centrifugation overnight.

#### 6.2.5 Characterization

$^1\text{H-NMR}$  measurements were recorded on a Bruker Avance 300 A (300.13 MHz, Billerica, MA, USA) spectrometer using  $\text{CDCl}_3$  as the solvent.

The molecular weight distributions were determined by size exclusion chromatography (SEC) with THF as eluent with a flow rate of  $0.5 \text{ mL}\cdot\text{min}^{-1}$  at  $25 \text{ }^\circ\text{C}$ , using a linear polystyrene standard obtained from Polymer Standard Service (PSS, Mainz, Germany, the Knauer, Berlin, Germany system is equipped with a PSS-SDV (10  $\mu\text{m}$ ) 50 mm x 8 mm column, two 600 mm x 8 mm columns, and a differential refractive index detector).

Ultraviolet and visible light (UV/Vis) spectra were measured with an Analytik Jena SPECORD 250 Plus spectrophotometer (Jena, Germany). As cuvettes, high-precision cells made of quartz SUPRASIL from Hellma Analytics (Müllheim, Germany) with a light path of 10 mm were used.

A Sigma 3-30KS centrifuge (Sigma Laborzentrifugen GmbH, Osterode am Harz, Germany) equipped with a Sigma 19776-H or a Sigma 12111-H rotor was used for centrifugation procedures. The latter rotor was only used for the  $\theta$ -centrifugation with 10 mL Sigma 15,000 polyfluor tubes, whereas the first was used for both, normal and  $\theta$ -centrifugation steps with 50 mL polypropylene tubes purchased from VWR (Radnor, PA, USA).

Light scattering experiments were performed on a 3D spectrometer from LS Instruments AG (Fribourg, Switzerland) equipped with a HeNe-laser ( $\lambda = 632.8$  nm, maximum constant power output of 35 mW). Experiments were performed in 2D operation. The samples dispersed in cyclohexane were heated to 45 °C and directly filtered (hydrophobic PTFE filter, pore size 5  $\mu\text{m}$ ) into dust free quartz cuvettes with a diameter of 10 mm (Hellma Analytics, Müllheim, Germany). The quartz cuvettes were heated to 45 °C and vortexed for aggregates to disperse completely. For the measurements the cuvettes were placed in a temperature controlled decalin bath (stability  $\pm 100$  mK) preheated to a temperature of 44 °C. The temperature was followed by a PT100 thermoelement placed close to the sample position in the decalin bath. Measurements were performed after an equilibration time of 30 min at temperatures of 44 °C followed by 34 °C followed by 24 °C. The scattered light was detected by two avalanche-photo-diodes operating in pseudo cross correlation. Three intensity-time autocorrelation functions were measured for 30 s at a scattering angle of  $\theta = 90^\circ$  for all three temperatures. Analysis of the recorded autocorrelation functions was performed by CONTIN analysis (inverse Laplace transformation) with the software AfterALV (v1.06d, Dullware Inc., Amsterdam, The Netherlands).

thermal gravimetric analysis (TGA) was performed on a Mettler Toledo TGA/STDA 851e Star System (Columbus, OH, USA) at a heating rate of 10 K $\cdot$ min $^{-1}$  in a temperature range between 30 °C and 700 °C and a nitrogen flow of 50 mL $\cdot$ min $^{-1}$ .

A JEOL JEM-2200FS (Akishima, Japan) and a Zeiss EM922 Omega (Jena, Germany) transmission electron microscope (TEM) were used to record TEM images of the nanoparticle and nanocomposite samples. ImageJ 1.49v (National Institute of Mental Health, Bethesda, MD, USA) was utilized to evaluate the TEM images. This analysis provided the average particle size and the edge-to-edge interparticle distance.

### 6.3 Results and Discussion

The polystyrene ligands were synthesized by a RAFT polymerization. We chose thermal initiation at 110 °C and used CPDTTC as the CTA. The polymerization was conducted in bulk. The reaction scheme is shown in Figure 6.1

The desired molecular weight was adjusted by the ratio of styrene and CTA and the conversion of the reaction. For calculation of the molecular weight we used a simplified equation from the literature<sup>[27]</sup>:

$$M_n(\text{calc}) = \frac{[\text{styrene}]}{[\text{CTA}]} \cdot \text{conversion} \cdot M_{\text{styrene}}, \quad (6.1)$$

The calculated number averages of the molecular weight ( $M_n(\text{calc})$ ) are in good agreement with the experimental  $M_n$  values, as it can be seen in Table 6.1 Especially in the range from 1000 to 8000 g/mol the predictions were accurately met. Beyond 8000 g/mol the deviation increases slightly. Nevertheless, the high conformity of the calculated and experimental  $M_n$  and the low polydispersities of 1.05 show the high control over the reaction. The narrow distribution of the molecular weights before aminolysis is presented by the solid lines in Figure 6.2a.

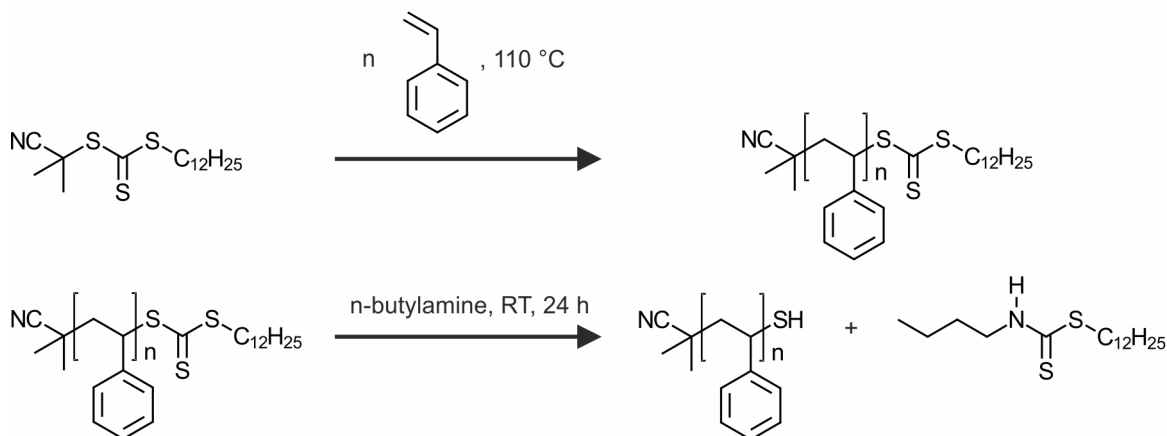


Figure 6.1: Reaction scheme of the RAFT polymerization (**top**) and the aminolysis to yield a thiol functionalization (**bottom**).

Based on the RAFT polymerization, every chain bears a trithiocarbonate end-group. We converted this to a thiol group, which provides a smaller footprint anchor group for the silver nanoparticle surface. Consequently, higher grafting densities are likely to be reached. For the thiol generation, an aminolysis is conducted, as illustrated in Figure 6.1. This decreases the molecular weight slightly (dashed lines in Figure 6.2a) and in some samples a second peak at the double molecular weight emerges. The second peak belongs to a small fraction of chains, which have been connected by

disulfide bonds. The presence of disulfide bonds evidences the successful cleavage of the trithiocarbonate groups. It is assumed that the relatively weak disulfide bonds do not disturb the ligand exchange, because they will dissociate and form stronger Ag-S bonds, as it was reported for gold interfaces<sup>[29]</sup>. Furthermore, the color of the polymers changed from yellow to white after the aminolysis. The UV/Vis spectra of three different ligands before and after the aminolysis are given in Figure 6.2b. The solid lines present the spectra before the aminolysis. A peak at around 420 nm, attributed to the  $n \rightarrow \pi^*$  transition can be seen<sup>[30]</sup>. This peak completely vanishes in the spectra after the aminolysis represented by the dashed lines. Overall, we could show that the RAFT polymerization is a straightforward method to yield thiol terminated polystyrene ligands with low polydispersity and a good control of the molecular weight. In addition, we want to note that RAFT synthesis is suitable for many other monomers. In consequence the synthesis could be easily assigned to design ligands from a wide range of polymers

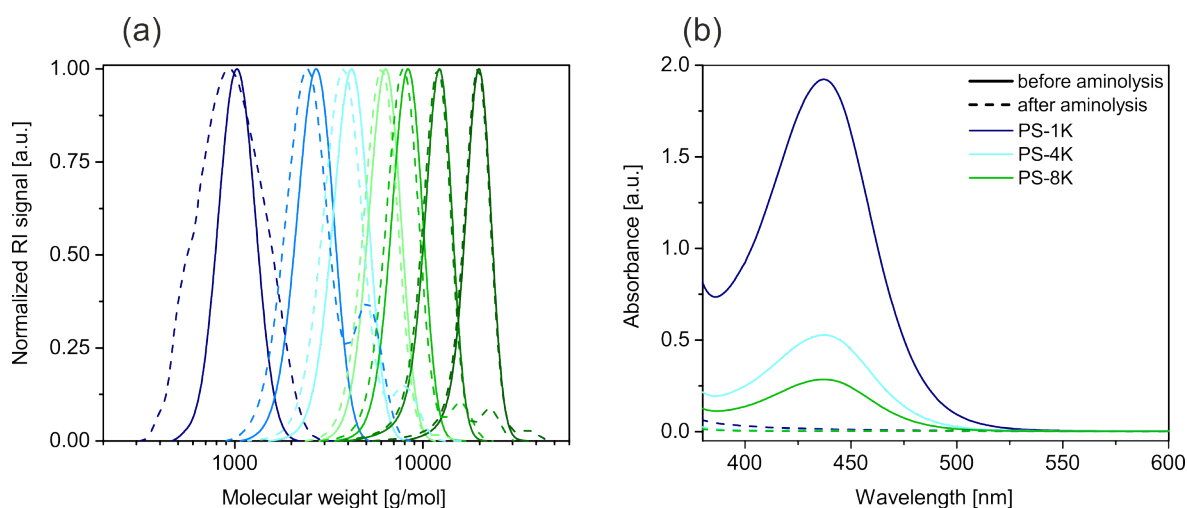


Figure 6.2: (a) Molecular weight distributions of the polystyrene ligands before (solid lines) and after (dashed lines) the aminolysis. (b) UV-VIS spectra of the 1K, 4K, and 8K ligands before (solid lines) and after (dashed lines) the aminolysis. The absence of the  $n \rightarrow \pi^*$  transition proves the successful reaction. The absorbance decreases with increasing molecular weight, which correlates well to the ratio between trithiocarbonate end-groups and the ligand length.

The synthesized polymers were then used in a homogeneous ligand exchange reaction. Therefore, an excess of polystyrene ligands was mixed with separately synthesized silver nanoparticles in toluene. The monodisperse silver nanoparticles were produced according to Yamamoto et al.<sup>[28]</sup>. The resulting particles are stabilized by myristate, which binds with its carboxylic moiety to the Ag nanoparticle surface. The thiol group of the polymer ligand replaces the myristate due to the weaker binding strength of the carboxylic acid groups. Still, a large excess of polymer ligand is needed to fully drive the exchange reaction towards completion<sup>[21]</sup>. The lig-

and exchange is additionally aided by a quantitative precipitation step. Here, the nanocomposite and the free polymer is completely precipitated by the addition of a non-solvent, in our case, ethanol. This step is crucial for the complete ligand exchange and the generation of a high grafting density, as the local polymer concentration at the nanoparticle surface is strongly increased by the precipitation. Subsequently, the sample is centrifuged and the precipitate with the nanocomposites and the free polymer is separated from the supernatant, which is enriched by the unbound myristate molecules<sup>[21]</sup>. After the complete functionalization of the Ag nanoparticle with the desired polymer ligand, the excess free polymer has to be removed. Several strategies can be followed for this. Ehlert et al.<sup>[21]</sup> introduced a second, so called selective, precipitation step. The non-solvent is added stepwise, until only the nanocomposites precipitate, but not the free polymer. Experimentally, this is a great effort because the sample has to be centrifuged after every addition of non-solvent to check if there is still nanocomposite in the dispersion. Additionally, the added amount can be too high and an additional quantitative precipitation instead of a selective precipitation was performed. Dialysis represents a well-established alternative, but is mainly applicable to water-based polymers. Furthermore, dialysis is a time-consuming procedure and requires a large hydrodynamic size mismatch between the functionalized nanoparticle and the ligand.

For these reasons, we suggest another method to purify the nanocomposites in organic solvents from excess ligands. Instead of using solvent and non-solvent mixtures, we recommend to use a  $\theta$ -solvent and centrifugation at the  $\theta$ -temperature. This is a convenient and reproducible strategy, because one does not have to exactly adjust the right amount of non-solvent, but can set the temperature to  $\theta$ -conditions, which is well known for many polymer/solvent combinations. By definition, the enthalpic interaction between polymer and solvent is equal to the polymer-polymer interaction at the  $\theta$ -temperature. Consequently, the steric repulsion of the polymer brushes decreases<sup>[31]</sup>. Below the  $\theta$ -temperature the solvent becomes enthalpically unfavorable, while it approaches good solvent conditions at higher temperatures. This general behavior is known from the Flory-Huggins theory. Temperature-dependent DLS measurements on our nanocomposite particles confirm this behavior (Figure 6.3). Figure 6.3a,c,e show intensity-time autocorrelation functions measured for the PNCs with different molecular weight ligands at 24, 34 and 44 °C. At first glance one recognizes a monomodal decay at relatively short decay times for all samples measured at elevated temperatures (34 and 44 °C). Furthermore, the autocorrelation functions for each sample at these temperatures almost match, indicating only slight differences in object size. Only for the shortest polymer ligand (AgPS-4K) a small second decay is observed at longer decay times pointing to a small fraction of larger objects, i.e., aggregates. At 24 °C, i.e., well below the  $\theta$ -temperature, the

decay of the autocorrelation functions is shifted significantly to longer decay times, which points to much larger objects. Figure 6.3b,d,f show distribution functions of the hydrodynamic radii  $R_h$  obtained from CONTIN analysis of the autocorrelation functions. These distribution profiles confirm the trends observed from the autocorrelation functions. The data show, that the PNCs form aggregates with large  $R_h$  values on the order of 500 nm below the  $\theta$ -temperature at 24 °C. In contrast, the PNCs remain dispersed at the  $\theta$ -temperature and above (34 and 44 °C, respectively). Only for the smaller samples, AgPS-4K and AgPS-8K, a small fraction of larger objects is found. We want to highlight that the latter size populations that we attribute to small fractions of aggregates resemble the minority of the samples since the data are intensity weighted and not number weighted. The DLS measurement confirms the expected influence of the temperature on the PNCs stability in solution.

The  $\theta$ -temperature itself is a function of the polymer molecular weight. One can, therefore, expect that the grafted polymer chains possess a lower  $\theta$ -temperature than their freely dissolved counterparts. Distinct differences between the tethered and the free polymer additionally help the selective purification. At the  $\theta$ -temperature the tethered and free polymer will be less extended, compared to a good solvent<sup>[32]</sup>. Furthermore, the height contraction of tethered polymers is larger than the decrease of  $R_g$  of free polymer coils<sup>[33]</sup>. Consequently, the solubility of tethered polymer chains is much more decreased compared to the solubility of free polymer chains at  $\theta$ -conditions. Whereas the mentioned studies were performed for polymer brushes attached to planar surfaces, an analogous behavior can be expected for spherical brush particles. Hence, the steric stabilization is sufficiently suppressed and the polymer functionalized nanoparticles can be separated via centrifugation, whereas the free polymer chains remain dissolved in the supernatant. We applied this simplified purification method to a large range of polystyrene ligands with molecular weights ranging from 1 up to 18 kg/mol. The systematic increase in interparticle distance, observed in the TEM images in Figure 6.4, is a strong indication for the removal of all excess free polymer and the successful coating with the desired polymer ligand.

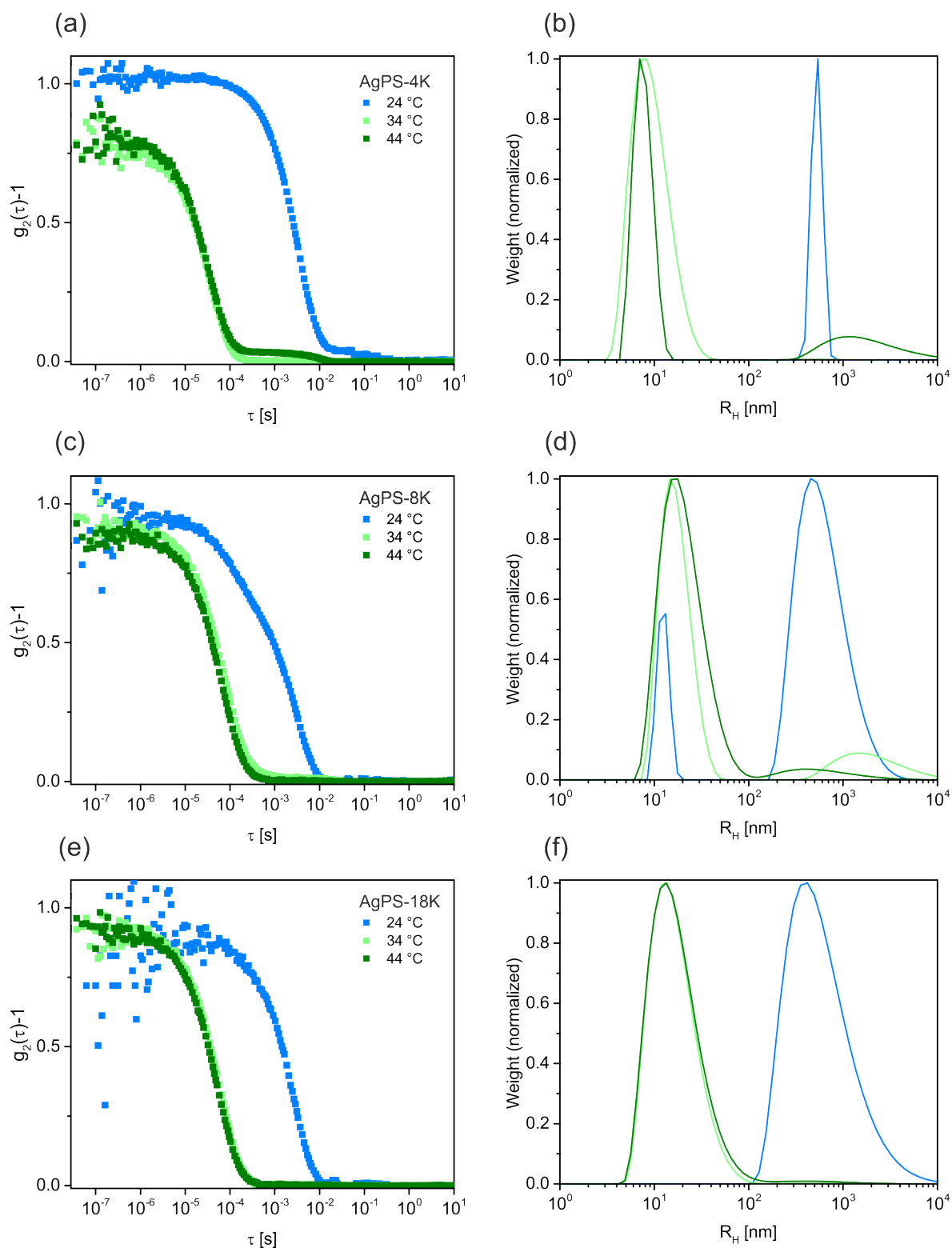


Figure 6.3: Dynamic light scattering measurements of PNCs in cyclohexane. Left panel: intensity-time autocorrelation functions. Right panel: corresponding size distribution of the samples obtained from CONTIN analysis. The measurements were performed at three different temperatures. Below ( $24\text{ }^{\circ}\text{C}$ ), at ( $34\text{ }^{\circ}\text{C}$ ) and above ( $44\text{ }^{\circ}\text{C}$ ) the  $\theta$ -temperature. The ligand length increases from top to bottom: (a,b) AgPS-4K sample, (c,d) AgPS-8K sample and (e,f) AgPS-18K sample. All samples show aggregates below the  $\theta$ -temperature.

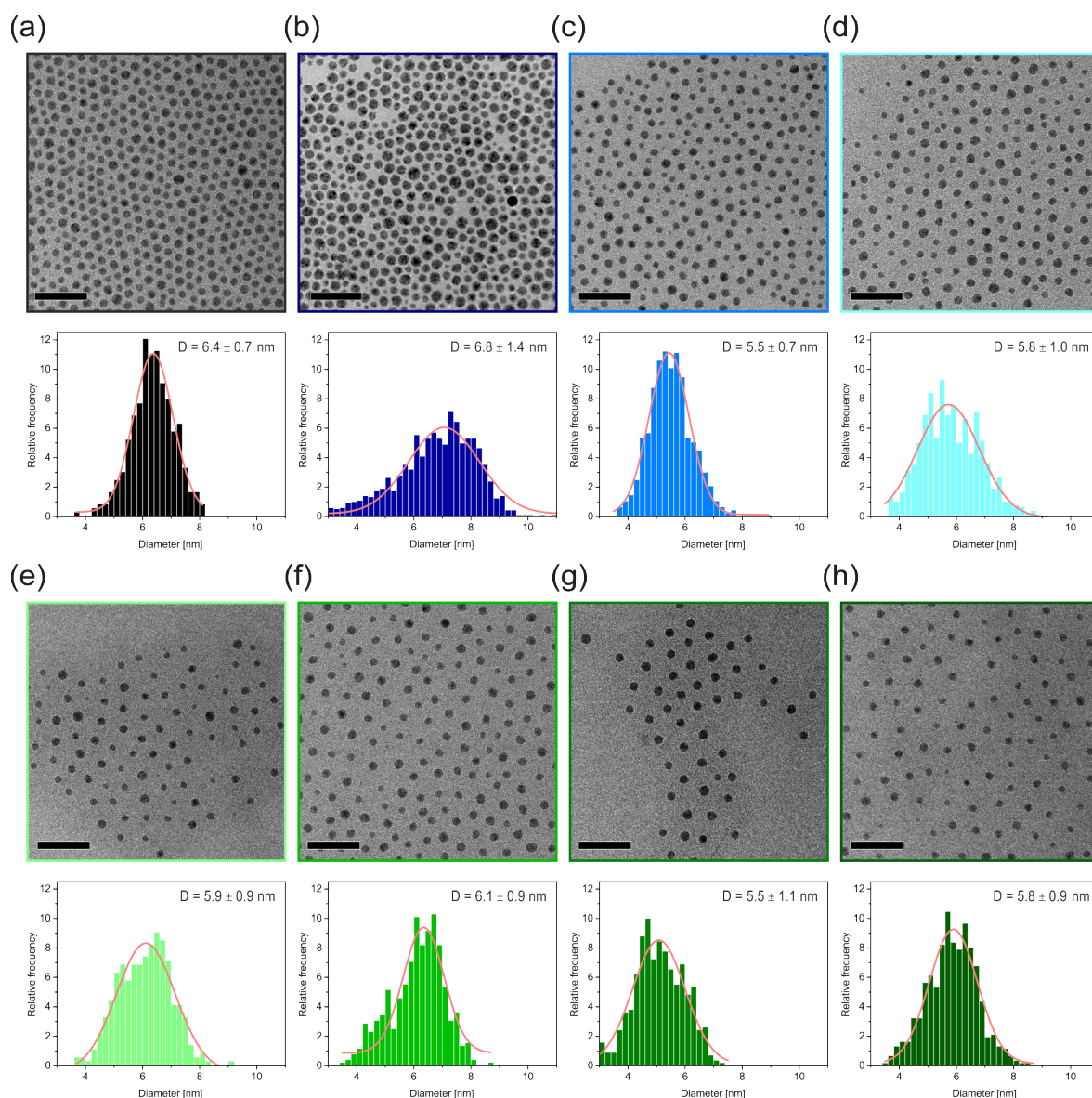


Figure 6.4: (a) Pure Ag@myristate nanoparticles. (b–h) nanocomposite samples with the following molecular weight of the polystyrene ligands: (b) 1 kg/mol; (c) 3 kg/mol; (d) 4 kg/mol; (e) 6 kg/mol; (f) 8 kg/mol; (g) 12 kg/mol; and (h) 18 kg/mol. The interparticle distance increases with increasing molecular weight. All scale bars are 50 nm. The histograms in the bottom panel show the size distributions of the Ag core particle diameter of the respective sample.

The TEM images show monodisperse and well-separated particles. The monodispersity of the Ag core is pointed out by the size distribution histogram below the respective TEM image. All samples show a normal size distribution, as indicated by a Gaussian fit to the histogram. From this we obtained a mean diameter and standard deviation. Only the nanocomposite sample with the smallest ligand (AgPS-1K) shows a slightly increased size distribution. We suppose that some Ostwald ripening took place during the ligand exchange, owing to the reduced steric stabilization compared to longer ligands. In Figure 6.4a the pure Ag@myristate particles

are presented. After the ligand exchange the myristate is substituted by polystyrene ligands. This directly translates into a molecular weight dependence of the interparticle distance (Figure 6.5 The interparticle distance, which we determined between the respective particle surfaces (i.e., edge-to-edge), is plotted against the molecular weight in Figure 6.5a. The interparticle distance ranges from around 2 to 16 nm and increases monotonically with the molecular weight. This allows a very controlled adjustment of the interparticle distance in such nanocomposite materials. The shortest polystyrene ligand with a  $M_n$  of 1000 g/mol features an even shorter interparticle distance as the myristate stabilized particles (2.5 nm), as already observed by Ehlert et al.<sup>[21]</sup>. This offers the opportunity not only to increase the interparticle distance by coating with polymer ligands, but also to decrease it. The interplay between the degree of polymerization, the grafting density and the core particle curvature have been investigated by other groups in detail<sup>[34–36]</sup>. The theoretical brush height can be described by the Daoud-Cotton model for star polymers shown in Equation 6.2.

$$h \propto l_0 \cdot N^{\frac{3}{5}} \cdot f^{\frac{1}{5}} \cdot v^{\frac{1}{5}}, \quad (6.2)$$

where  $l_0$  is the length of one monomer unit,  $N$  is the degree of polymerization,  $f$  the number of arms of the star-polymer and  $v$  the second virial coefficient. It has been shown that their model can predict the brush height of polymer chains tethered to a particle surface, too. The dry interparticle distance of our grafted samples are well described by Equation 6.2, illustrated by the red line (Figure 6.5a). This can be assigned to the semi-dilute brush regime. The red line was calculated with the mean values of all PNC samples ( $f = 141$ ). This is an unexpectedly low scaling behavior with respect to the ligand molecular weight and the high grafting density as determined below. We want to stress that the theory is based on brush stabilized nanoparticles in a solvent, while we investigated dried samples adsorbed on a TEM grid. Consequently, the particles on the TEM images are closely packed and possible entanglement between brushes of neighboring particles is not taken into account. Yet, the universal applicability of this scaling theory to all our samples with vastly different molecular weights corroborates the successful ligand exchange. Most importantly it rules out the presence of free, unbound polymer, which would result in larger and non-systematic interparticle distances. We determined the grafting densities of the PNCs separately by TGA analysis. The grafting density  $D$  was calculated by Equation 6.3<sup>[21]</sup>:

$$D = \frac{4 \cdot r_n^3 \cdot \rho_n \cdot N_A \cdot (100 - X_n)}{3 \cdot (2 \cdot r_n)^2 \cdot M_p \cdot X_n}, \quad (6.3)$$

where  $r_n$  is the radius of the nanoparticle,  $\rho_n$  is the bulk density of silver,  $N_A$  the Avogadro constant,  $M_p$  the molecular weight of the ligand and  $X_n$  the weight percentage of the silver, measured by TGA. The TGA measurements of all nanocomposites are shown in Figure 6.5b. Additionally, a reference measurement of the pure Ag myristate particles before the ligand exchange is shown. It can be seen that the main step of thermal degradation shifts to higher temperatures when exchanging the myristate with the polystyrene ligands. No sign of residual myristate was found in the decomposition behavior of the polymer nanocomposites, indicating a quantitative ligand exchange. Furthermore, the residual mass depends on the molar mass of the polymeric ligand. The residual mass decreases with increasing ligand length.

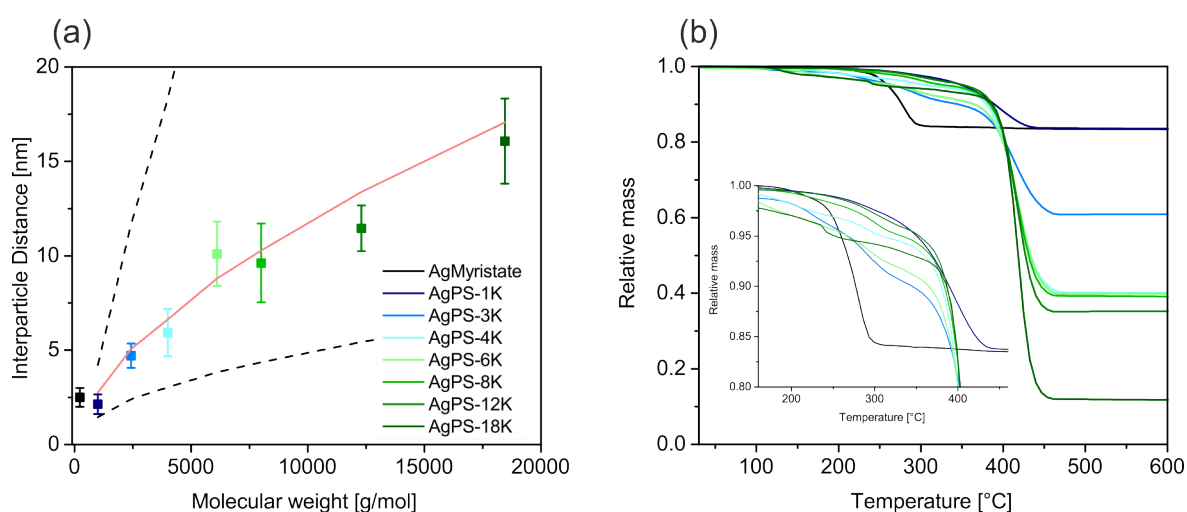


Figure 6.5: (a) The edge-to-edge interparticle distance in the nanocomposites increases systematically with higher molecular weight. The dashed lines present the upper (fully-stretched chain) and lower limit (random coil  $R_g \approx l_0 N^{1/2}$ ). The red line was calculated by Equation 6.2 and represents the theoretical interparticle distance of a polymer brush in the semi dilute regime. (b) TGA curves of the nanocomposites and of pure silver particles with myristate ligand as a reference. The inset emphasizes the onset of thermal degradation. The myristate ligand decomposes at much lower temperatures than the polystyrene ligand.

The relatively low difference in residual Ag content in the Ag@PS-4K to 8K samples is ascribed to differences in the grafting densities in these samples. The grafting densities with the related silver contents and the interparticle distances are listed in Table 6.2. The grafting densities are 0.8 to 2.5 ligands per  $\text{nm}^2$ . These are high grafting densities and compare to values reported for the ligand exchange method (1.2 ligands per  $\text{nm}^2$ )<sup>[21]</sup>. Furthermore, our grafting densities are as high as the grafting density of CTA reported for grafting-from approaches by RAFT polymerization<sup>[37]</sup>. Accordingly, our particles show a higher polymer grafting density, because not every CTA will lead to a polymer chain in a grafting-from approach. Typically, the resulting grafting density in grafting-from approaches lies in the region of 0.6 lig-

ands per nm<sup>2</sup>[37–39]. Therefore, our homogeneous ligand exchange, in combination with quantitative precipitation and  $\theta$ -condition purification, results in highly-functionalized nanocomposites and even compares well to grafting-from approaches.

Table 6.2: Overview of the silver content, grafting density, and edge-to-edge interparticle distance (IPD with standard deviation  $\sigma_{IPD}$ ) of the nanocomposite samples.

Sample name	Ag content	Grafting density	IPD	$\sigma_{IPD}$
	wt%	ligands/nm <sup>2</sup>	nm	nm
<b>Ag@PS1K</b>	83.6	1.2	2.1	0.5
<b>Ag@PS3K</b>	60.9	1.4	4.8	1.3
<b>Ag@PS4K</b>	44.8	2.0	5.9	1.3
<b>Ag@PS6K</b>	39.9	1.4	10.1	1.9
<b>Ag@PS8K</b>	39.1	1.1	9.6	2.1
<b>Ag@PS12K</b>	35.2	0.8	11.3	2.4
<b>Ag@PS18K</b>	11.8	2.5	16.1	1.7

## 6.4 Conclusion

In this work we demonstrated a simple and high yield synthesis for nanocomposites composed of polymer functionalized silver nanoparticles. The 5 nm diameter silver cores are densely decorated by thiol-terminated polystyrene ligands, obtained from RAFT syntheses. The molecular weight was controlled by the ratio of styrene and chain transfer agent. Seven ligands of different lengths, determined by the molecular weight, were used in a ligand exchange process. We introduced the  $\theta$ -centrifugation as a new method to purify the polymer nanocomposites from excess polymer after the ligand exchange. The concept of this purification method was supported by temperature-dependent DLS measurements to demonstrate the nanocomposite stability. Stable particles were found close to, and above, the  $\theta$ -temperature, whereas aggregated particles formed at lower temperatures. The feasibility of the purification procedure was verified by TGA and TEM measurements. The systematic dependence of the interparticle distance on the molecular weight was manifested by TEM images. At the same time, high grafting densities comparable to grafting-from methods could be realized. Overall, our contribution highlights the strength of the grafting-to method to access well-defined nanocomposites. The introduction of an alternative purification protocol adds increased reproducibility and scalability to the fabrication of future nanocomposite materials.

**Acknowledgments:** Patrick Hummel and Markus Retsch acknowledge the funding by the Lichtenberg program provided by the Volkswagen foundation. Support was provided by the German Research Foundation (SFB 840).

**Author Contributions:** Patrick Hummel and Markus Retsch conceived and designed the experiments; Patrick Hummel and Sebastian Manfred Goller prepared the PNCs and characterized them; Arne Lerch performed the DLS measurements; Arne Lerch and Matthias Karg analyzed the DLS data; and Patrick Hummel and Markus Retsch wrote the manuscript.

**Conflicts of Interest:** The authors declare no conflict of interest. The founding sponsors had no role in the design of the study; in the collection, analyses, or interpretation of data; in the writing of the manuscript; or in the decision to publish the results.

## References

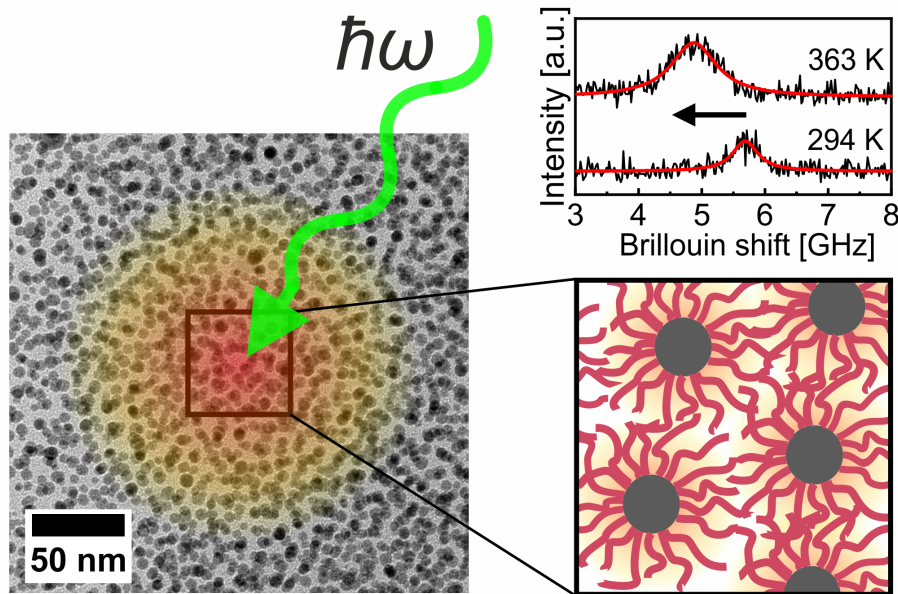
- [1] D. R. Paul, L. M. Robeson, *Polymer* **2008**, *49*, 3187–3204.
- [2] Y. Yuan, M. Kruger, *Polymers* **2012**, *4*, 1–19.
- [3] M. A. Schreuder, J. D. Gosnell, N. J. Smith, M. R. Warnement, S. M. Weiss, S. J. Rosenthal, *Journal of Materials Chemistry* **2008**, *18*, 970–975.
- [4] J. Bomm, A. Buchtemann, A. Fiore, L. Manna, J. H. Nelson, D. Hill, W. G. van Sark, *Beilstein J Nanotechnol* **2010**, *1*, 94–100.
- [5] H. Liu, M. Dong, W. Huang, J. Gao, K. Dai, J. Guo, G. Zheng, C. Liu, C. Shen, Z. Guo, *Journal of Materials Chemistry C* **2017**, *5*, 73–83.
- [6] H. Liu, J. Gao, W. Huang, K. Dai, G. Zheng, C. Liu, C. Shen, X. Yan, J. Guo, Z. Guo, *Nanoscale* **2016**, *8*, 12977–12989.
- [7] H. Liu, W. Huang, X. Yang, K. Dai, G. Zheng, C. Liu, C. Shen, X. Yan, J. Guo, Z. Guo, *Journal of Materials Chemistry C* **2016**, *4*, 4459–4469.
- [8] H. Liu, Y. Li, K. Dai, G. Zheng, C. Liu, C. Shen, X. Yan, J. Guo, Z. Guo, *Journal of Materials Chemistry C* **2016**, *4*, 157–166.
- [9] J.-X. Zhang, Y.-X. Liang, X. Wang, H.-J. Zhou, S.-Y. Li, J. Zhang, Y. Feng, N. Lu, Q. Wang, Z. Guo, *Advanced Composites and Hybrid Materials* **2017**, *1*, 300–309.
- [10] C. Wang, M. Zhao, J. Li, J. Yu, S. Sun, S. Ge, X. Guo, F. Xie, B. Jiang, E. K. Wujcik, Y. Huang, N. Wang, Z. Guo, *Polymer* **2017**, *131*, 263–271.
- [11] K. Sun, P. Xie, Z. Wang, T. Su, Q. Shao, J. Ryu, X. Zhang, J. Guo, A. Shankar, J. Li, R. Fan, D. Cao, Z. Guo, *Polymer* **2017**, *125*, 50–57.
- [12] S. M. Aqeel, Z. Huang, J. Walton, C. Baker, D. Falkner, Z. Liu, Z. Wang, *Advanced Composites and Hybrid Materials* **2017**, *1*, 185–192.
- [13] M. Schwartzkopf, A. Buffet, V. Korstgens, E. Metwalli, K. Schlage, G. Bencke, J. Perlich, M. Rawolle, A. Rothkirch, B. Heidmann, G. Herzog, P. Müller-Buschbaum, R. Rohlsberger, R. Gehrke, N. Stribeck, S. V. Roth, *Nanoscale* **2013**, *5*, 5053–5062.
- [14] M. Schwartzkopf, G. Santoro, C. J. Brett, A. Rothkirch, O. Polonskyi, A. Hinz, E. Metwalli, Y. Yao, T. Strunskus, F. Faupel, P. Müller-Buschbaum, S. V. Roth, *ACS Applied Materials & Interfaces* **2015**, *7*, 13547–13556.
- [15] M. Schwartzkopf, A. Hinz, O. Polonskyi, T. Strunskus, F. C. Löhner, V. Körstgens, P. Müller-Buschbaum, F. Faupel, S. V. Roth, *ACS Applied Materials & Interfaces* **2017**, *9*, 5629–5637.

- [16] C. H. Hung, W. T. Whang, *Journal of Materials Chemistry* **2005**, *15*, 267–274.
- [17] M. Iacono, A. Heise, *Polymers* **2015**, *7*, 1427–1443.
- [18] C. Li, B. C. Benicewicz, *Macromolecules* **2005**, *38*, 5929–5936.
- [19] S. Fischer, A. Salcher, A. Kornowski, H. Weller, S. Forster, *Angew. Chem. Int. Ed.* **2011**, *50*, 7811–4.
- [20] M. Bieligmeyer, S. M. Taheri, I. German, C. Boisson, C. Probst, W. Milius, V. Altstadt, J. Breu, H. W. Schmidt, F. D’Agosto, S. Forster, *J Am Chem Soc* **2012**, *134*, 18157–60.
- [21] S. Ehlert, S. M. Taheri, D. Pirner, M. Drechsler, H. W. Schmidt, S. Forster, *ACS Nano* **2014**, *8*, 6114–22.
- [22] S. Ehlert, T. Lunkenbein, J. Breu, S. Forster, *Colloids and Surfaces a-Physicochemical and Engineering Aspects* **2014**, *444*, 76–80.
- [23] P. E. Williams, S. T. Jones, Z. Walsh, E. A. Appel, E. K. Abo-Hamed, O. A. Scherman, *Acs Macro Letters* **2015**, *4*, 255–259.
- [24] B. Ebeling, P. Vana, *Macromolecules* **2013**, *46*, 4862–4871.
- [25] G. Moad, E. Rizzardo, S. H. Thang, *Polymer International* **2011**, *60*, 9–25.
- [26] G. Santoro, S. Yu, M. Schwartzkopf, P. Zhang, S. Koyiloth Vayalil, J. F. H. Risch, M. A. Rübhausen, M. Hernández, C. Domingo, S. V. Roth, *Applied Physics Letters* **2014**, *104*, 243107.
- [27] R. T. A. Mayadunne, E. Rizzardo, J. Chiefari, J. Krstina, G. Moad, A. Postma, S. H. Thang, *Macromolecules* **2000**, *33*, 243–245.
- [28] M. Yamamoto, Y. Kashiwagi, M. Nakamoto, *Langmuir* **2006**, *22*, 8581–6.
- [29] H. Grönbeck, A. Curioni, W. Andreoni, *Journal of the American Chemical Society* **2000**, *122*, 3839–3842.
- [30] K. Skrabania, A. Miasnikova, A. M. Bivigou-Koumba, D. Zehm, A. Laschewsky, *Polymer Chemistry* **2011**, *2*, 2074–2083.
- [31] A. M. Forster, J. W. Mays, S. M. Kilbey, *Journal of Polymer Science Part B-Polymer Physics* **2006**, *44*, 649–655.
- [32] V. N. Michailidou, B. Loppinet, D. C. Vo, O. Prucker, J. Rühle, G. Fytas, *Journal of Polymer Science Part B: Polymer Physics* **2006**, *44*, 3590–3597.
- [33] S. M. Kilbey, H. Watanabe, M. Tirrell, *Macromolecules* **2001**, *34*, 5249–5259.
- [34] M. Daoud, J. Cotton, *J. Phys. France* **1982**, *43*, 531–538.
- [35] D. Dukes, Y. Li, S. Lewis, B. Benicewicz, L. Schadler, S. K. Kumar, *Macromolecules* **2010**, *43*, 1564–1570.

- [36] K. Ohno, T. Morinaga, S. Takeno, Y. Tsujii, T. Fukuda, *Macromolecules* **2007**, *40*, 9143–9150.
- [37] R. Ranjan, W. J. Brittain, *Macromolecular Rapid Communications* **2008**, *29*, 1104–1110.
- [38] J. Choi, C. M. Hui, J. Pietrasik, H. C. Dong, K. Matyjaszewski, M. R. Bockstaller, *Soft Matter* **2012**, *8*, 4072–4082.
- [39] K. Ohno, K.-m. Koh, Y. Tsujii, T. Fukuda, *Macromolecules* **2002**, *35*, 8989–8993.

## 7 Well-defined metal-polymer nanocomposites: The interplay of structure, thermoplasmonics, and elastic mechanical properties

David Saleta Reig, Patrick Hummel, Zuyuan Wang, Sabine Rosenfeldt, Bartłomiej Graczykowski, Markus Retsch, and George Fytas



Reprinted with permission from Saleta Reig et al., *Physical Review Materials* **2018**, 2, 123605. Copyright 2018 by the American Physical Society.

**Abstract:** Metal-polymer nanocomposites are hybrid materials combining the superior plasmonic, electrical, and thermal properties of metals with the good elasticity and manufacturability of polymers. This renders metal-polymer nanocomposites promising candidates for conductive filler and coating applications, where mechanical properties are opto-thermally coupled. Here, we study the interplay of nanostructure, thermoplasmonics, and elastic mechanical properties of silver-polystyrene nanocomposites (AgPS) by transmission electron microscopy (TEM), small-angle-X-ray scattering (SAXS), Brillouin light scattering (BLS), and other supplemental techniques. We utilize the well-known particle-brush architecture to ensure a homogeneous and isotropic nanoparticle distribution throughout the composite material. The effective longitudinal modulus of the as-prepared samples is found to decrease from 5.7 to 4.8 GPa with increasing Ag content from 0 to 4.4 vol%. Temperature-dependent BLS measurements reveal the unique contribution of local thermoplasmonic heating that depends on the Ag nanoparticle composition. This thermoplasmonic effect results in a lower apparent glass transition temperature ( $T_g$ )

and a stronger laser power dependence of the speed of sound. Exceeding moderate thermal annealing temperatures ( $> 150\text{ }^{\circ}\text{C}$ ) leads to a strong structural rearrangement within the homogeneous nanocomposite material with a peculiar clustering – redispersion effect, which also translates into altered mechanical properties. The annealing-induced Ag nanoparticle aggregation results in an even stronger thermoplasmonic effect. We validate our experimental findings with complementary thermographic measurements and finite element modeling. Overall, this work demonstrates the combined effects of composition and (reversible) aggregation on the mechanical and thermoplasmonic properties of metal-polymer nanocomposites. It not only deepens our understanding of the interaction between light, temperature, and mechanical properties in metal-polymer nanocomposites but also provides a guide for customizing AgPS nanocomposites for potential applications.

## 7.1 Introduction

Composite materials strive to combine the unique properties of vastly different materials. Classic examples are carbon fiber reinforced polymers, which marry the high mechanical strength of carbon fibers with the low density of polymers. Ideally, the combination of two materials leads to superior properties exceeding the bulk behavior of the constituents owing to a synergistic interplay between the two components. In particular, composite materials at the nanoscale could possess unforeseen effective material properties due to the local confinement of the two components. As a consequence, such materials feature novel structural, mechanical, optical, semiconducting and thermal properties<sup>[1-11]</sup>.

Nanocomposite materials can be classified concerning their constituting entities, which can comprise any combination of metals, metal oxides, and organic materials, in particular, polymers. Alternatively, the shape of the nanocomposite object can be used as a distinctive criterion. These include two-dimensional sheets, layers or stacks, isotropic and anisotropic nanoparticles, and fibers. Most widespread are particulate nanocomposites, comprising a spherical core and a corona. Within this class of nanocomposite materials, polymer shell/rigid core nanoparticles have recently attracted considerable interest<sup>[6,12]</sup>. The usage of a suitable polymer corona increases the uniformity and stability of the nanoparticle dispersion in a polymer matrix. Still, the nanoconfinement of the polymer corona tethered to a rigid core evokes conformational changes and reduces the entropy, which can result in isotropic or anisotropic aggregates<sup>[12]</sup>. Only polymer brush architectures of sufficiently high grafting density yield thermodynamically stable and fully miscible polymer nanocomposites<sup>[13]</sup>. This brush architecture not only strongly encapsulates the inorganic core but also provides sufficient entropic freedom at the periphery to intimately blend them into the surrounding polymer matrix. The conformation of the “hairy” polymer layer around the rigid core depends on the polymer length and grafting density<sup>[14]</sup>. In the absence of additional matrix polymers, the grafted polymer corona solely governs the volume fraction and distance of the inorganic core particles. Concomitantly, self-assembled films of such nanocomposite particles represent a homogeneous, one-component material with the core-shell nanoparticle architecture as the repetitive motif.

The fabrication of such fully miscible nanocomposite materials poses a particular challenge. Nanoscale objects inherently tend to form aggregates owing to the tendency to reduce the overall surface area and to release adsorbed molecules. Metallic nanoparticles exhibit a particularly large tendency towards clustering, due to their strong, attractive van der Waals interactions. This aggregation trend can be counter-

acted using specific functional or polymer groups on the particle surface. Grafting-to<sup>[13,15]</sup> and grafting-from<sup>[7]</sup> approaches are both suitable to produce densely grafted and stable nanocomposite materials. Hummel et al. recently introduced a scalable and reproducible method to synthesize polymer ligand-coated silver nanoparticles with high grafting densities, allowing for a precise adjustment of the interparticle distance<sup>[16]</sup>. Although the thermodynamical equilibrium structure should be an fcc crystal as for the case of large dense polymer-tethered dielectric particles<sup>[17]</sup>, the strong, attractive van der Waals forces along with the self-assembly procedure can result in less ordered nanostructures as well<sup>[18]</sup>.

Whereas many nanocomposite materials base on metal-oxide (most commonly SiO<sub>2</sub>) cores<sup>[17,19]</sup>, we want to emphasize the added functionality provided by plasmonic cores. Plasmonic nanocomposites may exhibit cooperative effects such as local plasmonic hotspot or lattice plasmon formation, owing to the small interparticle distance<sup>[20]</sup>. These can change the effective spectral response and the optical density<sup>[21,22]</sup>. Furthermore, plasmonic nanoparticles efficiently convert light into heat<sup>[23,24]</sup>. Thus, plasmonic nanocomposites are amenable to optically controlled, localized heating. This localized heating is well-known in the field of thermoplasmonics, where predominantly dispersed plasmonic nanoparticles and their individual properties or interactions with the living matter have been investigated<sup>[25]</sup>. The structure–thermoplasmonics relationship manifested in the absorption spectra will also impact the glass-rubber transition and elastic mechanical properties, i.e., the thermomechanical behavior of the polymer nanocomposite films. The latter studies being important for applications of these materials as gas permeation membranes<sup>[26,27]</sup> are somewhat rare rendering a predictive power premature.

In this contribution, we employ BLS as a powerful and non-destructive method to determine the mechanical properties of homogeneous silver-polystyrene (AgPS), one-component hybrid materials with low metal volume fractions. We focus on two major aspects: (i) the influence of the structural control provided by the synthesis of the polymer grafted silver nanoparticles and (ii) the external (global) and plasmonic (local) heating, which entails distinct structural changes. The plasmonic heating contribution constitutes a localized heating effect. This allows creating hot microscopic areas in the bulk film, which are directly probed by BLS. Plasmonic heating is a fast and instantaneous heating effect, owing to the radiative transfer of energy to the metallic nanoparticles. It is, therefore, different from conventional sample heating achieved via convection and conduction in a thermal bath. We complement our investigation with UV/Vis spectroscopy, transmission electron microscopy (TEM) tomography, SAXS measurements, and finite element method (FEM) simulations to unravel the temperature-induced structural changes fully.

## 7.2 Experimental

### 7.2.1 Materials

The synthesis of the AgPS nanocomposites is described elsewhere<sup>[16]</sup>. The PS ligands were prepared by RAFT polymerization. The trithiocarbonate end group was transferred into a thiol group by aminolysis. We synthesized ligands with molecular weights of 8, 12, and 18 kg/mol. The Ag nanoparticles were synthesized according to the method by Yamamoto et al.<sup>[28]</sup>: A silver myristate precursor was heated in trimethylamine to 80 °C for 4 h. The obtained Ag nanoparticles were mixed with an excess of PS ligands to achieve a theoretical grafting density of 10 ligands/nm<sup>2</sup>. After that, the mixture was stirred for 65 h. The nanocomposites were purified by three qualitative precipitation steps and a subsequent centrifugation step at the  $\Theta$ -condition of the PS ligand. We name our samples PS8k, PS18k, etc. for the respective pure polymer ligand; the Ag nanoparticles grafted with these polymers are termed AgPS8k, AgPS18k, etc., indicating the respective ligand molecular weight.

### 7.2.2 Film preparation and characterization

The films were prepared by spin coating of a 15 wt.% toluene solution on microscope slides with a thickness in the range from 483 to 1598 nm. The films were kept for 10 h in a vacuum oven at 100 °C to remove the residual toluene. The internal structure of the nanocomposite film can be strongly altered using thermal annealing. The as-prepared films were, therefore, subjected to an annealing procedure. Figure 7.8 in Supplemental Material<sup>[29]</sup> shows the annealing procedure based on a hot plate. The nanocomposite films were annealed for 1 and 30 min, respectively, on a hot stage with a set temperature of 200 °C. The color of the films changed during the annealing procedure, which can be related to the altered internal structure of the nanocomposite films.

### 7.2.3 Optical spectroscopy

An Analytik Jena SPECORD 250 Plus spectrophotometer was used to measure the UV/Vis spectra.

## 7.2.4 Transmission electron microscopy

Thin films (2.5 wt.% for AgPS18k and 5 wt.% for AgPS8k) were prepared on glass slides with a sacrificial ZnO layer for TEM characterization. Immersion of the coated substrates in a 1 M HCl bath released the nanocomposite film, which floated on the water surface and was subsequently transferred to a TEM grid. The measurements were conducted on a Zeiss EM922 Omega.

## 7.2.5 Electron tomography

For electron tomography analysis, the samples were carbon-sputtered with a Leica EM ACE600 with a thickness of about 3 nm and the TEM grids were cut in half with a razor blade. The samples were measured on a JEOL 2200FS instrument in bright-field mode, operating at an accelerating voltage of 200 kV. Images were taken with a 16-bit 2048 x 2048 Ultra-Scan 1000XP charge-coupled device camera (Gatan) in a range from  $-40^\circ$  to  $+40^\circ$  at a  $2^\circ$  interval using the GATAN software (version 2.31.734.0). Prealignment of the tilt image series was done with IMOD<sup>[30]</sup>. After prealignment, videos were compiled using the FIJI open-source software package<sup>[31]</sup>.

## 7.2.6 Small-Angle-X-ray Scattering

For the SAXS measurements, the samples were spin coated on a Kapton<sup>®</sup> foil, and the measurements were performed at room temperature in a transmission geometry using a Double Ganesha AIR system (SAXSLAB, Denmark). The x-ray source of this laboratory-based system is a rotating copper anode (MicroMax 007HF, Rigaku Corporation, Japan). A position-sensitive detector (PILATUS 300 K, Dectris) recorded the data. To cover the range of scattering vectors  $q_{SAXS}$  between 0.03 and  $10 \text{ nm}^{-1}$  different detector positions were used with beam sizes between  $0.3 \times 0.3$  and  $0.9 \times 0.9 \text{ mm}^2$ . The circularly averaged data were normalized to the incident beam, an assumed sample thickness of 1 mm, and the measurement time before subtraction of the Kapton<sup>®</sup> foil background. Calculations were done using the software SASFIT (version 0.94.1) written by Kohlbrecher and Bressler<sup>[32]</sup>. Section 7.5.3 of Supplemental Material provides more information about the fit<sup>[29]</sup>.

## 7.2.7 Brillouin light scattering spectroscopy<sup>[17]</sup>

BLS measurements were performed in a transmission configuration, which allows probing the in-plane, thermally exsuperated phonons in the nanocomposite films along the direction of the scattering wave vector  $\mathbf{q} = \mathbf{k}_s - \mathbf{k}_i$ , where  $\mathbf{k}_i$  and  $\mathbf{k}_s$  denote

the wave vectors of the incident and scattered photons, respectively. In this configuration, the scattering vector is independent of the sample's refractive index, and can be computed as  $q = \sin(\theta/2)4\pi/\lambda$ , with  $\theta$  being the scattering angle and  $\lambda = 532$  nm the wavelength of the incident light. The resultant frequency shift of scattered light [in the hypersonic (GHz) region] is resolved by a high-resolution tandem, six-pass Fabry-Pérot interferometer (JRS Instruments). All the results presented were obtained from polarized (VV) BLS measurements. As a result, only longitudinal sound waves are considered. The free spectral range was fixed at 10 GHz by using a mirror spacing of 15 mm. For the temperature scan measurements, the sample temperature was monitored with a platinum resistance detector and adjusted with a homemade temperature controller. At each temperature, the sample was allowed to isothermally equilibrate for 20 min before the spectra were recorded.

### 7.2.8 Differential scanning calorimetry

DSC measurements were conducted on a TA instruments Discovery DSC 2500 using a heating rate of  $20 \text{ K min}^{-1}$ . Four heating curves were measured. The first run (-40 to  $100 \text{ }^\circ\text{C}$ ) cleared the thermal history of the samples without inducing any structural changes and improved the contact between the sample and the pan. The  $T_g$  was determined in the second run (-40 to  $120 \text{ }^\circ\text{C}$ ). The samples were heated up to  $175 \text{ }^\circ\text{C}$  in the third run to mimic the thermal annealing steps. The fourth heating curve (-40 to  $120 \text{ }^\circ\text{C}$ ) was used to evaluate the  $T_g$  of the annealed samples.

### 7.2.9 Thermographic measurements

For thermographic measurements, a VarioCam<sup>®</sup> HD research 900 IR camera with close-up lens from InfraTec GmbH was used. The camera was mounted in front of the film with an angle of around  $60^\circ$  with respect to the sample plane. The pixel resolution of the IR camera was around  $30 \mu\text{m}$  at the used working distance. The laser beam ( $\lambda = 532 \text{ nm}$ ) had an incident angle of around  $85^\circ$ . The laser was focused to a spot size of  $90 \mu\text{m}$ . Before the measurements, the emissivity of the films was determined using a reference sample with a known emissivity. The power of the incident laser light was varied between 1 and 90 mW. After thermal equilibration of the sample at each laser power, an image of the temperature distribution was taken, from which the maximum temperature was evaluated. This value is the average temperature over an area of  $30 \times 30 \mu^2$ .

## 7.3 Results and Discussion

### 7.3.1 Materials

Transmission electron microscopy images of drop-cast AgPS8k and AgPS18k [Figs. 7.1a and 7.1b] and a side-view SEM image of a spin-cast film [Fig. 7.1c] demonstrate the high uniformity of the individual Ag-polymer ligand nanoparticles and highlight their distribution across the entire polymer nanocomposite film. Also, a TEM tilt series (videos in section 7.5.2 of Supplemental Material<sup>[29]</sup>) demonstrates the homogeneous nanoparticle distribution and lack of clusters. The SAXS intensity patterns confirm the homogeneity and structural control [Fig. 7.1e]. Due to the low contrast of the polystyrene shell, the signal is most sensitive to the silver core of the nanoparticles. At high scattering vectors,  $q_{SAXS}$ , the intensity is dominated by the form factor of the particles, whereas at low  $q_{SAXS}$  the scattering also refers to the arrangement of the particles, i.e., it is sensitive to the structure factor. Figure 7.1e shows the experimental scattering intensities of the films AgPS8k (blue circles) and AgPS18k (red triangles) along with their corresponding modeling (solid lines): The spheres have a radius of 3.0 nm and a Gaussian particle size distribution with a standard deviation of 0.4 nm. The Percus-Yevick structure factor is based on an effective interaction distance of 6.5 nm and an effective volume fraction of  $\phi = 0.35$ . For both films, the minimum at  $q = 1.5 \text{ nm}^{-1}$  is attributed to the particle size. Hence, the silver core is well defined and homogeneously distributed all over the film.

The system with the short polymer ligand (AgPS8k) exhibits a Bragg reflection at  $q_{SAXS} \approx 0.5 \text{ nm}^{-1}$ , resulting from an effective particle-particle interaction distance of 6.5 nm. For AgPS18k this feature is less pronounced, and the scattering pattern can be well approximated with a pure form factor. This result gives a hint to the influence of increasing shell thickness to the film morphology: With increasing ligand length, the core-core interaction becomes weaker. According to the Hansen criteria, the structure factor must be  $>2.85$  for crystalline order. In our case, the experimental structure factor has a maximum of 1.5 demonstrating a glasslike order. Overall, the spin coating of the particle-brush dispersion in toluene leads to a homogeneous film. The homogeneity also becomes apparent in the UV-Vis spectra [Fig. 7.1f]. These show a single and well-defined plasmonic peak originating from the individual Ag nanoparticles (NPs) with no discernible aggregation.

The TEM images [Figs. 7.1a and 7.1b] were used to evaluate the interparticle distance  $d$ , from which we computed the PS height,  $h = (d - D)/2$ , where  $D$  is the diameter of the Ag nanoparticles. Figure 7.1d depicts  $h$  versus degree of polymerization of the grafted PS chains,  $N$ , in a double-logarithmic presentation. A scaling relation  $h \sim N^{\nu}$  is observed, with the value  $\nu = 0.67 \pm 0.05$  exceeding the random coil

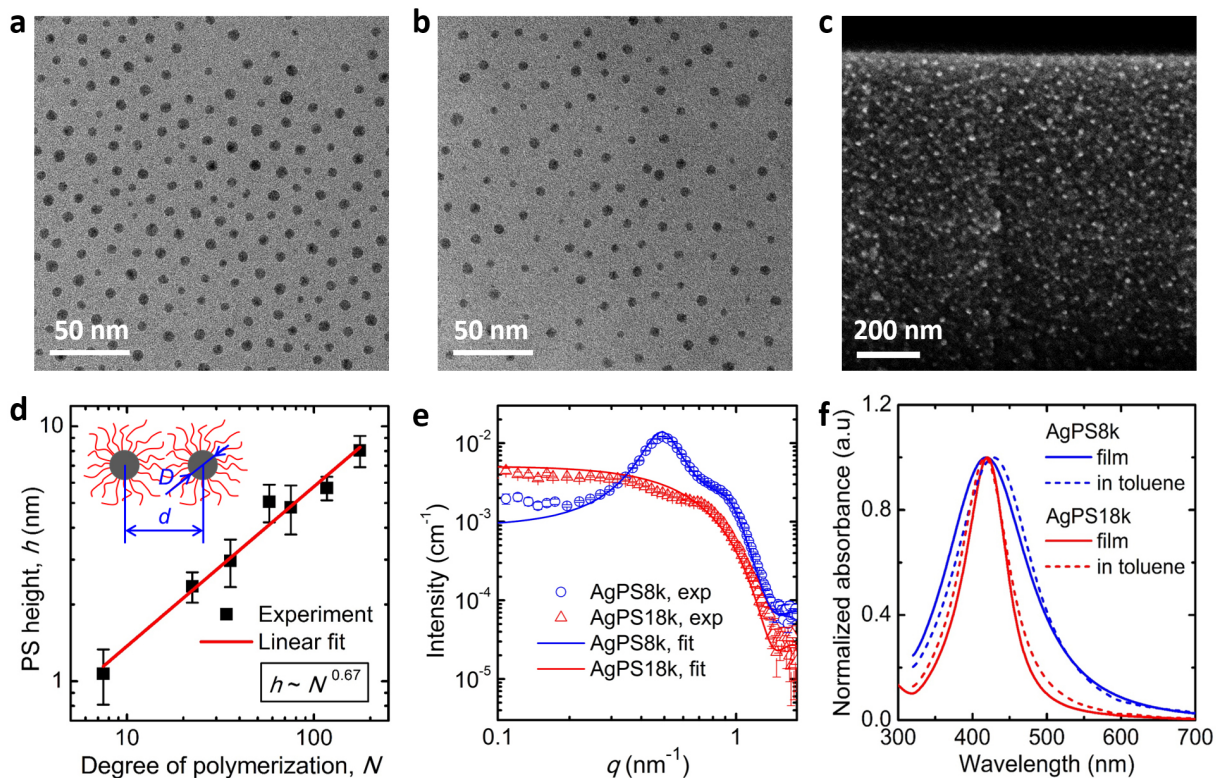


Figure 7.1: (a,b) TEM images of the AgPS8k and AgPS18k samples with silver volume fractions,  $\varphi_{\text{Ag}} = 0.05$  and  $0.014$ , respectively. (c) Scanning electron microscope (SEM) image (side view) of an AgPS18k film, where the bright spots indicate the well dispersed Ag nanoparticles over the whole thickness of the film. (d) The polymer height determined from the TEM images is plotted as a function of the degree of polymerization, which shows a linear relation in the double logarithmic plot. (e) SAXS patterns of the AgPS8k and AgPS18k films (symbols) and theoretical descriptions (lines, for details, see section 7.5.3 in Supplemental Material). (f) UV/Vis spectra of the AgPS8k and AgPS18k samples measured in solid films (solid lines) and toluene (dashed lines).

value (0.5), and implying an extended conformation of the PS chains. Much larger dielectric particle-brush systems also showed a similar scaling exponent<sup>[7]</sup>, which is indicative of high grafting density justifying a brushlike behavior. The interparticle distance in the as-prepared films can be controlled between 2 and 10 nm through the synthesis of densely tethered PS chains. We next examine the elastic properties of the as-prepared films.

The inset to Fig. 7.2a depicts isotropic BLS spectra for the AgPS18k film at three different scattering wave vectors  $q$  at 293 K and low laser power (45 mW), displaying a single acoustic phonon. We will see later that the laser power used here is low enough to leave the speed of sound of the sample unaffected. The linear dispersion in the main plot of Fig. 7.2a shows the acoustic nature of the probed phonons in the AgPS12k and AgPS18k films along with the constituent PS18k film. From the

linear dispersions, we calculate the effective medium longitudinal sound velocity as  $c_{L,eff} = 2\pi f/q$ , where  $f$  is the phonon frequency. The presence of a single acoustic phonon supports the homogeneity of the films on a length scale larger than the probing phonon wavelength range (about 300-800 nm). This homogeneity is consistent with the structures presented in Fig. 7.1. Counterintuitively, the speed of sound drops with increasing, yet low, volume fraction,  $\phi$ , of Ag nanoparticles as shown in Fig. 7.2b. Applying the Wood's law (section 7.5.4 in Supplemental Material<sup>[29]</sup>), using the density and the longitudinal sound velocity of the individual components fixed to the bulk Ag and PS values, the decrease of  $c_{L,eff}$  with  $\phi$  can be semiquantitatively represented [solid line in Fig. 7.2b]. The drop of  $c_{L,eff}$  is mainly the result of the considerable density mismatch between Ag and PS, while application of the effective medium presentation assumes good adhesion between the Ag core and PS brush in the glassy state.

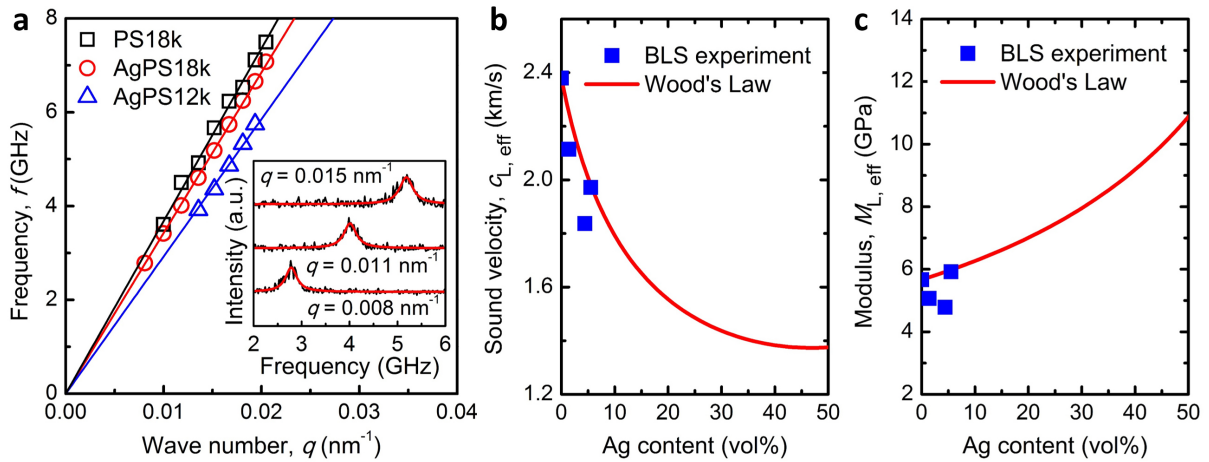


Figure 7.2: (a) Linear acoustic dispersion of the longitudinal phonon in the as-prepared AgPS18k and AgPS12k nanocomposite films (red circles and blue triangles), and bulk PS18k (black squares) recorded by BLS. Inset: BLS spectra of a 1.4  $\mu\text{m}$  thick AgPS18k film, recorded at three different wave numbers using a 532 nm laser at 45 mW, and represented by Lorentzian line shapes (solid red lines). (b) Effective longitudinal sound velocity  $c_{L,eff}$  vs. Ag volume fraction. Wood's law representation (red line) was conducted using Eq. 7.7 in section 7.5.4 in [32] without any adjustable parameter. The densities and sound velocities assume the values of bulk Ag and PS. (c) Computed effective longitudinal modulus of the AgPS nanocomposites in b) as a function of the Ag volume fraction.

Interestingly, Wood's law failed to predict the increase of  $c_{L,eff}(\phi)$  in a  $\text{TiO}_2$  polymer nanocomposite<sup>[33]</sup>, where a soft interlayer had to be introduced<sup>[34]</sup>. The longitudinal elastic modulus,  $M_{L,eff} = \rho_{eff} c_{L,eff}^2$ , an important material property, is shown in Fig. 7.2c. Here the effective density,  $\rho_{eff}(\phi) = \rho_{Ag}\phi + \rho_{PS}(1 - \phi)$  is assumed to be a linear function of the Ag volume fraction using the bulk densities of the two constituents. The Wood's law's prediction (solid red line) with no adjustable pa-

rameters is a monotonic increase of  $M_{L,eff}$  with Ag volume fraction. The computed  $M_{L,eff}$  assuming the particular  $\rho_{eff}(\varphi)$  does not capture the observed decrease at low experimental Ag content; an effective lower density for Ag would be needed<sup>[33]</sup>.

The temperature dependence of the modulus is a characteristic feature of hybrid systems that can change their phase state upon heating. In the case of bulk PS film, it is well known that the rate of the decrease of the sound velocity with temperature changes abruptly at the glass-rubber transition as shown for PS18k in Fig. 7.3 (gray shaded area). The transition occurs about 8 K lower compared to the  $T_g$  ( $\sim 373$  K) obtained from DSC (Supplemental Material, section 7.5.5, Fig. 7.11<sup>[29]</sup>). The much lower heating rate can explain this deviation in the BLS experiment<sup>[7]</sup>. The  $T_g$  is more accurately defined in the plot of  $c_{L,eff}$  versus  $(1/T)$ <sup>[35]</sup>. For AgPS18k, this transition occurs at a much lower temperature ( $\sim 325$  K) compared to the DSC data ( $T_g = 373$  K). The temperature effect is reversible as indicated by the BLS spectra in the inset of Fig. 7.3. The discrepancy between the BLS and DSC measurements can be understood by the additional heating effect of the laser light within the focal volume of the laser spot. In the case of AgPS8k ( $T_g = 369$  K) with a higher Ag volume fraction than AgPS18k, the even larger disparity of the transition temperature ( $\sim 310$  K) with the DSC corroborates the notion of laser heating. Given the weak  $c_{L,eff}(T)$  dependence in the glass regime (below  $T_g$ ), the localized heating effect plays a negligible role at 293 K, rendering the composition dependence of the sound velocity in Fig. 7.2b reliable.

Since PS is the majority component, the slopes  $c_{L,eff}^{-1}(T=0)dc_{L,eff}/dT$  in the glassy ( $\sim 4 \times 10^{-4} \text{ K}^{-1}$ ) and rubbery ( $1.4 \times 10^{-3} \text{ K}^{-1}$ ) states of the polymer nanocomposites were expectedly found similar to the PS matrix (Table 7.1 in Ref.<sup>[29]</sup>); a constant, laser-induced temperature increase  $\Delta T$  would not significantly impact the values of the PS slopes. The plasmonic origin of the heating is also demonstrated by the very similar transition temperature and temperature dependence of  $c_{L,eff}$  in a SiO<sub>2</sub>-PS particle-brush film (Fig. 7.12 in Ref.<sup>[29]</sup>), where no local laser heating occurs (note Ag nanoparticles induce plasmonic heating, but SiO<sub>2</sub> nanoparticles do not).

To entirely eliminate the laser heating and to have the laser serving as a probe as it is the case for PS (Fig. 7.3), very low incident light intensities would be necessary. This, however, renders a reliable temperature-dependent study very time-consuming. Instead, we examine next the influence of the local heating on the  $c_{L,eff}$  measurement at different laser powers,  $P$ . This way we harness the laser source as both a local heater and a probe. For the as-prepared AgPS18k film, the inset to Fig. 7.4 depicts the BLS redshift when the laser power increases from 45 to 100 mW at an external temperature of 293 K. This is due to the slowdown of  $c_{L,eff}$  as a result of the laser-induced local heating. The drop of  $c_{L,eff}$  for different laser powers is shown for the

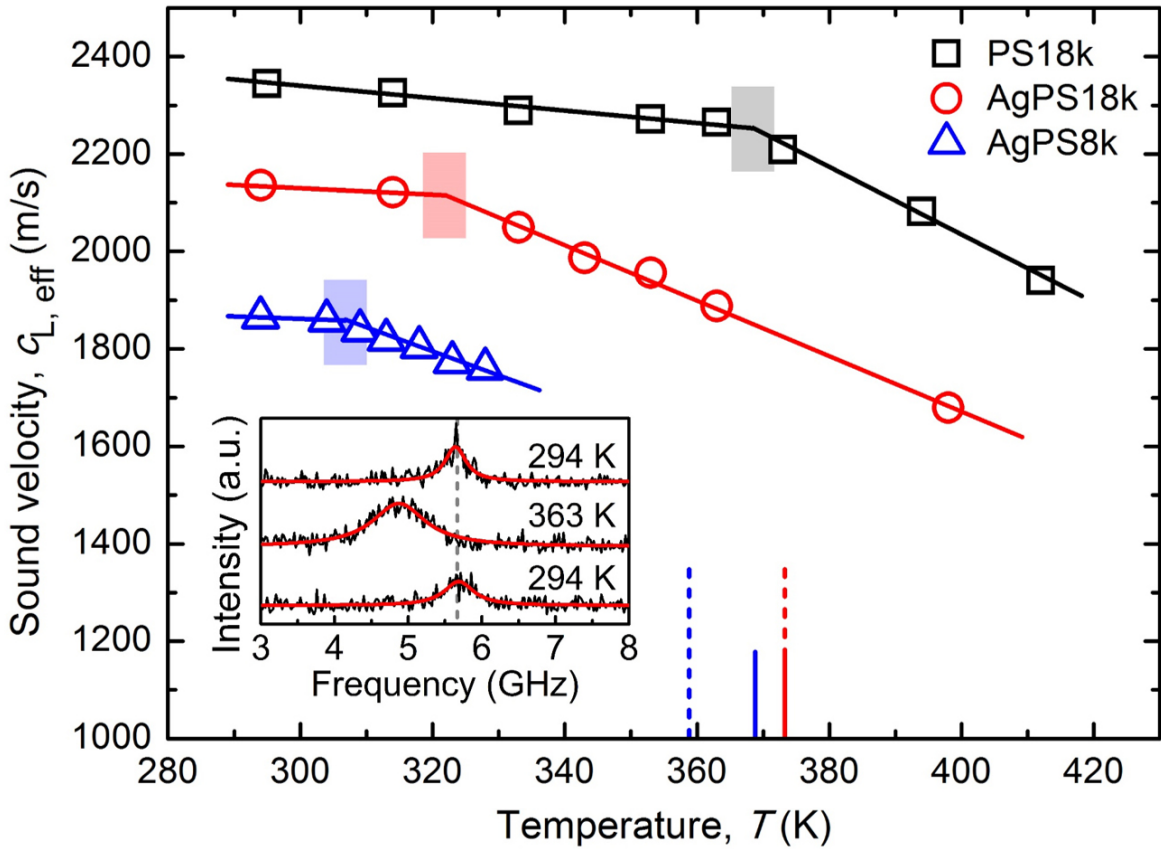


Figure 7.3: Longitudinal sound velocities in the as-prepared AgPS18k and AgPS8k nanocomposite films and the bulk PS18k film as a function of temperature. The shaded areas indicate the glass transition temperatures, and the four vertical lines denote the glass transition temperatures obtained from the DSC traces of bulk AgPS18k (solid red), AgPS8k (solid blue), PS18k (dashed red), and PS8k (dashed blue) films. Inset: Anti-Stokes BLS spectra of AgPS18k at three temperatures as indicated in the plot. The BLS spectrum in the lower panel was recorded at the end of the temperature scan after cooling the sample from 398 K back to 294 K. For the AgPS8k and AgPS18k films, the BLS spectra were recorded with laser powers of 45 and 60 mW, respectively.

as-prepared AgPS8k and AgPS18k films in Fig. 7.4 and contrasts the expected constant  $c_{L,PS}$  in the bulk PS film (squares) due to the absence of light absorption. In the presence of light absorption, the dependence  $c_{L,P}(P)$ , shown in Fig. 7.4, is not linear for both as-prepared nanocomposite films, displaying a stronger dependence on the laser power at high power levels. This relation should also hold for the temperature variation with the laser power due to the linear dependence of  $c_{L,eff}$  on temperature. We, therefore, construct  $T(P)$  through a combination of  $c_{L,eff}(T)$  and  $c_{L,eff}(P)$ . The former is estimated based on the temperature dependence of the longitudinal speed of sound in bulk PS  $c_{L,PS}(T)$  (Fig. 3) and the ratio  $\gamma = c_{L,eff}/c_{L,PS}$  at 293 K, i.e.,  $c_{L,eff}(T) = \gamma c_{L,PS}(T)$  (Fig. 7.13 in the Supplemental Material<sup>[29]</sup>).

The relation  $T(P)$ , depicted in Fig. 7.5 for AgPS8k and AgPS18k, shows the an-

anticipated (Fig. 7.4) nonlinear dependency and a change of the slope in the range 360–370 K, corresponding to the  $T_g$ 's of AgPS8k and AgPS18k. The change of the slope occurs at an external temperature of 293 K because of the local laser heating with an intensity of about  $4.4 \cdot 10^7 \text{ W/m}^2$  (55 mW over a laser spot with a diameter of  $40 \mu\text{m}$ ) and  $8.0 \times 10^7 \text{ W/m}^2$  (100 mW), respectively. For independent support, we directly measured the laser-power-dependent temperature  $T(P)$  using an IR camera. A laser light beam ( $\lambda = 532 \text{ nm}$ ) was focused on the nanocomposite film to a spot with a diameter of  $90 \mu\text{m}$ , and the average temperature in the laser spot at steady state was measured [Fig. 7.5b]. The  $T(P)$  diagram from the IR thermometry is in good, semiquantitative agreement with measurements deduced from BLS. Using a correction factor of  $P_{IR}(= 1.84P_{BLS})$  both measurements can be fully overlaid for both nanocomposite films; this factor accounts for the differences in the actual laser power at the focal spot owing to the different laser setups used. The glass-rubber transition is more clearly evident in AgPS18k occurring in the range 90–110 mW and is reversible as indicated in the inset of Fig. 7.3.

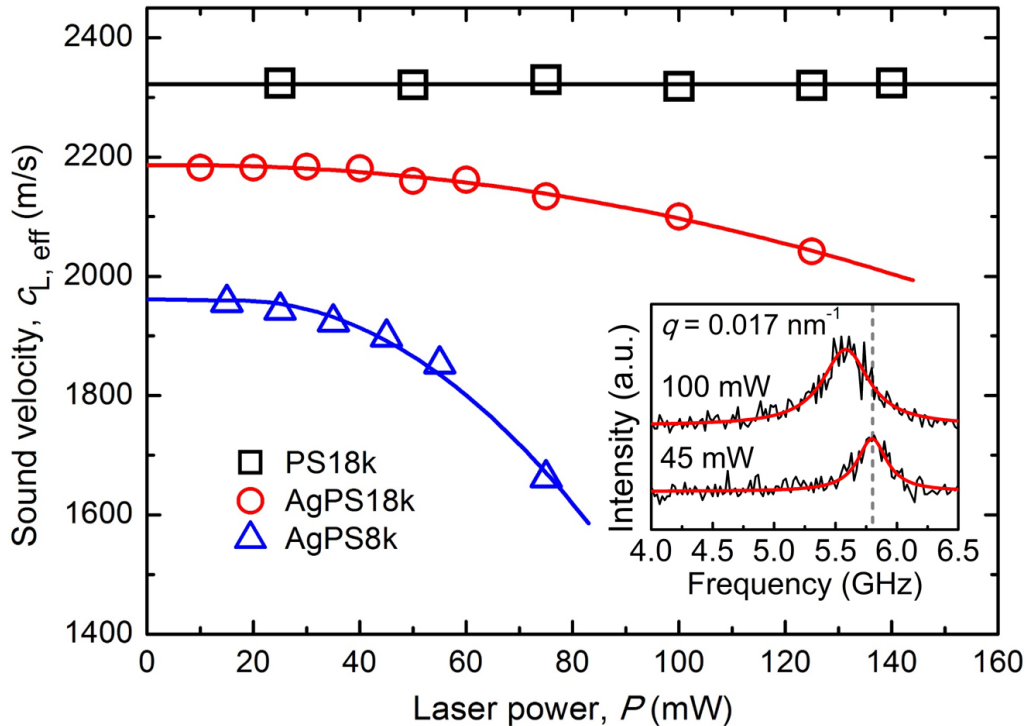


Figure 7.4: Effective longitudinal sound velocity in the as-prepared AgPS18k (red circles) and AgPS8k (blue triangles) nanocomposite and PS18k (black squares) films as a function of the laser power at 532 nm. The red and blue solid lines denote a parabolic representation of the experimental sound velocities in AgPS18k and AgPS8k, respectively, whereas the solid black line indicates the power independent sound velocity in bulk PS18k. Inset: Anti-Stokes BLS spectra at  $q = 0.0167 \text{ nm}^{-1}$  at laser powers of 45 and 100 mW represented by Lorentzian line shapes.

At higher power and hence in the rubber regime the rate of the temperature increase is reduced. Figures 7.5a and 7.5b allow for a semiquantitative inspection of the surprisingly low apparent  $T_g$ 's of the nanocomposite films as shown in Fig. 7.3; here, 310 K for AgPS8k and 325 K for AgPS18k were recorded with intensities of  $3.6 \times 10^7 \text{ W/m}^2$  (45 mW) and  $4.8 \times 10^7 \text{ W/m}^2$  (60 mW) (Fig. 7.3), respectively. Using the laser heating correlation plots of Fig. 7.5a at ambient temperature, the estimated temperature increase is about  $\Delta T = 30 \pm 7 \text{ K}$  for AgPS8k at 40 mW and AgPS18k at 60 mW. Assuming a temperature-independent laser heating, the transition temperatures in Fig. 7.3 should occur at about  $T_g - \Delta T$ , i.e., at about 330 and 340 K for AgPS8k and AgPS18k, respectively. The overestimation of the transition temperatures (Fig. 7.3) corroborates the notion of a temperature-dependent laser heating effect. The solid lines in Fig. 7.5a represent simulation results based on a 2D, axis-symmetric model (see Supplemental Material, section 7.5.6 and Table 7.1 for more details<sup>[29]</sup>) implemented in COMSOL MULTIPHYSICS based on the FEM. By using absorption coefficients linearly dependent on temperature, the  $T(P)$  relations obtained from the BLS measurements were successfully captured. We obtained larger absorption coefficients for the AgPS8k film than the AgPS18k film. For both films, the variation of the absorption coefficient with temperature was weaker in the rubbery state than the glassy state.

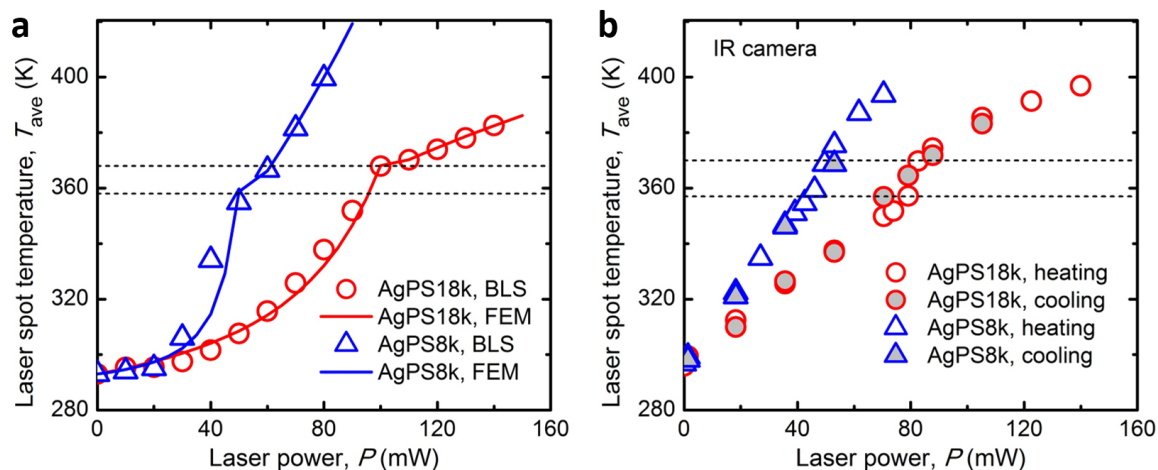


Figure 7.5: The local temperature in the laser spot as a function of the laser power in the AgPS18k (red circles) and AgPS8k (blue triangles) films estimated from (a) the data of Figure 7.3 and Figure 7.4 as described in the text, and (b) using an IR camera. The solid lines indicate the simulation results (ESI section 7.5.6, Fig. 7.14), whereas the horizontal dashed lines indicated the local  $T_g$  induced by the laser heating at ambient temperature.

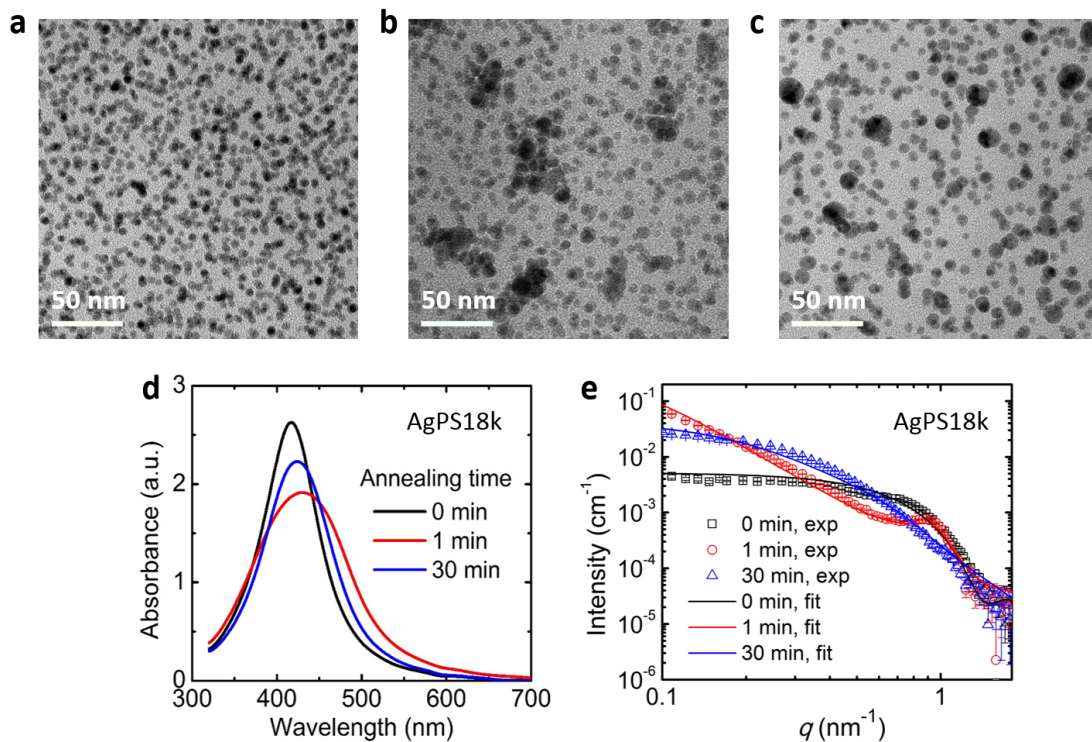


Figure 7.6: (a-c) TEM images of the AgPS18k films (a) as prepared from spin-coating, (b) after 1 min annealing at 200 °C, and (c) after 30 min annealing at 200 °C. The (d) UV-Vis and (e) SAXS patterns (symbols) and fits (lines, details in ESI section S3) of the as-prepared and annealed AgPS18k films.

### 7.3.2 Structural changes induced by thermal annealing

The as-prepared films display homogeneously distributed structures, but the thermodynamic stability is not warranted. Entropic contributions can strongly alter the NP distribution in composite films as shown recently for AuPS NPs.<sup>[36]</sup> Thermal treatment also led to significant structural changes in the pure (no additional matrix polymer) nanocomposite films. The structural changes were consistently followed by TEM images, UV/Vis absorption spectra, and SAXS patterns in Fig. 7.6. Heating well above the  $T_g$  the polymer corona ( $T > 423$  K) allows the as-prepared film to relax via the speed-up of the translational motion of the untangled PS chains in the nanocomposite film. The randomly dispersed Ag NPs aggregate after annealing for 1 min leading to a local increase of the Ag concentration. The SAXS patterns [Fig. 7.6e] underpin the effect of annealing on the aggregation and dispersion behaviors of the Ag NPs. The AgPS18k sample demonstrates less distinct peaks compared to the AgPS8k sample (both are compared in Fig. 7.9 in Ref. [29]). Both samples show a qualitatively comparable trend. The intensities obtained after 1 min annealing exhibit the most pronounced forward scattering. Aggregated NPs cause this forward scattering. The scattering at low  $q$  of the other films (0 and

30 min) is more even, excluding a large number of clusters. The scattering data can be sufficiently well fitted by a pure form factor of monodisperse spheres at annealing times of  $t = 0$  min ( $R = 3.0 \pm 0.4$  nm) and  $t = 30$  min ( $R = 3.0 \pm 0.9$  nm). The aggregated structure at  $t = 1$  min is a combination of the Percus-Yevick model ( $R = 3.0 \pm 0.4$  nm,  $R_{out} = 3.3$  nm, and  $\phi = 0.35$ ) and clusters ( $R_H = 15$  nm). The UV/Vis spectra corroborate these structural changes undergoing a redshift and line broadening [Fig. 7.6d]. Surprisingly, prolonged annealing (for 30 min) leads to a redispersion of the nanoparticles and a recovery of the plasmonic resonance spectrum—but at the expense of increased size and polydispersity compared to the as-prepared film [Figs. 7.6a and 7.6d]. These severe structural changes are also confirmed by a TEM tilt series, which highlights the three-dimensional distribution of the Ag nanoparticles (videos in Section 7.5.2 of Supplemental Material<sup>[29]</sup>). Furthermore, this unusual aggregation/redispersion phenomenon is universal to Ag-PS corona films. The same effect has also been observed for AgPS6k and AgPS12k films (Section 7.5.7, Fig. 7.15 in Ref.<sup>[29]</sup>). Even longer annealing times exceeding 60 min at  $> 150$  °C lead to Ostwald ripening of the Ag nanoparticles and a further coarsening of the nanostructure. BLS examined the influence of this structural modification on the elastic properties of the nanocomposite films. In particular, the change of the optical resonance spectrum might impact the local heating by the laser light.

Figure 7.7 presents the BLS-measured sound velocities of two annealed AgPS18k films in comparison with the as-prepared one. The inset depicts the BLS spectra of the two annealed AgPS18k films at two laser powers (45 and 100 mW). In addition to the expected redshift, a second acousticlike phonon peak emerges at high laser powers. In agreement with the structural changes demonstrated in Fig. 7.6 the  $c_{L,eff}(P)$  of the 30-min annealed film falls between the as-prepared and 1-min annealed ones. For the latter, two phonons are present above 60 mW, whereas for the longer annealed film the second phonon appears at higher powers ( $> 75$  mW). The  $c_{L,eff}(P)$  of the harder phonon in the 30-min annealed film is very similar to the single phonon in the nonannealed film, whereas the 1-min annealed film displays a stronger  $c_{L,eff}(P)$  dependence. We rationalize the correspondence between large nanoparticle clusters and stronger laser heating effects, using qualitative FEM simulations based on a 2D model in COMSOL (detailed information in Section 7.5.8, Fig. 7.16, Table 7.1 in Supplemental Material<sup>[29]</sup>). The results show that the aggregation of the heat sources lead to higher average temperatures in the surrounding area, which agrees with our experimental findings. This clustering effect on heating is similar to the previously reported, collective heating effect in noble-metal-nanoparticle-based solutions and thermoplasmonic materials.<sup>[23,37]</sup> The appearance of two phonons at the same acoustic wave number  $q$  implies a structural inhomogeneity with length scales larger than the probed phonon wave-

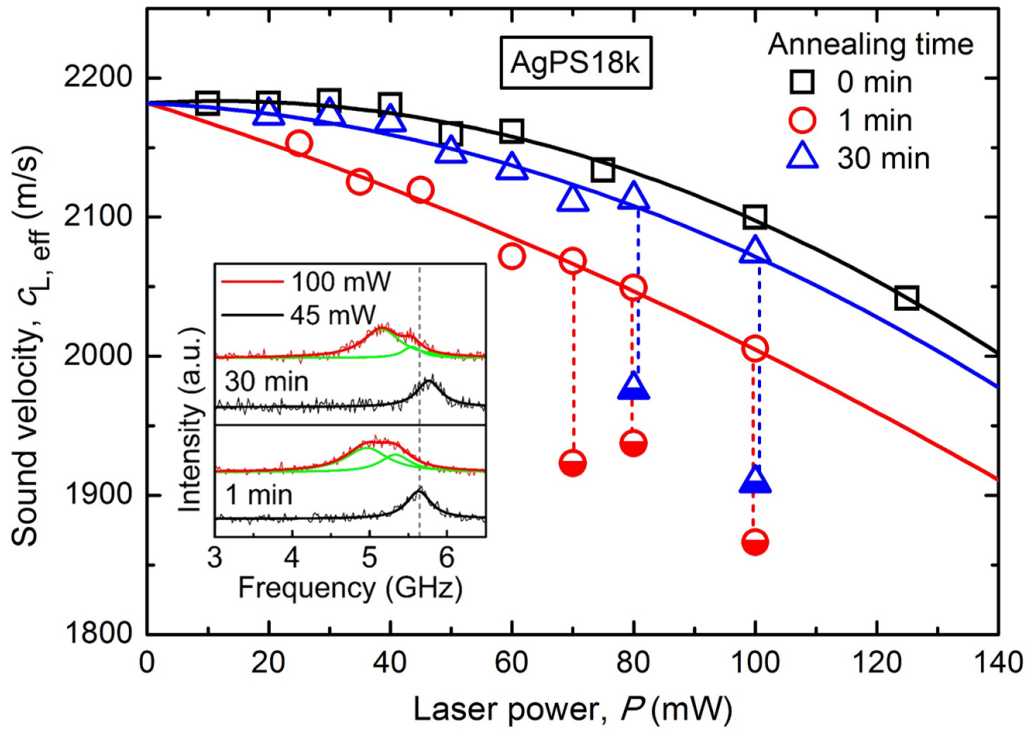


Figure 7.7: Effective medium longitudinal sound velocity in annealed AgPS18k nanocomposite films as a function of the laser power, in comparison with the results for the as-prepared AgPS18k film (black squares). The data for the short and long annealing times are indicated by red circles (1 min) and blue triangles (30 min). The half-filled symbols represent the presence of a secondary softer phonon in the BLS spectra. Inset: anti-Stokes BLS spectra at  $q = 0.0167 \text{ nm}^{-1}$  for the AgPS18k films annealed for 1 and 30 min. The spectra at 45 mW (black) and 100 mW (red) are represented by one (black) and two (green) Lorentzian peaks, respectively.

length ( $\sim 2\pi/q = 500 \text{ nm}$ ). Figure 7.6b, however, suggests much smaller cluster sizes of about 50 nm. Consequently, it is not clear how the light-induced local heating can lead to a structure coarsening that is responsible for the second soft phonon. Based on Fig. 7.2b, its lower sound velocity suggests a higher local Ag composition. For AgPS18k-1-min, with a total volume fraction  $\varphi = 0.05$ , the local concentration  $\varphi = 0.07$  is about 40 % higher. Furthermore, this second phonon only becomes measurable at temperatures exceeding the  $T_g$ , implying the necessity to have some degree of viscoelastic coupling between the nanoparticle clusters. Note that the laser powers used for this measurement are capable of exceeding the  $T_g$  in the focal volume but are lower than the temperature used for the actual annealing ( $200 \text{ }^\circ\text{C}$ ).

Consequently, the appearance of the second phonon is a reversible phenomenon. The appearance of a second softer phonon is unique to our system. Previous literature reports two longitudinal phonons in a silica poly(2-vinyl pyridine) matrix. Here a *harder* phonon emerged and was justified by solvent selection and annealing-induced microphases where coupling between a percolating silica network was

found.<sup>[38]</sup> The finding of a softer phonon in our case is consistent with the Ag-NP content-dependent  $c_{L,eff}$  discussed in Fig. 7.2b. The strong binding of the polymer ligand to the Ag core causes this counterintuitive behavior, which is even robust enough to couple across clusters of AgNPs.

## 7.4 Conclusion

Homogeneously loaded nanocomposite materials exhibit a wealth of properties, which are still far from being understood. Our contribution bases on dense polymer grafted Ag nanoparticles, where the effective longitudinal speed of sound decreases with increasing Ag content - a counterintuitive finding. The reduction in the speed of sound is, however, analytically captured by Wood's law and is based on the strong binding of the ligand molecule to the AgNP surface. Furthermore, we have been able to show the significant influence of thermoplasmonic heating on the acoustic and consequently mechanical properties of these nanocomposite samples. The intense local laser heating became apparent when assessing the temperature-dependent  $c_{L,eff}$ . Here, an apparent reduction in the glass transition temperature could be explained by the strong heating of the nanocomposite sample in the focal measurement volume. The degree of heating depends on the AgNP concentration and shows a nonlinear behavior. This thermoplasmonic effect can reach local temperatures in excess of the actual glass transition temperature of the hybrid material ( $\sim 100$  °C of the PS ligand). BLS further elucidated the importance of the overall film morphology. Here, we exploited a particularly unusual behavior of our nanocomposite films: At temperatures much higher than the glass transition temperature ( $\sim 200$  °C), rapid AgNP clustering sets in. Prolonged annealing at these temperatures led to a redispersion of the clusters at the expense of larger nanoparticles with a higher polydispersity compared to the initial state. This peculiar morphology change was observed consistently in nanocomposites with ligands of various molecular weights. Concomitant to this change in morphology is the appearance of a second, softer phonon mode. This softer mode is only active at local temperatures exceeding the glass transition temperature of the polymer ligand and appears only after the temperature-driven cluster formation. It is indicative of the importance of the local microstructure, in this case, a local increase in AgNP concentration, along with the strong ligand adhesion to the AgNP core. Our paper revealed several unusual properties of well-defined nanocomposite films. Not only did we show how the microstructure itself influences the effective mechanical properties of the nanocomposite film, but we also showed multiple possibilities to influence the longitudinal speed of sound in an (ir)reversible manner by global external and local thermoplasmonic heating.

**Acknowledgements:** The authors thank Prof. Dr. André H. Gröschel for electron tomography measurements. P.H. thanks Alexandra Philipp for help with the thermographic measurements. P.H. and M.R. acknowledge the funding by the Lichtenberg Professorship provided by the Volkswagen Foundation. BG thanks the Alexander von Humboldt Foundation for the Fellowship. The work was supported by the SFB 840 and DFG project RE3550/2-1 (Bayreuth) and ERC AdG SmartPhon (No. 694977) (Mainz).

**Author Contributions:** The manuscript was written through the contributions of all authors. All authors have approved the final version of the manuscript. P.H. synthesized the polymer nanocomposites and prepared the spin-coated samples. P.H. performed UV/Vis, TEM, DSC, and thermographic measurements. D.S. measured the BLS spectra. Z.W. performed the COMSOL calculations. S.R. performed SAXS measurements and interpretation. All authors discussed the results and jointly wrote the manuscript.

**Conflicts of Interest:** The authors declare no competing financial interest.

## 7.5 Supporting Information

### 7.5.1 Annealing procedure

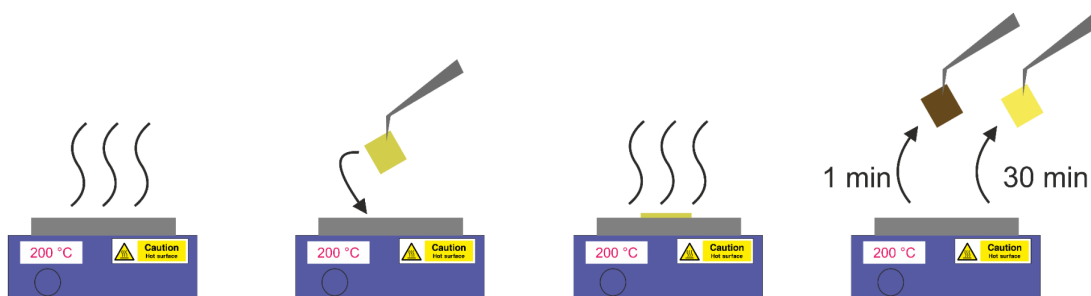


Figure 7.8: Schematic of the annealing procedure of the nanocomposite films. The films were put on a hot plate with a temperature of 200 °C, and removed after 1 or 30 min, respectively. After 1 min annealing, the color of the films turns brown, due to the clustering of the particles. The color changes back to yellow after 30 min annealing, as the particles disperse individually again.

### 7.5.2 Video TEM tilt series

We provide six tilt series movies for a better particle distribution impression on various nanocomposite films:

SV1: AgPS8K\_as\_prepared

SV2: AgPS8K\_1min\_annealed

SV3: AgPS8K\_30min\_annealed

SV4: AgPS18K\_as\_prepared

SV5: AgPS18K\_1min\_annealed

SV6: AgPS18K\_30min\_annealed

### 7.5.3 SAXS characterization

The thermodynamical stability of the films is studied by annealing experiments. Figure 7.9 shows the scattering intensities of the AgPS8k (left) and AgPS18k (right) films after different annealing times. In detail, the films were measured at room temperature before annealing (blue circles), after 1 min annealing at 200 °C (red squares) and after 30 min of annealing at 200 °C (black triangles). Unexpectedly, the intensities obtained after 1 min annealing exhibit the most pronounced forward scattering and a shoulder at  $q \approx 0.09 \text{ \AA}^{-1}$ . According to the Bragg's law, this can

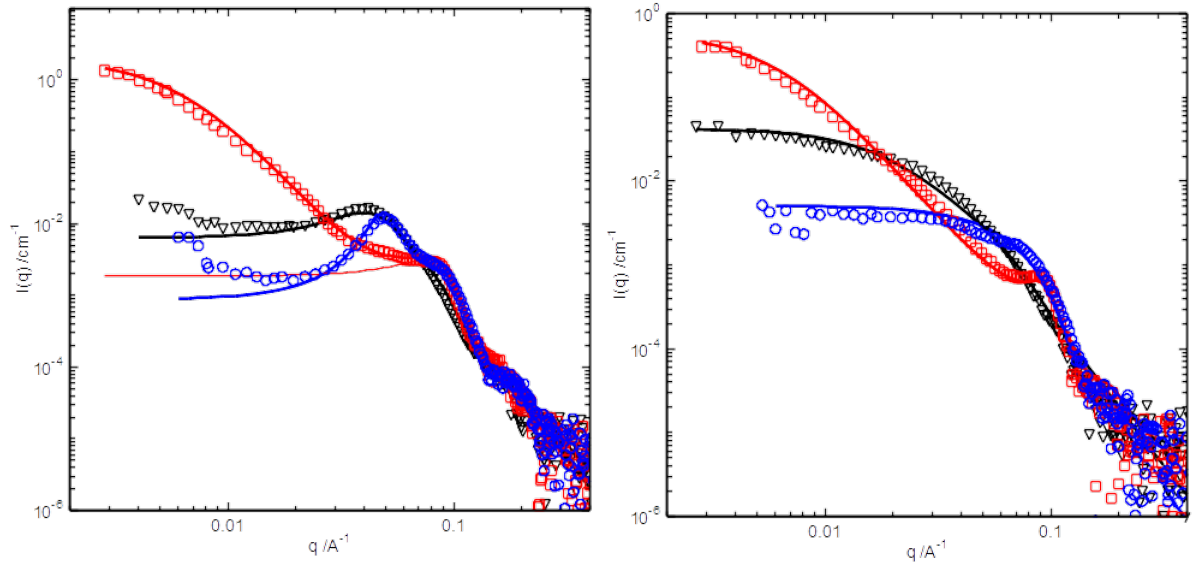


Figure 7.9: Experimental (symbols) and theoretical (lines) SAXS intensities of AgPS8k (left) and AgPS18k (right). The black data represent the as-prepared films, while the 1 min and 30 min annealed films are displayed by the red and blue data, respectively. The calculation of the theoretical intensities is described below in the text in Section 7.5.6.

be assigned to a characteristic distance of  $d = 2\pi/q \approx 70 \text{ \AA}$ . This value corresponds approximately to the size of the silver cores obtained in TEM studies. The clustering of the nanoparticles is indicated by the characteristic increase of the forward scattering. The scattering at low  $q$  of the other films is more even, excluding a big amount of clusters. Further Bragg reflexes are observed for AgPS8k after 0 min and 30 min annealing time in the range of  $q \approx 0.045\text{-}0.050 \text{ \AA}^{-1}$ . This corresponds to a characteristic length of  $130 \text{ \AA}$  and can be assigned to the particle-particle distance. For the AgPS18k system similar Bragg signals are hardly visible – even for AgPS18k without thermal treatment a smeared shoulder around  $q \approx 0.025 \text{ \AA}^{-1}$  ruled out. The scattering patterns data were modeled assuming a hard sphere interaction potential (Percus-Yevick model) using spheres with a radius of  $30 \pm 4 \text{ \AA}$  (silver core). The scattering intensity  $I(q)$  of a sphere with radius  $R$  and excess electron density  $\Delta\rho$  is given by

$$I(q) = \left( \frac{4\pi}{3} R^3 \Delta\rho^3 \frac{\sin(qR) - qR \cos(qR)}{(qR)^3} \right)^2 \quad (7.1)$$

The hard sphere interaction potential  $U(r)$  is

$$U(r) = \begin{cases} \infty & \text{for } 0 < r < R_{out} \\ 0 & \text{for } r > R_{out} \end{cases}, \quad (7.2)$$

where  $R_{out}$  can be imagined as contact radius. The potential is associated with the structure factor  $S(q, R_{out}, \Phi) = \left(1 + 24\Phi \frac{G(\Phi, A)}{A}\right)^{-1}$ , with

$$\begin{aligned} G(q) &= \alpha \frac{\sin(A) - A \cos(A)}{A^2} + \beta \frac{2A \sin(A) + (2 - A^2) \cos(A) - 2}{A^3} \\ &+ \gamma \frac{-A^4 \cos(A) + 4\{(3A^2 - 6) \cos(A) + (A^3 - 6A) \sin(A) + 6\}}{A^5} \\ A &= 2R_{out}q, \quad \alpha = \frac{(1 + 2\Phi)^2}{(1 - \Phi)^4}, \\ \beta &= -6\Phi \frac{(1 + 0.5\Phi)^2}{(1 - \Phi)^4}, \quad \gamma = \frac{\alpha\Phi}{2}. \end{aligned} \quad (7.3)$$

The effective radius  $R_{out}$  of the AgPS core-shell particle and the effective volume fraction  $\Phi$  were fitting parameters. This way the data of AgPS8k before annealing can be well described, leading to  $R_{out} = 65 \text{ \AA}$  and  $\Phi = 0.35$  (left, blue line). The theoretical intensity for AgPS8k after 30 min annealing time (left, black line) base on  $R_{out} = 65 \text{ \AA}$  and  $\Phi = 0.25$ , but at the cost of a slightly increased polydispersity of the core radius,  $R = 30 \pm 9 \text{ \AA}$ . The Percus-Yevick model alone failed for the data after 1 min at  $200 \text{ }^\circ\text{C}$  (thin red line). As discussed, the forward scattering of bigger objects dominates the scattering intensity, which is most likely aggregated silver cores. Thus, the intensity was modelled by two independent contributions, (i) the interaction of hard spheres ( $R = 30 \pm 4 \text{ \AA}$ ,  $R_{out} = 33 \text{ \AA}$  and  $\Phi = 0.25$ ) and (ii) a mass fractal with a characteristic radius of  $R_H = 150 \text{ \AA}$  and a fractal dimension of  $D = 2.9$ . The structure factor of a fractal object can be calculated via the pair correlation function, which describes the total number of particles with a characteristic dimension of  $R$  within a sphere,

$$S(q) = 1 + \frac{D}{RD} \int_0^\infty r^{D-3} h(r, \epsilon) \frac{\sin(qr)}{qr} r^2 dr, \quad (7.4)$$

with the cut-off function  $h(r, \epsilon, \alpha)$

$$h(r, \epsilon, \alpha) = e^{\left\{\frac{r}{\epsilon}\right\}^\alpha}, \quad (7.5)$$

where  $\epsilon$  is a cut-off length to describe the behavior of the pair correlation function at large distances. Here, this characteristic distance is interpreted as radius  $R_H$  of the aggregate.

The corresponding intensity agrees with the data qualitatively. Hence, it is a strong indication of a thermodynamic non-equilibrium, caused by a temporary clustering of silver NPs. The same results should also apply to AgPS18k. Unfortunately, the fitting of  $R_{out}$  is not possible due to an ill-defined or missing Bragg signal. Even if AgPS18k have a significantly larger polymeric shell, the scattering contribution of

the shell should be minor due to the extremely low contrast of polystyrene compared to silver. Thus, the films initially consist of well-dispersed monodisperse particles, which undergo a temporary core-clustering for short annealing before re-dispersion with prolonged annealing time. Indeed, the pure form factor of monodisperse spheres is suitable to approximate the scattering at annealing times of  $t = 0$  min ( $R = 30 \pm 4 \text{ \AA}$ ) and  $t = 30$  min ( $R = 30 \pm 9 \text{ \AA}$ ). The non-equilibrium description at  $t = 1$  min is again a combination of the Percus-Yevick model ( $R = 30 \pm 4 \text{ \AA}$ ,  $R_{out} = 33 \text{ \AA}$  and  $\Phi = 0.35$ ) and clusters ( $R_H = 150$ ,  $D = 2.7$ ).

#### 7.5.4 Effective medium analysis

Effective medium analysis has been widely used to evaluate the properties of composites. To understand the composition dependence of the mechanical properties of the AgPS nanocomposite thin films, we use the Wood's Law<sup>[39,40]</sup> to predict the effective longitudinal modulus and sound velocity of the thin films over a wide range of the silver volume fraction.

The Wood's Law reads,

$$\frac{1}{M_{L,eff}} = \frac{\phi_{Ag}}{M_{L,Ag}} + \frac{1 - \phi_{Ag}}{M_{L,PS}}, \quad (7.6)$$

which can be combined with  $M_L = \rho c_L^2$ , and  $\rho_{eff} = \rho_{Ag}\phi_{Ag} + \rho_{PS}(1 - \phi_{Ag})$  to give

$$M_{L,eff} = \left[ \frac{\phi_{Ag}}{\rho_{Ag}c_{L,Ag}^2} + \frac{1 - \phi_{Ag}}{\rho_{PS}c_{L,PS}^2} \right]^{-1}, \quad (7.7)$$

and

$$c_{L,eff} = \left\{ [\rho_{Ag}\phi_{Ag} + \rho_{PS}(1 - \phi_{Ag})] \left[ \frac{\phi_{Ag}}{\rho_{Ag}c_{L,Ag}^2} + \frac{1 - \phi_{Ag}}{\rho_{PS}c_{L,PS}^2} \right] \right\}^{-0.5}. \quad (7.8)$$

Here,  $M_L$  is longitudinal modulus,  $\phi$  is volume fraction,  $\rho$  is density,  $c_L$  is longitudinal sound velocity, and the subscripts "eff", "Ag", and "PS" indicate that the properties are for the AgPS composite (i.e., effective medium), Ag NPs, and polystyrene matrix, respectively. In the analysis, we use the following properties for the two components: (1) Ag:  $\rho_{Ag} = 10.5 \cdot 10^3 \text{ kg/m}^3$ ,  $c_{L,Ag} = 3650 \text{ m/s}$ ; (2) PS:  $\rho_{PS} = 1.04 \cdot 10^3 \text{ kg/m}^3$ ,  $c_{L,PS} = 2350 \text{ m/s}$ .

Figure 7.10a - d show the predicted results as red curves, where a and c show the data in the full range of Ag volume fractions, and b and d show the data in the

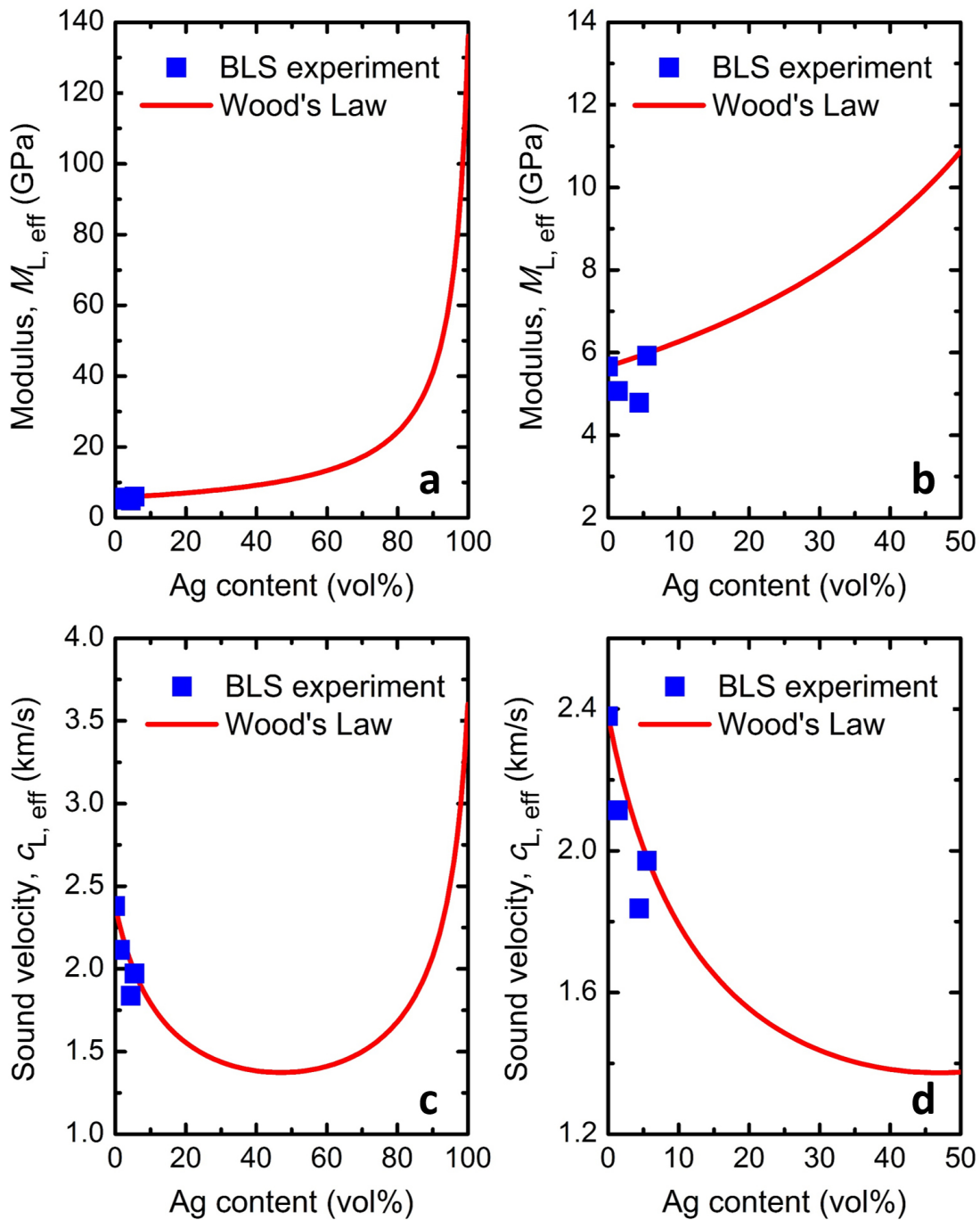


Figure 7.10: Effective longitudinal modulus (a), (b) and effective longitudinal sound velocity (c), (d) of AgPS thin films with Ag content in the ranges (a) from 0 to 100 vol% and (b) from 0 to 50 vol%. The experimental data are compared with the Wood's Law's predictions (solid red lines in a-d).

range of Ag volume fractions from 0 to 50 %, for better visibility. As the Ag volume fraction increases, the effective longitudinal modulus (a, b) first decreases in contrast to the monotonic increase predicted (solid red line) by the effective medium Wood's model (Eq. 7.6). This drop is stronger in the effective longitudinal sound velocity (Figure 7.10c and d) compared to  $M_{L,eff} = \rho_{eff}c_{L,eff}$  due to the increase of density

$\rho_{eff}$  with Ag composition. The experimental  $c_{L,eff}$  first decreases and then increases with the increasing Ag volume fraction (last data point), showing a bathtub-shaped curve. The predicted  $c_{L,eff}$  (solid red lines) also drops with Ag composition but overestimates the experimental sound velocities at the first two Ag compositions. The initial decrease stems from the large mismatch of the acoustic impedances of Ag and PS, whereas the later increase can be attributed to the hardening effect. As a comparison, the experimental data are plotted against the predicted ones. We point out that the four samples considered in this study all have quite low silver volume fractions (PS18k — 0.0 %, AgPS18k — 1.4 %, AgPS12k — 4.4 %, and AgPS8k — 5.5 %).

### 7.5.5 Glass Transition

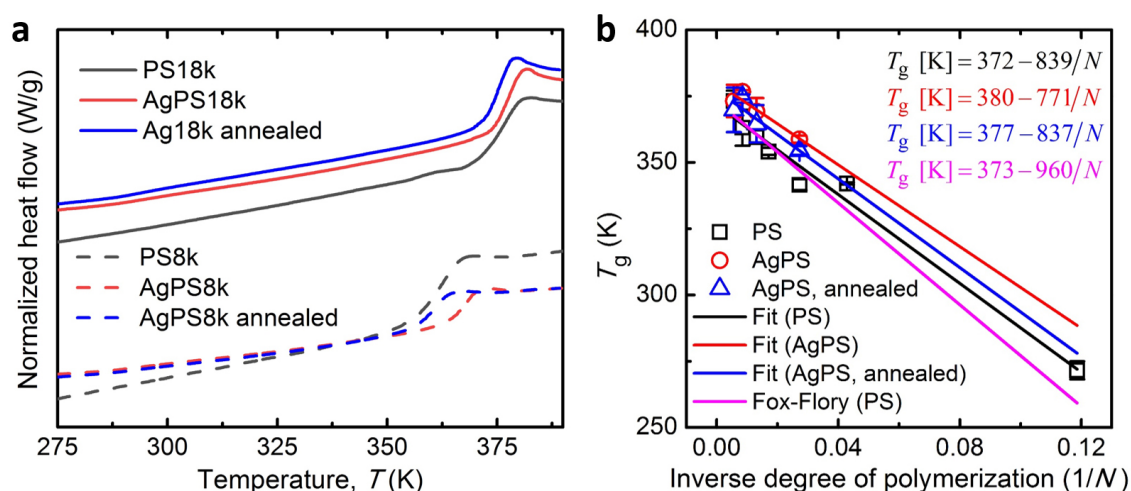


Figure 7.11: (a) DSC curves of the nanocomposite and corresponding polymer. The measured  $T_g$ s are 86 °C for the PS8k ligand, 96 °C for AgPS8k, 91 °C for AgPS8k annealed, 100 °C for PS18k, 100 °C for AgPS18k and 97 °C for AgPS18k annealed. In (b) the glass transition temperatures are plotted according to the Fox-Flory formula. The polystyrene data agrees well with the data of Fox and Flory<sup>[41]</sup>. The nanocomposites also show a linear behavior.

Table 7.1: Parameters obtained from the fits in Figure 7.3 (main manuscript)

$c(T) = A + \frac{B}{T}$	Glass			Rubber		
	A (m/s)	B (m/sK)	B/A (1/K) $\pm 5\%$	A (m/s)	B (m/sK)	B/A (1/K) $\pm 5\%$
<b>PS18K</b>	2712	-1.25	$-4.6 \times 10^{-4}$	4706	-6.69	$-6.69 \times 10^{-3}$
<b>AgPS18K</b>	2358	-0.76	$-3.2 \times 10^{-4}$	3952	-5.69	$-5.69 \times 10^{-3}$
<b>AgPS8K</b>	2100	-0.81	$-3.9 \times 10^{-4}$	3187	-4.36	$-1.3 \times 10^{-3}$

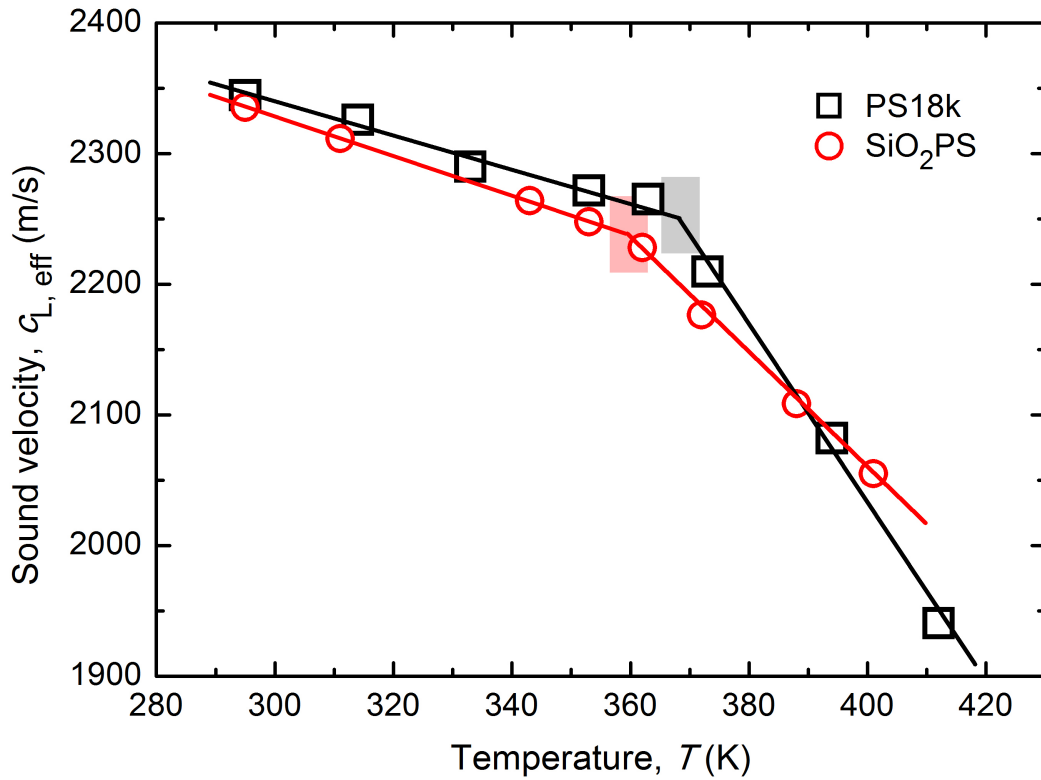


Figure 7.12: The longitudinal sound velocity of the bulk polystyrene film (black squares) and a SiO<sub>2</sub>PS nanocomposite film (red circles). In contrast to Ag, SiO<sub>2</sub> nanoparticles do not show additional heating effects due to the non-absorbing nature of SiO<sub>2</sub> nanoparticles at the laser wavelength (see Figure 7.3).

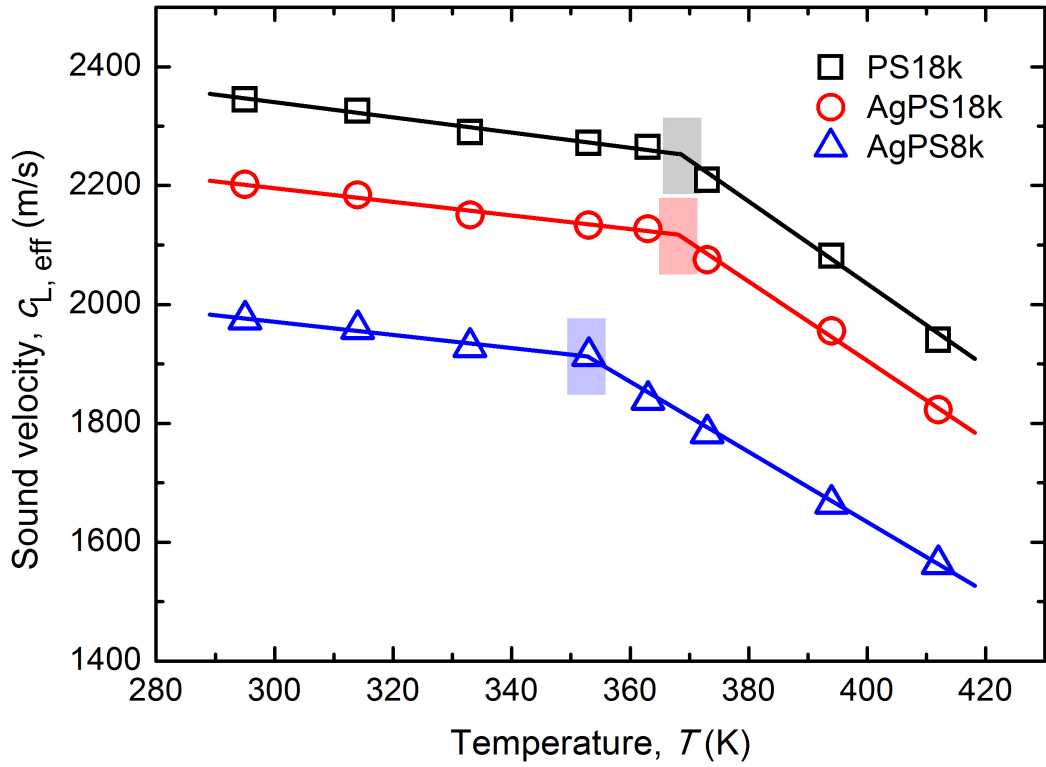


Figure 7.13: Estimated longitudinal sound velocity in the absence of laser heating. The nanocomposites data are normalized to the PS slopes shifted by the ratio of  $\gamma = c_{AgPS}/c_{PS}$ , in each case. For the AgPS8k data, the lower  $T_g$  of PS8k is considered. The calibration of local temperature as a function of laser power,  $T(P)$  (Figure 7.5, main manuscript) is obtained from these estimations.

### 7.5.6 Absorption coefficients

The analysis starts with the Lambert-Beer Law, which is a widely used formula for characterizing the attenuation of light by materials. The Lambert-Beer Law reads,

$$Tr = \frac{\dot{q}_{tr}}{\dot{q}_{in}} = 10^{-A}, \quad (7.9)$$

where  $Tr$  is the transmittance of the material,  $\dot{q}_{in}$  is the incident energy density ( $W/m^3$ ),  $\dot{q}_{tr}$  is the transmitted energy density ( $W/m^3$ ), and  $A$  is the absorbance of the material. Assuming the reflected energy is negligible, then the absorbed energy density is

$$\dot{q}_{ab} = \dot{q}_{in}(1 - Tr), \quad (7.10)$$

or

$$\dot{q}_{ab} = \dot{q}_{in}(1 - 10^{-A}), \quad (7.11)$$

or

$$\dot{q}_{ab} = \dot{q}_{in}(1 - e^{-(\ln 10)\alpha H}). \quad (7.12)$$

Here,  $\alpha$  is the absorption coefficient (unit: 1/cm) that we refer to in this section, and  $H$  is the thickness of the sample film.

To provide a more realistic representation of the laser, we consider the spatial variation of the absorbed energy density as follows,

$$\dot{q}_{dist}(r, z) = \frac{2\alpha\dot{q}_{in}}{\pi R_1^2} \exp\left(-\frac{2r^2}{R_1^2}\right) \exp(-\alpha z). \quad (7.13)$$

This means the absorbed energy density decays exponentially in the  $z$  direction and has a Gaussian distribution in the  $r$  direction. Figure 7.14a shows a schematic of the coordinates and characteristic dimensions. We use the COMSOL Multiphysics, a widely used simulation package based on the FEM, to obtain the temperature distributions in the samples. Because of the large aspect ratios of the samples ( $R_2 \gg H$ ) and the symmetric boundary conditions, the simulation domains can be simplified from 3D to 2D-axisymmetric. The governing equation of the problem is the steady state heat diffusion equation,

$$\nabla[k\nabla T(r, z)] + \dot{q}_{ab}(r, z) = 0 \quad (7.14)$$

The boundary conditions are:

(1) Left:  $r = 0, -H \leq z \leq 0$ ; symmetry boundary

$$\frac{dT(r, z)}{dr} = 0 \quad (7.15)$$

(2) Right:  $r = R_2, -H \leq z \leq 0$ ; convection and radiation

$$-k \frac{dT(r, z)}{dr} = h(r, z)[T(r, z) - T_\infty] + \epsilon\sigma[(T(r, z))^4 - T_\infty^4] \quad (7.16)$$

(3) Bottom:  $0 \leq r \leq R_2, z = -H$ ; convection and radiation

$$-k \frac{dT(r, z)}{dz} = h(r, z)[T(r, z) - T_\infty] + \epsilon\sigma[(T(r, z))^4 - T_\infty^4] \quad (7.17)$$

(4) Top:  $0 \leq r \leq R_2, z = 0$ ; convection and radiation

$$-k \frac{dT(r, z)}{dz} = h(r, z)[T(r, z) - T_\infty] + \epsilon\sigma[(T(r, z))^4 - T_\infty^4] \quad (7.18)$$

Here,  $\sigma (= 5.67 \cdot 10^{-8} \text{ W} \cdot \text{m}^{-2} \cdot \text{K}^{-4})$

A summary of the FEM simulation parameters for AgPS18k and AgPS8k is given in Table 7.2. Particularly, the effective densities of the samples are calculated as  $\rho_{eff} = \rho_{Ag}\phi_{Ag} + \rho_{PS}(1 - \rho_{Ag})$ ; the effective thermal conductivity of the samples is calculated by eff Ag Ag PS Ag using the Maxwell model<sup>[42]</sup>,

$$k_{eff} = k_{PS} \frac{(k_{Ag} + 2k_{PS}) + 2\phi_{Ag}(k_{Ag} - k_{PS})}{(k_{Ag} + 2k_{PS}) - \phi_{Ag}(k_{Ag} - k_{PS})}, \quad (7.19)$$

which has proven to be suitable for calculating the effective thermal conductivity of composite materials with low filler concentrations. Considering the main content of the AgPS films is PS, and the thermal conductivity of PS has a weak dependence on temperatures<sup>[43]</sup>, we use constant thermal conductivities in the simulations. Since the thermal conductivity of PS decreases slightly upon glass transition<sup>[43]</sup>, the obtained absorption coefficients in the rubbery state in this study are expected to be slightly lower than the actual ones.

From the FEM simulations, we obtain the temperature distributions in the samples. Figure 7.14b shows an example of temperature distribution. Because the simulation domain has a large aspect ratio ( $R_2 \gg H$ ), only a portion of it (near the laser spot) is shown for better visibility. It is seen that the temperature decreases from the laser-heated region to the periphery. After gaining some appreciation on the temperature distributions, we focused on the average temperature in the laser spot, indicated as  $T_{ls,ave}$  in Figure 7.14a, which represents the average temperature in the yellow disk (note the simulation domain is 2D-axis-symmetric). In the BLS measurement, we characterize the sound velocity in the laser spot region, and the sound velocity corresponds to  $T_{ls,ave}$ . Therefore,  $T_{ls,ave}$  plays a similar role in the BLS experiments and FEM simulations. From the BLS measurement, we have obtained the relationship between  $T_{ls,ave}$  and the laser incident power. On the other hand, it is obvious that  $T_{ls,ave}$  depends on the absorbed laser power. The more the absorbed laser power, the higher the  $T_{ls,ave}$ . This means that by matching the  $T_{ls,ave}$  from the FEM simulations, which can be tuned by modifying the absorbed laser power (or the absorption coefficient), with the corresponding experimental values, we can obtain the absorption coefficients of the samples. After obtaining the absorption coefficients under all laser power conditions, we can also obtain the relation between the absorption coefficient and  $T_{ls,ave}$  study, we obtain the following relations.

AgPS18k:

$$\text{Glassy state} : \alpha(T) = 0.0182 \cdot T[\text{K}] - 4.9250 \quad (7.20)$$

$$\text{Rubbery state} : \alpha(T) = -0.0109 \cdot T[\text{K}] + 5.7682 \quad (7.21)$$

AgPS8k:

$$\text{Glassy state} : \alpha(T) = 0.0638 \cdot T[\text{K}] - 18.2972 \quad (7.22)$$

$$\text{Rubbery state} : \alpha(T) = -0.0170 \cdot T[\text{K}] - 1.7821 \quad (7.23)$$

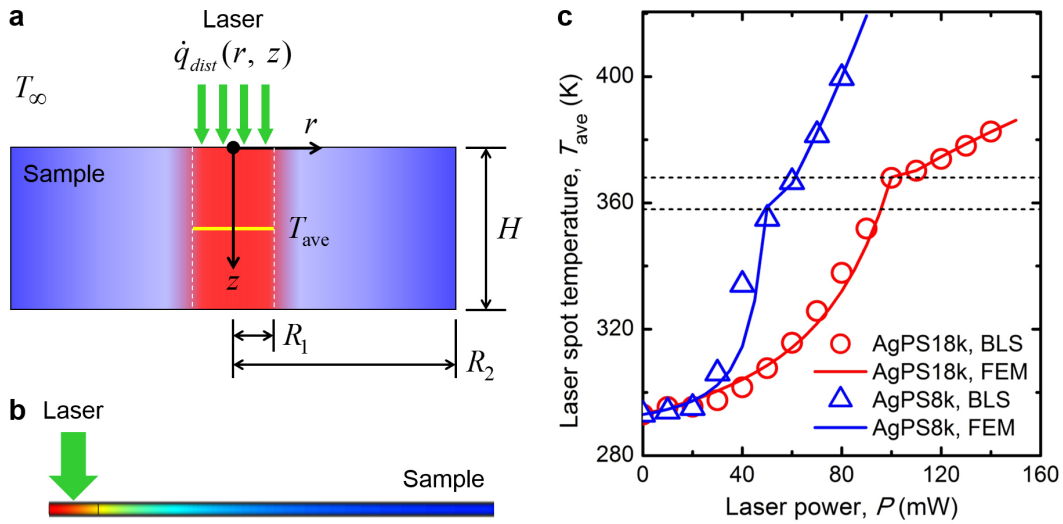


Figure 7.14: (a) Schematic of the FEM simulations used to obtain the absorption coefficients of the AgPS thin film. (b) An example of temperature distribution in the AgPS18k sample. The temperature is high in the laser-heated region and low in the periphery. Because the simulation domain has a large aspect ratio ( $R_2 \gg H$ ), only a portion of it (near the laser spot) is shown for better visibility. (c) The laser spot average temperature plotted against the laser power for AgPS18k and AgPS8k. Both experimental (BLS) and simulation (FEM) results are shown.

The simulated  $T_{ls,ave}$  vs. laser power relations for AgPS18k and AgPS8k are shown in Figure 7.14c, in comparison to the experimental data. It is seen that by using absorption coefficients linearly dependent on the temperature the experimental  $T_{ls,ave}$  vs. laser power relations are well captured. We also observe a transition point for both AgPS18k and AgPS8k, implying the occurrence of the glass transition in the samples. The transition temperatures are in the range from 358 K to 368 K, as marked by the horizontal dashed lines in Figure 7.14c. These temperatures are simi-

lar to the glass transition temperature of PS ( $T_g \sim 100$  °C), which is expected because more than 90 % of the sample content is PS.

Previously, linearly increasing extinction coefficients with temperature have been reported for fused silica<sup>[44]</sup>,  $\text{NH}_3$ <sup>[45]</sup>, and several inorganic solutions<sup>[46,47]</sup>. For the AgPS samples in this study, the temperature dependence of the absorption coefficients could be attributed to the excitation of electrons in Ag from the valence band to the conduction band. At higher temperatures, more free electrons become available, which lead to stronger plasmonic enhancement effects and thus higher  $T_{ls,ave}$ . Following this logic, the absorption coefficient is expected to increase with increasing temperature, which is true for all relations we get, except the one for the rubbery state of AgPS18k. The abnormal, decreasing absorption coefficient of the rubbery state of AgPS18k with increasing temperature could be ascribed to the measurement uncertainty at this low Ag volume fraction (i.e., 1.4 % for AgPS18k). In the rubbery state, the PS chains can flow, which could cause inhomogeneity in the film. In other words, at  $T$  above  $T_g$  sample region covered by the laser spot could have varying compositions and structures at different temperatures. Furthermore, the smaller slopes of the absorption coefficients in the rubbery state than the glassy state could be explained by the fact that the PS chains can "flow" at temperatures above  $T_g$ , which means the plasmonic effect, depending on the collective motions of the free electrons, could be deteriorated as the matrix flows. As a result, the deteriorated plasmonic effect leads to slower variations in the absorption coefficients as temperature increases.

Table 7.2: Summary of FEM simulation parameters for AgPS18k and AgPS8k.

Parameter	Symbol (unit)	AgPS18k	AgPS8k
Ag content	$\phi_{Ag}$ (vol%)	1.4	5.5
Film thickness	$H$ ( $\mu\text{m}$ )	1.276	0.430
Laser spot radius	$R_1$ ( $\mu\text{m}$ )	20	20
sample radius	$R_2$ ( $\mu\text{m}$ )	500	200
Density	$\rho_{eff}$ ( $\text{kg}/\text{m}^3$ )	1172.4	1560.3
Heat capacity	$c_{P,eff}$ ( $\text{J}/\text{kgK}$ )	$-3.9 \cdot 10^{-4}$	1335.9
Thermal conductivity	$k_{eff}$ ( $\text{W}/\text{mK}$ )	-0.156	0.176
Surrounding temperature	$T_\infty$ (K)	293	293
Emissivity	$\epsilon$ (1)	1	1

### 7.5.7 Annealing effects

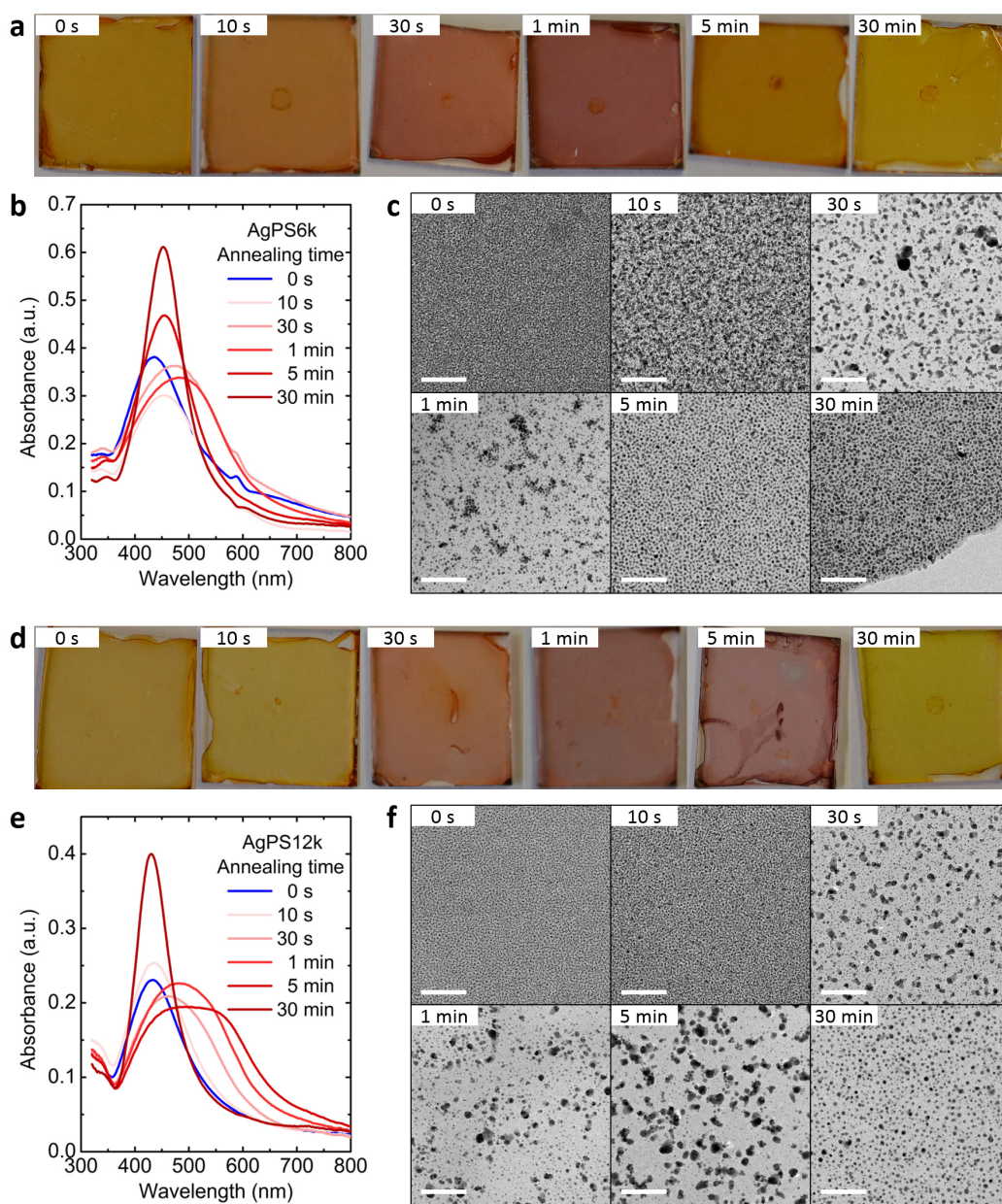


Figure 7.15: (a) Photos, (b) UV-Vis absorption spectra, and (c) TEM images of the AgPS6k samples subjected to different annealing time. (d) Photos, (e) UV-Vis absorption spectra, and (f) TEM images of the AgPS12k samples subjected to different annealing time. “0 s” indicates the as-prepared, non-annealed samples. The scale bars in (c) and (f) represent 200 nm.

### 7.5.8 Collective heating effect

From the TEM images of the annealed sample films, we observe aggregation of Ag nanoparticles. Specifically, no aggregation exists in the non-annealed sample, and larger aggregates of Ag nanoparticles are found in the AgPS18k-1min sample than the AgPS18k-30min sample. In the sound velocity vs. laser power measurements, we find the variation of the sound velocity shows a corresponding trend with the variation of the aggregation size: a larger variation of the sound velocity for a sample with a larger aggregation size. Regarding  $T_{ls,ave}$ , the trend can be translated as a larger  $T_{ls,ave}$  for a sample with a larger aggregation size. In other words, the aggregation of Ag nanoparticles could lead to some collective heating effect, leading to a higher  $T_{ls,ave}$ .

Here we use FEM simulations to demonstrate the collective heating effect. The simulations are conducted with the COMSOL Multiphysics package. To better visualize the collective heating effect and meanwhile reduce the computation cost, we conduct 2D simulations, instead of 3D ones. As a result, the model represents infinitely long Ag cylinders embedded in an infinitely long PS pillar. Figure 7.16a shows a schematic of the simulation domain. Because of symmetry, only a quarter of the simulation domain is considered. We consider uniform heat generation in the Ag cylinders. The governing equation of the problem is the steady state heat diffusion equation,

$$\nabla[k(x, y)\nabla T(x, y)] + \dot{q}_{ab}(x, y) = 0. \quad (7.24)$$

The boundary conditions are:

(1) Left:  $x = 0, 0 \leq y \leq L$ ; symmetry boundary

$$\frac{dT(x, y)}{dx} = 0 \quad (7.25)$$

(2) Right:  $x = L, 0 \leq y \leq L$ ; constant temperature

$$T(x, y) = T_0 \quad (7.26)$$

(3) Bottom:  $0 \leq x \leq L, y = 0$ ; symmetry

$$\frac{dT(x, y)}{dy} = 0 \quad (7.27)$$

(4) Top:  $0 \leq x \leq L, z = 0$ ; constant temperature

$$T(x, y) = T_0 \quad (7.28)$$

For simplicity, we fix the temperature at the external boundaries, instead of considering convective and radiative boundary conditions, as in the Section 7.5.6 We set the material properties as follows: (1) Ag:  $\rho_{Ag} = 10.5 \cdot 10^3 \text{ kg/m}^3$ ,  $cp_{Ag} = 235 \cdot \text{J/kg-K}$ ,  $k_{Ag} = 429 \cdot \text{W/m-K}$ ; (2) PS:  $\rho_{PS} = 1.040 \cdot 10^3 \text{ kg/m}^3$ ,  $cp_{PS} = 1400 \cdot \text{J/kg-K}$ ,  $k_{PS} = 0.15 \cdot \text{W/m-K}$ . A summary of some relevant FEM simulation parameters is given in Table 7.3. Particularly, we use the same heat generation rate in all simulations. Using the model, we conduct two sets of simulations, investigating the effects of (1) varying the number of heaters and (2) varying the separation between heaters on the temperature distribution. The results for (1) are shown in Figure 7.16b-d, while those for (2) in Figure 7.16e-g. As the number of heaters increases, the temperature increases, which is expected. As the heaters aggregate (i.e., the distance between the heaters decreases), the temperature also increases. In Figure 7.16b-g, we also show the average temperatures over the simulation domain, which can serve as quantitative indicators of the temperature changes. To eliminate the effect of the constant-temperature boundary conditions, we also tried convective boundary conditions but obtained qualitatively similar results. Therefore, the trend should be independent of the boundary conditions. We note that both (1) and (2) could happen in the annealing-induced aggregation of the Ag nanoparticles. That is, more Ag nanoparticles could be brought to the laser spot region, and the separation between the Ag nanoparticles in the laser spot region could reduce, both of which can result in higher  $T_{ls,ave}$ . As a conclusion, the FEM simulations support the experimental finding that the aggregation of Ag nanoparticles leads to enhanced heating effects. Similar collective heating effects have been reported for the photoheating of gold nanoparticles solutions<sup>[23]</sup> and gold-based thermoplasmonics systems<sup>[37]</sup>.

Finally, we point out the limitations of the FEM simulations in this section. First, the simulations are 2D and thus qualitative. 3D simulations are expected to provide more accurate results, but the trends should be similar. Second, only a small number of heaters is considered. It is expected that more heaters will lead to stronger collective heating effects. Third, the geometrical dimensions do not reflect the experimental conditions. Because of the linearity of the governing equation, the FEM simulations can be scaled down or up via:  $x \rightarrow ax$ ,  $y \rightarrow ay$ , and  $\dot{q} \rightarrow \dot{q}/a^2$ , which can be obtained through some scaling analysis. Here,  $a$  ( $\neq 0$ ) represents the scaling factor. Fourth, the heat generation rate ( $1 \cdot 10^{10} \text{ W/m}^3$ ) is not realistic. The value is chosen to provide moderate temperature increases in the simulation domain.

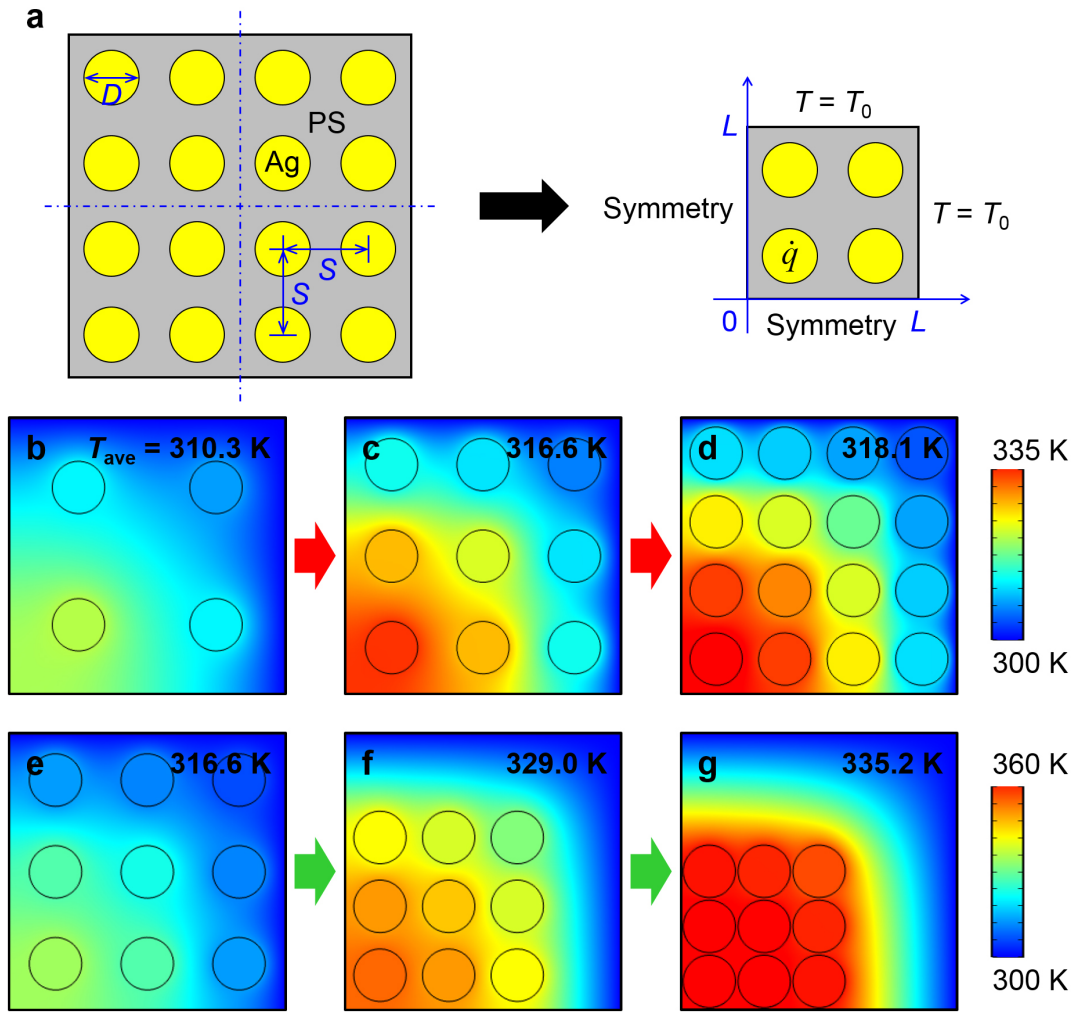


Figure 7.16: (a) Schematic of the FEM simulations used to show the effect of collective heating. Because of symmetry, only a quarter of the domain is simulated. (b), (c), and (d) show the temperature distributions with 4, 9, and 16 heaters in the quarter domain, respectively. More heaters lead to higher temperatures. (e), (f), and (g) show the temperature distributions with increasing levels of aggregation of the heaters. More clustered heaters result in higher temperatures. In (b)-(g), the average temperatures in the quarter domain are indicated.

Table 7.3: Summary of parameters for collective heating effect simulations.

Configuration	$D$ ( $\mu\text{m}$ )	$L$ ( $\mu\text{m}$ )	$S$ ( $\mu\text{m}$ )	$\dot{q}$ ( $\text{W}/\text{m}^3$ )	$T_0$ (K)
(b)	20	105	52.5	$1 \cdot 10^{10}$	300
(c)	20	105	35	$1 \cdot 10^{10}$	300
(d)	20	105	26.25	$1 \cdot 10^{10}$	300
(e)	20	105	35	$1 \cdot 10^{10}$	300
(f)	20	105	26.25	$1 \cdot 10^{10}$	300
(g)	20	105	21	$1 \cdot 10^{10}$	300

## 7.6 Appendix

### 7.6.1 Thermal conductivity of one-component nanocomposites

The following results about the thermal conductivity of PNC are no official part of the previous publication. Nevertheless, the results present a great addition to the characterization of the PNC and are an important part of this thesis. The target of producing one-component PNCs was to study the influence of the IPD on the thermal conductivity. For this reason, some of the PNC samples were measured on a PA setup to find out their thermal conductivity. The measurements were performed at the Heat Lab of the Georgia Institute of Technology. The setup has a slightly different layout compared to the setup at Bayreuth. The main differences persist in a lens in front of the sample, the use of a laser with a wavelength of  $\lambda = 1100$  nm and an acousto-optic modulator (AOM) instead of an EOM. Details of the PA setup used in this section can be found in various publications.<sup>[48–50]</sup>

For the study, AgPS3k, AgPS6k, AgPS12k and AgPS18k were investigated. Furthermore, the thermal conductivities of the pure polymer samples, PS3k, PS6k, PS12k and PS18k, were determined to monitor the influence of the molecular weight. The samples were spin-coated as described in Section 3.1.4. Here, three different concentrations per sample were used. In that manner, all samples were obtained with three different thicknesses.

Consequently, a bias towards the thermal conductivity deriving from the film thickness was ruled out. Additionally, three measurements of each sample were performed. All samples, their thicknesses, as well as the determined  $R_{tot}$  and  $k_{eff}$ , are listed in Table 7.4.

The sample thickness did not bias the determined  $k_{eff}$  values. However, the deviation between the samples was considerably high. The values are in a range between  $114 \text{ mW m}^{-1} \text{ K}^{-1}$  and  $174 \text{ mW m}^{-1} \text{ K}^{-1}$ , with deviations up to  $18.5 \text{ mW m}^{-1} \text{ K}^{-1}$ . The significant scattering of the determined values makes the interpretation of the results difficult.

Nevertheless, we want to conclude our results. The effective thermal conductivities of the polymers are consistent. PS3k, PS6k and PS12k have all a thermal conductivity of  $128 \text{ mW m}^{-1} \text{ K}^{-1}$ . Only the sample with the highest molecular weight, PS18k, has a slightly higher thermal conductivity of  $138 \text{ mW m}^{-1} \text{ K}^{-1}$ . The mean thermal conductivity of the pure PS samples is depicted as the dashed lines in Figure 7.17.

From Figure 7.17a, it is apparent that the thermal conductivity of the PNC samples rises with increasing Ag ratio. The IPD inversely depends on the Ag ratio, due to the nature of our one-component system. The greater the IPD the higher the

Table 7.4: PA measurement values of the PNC samples.

Sample name	Thickness nm	$R_{tot}$			$k_{eff}$ $W m^{-1} K^{-1}$	SD $W m^{-1} K^{-1}$
		Run 1	Run 2	Run 3		
PS3k	355.6	2.84	2.83	2.88	0.1248	0.0012
PS3k	528.4	3.96	3.93	3.93	0.1341	0.0006
PS3k	678.0	5.27	5.26	5.66	0.1258	0.0052
PS6k	407.0	3.12	3.14	3.17	0.1295	0.0010
PS6k	645.4	4.70	4.65	4.61	0.1387	0.0013
PS6k	785.2	6.90	6.74	7.02	0.1140	0.0023
PS12k	419.2	3.33	3.47	3.41	0.1232	0.0026
PS12k	746.6	5.25	5.52	5.50	0.1377	0.0039
PS12k	880.2	7.10	7.30	7.15	0.1226	0.0018
PS18k	507.6	3.91	4.01	3.95	0.1283	0.0016
PS18k	819.8	6.02	6.41	6.07	0.1330	0.0045
PS18k	1268	8.21	8.08	8.35	0.1544	0.0025
AgPS3k	222.8	1.31	1.33	1.30	0.1697	0.0020
AgPS3k	397	2.23	2.47	2.16	0.1742	0.0120
AgPS3k	384.8	2.45	2.43	2.41	0.1584	0.0013
AgPS6k	266.4	1.88	1.93	1.90	0.1400	0.0018
AgPS6k	431.4	2.89	2.91	2.94	0.1481	0.0013
AgPS6k	474.2	3.61	3.51	3.27	0.1372	0.0071
AgPS12k	382.2	2.92	2.90	2.92	0.1312	0.0005
AgPS12k	903.2	5.67	7.35	6.10	0.1487	0.0185
AgPS12k	915.6	6.13	6.22	6.11	0.1488	0.0014
AgPS18k	613.2	5.04	5.09	5.41	0.1185	0.0045
AgPS18k	1346	8.37	8.34	8.15	0.1624	0.0024
AgPS18k	1276	7.33	8.25	8.17	0.1616	0.0108

PS ratio in the system, and therefore, the lower the Ag content. Consequently, the effective thermal conductivity decreases with the IPD, as shown in Figure 7.17b.

These findings are not surprising. When calculating the thermal conductivity with the Maxwell model, describing a composite consisting of a matrix and spherical inclusions, we find the same trend.<sup>[51]</sup> The blue lines in Figure 7.17a and b represent the Maxwell model. The calculations agree well with the experimental data for small Ag contents, and far IPDs.

Nevertheless, it becomes obvious that the Maxwell model overestimates the experimental data for elevated Ag contents, and near IPDs. The tremendous number of interfaces in samples with small IPD decreases the expected thermal conductivity. The Hasselman-Johnson model (HJ), which adds a finite interfacial thermal conductance to the Maxwell model is in better accordance with the experimental values.<sup>[52]</sup> Here, an interfacial thermal conductance of  $300 \text{ MW m}^{-2} \text{ K}^{-1}$  was used to fit the data. This value is in the same region as the values for a PbS oleate system with a comparable structure to our PNCs. The interfacial thermal conductance of the PbS oleate system is in the range between 60 to  $310 \text{ MW m}^{-2} \text{ K}^{-1}$ .<sup>[9]</sup>

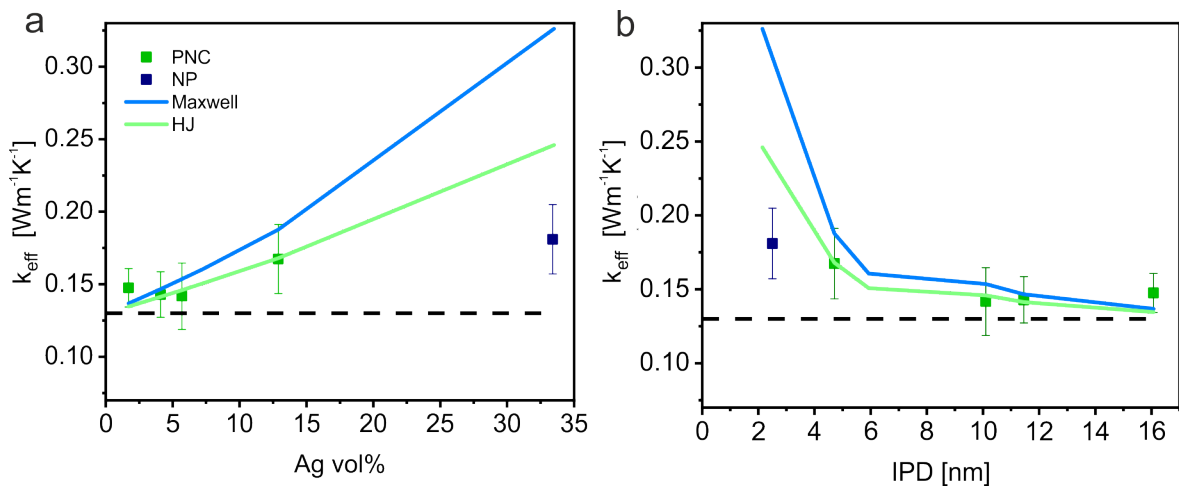


Figure 7.17: Thermal conductivity values of different PNC samples. The values were determined by PA measurements. The effective thermal conductivity is plotted against the silver volume ratio (a) and the interparticle distance (IPD) (b), respectively. The lines represent calculated values from two different effective medium models. The blue lines represent the Maxwell model, which describes a two-phase system consisting of a matrix and spherical inclusions. The Hasselman-Johnson (HJ) model is depicted by the green lines and an adaption of the Maxwell model. Here, an interfacial thermal conductance between matrix and inclusion is added. The dashed line is the thermal conductivity of the PS matrix.

In summary, our data proves the impact of interfaces on the thermal conductivity of composite materials. It is demonstrated by the necessity of a finite interfacial thermal conductance when describing the data with a mixing model. Nevertheless, the Maxwell model sufficiently describes the data points with low silver content. Hence, the influence of the interfaces decreases with a decreasing number of silver inclusions. Our data suggest the existence of a transition point, where the number

of interfaces falls under a value beneath that the interfaces have no more significant influence. However, it is difficult to exactly determine this point, due to the already-mentioned considerable deviations.

## References

- [1] D. K. Avasthi, Y. K. Mishra, D. Kabiraj, N. P. Lalla, J. C. Pivin, *Nanotechnology* **2007**, *18*, 125604.
- [2] L. Balan, D. Burget, *European Polymer Journal* **2006**, *42*, 3180–3189.
- [3] V. Torrisi, F. Ruffino, *Coatings* **2015**, *5*, 378–424.
- [4] X. Y. Huang, P. K. Jiang, L. Y. Xie, *Applied Physics Letters* **2009**, *95*, 242901.
- [5] X. Li, W. Park, Y. P. Chen, X. Ruan, *Journal of Heat Transfer* **2016**, *139*, 022401.
- [6] C. A. Grabowski, H. Koerner, J. S. Meth, A. Dang, C. M. Hui, K. Matyjaszewski, M. R. Bockstaller, M. F. Durstock, R. A. Vaia, *ACS Appl. Mater. Interfaces* **2014**, *6*, 21500–9.
- [7] Y. Cang, A. N. Reuss, J. Lee, J. Yan, J. Zhang, E. Alonso-Redondo, R. Sainidou, P. Rembert, K. Matyjaszewski, M. R. Bockstaller, G. Fytas, *Macromolecules* **2017**, *50*, 8658–8669.
- [8] W. L. Ong, S. Majumdar, J. A. Malen, A. J. H. McGaughey, *Journal of Physical Chemistry C* **2014**, *118*, 7288–7295.
- [9] W. L. Ong, S. M. Rupich, D. V. Talapin, A. J. McGaughey, J. A. Malen, *Nat. Mater.* **2013**, *12*, 410–5.
- [10] S. Li, M. Meng Lin, M. S. Toprak, D. K. Kim, M. Muhammed, *Nano Rev.* **2010**, *1*, 5214.
- [11] X. Bouju, E. Duguet, F. Gauffre, C. R. Henry, M. L. Kahn, P. Melinon, S. Ravaine, *Adv. Mater.* **2018**, *30*, 1706558.
- [12] P. Akcora, H. Liu, S. K. Kumar, J. Moll, Y. Li, B. C. Benicewicz, L. S. Schadler, D. Acehan, A. Z. Panagiotopoulos, V. Pryamitsyn, V. Ganesan, J. Ilavsky, P. Thiagarajan, R. H. Colby, J. F. Douglas, *Nat. Mater.* **2009**, *8*, 354–9.
- [13] S. Fischer, A. Salcher, A. Kornowski, H. Weller, S. Forster, *Angew. Chem. Int. Ed.* **2011**, *50*, 7811–4.
- [14] D. Dukes, Y. Li, S. Lewis, B. Benicewicz, L. Schadler, S. K. Kumar, *Macromolecules* **2010**, *43*, 1564–1570.
- [15] S. Ehlert, C. Stegelmeier, D. Pirner, S. Forster, *Macromolecules* **2015**, *48*, 5323–5327.
- [16] P. Hummel, A. Lerch, S. Goller, M. Karg, M. Retsch, *Polymers* **2017**, *9*, 659.
- [17] E. Alonso-Redondo, M. Schmitt, Z. Urbach, C. M. Hui, R. Sainidou, P. Rembert, K. Matyjaszewski, M. R. Bockstaller, G. Fytas, *Nat. Commun.* **2015**, *6*, 8309.

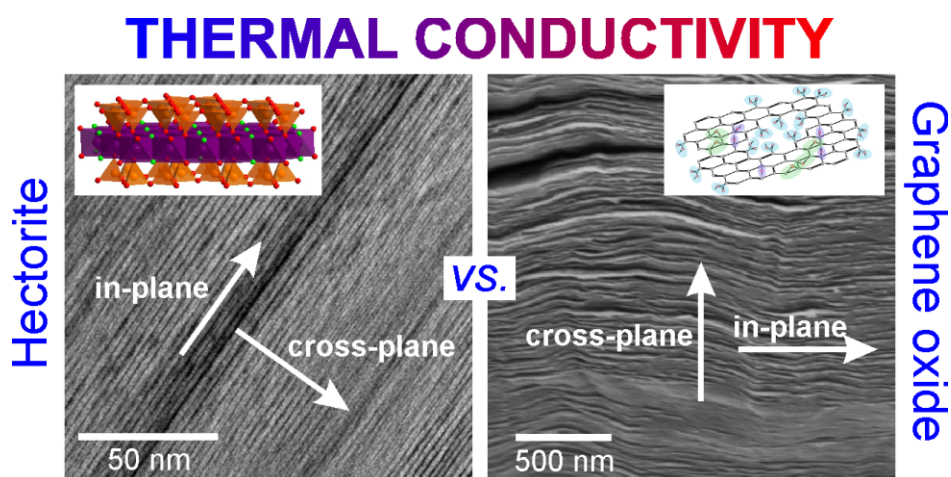
- [18] S. Ehlert, S. M. Taheri, D. Pirner, M. Drechsler, H. W. Schmidt, S. Forster, *ACS Nano* **2014**, *8*, 6114–22.
- [19] S. A. Kim, R. Mangal, L. A. Archer, *Macromolecules* **2015**, *48*, 6280–6293.
- [20] W. Lewandowski, M. Fruhnert, J. Mieczkowski, C. Rockstuhl, E. Gorecka, *Nat. Commun.* **2015**, *6*, 6590.
- [21] K. Volk, J. P. S. Fitzgerald, P. Ruckdeschel, M. Retsch, T. A. F. König, M. Karg, *Advanced Optical Materials* **2017**, *5*, 1600971.
- [22] K. Volk, J. P. Fitzgerald, M. Retsch, M. Karg, *Adv. Mater.* **2015**, *27*, 7332–7.
- [23] H. H. Richardson, M. T. Carlson, P. J. Tandler, P. Hernandez, A. O. Govorov, *Nano Letters* **2009**, *9*, 1139–1146.
- [24] O. Neumann, A. S. Urban, J. Day, S. Lal, P. Nordlander, N. J. Halas, *ACS Nano* **2013**, *7*, 42–9.
- [25] G. Baffou, R. Quidant, *Laser Photonics Rev.* **2013**, *7*, 171–187.
- [26] T. C. Merkel, B. D. Freeman, R. J. Spontak, Z. He, I. Pinnau, P. Meakin, A. J. Hill, *Science* **2002**, *296*, 519–22.
- [27] C. R. Bilchak, E. Buenning, M. Asai, K. Zhang, C. J. Duming, S. K. Kumar, Y. C. Huang, B. C. Benicewicz, D. W. Gidley, S. W. Cheng, A. P. Sokolov, M. Minelli, F. Doghieri, *Macromolecules* **2017**, *50*, 7111–7120.
- [28] M. Yamamoto, Y. Kashiwagi, M. Nakamoto, *Langmuir* **2006**, *22*, 8581–6.
- [29] See Supplemental Material at <http://link.aps.org/supplemental/10.1103/PhysRevMaterials.2.123605> for a schematic of the annealing procedure, details of the effective medium analysis, further investigations of the glass transition temperature of the samples, SAXS characterizations of the samples, the annealing effect on the samples' morphology, COMSOL simulation results of the particles' collective heating effect on the laser spot temperature, and a video on the electron tomography tilt series.
- [30] J. R. Kremer, D. N. Mastrorarde, J. R. McIntosh, *J. Struct. Biol.* **1996**, *116*, 71–6.
- [31] J. Schindelin, I. Arganda-Carreras, E. Frise, V. Kaynig, M. Longair, T. Pietzsch, S. Preibisch, C. Rueden, S. Saalfeld, B. Schmid, J. Y. Tinevez, D. J. White, V. Hartenstein, K. Eliceiri, P. Tomancak, A. Cardona, *Nat. Methods* **2012**, *9*, 676–82.
- [32] I. Bressler, J. Kohlbrecher, A. F. Thunemann, *J. Appl. Crystallogr.* **2015**, *48*, 1587–1598.
- [33] E. Schechtel, Y. Yan, X. Xu, Y. Cang, W. Tremel, Z. Wang, B. Li, G. Fytas, *Journal of Physical Chemistry C* **2017**, *121*, 25568–25575.

- [34] S. Cheng, V. Bocharova, A. Belianinov, S. Xiong, A. Kisliuk, S. Somnath, A. P. Holt, O. S. Ovchinnikova, S. Jesse, H. Martin, T. Etampawala, M. Dadmun, A. P. Sokolov, *Nano Lett.* **2016**, *16*, 3630–7.
- [35] S. Mirigian, K. S. Schweizer, *J. Chem. Phys.* **2014**, *140*, 194507.
- [36] R. Zhang, B. Lee, C. M. Stafford, J. F. Douglas, A. V. Dobrynin, M. R. Bockstaller, A. Karim, *Proc. Natl. Acad. Sci. USA* **2017**, *114*, 2462–2467.
- [37] G. Baffou, R. Quidant, C. Girard, *Physical Review B* **2010**, *82*, 165424.
- [38] D. Zhao, D. Schneider, G. Fytas, S. K. Kumar, *ACS Nano* **2014**, *8*, 8163–73.
- [39] A. B. Wood, *A textbook of sound; being an account of the physics of vibrations with special reference to recent theoretical and technical developments*, The Macmillan company, New York, **1930**.
- [40] D. Torrent, J. Sánchez-Dehesa, *New J. Phys.* **2007**, *9*, 323.
- [41] T. G. Fox, P. J. Flory, *J. Polym. Sci.* **1954**, *14*, 315–319.
- [42] J. C. Maxwell, *A Treatise on Electricity and Magnetism*, Dover Publications, New York, **1954**.
- [43] W. N. dos Santos, J. A. de Sousa, R. Gregorio, *Polymer Testing* **2013**, *32*, 987–994.
- [44] A. D. McLachlan, F. P. Meyer, *Applied Optics* **1987**, *26*, 1728–1731.
- [45] F. Aousgi, S. Haddad, H. Aroui, *International Journal of Spectroscopy* **2011**, *2011*, 7.
- [46] B. K. Mukerji, A. K. Bhattacharji, N. R. Dhar, *J. Phys. Chem.* **1927**, *32*, 1834–1840.
- [47] A. K. Bhattacharya, N. R. Dhar, *J. Phys. Chem.* **1930**, *35*, 653–655.
- [48] B. A. Cola, J. Xu, C. R. Cheng, X. F. Xu, T. S. Fisher, H. P. Hu, *Journal of Applied Physics* **2007**, *101*, 054313.
- [49] J. H. Taphouse, T. L. Bougher, V. Singh, P. P. S. S. Abadi, S. Graham, B. A. Cola, *Nanotechnology* **2013**, *24*, 105401.
- [50] V. Singh, T. L. Bougher, A. Weathers, Y. Cai, K. Bi, M. T. Pettes, S. A. McMenamin, W. Lv, D. P. Resler, T. R. Gattuso, D. H. Altman, K. H. Sandhage, L. Shi, A. Henry, B. A. Cola, *Nat Nanotechnol* **2014**, *9*, 384–90.
- [51] J. K. Carson, S. J. Lovatt, D. J. Tanner, A. C. Cleland, *International Journal of Heat and Mass Transfer* **2005**, *48*, 2150–2158.
- [52] D. P. H. Hasselman, L. F. Johnson, *Journal of Composite Materials* **1987**, *21*, 508–515.



## 8 Anisotropic thermal transport in spray coated single-phase 2D materials: synthetic clay vs. graphene oxide

by Alexandra Philipp, Patrick Hummel, Theresa Schilling, Patrick Feicht, Sabine Rosenfeldt, Michael Ertl, Marius Schöttle, Anna M. Lechner, Zhen Xu, Chao Gao, Josef Breu and Markus Retsch



This work was published in *ACS Appl Mater Interfaces*, **2020**, *12*, 18785-18791.

**Abstract:** Directional control on material properties such as mechanical moduli or thermal conductivity are paramount for the development of next generation nanostructured devices. Two-dimensional materials are particularly interesting in this context owing to their inherent structural anisotropy. Here, we compare graphene oxide (GO) and the synthetic clay sodium fluorohectorite (Hec) with respect to their thermal transport properties. The unique sheet structure of both allows preparing highly ordered Bragg stacks of these pure materials. The thermal conductivity parallel to the platelets strongly exceeds the thermal conductivity perpendicular to them. We find a significant difference in the performance between GO and synthetic clay. Our analysis of the textured structure, size of the platelets and chemical composition shows that synthetic clay is a superior two-dimensional component compared to GO. Consequently, synthetic clay is a promising material for thermal management applications in electronic devices, where electrically insulating materials are prerequisite.

## 8.1 Introduction

Modern electronics crucially depend on materials and structures that are capable of dissipating their ever-increasing thermal energy density. Materials with a high thermal conductivity manage to divert heat away from hot spots efficiently. At the same time, the thermal management in the entire device needs to be considered, where areas of high and low-temperature tolerance may be located in close vicinity. Consequently, materials that are capable of directing the flow of heat are required. Two-dimensional (2D) materials with an anisotropic thermal conductivity match this requirement.<sup>[1]</sup> Well-known representatives of such materials are graphite<sup>[2]</sup> and graphene<sup>[3]</sup>. Both exhibit a high in-plane thermal conductivity, while the cross-plane thermal conductivity is much lower. However, they are both also electrically conductive and consequently not suitable in most electronic applications. To prevent shortcuts the use of nonconductive materials is mandatory. This demand is represented in the field of thermal interface materials.<sup>[4,5]</sup> The right selection of matrix and filler, as well as the processing and structure formation are essential for achieving an optimum performance.<sup>[6,7]</sup>

Two materials have been widely used to prepare electrically nonconductive composites with anisotropic thermal conductivity, namely graphene oxide (GO) and the graphene analog hexagonal boron nitride (hBN). Strong oxidation of graphite allows for the water processability of GO. However, at the expense of the extremely high in-plane thermal conductivity compared to graphite/graphene. The degree of oxidation relates to the in-plane thermal conductivity.<sup>[8]</sup> In most cases GO is reduced (rGO) to restore the high in-plane thermal conductivity partially. Concomitantly, the electrical conductivity increases.<sup>[9–12]</sup> Consequently, the anisotropy ratio in GO-based materials depends on the oxidation state and can reach values of 19 for GO<sup>[8]</sup> and up to 675 for rGO<sup>[9]</sup>. An additional drawback of this reduction step is the necessity to apply either reducing chemicals (such as hydrazine) or high thermal temperatures, which both needed to be tolerated by the entire devices or composite.

The structure and properties of hBN are comparable to graphite/graphene. The most significant difference exists in the electrical conductivity. In comparison to graphene, hBN is not electrically conductive. The thermal transport properties, however, are comparable. Meaning a high in-plane thermal transport and, therefore, a high anisotropic thermal conductivity. A fundamental study of bulk single crystalline hBN demonstrated a promising anisotropy ratio of 87.5.<sup>[13]</sup> However, the sample was a 1-mm-sized flake, and it is, yet, not possible to produce large-area samples of single-crystalline hBN. Nevertheless, hBN can be mixed with polymers to achieve composite materials. In contrast to GO the hydrophobic hBN

is still challenging to fully exfoliate, especially in water. A simple sonication assisted hydrolyzation process in water leads only to a mixture of monolayers and multilayers.<sup>[14]</sup> Therefore, studies about the anisotropic thermal conductivity of hBN/polymer composites lack structural control and cannot reach the value of the single crystal.<sup>[15–19]</sup> A maximum ratio up to 39 could be realized by stretching the composite, which improves the alignment and therefore demonstrates the difficulty in controlling the composite structure during processing.<sup>[18]</sup>

Synthetic clays are less known materials in the context of thermal interface materials. Nevertheless, this material class offers a range of advantages particularly regarding the structural control of the assembled composite structure. Due to superior control over the aspect ratio and the delamination process, highly ordered composites with outstanding mechanical,<sup>[20–22]</sup> gas barrier<sup>[23,24]</sup>, and fire resistance<sup>[21,22]</sup> properties have already been realized. Additionally, the high phase purity of Hec leads to optically clear and transparent films, which is relevant for optical applications. Furthermore, ultralow cross-plane thermal conductivity was demonstrated in organoclays<sup>[25]</sup> and hybrid Bragg stacks<sup>[26]</sup>. Although this hints towards the high potential of this material class for high anisotropic thermal conductivity, little is known about the direction-dependent heat spreading in the pure filler components.

Our contribution aims to close this knowledge gap. We focus on pure, single-phase components to elaborate the fundamental filler properties without introducing additional complications originating from filler/matrix interactions. Our study bases on a synthetic clay sodium fluorohectorite of different platelet diameter. For a better classification of this unnoticed material in the context of anisotropic thermal conductivity, we compare our results to two types of GO samples stemming from different sources.

## 8.2 Results and Discussion

Our investigation bases on four samples: synthetic clay sodium fluorohectorite (Hec,  $[\text{Na}_{0.5}]^{\text{inter}}[\text{Mg}_{2.5}\text{Li}_{0.5}]^{\text{oct}}[\text{Si}_4]^{\text{tet}}\text{O}_{10}\text{F}_2$ ) in its native form termed Hec-L, consisting of large platelets (tens of  $\mu\text{m}$  in lateral size) and Hec-S, consisting of small platelets (sub- $\mu\text{m}$ ) received after sonication of Hec-L. We compare the Hec samples to GO, which was synthesized following a modified Hummers/Offeman procedure<sup>[27]</sup> termed GO-syn, and a commercially available GO, termed GO-com. In all samples, we focus on the contribution of the platelet dimensions, platelet defect concentration and chemical composition on the thermal transport anisotropy. All materials were processed by spray coating of a dilute aqueous dispersion (0.5 wt%) onto a substrate (polyethylene terephthalate (PET) film or glass). Thereby, the Hec and GO sheets

align parallel to the substrate introducing a macroscopic orientation to the individual nanosheets. After drying for 5 h at 100 °C, free-standing samples were obtained by peeling off the films from PET. These films were used to determine the in-plane thermal conductivity by lock-in thermography. The cross-plane thermal conductivity was measured using the photoacoustic method with thin films immobilized on a glass substrate. The obtained thermal conductivity values are summarized in Figure 8.1a. We found comparable in-plane and cross-plane thermal conductivities for Hec-L (in-plane:  $5.7 \pm 0.1 \text{ Wm}^{-1}\text{K}^{-1}$ , cross-plane:  $0.21 \pm 0.03 \text{ Wm}^{-1}\text{K}^{-1}$ ) and for Hec-S (in-plane:  $5.6 \pm 0.2 \text{ Wm}^{-1}\text{K}^{-1}$ , cross-plane:  $0.18 \pm 0.02 \text{ Wm}^{-1}\text{K}^{-1}$ ). Compared to literature values of related structures, the in-plane thermal transport of our pure Hec samples is exceptionally high. Muscovite and biotite single crystals show in-plane thermal conductivities of  $3.89 \text{ Wm}^{-1}\text{K}^{-1}$  and  $3.14 \text{ Wm}^{-1}\text{K}^{-1}$ , respectively.<sup>[28]</sup> The thermal conductivity of a montmorillonite sample, which was prepared from a suspension of delaminated platelets showed an in-plane conductivity of only  $1.92 \text{ Wm}^{-1}\text{K}^{-1}$ <sup>[29]</sup>. The high in-plane thermal conductivity of pure Hec is very promising in the context of heat spreading, particularly since this high value is obtained without any further processing of the spray-coated film. By contrast the cross-plane thermal conductivity of muscovite and biotite are  $0.62 \text{ Wm}^{-1}\text{K}^{-1}$  and  $0.52 \text{ Wm}^{-1}\text{K}^{-1}$ , respectively,<sup>[28]</sup> and therefore more than twice as high as in our synthetic Hec samples. The montmorillonite sample, by contrast, has a cross-plane thermal conductivity of  $0.2 \text{ Wm}^{-1}\text{K}^{-1}$ <sup>[29]</sup>, which is comparable to our samples.

The in-plane and cross-plane thermal conductivities of the as-prepared GO samples are both lower compared to the clay samples. The in-plane values are  $1.7 \pm 0.1 \text{ Wm}^{-1}\text{K}^{-1}$  for GO-syn and  $1.0 \pm 0.1 \text{ Wm}^{-1}\text{K}^{-1}$  for GO-com, while the cross-plane values are  $0.12 \pm 0.01 \text{ Wm}^{-1}\text{K}^{-1}$  and  $0.13 \pm 0.01 \text{ Wm}^{-1}\text{K}^{-1}$ , respectively. The values of the cross-plane thermal conductivity are comparable to reports in literature of  $0.18 \text{ Wm}^{-1}\text{K}^{-1}$ <sup>[9]</sup> and  $0.15 \text{ Wm}^{-1}\text{K}^{-1}$ <sup>[8]</sup>. The in-plane thermal conductivities show a much higher degree of variability. Renteria et al. reported a value of  $2.94 \text{ Wm}^{-1}\text{K}^{-1}$ <sup>[9]</sup>, which is almost twice as high as the value for GO-syn. Meng et al. measured a value of  $1.6 \text{ Wm}^{-1}\text{K}^{-1}$ <sup>[8]</sup>, which is in good agreement with our value for GO-syn. The variation of the GO results indicates that the in-plane thermal conductivity is strongly sensitive to the exact synthesis and preparation of the GO samples. This result is in line with reported large spreads of in-plane moduli ranging from 170 GPa to 530 GPa<sup>[27]</sup>, which was attributed to holes formed in the GO sheets due to overoxidation as proposed by Hofmann et al.<sup>[30]</sup> This variation is also visible in the specific heat capacity (Figure 8.1b). Both Hec samples have comparable heat capacity, whereas GO-com has a higher heat capacity than GO-syn.

The Hec films exhibit a two - threefold higher anisotropy ratio ( $\kappa_{in-plane} / \kappa_{cross-plane}$ )

of thermal conductivity compared to the GO samples (grey numbers in Figure 8.1a). The anisotropy ratio of the GO-syn sample of 14 is in good agreement with other studies<sup>[9]</sup>, which reported a ratio of 16, while the anisotropy of GO-com (8) is even lower. The anisotropy values of the synthetic Hec ( $\sim 30$ ) exceed the anisotropy ratios of natural clays, like boom clay<sup>[31]</sup> ( $\sim 1.7$ ). Even the literature values of well-oriented samples like muscovite (6.3)<sup>[28]</sup>, biotite (6.0)<sup>[28]</sup>, and montmorillonite (9.6)<sup>[29]</sup> hardly compare to the anisotropy in our synthetic structure. The superior anisotropy underlines the very high textured orientation of our structure.

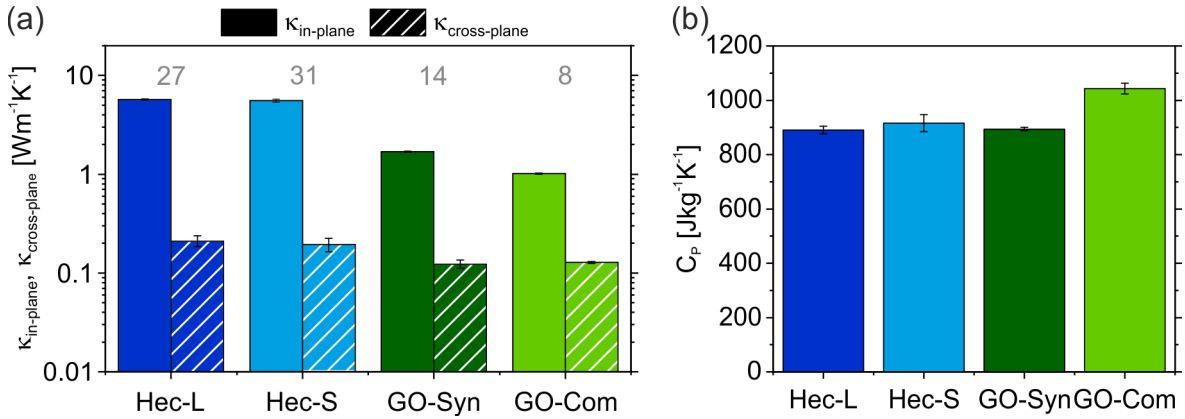


Figure 8.1: Thermal properties: (a) In-plane ( $\kappa_{in-plane}$ ) and cross-plane ( $\kappa_{cross-plane}$ ) thermal conductivity. The numbers in the graph represent the anisotropy ratio of the thermal conductivity ( $\kappa_{in-plane}/\kappa_{cross-plane}$ ). (b) Specific heat capacity ( $C_p$ ).

We next focus on the structure and composition of the samples under investigation to work out any potential influence on the thermal conductivity. Hec belongs to the trioctahedral 2:1 smectite family and shows a sandwich-like structure comprising two tetrahedral and one octahedral layer (Figure 8.2a) with the nominal composition of  $[Na_{0.5}]^{inter}[Mg_{2.5}Li_{0.5}]^{oct}[Si_4]^{tet}O_{10}F_2$ . The thickness of an individual Hec platelet is  $\approx 10$  Å (Figure 8.2b). The synthetic Hec applied here, has been shown to delaminate into individual single layers by repulsive osmotic swelling when immersed in deionized water.<sup>[32]</sup> For well-controlled delamination, a uniform intracrystalline reactivity is prerequisite, which comes along with phase purity and a homogeneous charge density. For synthetic Hec, this is achieved by a melt synthesis followed by long-term annealing. The delamination was studied by small-angle X-ray scattering (SAXS). The high orientational lamellar order in liquid crystals leads typically to (a) anisotropic 2D scattering patterns and (b) a rational series of  $00l$ -reflections due to the defined interlayer spacing  $d$  at  $d = 2\pi/q$ . Further, in that case the swelling behavior of 2D lamellae with volume fraction  $\phi$  and thickness  $t$  is expected to be  $d = t/\phi$ .<sup>[33]</sup> The homogeneous intracrystalline reactivity assures a rational  $00l$ -series with adjacent Hec nanosheets being separated in suspension to  $53 \pm 6$  nm (3 wt%) and  $38 \pm 4$  nm (5 wt%) for Hec-L and Hec-S, re-

spectively (Figure 8.2c). Due to the hindered polar rotation of Hec nanosheets in suspension, these Hec suspensions represent nematic phases. The observable rational series up to six higher-order reflections emphasize the superior positional order of adjacent individual nanosheets. The high positional order is further proved by an anisotropic 2D scattering pattern (Figure 8.4). Spray coating these nematic phases of dilute Hec suspensions led to homogeneous, one-dimensional (1D) crystalline (smectic films) comprised of largely overlapping individual sheets forming quasi-single crystalline band-like films.<sup>[26]</sup> The exceptional periodic homogeneity can be seen from the cross-sectional transmission electron microscopy (TEM) image (Figure 8.2b). The white arrows highlight the directions of the in-plane and cross-plane thermal conductivity measurements, respectively. X-ray diffraction (XRD) patterns (Figure 8.2d) of both samples show a rational  $00l$ -series up to the seventh order with sharp and intense basal reflections after spray-coating. The quality of the 1D crystalline order is further confirmed by a low coefficient of variation of the  $00l$ -series (Table 8.1) and a small full width at half maximum. Furthermore, both Hec-L and Hec-S samples have a comparable basal spacing of  $\approx 10 \text{ \AA}$  in the dry state, which represents the periodicity along the stacking direction. In Figure 8.5 the platelet area, measured by scanning electron microscopy (SEM) followed by evaluating the area with ImageJ, are compared for samples Hec-L and Hec-S. Sample Hec-L (Figure 8.6), which was used as received from the synthesis, consists of large platelets with areas up to  $800 \mu\text{m}^2$ . We fabricated Hec-S from Hec-L by ultrasound treatment, which reduced the platelet area by more than three orders of magnitude ( $< 0.4 \mu\text{m}^2$ , Figure 8.5 and Figure 8.6). Due to the ultrathin platelet thickness of 1 nm, both samples still have a high aspect ratio (20000 and 300, respectively). The sonication procedure for platelet-size reduction leaves the structure and chemical composition of Hec unaltered. Infrared (IR) spectroscopy (Figure 8.2e) and X-ray photoelectron spectroscopy (XPS) spectra (Figure 8.8) of both samples were measured to demonstrate this. In case of IR spectroscopy four main signals are visible which correspond to (i) OH stretching vibrations of water or cation-OH stretching vibrations at platelet edges, (ii) OH-bending vibrations of water, (iii) stretching vibration of SiO-groups in tetrahedral sheets, and (iv) bending vibration of SiO-groups and stretching vibration of MgF-groups in octahedral sheets.<sup>[34–36]</sup> Hec-L and Hec-S show good quantitative agreement of all these characteristic absorption peaks. Similarly, fitting of the element-specific bands in the XPS measurement results in comparable atomic ratios. Overall, sonication of Hec-L only reduced the size of the Hec platelets and did not affect the self-assembly, i.e. the basal spacing and order, as well as the chemical composition. Counterintuitively, we found that small Hec sheets are still great in-plane conductors. This can be explained by an in-plane mean free path that is still orders of magnitude smaller than the average platelet diameter. Consequently,

boundary effects become negligible, which would typically lead to reduced thermal conductivity.<sup>[26]</sup>

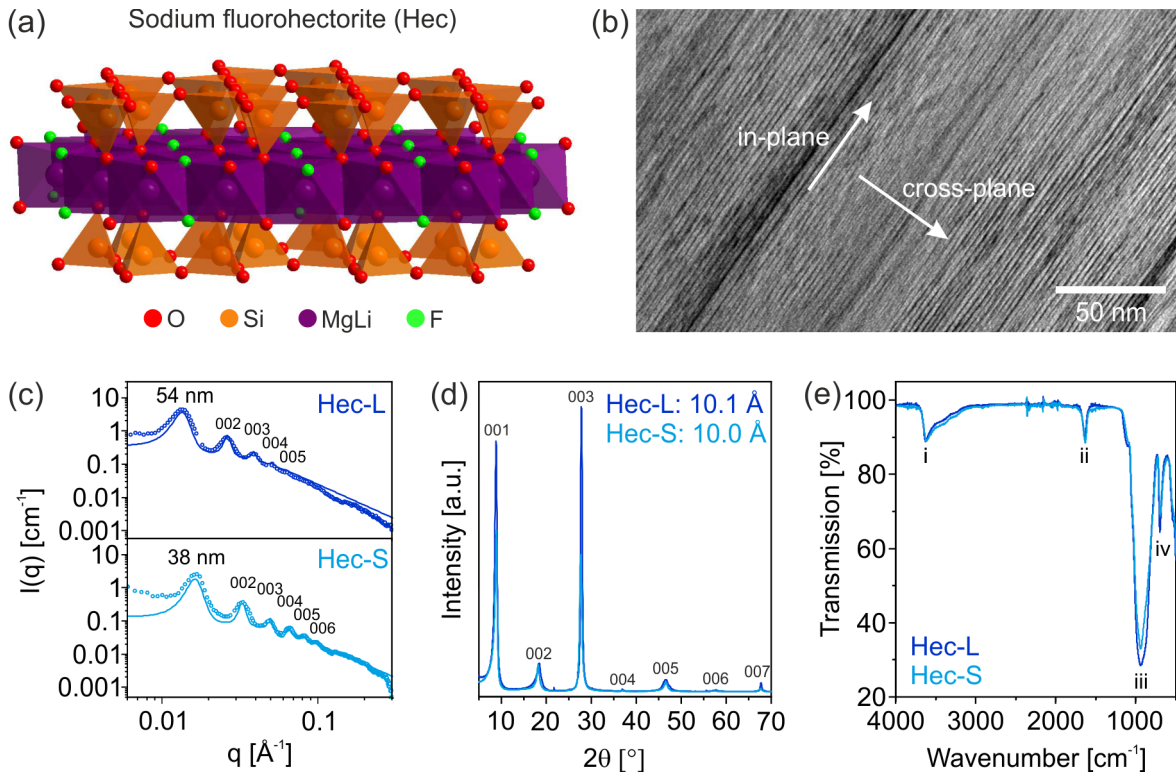


Figure 8.2: (a) Structure of a sodium fluorohectorite (Hec) platelet. Sodium counter ions are located between two Hec platelets. (b) A cross-sectional TEM image of an aligned smectic Hec film. White arrows illustrate the in-plane and cross-plane direction. (c) SAXS results of aqueous Hec suspensions showing a rational series of  $00l$  reflections. (d) XRD patterns of the free-standing Hec films showing intense  $00l$ -reflections. Both samples have a basal spacing around  $10 \text{ \AA}$ . (e) IR spectra prove the same chemical composition of both samples.

For GO, it is not possible to provide a chemical formula. Its chemical structure is based on graphene, but GO is ill-defined, and the number of defects, i.e. vacancies/holes in the 2D structure and functional groups, strongly depend on the synthesis route.<sup>[27]</sup> Figure 8.3a shows an exemplary structure of GO having various functional defects (epoxide, hydroxyl, and carboxylic groups) as well as a hole. SAXS was used to further investigate the graphene oxide dispersions of about 3.5 wt%. Diluted graphene oxide dispersions are expected to form nematic liquid crystalline phase in water via ordering of the sheets.<sup>[37]</sup> The scattering intensity  $I(q)$  of the two GO suspensions decrease with the scattering vector  $q$ , following a  $q^{-2}$  power law (Figure 8.3c). This scaling law is typically obtained for platelet-shaped scattering objects and proves the 2D morphology of the dispersed graphene oxide layers. The graphene oxide dispersions exhibit an anisotropic 2D SAXS pattern (Figure 8.4), indicating a nematic orientation. In contrast, Hec in a similar concentration shows

additionally a series of  $00l$  reflection.<sup>[33]</sup> The absence of these reflections in case of GO is mainly attributed to a much more pronounced dislocation of the lamellar order by slipping or tilting of the individual GO layers. This strongly hints to a more heterogeneous charge distribution of the graphene oxide sheets. Similar to the Hec samples, spray coating of dilute GO dispersions led to aligned stacks of overlapping individual sheets, as can be seen from the SEM image (Figure 8.3b). The white arrows highlight the directions of the in-plane and cross-plane thermal conductivity measurements, respectively. The XRD patterns in Figure 8.3d show one weak, a rather broad peak at  $6 \text{ \AA}$ <sup>[38]</sup> and no higher-order peaks as typical for randomly interstratified structures with varying layer separation. Thus, the stacking of the spray-coated GO sheets is less well-defined compared to the Hec platelets. Furthermore, the GO layers ( $\sim 6 \text{ \AA}$ ) are thinner than the Hec platelets ( $\sim 10 \text{ \AA}$ ). The analysis of the sheet area (Figure 8.5) revealed that GO-syn (Figure 8.7) is much smaller than Hec-L, whereas GO-com (Figure 8.7) is comparable to Hec-L, but very broadly distributed. Both are, however, much larger compared to Hec-S. Additionally, we measured Raman spectra (Figure 8.10) and XPS (Figure 8.3e and Figure 8.9) to analyze the degree of functional defects of the GO samples. The intensity ratios of the D and G band ( $I_D/I_G$ ) of both samples are around 1, which is a measure for a high number of defects within the graphene-based structure. The overview XPS spectra (Figure 8.7) reveal the presence of carbon (C), oxygen (O), and sulfur (S). The latter stems from sulfate groups and is typical for GO made by Hummers/Offeman protocols.<sup>[27]</sup> Integrating over the various C-1s species revealed that the main difference between the GO samples is the ratio of pristine  $sp^2$  vs. oxygenated C atoms. Figure 3e shows the C1s XPS spectra of GO-syn and GO-com. Three main peaks are visible, which are assigned to double-bonded carbon-oxygen (C=O;  $\approx 288.3 \text{ eV}$ ), single-bonded carbon-oxygen (C-O;  $\approx 286.8 \text{ eV}$ ), and  $sp^2$  and  $sp^3$  carbon (C=C/C-C;  $\approx 284.7 \text{ eV}$ ).<sup>[9]</sup> GO-com has a higher amount of oxygen-containing functional groups such as hydroxyl, epoxide, carbonyl, and carboxyl groups compared to GO-syn.

Since we found a two times lower in-plane thermal diffusivity for GO-com in comparison to GO-syn, we conclude that the difference in the degree of oxidation has a high impact on the in-plane thermal transport. These findings also support the results of Meng et al.<sup>[8]</sup> They investigated GO samples with different degrees of oxidation. In agreement with our findings, the sample with a higher degree of oxidation showed a lower thermal conductivity. The reason is the decrease in  $sp^2$  cluster size with an increasing amount of oxygen in the structure and holes in the 2D structure produced by overoxidation.<sup>[30]</sup> Consequently, phonon scattering is enhanced by the likewise increased  $sp^2/sp^3$  boundaries.<sup>[8]</sup>

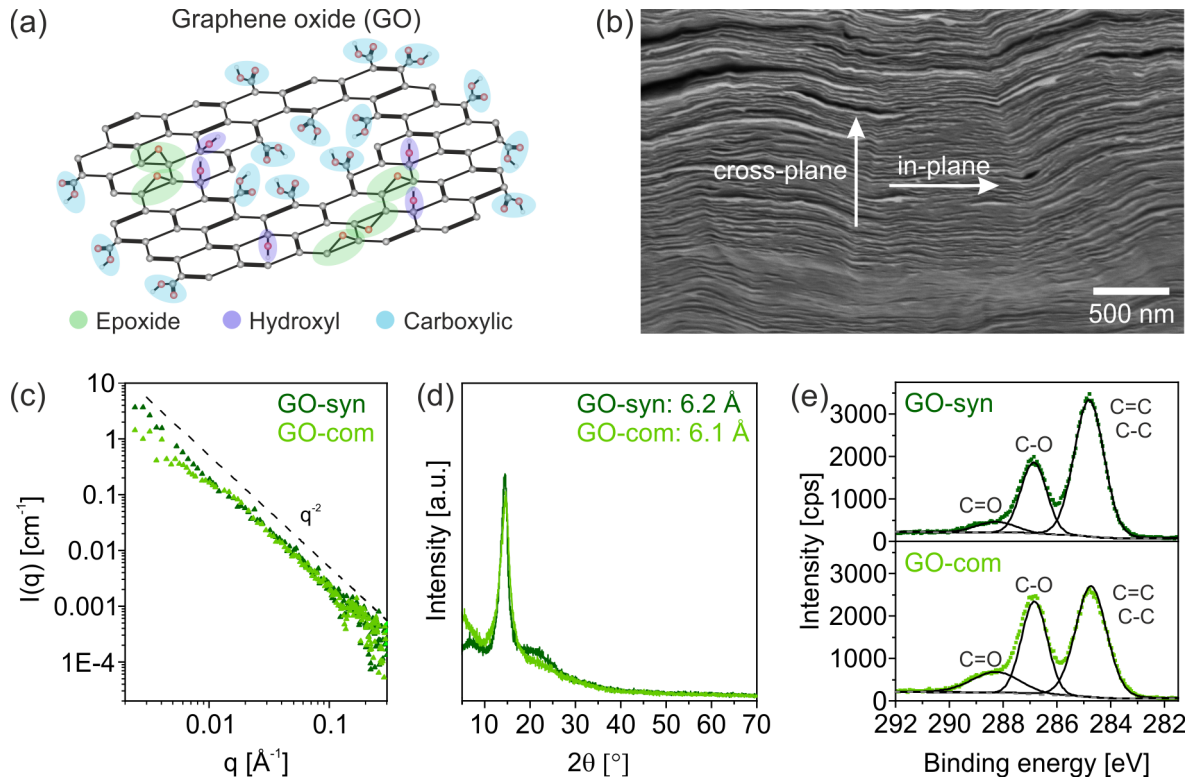


Figure 8.3: (a) Exemplary structure of graphene oxide (GO). (b) SEM image of an aligned GO film. White arrows illustrate the in-plane and cross-plane direction. (c) SAXS results of GO suspensions showing a  $q^{-2}$  scaling of the scattering intensity. (d) XRD patterns show no long-range order. Both samples have a spacing of approximately 6 Å. (e) XPS data of the carbon signatures.

### 8.3 Conclusion

In this study, we investigated the anisotropic thermal transport properties of thin films of synthetic clay sodium fluorohectorite (Hec) films and graphene oxide (GO). Whereas these materials are often used in the context of nanocomposite materials, we focused on the pure phase components and their thermal transport properties. The properties of such 2D materials are strongly governed by the chemical composition, vacancy defects in the layer structure, and the platelet size. We, therefore, determined the thermal transport properties of four different samples. All of them were fabricated into (free-standing) thin films via spray coating of diluted dispersions of Hec and GO, respectively. The superior long-range order in Hec films results in a significantly higher anisotropy ratio compared to the GO samples. Quite remarkably, the in-plane thermal conductivity reaches very high values of up to  $5.7 \text{ Wm}^{-1}\text{K}^{-1}$ , which makes Hec an attractive material for heat spreading applications. GO in its oxidized form as received directly after spray coating features in-plane thermal conductivities on the order of only  $1 \text{ Wm}^{-1}\text{K}^{-1}$ . The thermal transport properties are strongly affected by the chemical composition of the GO sam-

ples. In particular, the in-plane thermal conductivity is reduced with an increasing degree of functional groups containing oxygen. The cross-plane thermal conductivity is hardly affected and remains at a low value of  $\sim 0.12 \text{ Wm}^{-1}\text{K}^{-1}$ . Surprisingly, the platelet size does not influence the in-plane thermal conductivity, which can be concluded from comparing Hec-L and Hec-S films. The chemical composition remained unaltered between large and small platelets of Hec. However, even though the platelet diameters were drastically reduced by approximately two orders of magnitude, the superior in-plane heat spreading properties were retained.

Overall, anisotropic heat transport is gaining increased attention in applications of thermal interface materials or heat management in light-emitting diodes or batteries. Our contribution provides a better understanding of the interplay between platelet size and chemical composition on the direction-dependent thermal conductivity. Furthermore, synthetic hectorite is an up-and-coming alternative to the more established GO and hBN heat spreading materials.

## 8.4 Materials and Methods

### 8.4.1 Sample preparation and characterization

The synthetic clay sodium fluorohectorite (Hec,  $[\text{Na}_{0.5}]^{\text{inter}}[\text{Mg}_{2.5}\text{Li}_{0.5}]^{\text{oct}}[\text{Si}_4]^{\text{tet}}\text{O}_{10}\text{F}_2$ ) was delaminated by immersing it into Millipore water (0.5 wt%). For the synthesis of the small Hec platelets (Hec-S), a 0.5 wt% suspension of Hec-L was sonicated in an ice bath with the ultrasonic device UIP 1000hd. GO-syn, based on Hummers/Offeman's method, was synthesized according to an established procedure.<sup>[27]</sup> GO-com was provided by Hangzhou Gaoxi Technology Co. Ltd. (China). The self-supporting films and the thinner films sprayed on a glass substrate were prepared with a fully automatic spray coating system. Every spraying cycle is followed by a drying cycle of 90 s at a temperature of 55 °C. The films were characterized by X-ray diffraction, transmission electron microscopy, scanning electron microscopy, X-ray photoelectron, infrared, and Raman spectroscopy. Additional information about the sample preparation and characterization methods can be found in Section 8.5.1 (Supporting Information).

## 8.4.2 Thermal conductivity measurements

### *In-plane thermal conductivity measurements*

Lock-in thermography measures the temperature spreading within thin, free-standing samples upon thermal excitation by an intensity-modulated, focused laser beam. Measurements are conducted in a vacuum to prevent heat losses due to conduction and convection. The amplitude and phase data are obtained from the temperature oscillations. The slope method for thermally thin films is used to calculate the in-plane thermal diffusivity from the linear profiles of the radial phase and amplitude profiles.<sup>[39]</sup> In combination with the density, determined by helium pycnometry, and the specific heat capacity, determined by differential scanning calorimetry, the in-plane thermal conductivity can be calculated. More details are provided in Section 8.5.2 (Supporting Information).

### *Cross-plane thermal conductivity measurements*

The photoacoustic method exploits the photoacoustic effect to determine the thermal properties of a sample.<sup>[40,41]</sup> The sample is fixed to a gas-tight glass cell, filled with 20 psi helium. A modulated laser beam runs through the cell volume and periodically heats the transducer layer on top of the sample. The induced pressure change on the surface of the sample leads to an acoustic wave propagating into the gas. A microphone, coupled to a lock-in amplifier, detects the phase shift between the acoustic signal and the modulated laser dependent on the frequency. By comparing the data to a multilayer model, describing the temperature distribution in the sample, the total layer resistance of the sample is obtained. Together with the film thickness determined by atomic force microscopy (AFM), the effective thermal conductivity is calculated. Details about the photoacoustic characterization can be found in Section 8.5.2 (Supporting Information).

**Supporting Information:** Detailed information on the material fabrication and characterization, section 8.5.1. Material synthesis, film preparation, SAXS, XRD, TEM, SEM, XPS, RAMAN, IR analysis and instruments used. Detailed information on the thermal conductivity characterization, section 8.5.2. He-pycnometry, DSC, lock-in Thermography and photoacoustic characterization.

**Acknowledgments:** The Volkswagen Foundation funded this project through a Lichtenberg professorship. Additional support was provided by the German Research Foundation through DFG RE3550/2-1. Kai Herrmann is acknowledged for discussions on the PA method.

**Author Contributions:** The manuscript was written through contributions of all authors. All authors have given approval to the final version of the manuscript.

**Notes:** The authors declare no competing financial interests.

## 8.5 Supporting Information

### 8.5.1 Sample preparation and characterization

#### Materials

The synthetic clay sodium fluorohectorite (Hec,  $[\text{Na}_{0.5}]^{\text{inter}}[\text{Mg}_{2.5}\text{Li}_{0.5}]^{\text{oct}}[\text{Si}_4]^{\text{tet}}\text{O}_{10}\text{F}_2$ ) was synthesized with high-purity reagents of  $\text{SiO}_2$ , LiF,  $\text{MgF}_2$ , MgO and NaF in a gastight molybdenum crucible via melt synthesis followed by long-term annealing, according to an already published procedure.<sup>[42]</sup> To improve the charge density of the clay platelets and relating thereto the intracrystalline reactivity, the melt synthesis is followed by long-term annealing at 1045 °C for 6 weeks.<sup>[32]</sup> The material featured a cation exchange capacity of 1.27 mmol  $\text{g}^{-1}$ .<sup>[32,42]</sup> This sample is called Hec-L. For the fabrication of the small Hec platelets (Hec-S), a 0.5 wt% suspension of Hec-L was sonicated for 15 minutes in an ice bath with the ultrasonic device UIP 1000hd (Hielscher Ultrasonic GmbH, Germany), equipped with a ultrasonic horn BS2d22 and a booster B2-1.2, at 20 kHz with a maximal output power of 1000 W. GO-syn, based on Hummers/Offeman's method, was synthesized according to an established procedure.<sup>[27]</sup> GO-com was provided by Hangzhou Gaoxi Technology Co. Ltd. (China).

#### Film preparation

For the delamination, the synthetic Hec was immersed into Millipore water (0.5 wt%). The complete delamination was studied by small-angle X-ray scattering (SAXS).<sup>[33]</sup> The self-supporting films of Hec and GO were prepared by spray coating of 0.5 wt% suspensions of the respective material. The fully automatic spray coating system was equipped with a SATA 4000 LAB HVLP 1.0 mm spray gun (SATA GmbH & Co. KG, Germany). Suspensions were sprayed on a corona-treated PET foil (optimont 501, bleher Folientechnik, Germany). The spraying and nozzle pressure were set constant at values of 2 and 4 bar, respectively. The round per flat fan control was set to 6 with a flow speed of 3 mL  $\text{s}^{-1}$ . The distance between the spraying gun and the substrate was 17 cm. The thickness of the suspension layer applied in one spraying step is about 2  $\mu\text{m}$  which corresponds to about 20 nm dry film thickness. For drying the suspension layer, the sample is stopped under infrared lamps until evaporation of the solvent is complete. After every spraying cycle, a drying cycle of 90 s with a temperature of 55 °C took place. The spraying/drying cycle is repeated until the desired barrier film thickness of 50  $\mu\text{m}$  is obtained. Afterward, the film was dried at 100 °C for 3 days and peeled off from the PET foil for achieving self-supporting films. For characterization by photoacoustic analysis thinner films on the order of a few  $\mu\text{m}$  were spray-coated onto clean 1 mm microscope glass slides.

In total, we prepared four different samples: Hec-L, Hec-S, GO-syn, and GO-com.

### Small-angle X-ray Scattering (SAXS)

All SAXS data were measured using the small-angle X-ray system “Double Ganesha AIR” (SAXSLAB, Denmark). The X-ray source of this laboratory-based system is a rotating anode (copper, MicroMax 007HF, Rigaku Corporation, Japan), providing a micro-focused beam. The data were recorded by a position-sensitive detector (PILATUS 300 K, Dectris). To cover the range of scattering vectors different detector positions were used. The measurements of the suspensions were done in 1 mm glass capillaries (Hilgenberg, code 4007610, Germany) at room temperature. To improve the detection limit of the in-house machine, the suspensions were first concentrated by centrifugation at 10,000 rpm for 1 hour. The data were radially averaged and background corrected. As background, a water-filled capillary was used.

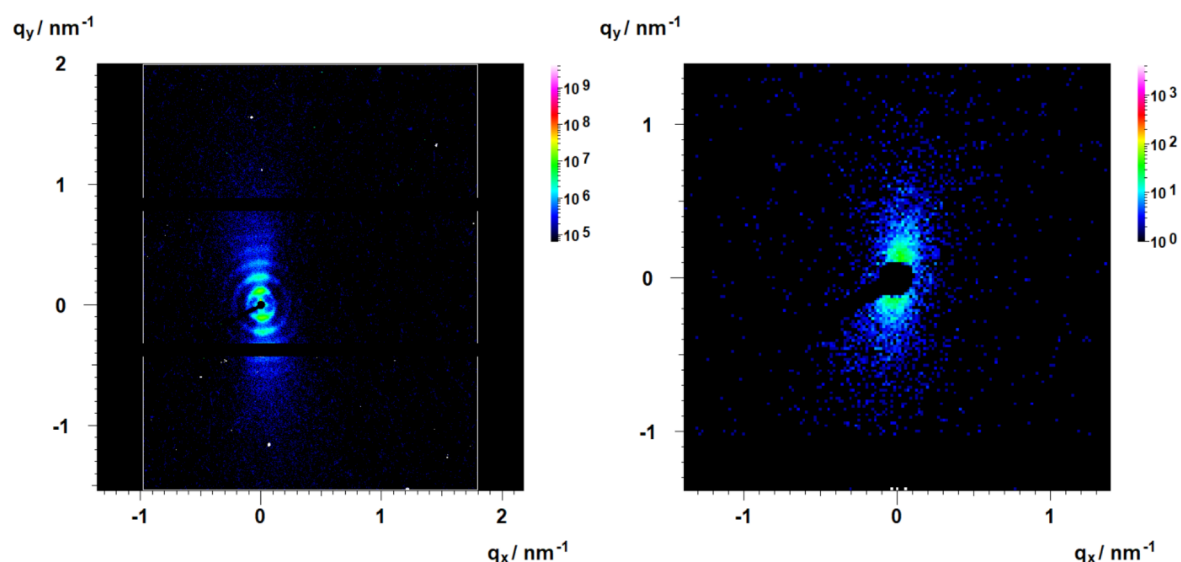


Figure 8.4: 2D SAXS patterns of an aqueous Hec suspension (left) and an aqueous GO suspension (right).

### X-ray diffraction (XRD) analysis

XRD patterns for the films were recorded in Bragg-Brentano-geometry on an Empyrean diffractometer (PANalytical B.V.; the Netherlands) using  $\text{Cu } K_\alpha$  radiation ( $\lambda = 1.54187 \text{ \AA}$ ). The self-supporting films were placed on glass slides (Menzel-Gläser; Thermo Scientific). Before the measurements, samples were dried at  $100 \text{ }^\circ\text{C}$  for one week in a vacuum chamber. As a measure of the quality of the one-dimensional crystallinity of the films, the coefficient of variation (CV) and the full width at half maximum (FWHM) were determined (Table 8.1). Large CV-values ( $\approx 3\%$ ,<sup>[33]</sup>) and large FWHM indicate non-rationality of the diffraction pattern as caused by a random interstratification of different interlayer heights.

Table 8.1: Overview of the structural characterization by XRD

Sample	Description	$d_{XRD}$ [Å]	CV [%]	FWHM [ $^{\circ}2\theta$ ]
Hec-L	Large Hec platelets	10.1	1.6	0.7
Hec-S	Small Hec platelets	10.0	1.1	0.6
GO-syn	Synthetic GO	40:60	-	3.1
GO-com	Commercial GO	31:69	-	3.5

### Transmission electron microscopy (TEM)

TEM images of the samples Hec-L and Hec-S were taken on a JEOL JEM-2200FS (JEOL GmbH, Germany) at an acceleration voltage of 200 kV. Cross-section pictures of the self-supporting films were prepared with a Cryo Ion Slicer IB-09060CIS (JEOL, Germany).

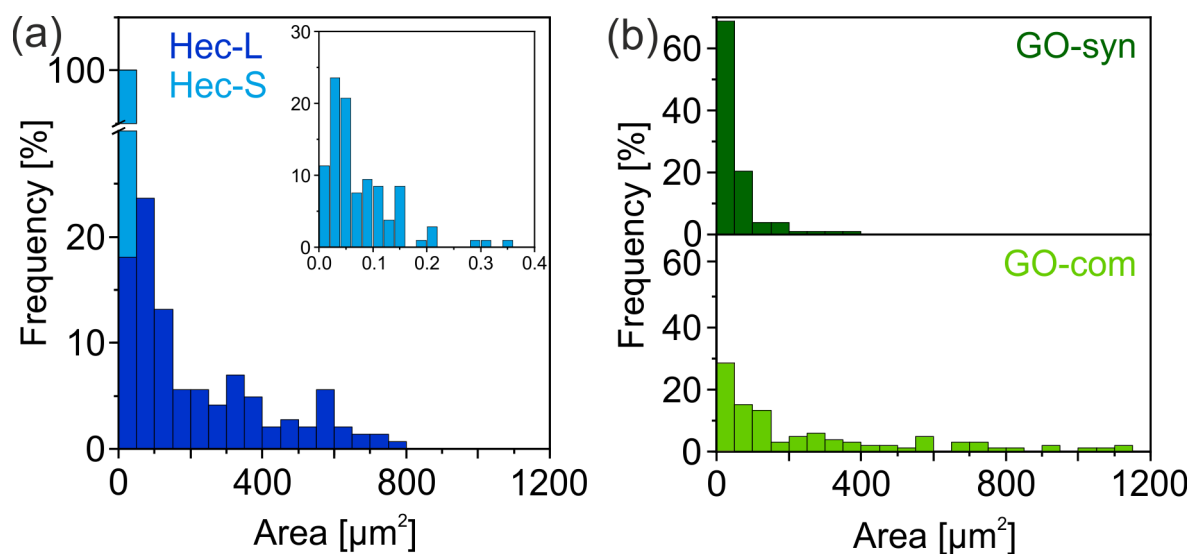


Figure 8.5: Histograms of platelet areas of Hec (a) and GO (b) samples evaluated from SEM images.

### Scanning electron microscopy (SEM)

SEM images were taken with a Zeiss Ultra plus (Carl Zeiss AG, Germany) at an operating voltage of 3 kV. Samples were prepared by drop coating a 0.001 wt% solution on a plasma-treated silicon wafer. The samples with Hec were sputtered with 10 nm carbon. For analyzing the area of the platelets, ImageJ was used, and at least 100 platelets were evaluated. Figure 8.5 shows the histograms of the platelet areas of Hec (a) and GO (b) samples. Figure 8.6 and 8.7 show exemplary SEM pictures of

Hec and GO, respectively.

Cross-sections of the films were prepared by cutting the self-supporting films with a razor blade and sputtering with 10 nm carbon.

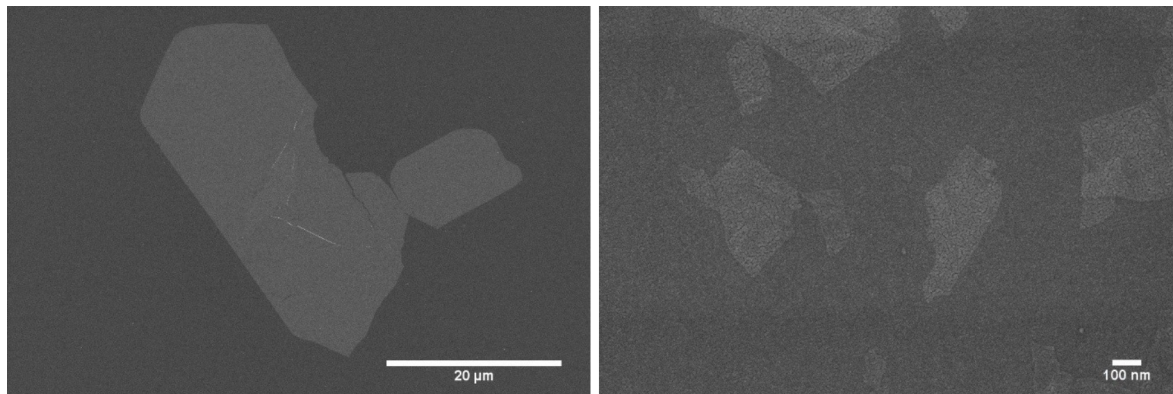


Figure 8.6: SEM pictures of Hec-L (left) and Hec-S (right).

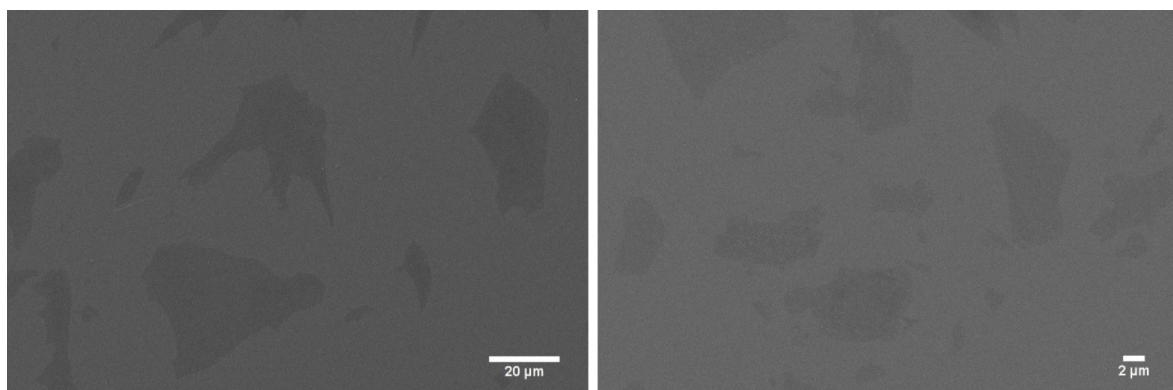


Figure 8.7: SEM pictures of GO-com (left) and GO-syn (right).

## X-ray photoelectron spectroscopy (XPS)

XPS measurements were carried out using a Versa Probe III from Physical electronics. Cu and Au were used for calibration. Shirley-type background-subtracted data is presented. Scotch tape was used to fixate the sample films on the measurement stage. The samples were sputtered with Argon after being introduced into the XPS chamber to remove adsorbed hydrocarbons. To minimize charging effects, a charge neutralization system was used. Figure 8.8 and 8.9 show the XPS spectra of Hec and GO samples. Peaks used for calculation of the elemental composition (Table 8.2 and 8.2) are marked.

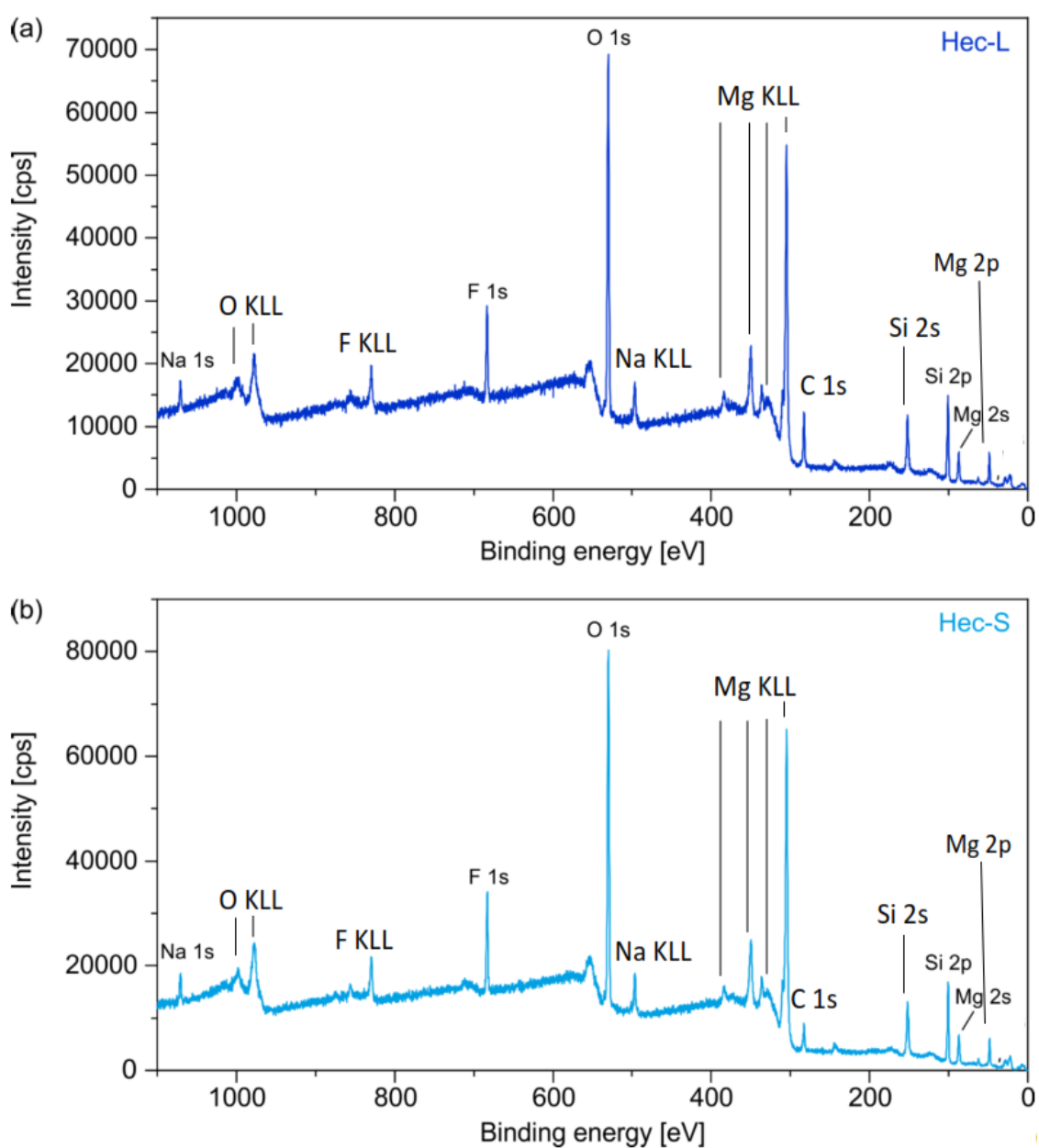


Figure 8.8: Overview XPS spectra of Hec-L (a) and Hec-S (b). Both spectra show the same chemical composition (see Table 8.2).

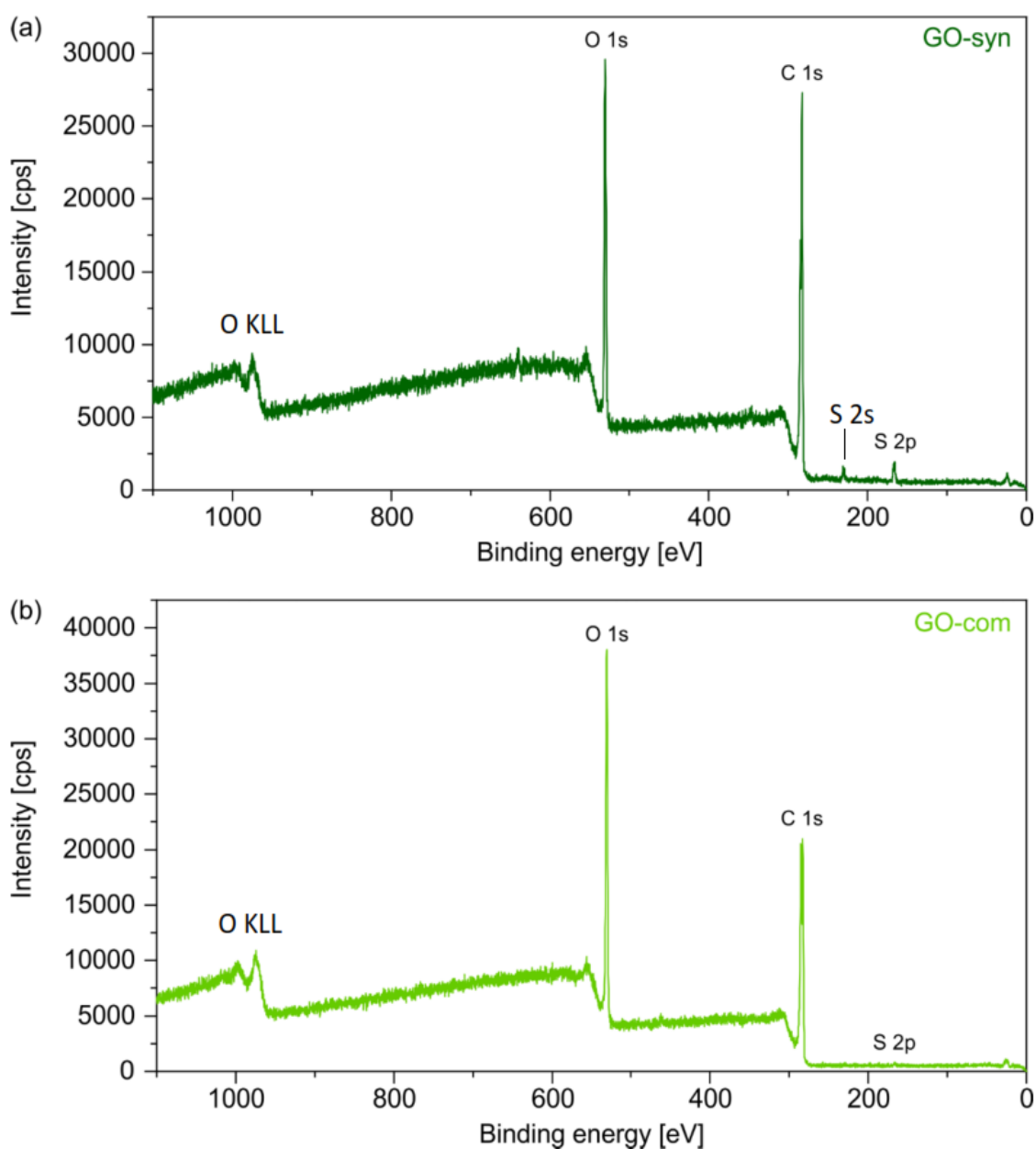


Figure 8.9: Overview XPS spectra of GO-syn (a) and GO-com (b). Two main differences are visible: GO-com contains more oxygen (O) than GO-syn, and GO-syn contains a little amount of sulfur (S), whereas GO-com contains almost no sulfur (see Table 8.2).

Table 8.2: Elemental composition of Hec samples extracted from XPS data.

Sample	Na	Mg	Li	Si	O	F
Hec-L	2.95 %	10.67 %	3.79 %	18.26 %	54.06 %	10.27 %
Hec-S	2.58 %	10.72 %	1.89 %	18.90 %	54.33 %	11.57 %

Table 8.3: Elemental composition of GO samples extracted from XPS data.

Sample	C	O	S
GO-syn	72.06 %	26.70 %	1.25 %
GO-com	68.74 %	30.94 %	0.31 %

### Raman spectroscopy

Raman spectroscopy was performed with a Raman microscope (Horiba Scientific, Olympus Ex41,  $\lambda_{Laser} = 635 \text{ nm}$ ) equipped with a Synapse CCD camera. The obtained Raman spectra are shown in Figure 8.10. The intensity ratios of the D and G band ( $I_D/I_G$ ) of both samples are around 1, which is a measure for a high number of defects within the GO structure.

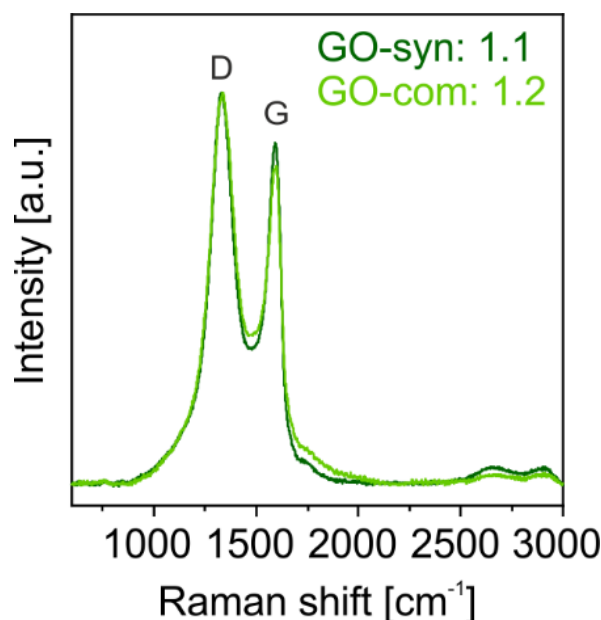


Figure 8.10: Raman spectra reveal a comparable degree of defects of both samples ( $I_D/I_G$  the ratio for both samples is around 1).

### Infrared (IR) spectroscopy

For IR spectra, a JASCO FT/IR-6100 Fourier transform IR spectrometer (JASCO Corporation, Japan) with an attenuated total reflection (ATR) unit was used.

## 8.5.2 Thermal measurements

Two different methods were used to characterize the thermal transport properties of the Hec and GO samples: lock-in thermography for the in-plane thermal diffusivity and the photoacoustic method for the cross-plane thermal conductivity.

For the calculation of the in-plane thermal conductivity and the determination of the cross-plane thermal conductivity, the density and the specific heat capacity are needed. Therefore, Helium pycnometry and differential scanning calorimetry have been used. Before all measurements, the samples have been dried for seven days at 100 °C in a vacuum oven.

### Helium pycnometry

The density of the samples was obtained from helium pycnometry using an Ultrapyc 1200e (Quantachrome Instruments). First of all, the volume of the (empty) measurement cell was measured. Then, small pieces of the free-standing films were weighed into the sample cell with a nominal volume of 1.8 cm<sup>3</sup>. One hundred runs were conducted to measure the volume of the films at room temperature. By knowing the mass (weighed on a fine balance) and the volume, the density of the samples was calculated. The obtained densities are summarized in Table 8.4.

Table 8.4: Densities of Hec and GO films (measured at room temperature).

Sample	Density [g · cm <sup>3</sup> ]
Hec-L	2.73 ± 0.01
Hec-S	2.57 ± 0.02
GO-syn	1.53 ± 0.01
GO-com	1.54 ± 0.01

### Differential scanning calorimetry (DSC)

The specific heat capacity was determined by DSC measurements on a TA instruments Discovery DSC 2500, according to the ASTM E1269 standard. All samples were freeze ground for better processability and contact with the DSC pans. Before the measurement, an isothermal step (1 h, 100 °C) was conducted to ensure dry conditions. Subsequently, two heating cycles were performed, whereas only the second cycle was evaluated. The temperature profile ranged in the case of the Hec samples from -40 °C to 250 °C and in case of the GO samples from -40 °C to 100 °C using a heating rate of 20 K min<sup>-1</sup> with a nitrogen flow of 50 mL min<sup>-1</sup>. Three samples per sample type were measured (Figure 8.11).

### Lock-in thermography (LIT)

The in-plane thermal diffusivity of free-standing Hec and GO films was obtained by lock-in thermography (LIT). Figure 8.12 shows the self-built LIT set-up.

A laser beam periodically heats the free-standing sample (Genesis MX 532-1000 SLM

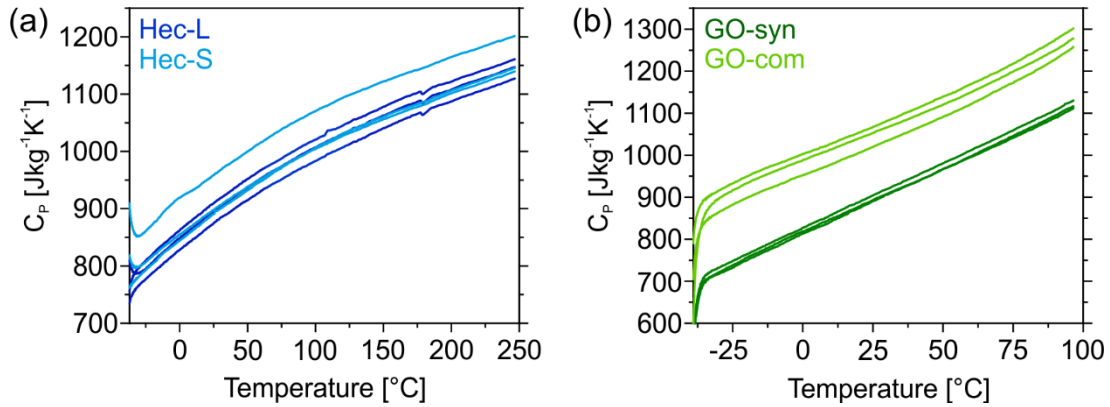


Figure 8.11: Specific heat capacity  $C_p$  versus temperature: (a) Hec-L and Hec-S. (b) GO-syn and GO-com. The  $C_p$  at 25  $^{\circ}\text{C}$  was used for the determination of the thermal conductivity.

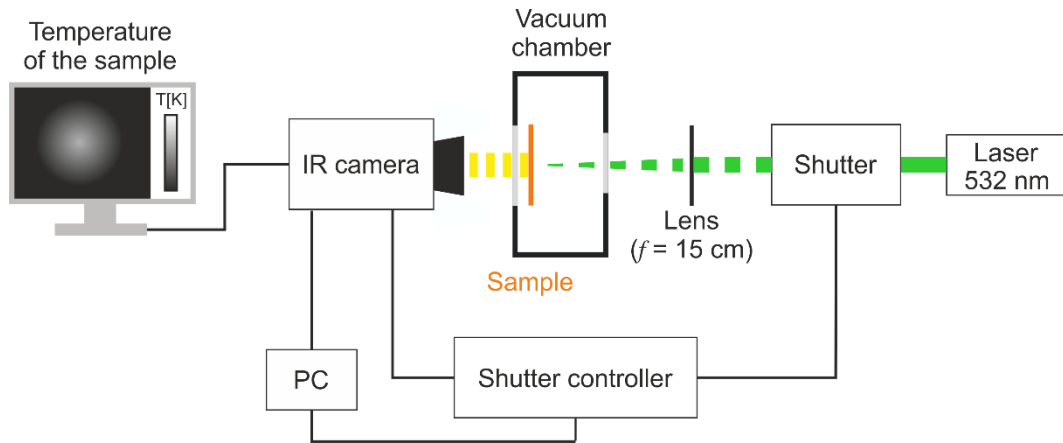


Figure 8.12: Scheme of the lock-in thermography set-up. The samples were measured in a vacuum chamber to avoid heat losses (convection and conduction) to the environment.

OPS, Coherent,  $\lambda = 532 \text{ nm}$ ) focused onto the sample surface by a lens of 150 mm focal length. For the modulation of the laser a shutter (SH05/M, Thorlabs) controlled by a shutter controller (SC10, Thorlabs) is used. The emitted IR radiation of the sample surface is detected in rear-face configuration (i.e. from the non-illuminated side) by an Infratec VarioCAM HD research IR camera (spectral window: 7.5-14  $\mu\text{m}$ ). The IR camera is equipped with a close-up lens which enables a spatial resolution of around 29  $\mu\text{m}$ . Since heat conduction to the gas and convection lead to an over-estimation of the thermal diffusivity<sup>[39,43]</sup> all samples were measured in a vacuum ( $3 \times 10^{-3} \text{ mbar}$ ). Furthermore, the Hec samples were coated with a 20 nm carbon layer for enhanced laser absorption. The coating of the sample was facing to the IR camera. Due to the blackish color of GO, the GO samples possess a proper laser absorption, and therefore a coating was not necessary. LIT measurements were performed using Infratec's IRBISactiveonline software. Measurements were conducted at several lock-in frequencies between 0.309 and 1.765 Hz. Furthermore, each mea-

surement was averaged over several (800-2000) lock-in periods to enhance the signal to noise ratio, with the first 100 periods being discarded. The software calculates the amplitude and phase of the sample's temperature oscillations automatically. Exemplary phase images are depicted in Figure 8.13. The red point marks the focal point of the laser excitation and thus the midpoint of the radial distribution.

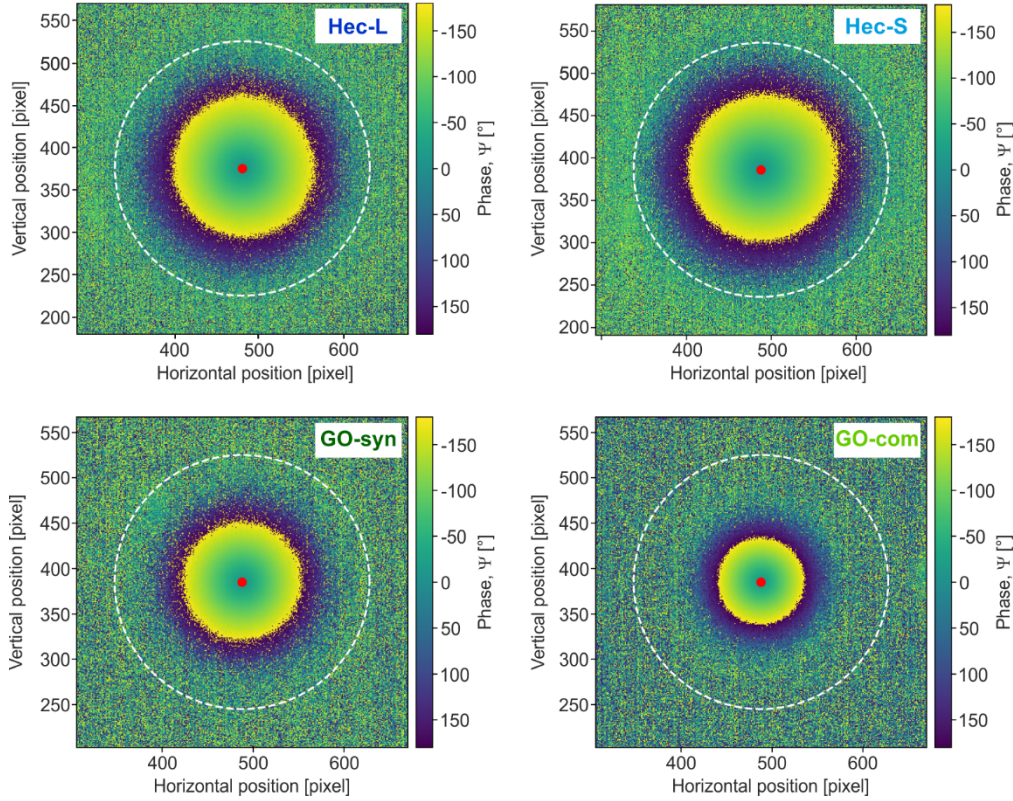


Figure 8.13: Exemplary two-dimensional phase images measured at a frequency of 1.111 Hz. The penetration depth of the temperature oscillations depends on the material's properties and decreases with decreasing thermal diffusivity. The red point in the center of the phase image marks the focal point of the laser.

Radial profiles for the phase and amplitude images (Figure 8.14) are extracted using a self-written Python script. The in-plane thermal diffusivity is calculated from the phase and amplitude slopes according to the slope method of a thermally thin film:

$$m_{\Psi} \cdot m_{\ln(T \cdot r^{0.5})} = \frac{\pi f_{lock-in}}{\alpha_{\parallel}} \quad (8.1)$$

Here,  $m_{\Psi}$  is the slope of the linear relation of the phase and the radial distance  $r$ ,  $m_{\ln(T \cdot r^{0.5})}$  is the slope of the linear relation of the natural logarithm of the amplitude  $T$  multiplied by the square root of the radial distance  $r$ ,  $f_{(lock-in)}$  is the lock-in frequency, and  $\alpha_{(in-plane)}$  is the in-plane thermal diffusivity. Three films have been measured for each sample type. An average in-plane thermal diffusivity value with a standard deviation was calculated from this data (Table 8.5).

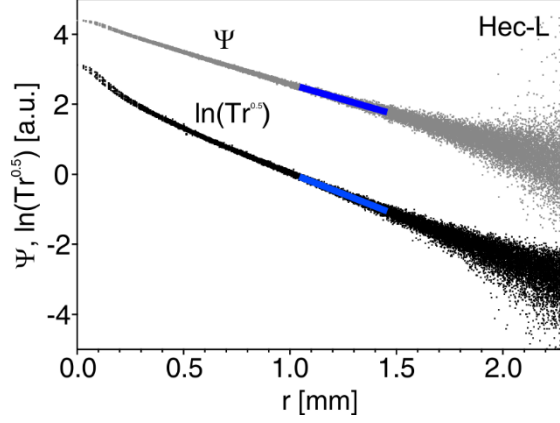


Figure 8.14: Exemplary phase  $\Psi$  and amplitude profiles of Hec-L. The blue lines indicate the regions where the linear fit was evaluated. This position is sufficiently far away from the central excitation spot.<sup>[44]</sup>

Table 8.5: In-plane thermal diffusivity values of Hec and GO films. Three films per sample type were measured, and an average thermal diffusivity with a standard deviation was calculated.

Sample	In-plane thermal diffusivity [ $\text{mm}^2 \cdot \text{s}^{-1}$ ]
Hec-L	$2.35 \pm 0.03$
Hec-S	$2.36 \pm 0.01$
GO-syn	$1.24 \pm 0.02$
GO-com	$0.63 \pm 0.01$

Finally, the in-plane thermal conductivity was calculated from the in-plane thermal diffusivity  $\alpha_{(in-plane)}$ , the density  $\rho$ , and the specific heat capacity  $c_p$ :

$$k_{\parallel} = \alpha_{\parallel} \cdot \rho \cdot C_p \quad (8.2)$$

### Photoacoustic method

The samples for the cross-plane thermal conductivity characterization were spray-coated on glass substrates. A gold transducer layer ( $\sim 150$  nm) was evaporated on top of the samples. In the photoacoustic measurement, a modulated laser beam ( $\lambda = 488$  nm) periodically heats the sample. Due to the photoacoustic effect an acoustic response is induced, which relies on the thermal properties of the sample. The schematic layout of the measurement cell is shown in Figure 8.15a. The gas-tight cell is filled with a helium pressure of 20 psi. The microphone (Bruel&Kjaer, 4398-A-011) connected to the cell detects the acoustic wave, which is induced by the periodic heat conduction from the sample surface to the gas phase. The microphone is linked to

a lock-in amplifier with integrated signal generator (Zurich instruments, HF2LI), as shown in Figure 8.15b. The signal generator targets the modulation frequency for the electro-optic modulator (EOM, Conoptics, M25A) and therefore controls the frequency of the laser beam. The lock-in amplifier then transfers the acoustic signal into amplitude and phase shift concerning the modulation of the incident laser beam.

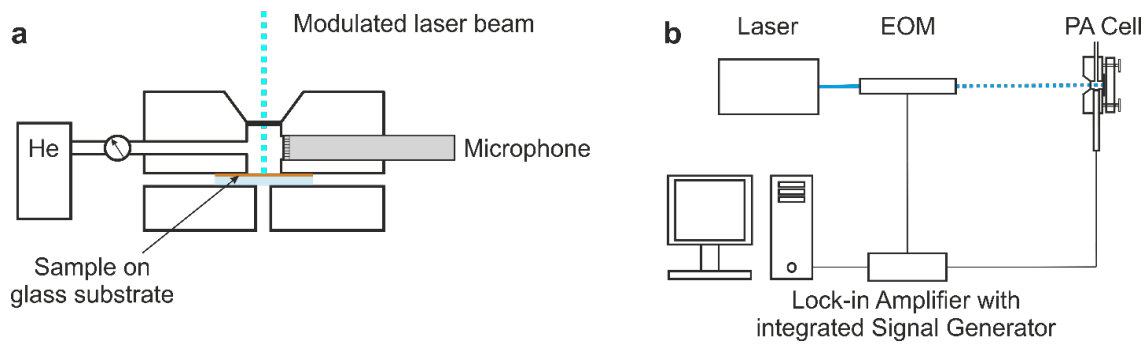


Figure 8.15: Scheme of (a) the photoacoustic cell and (b) the whole setup.

For measurement, we performed a frequency sweep in a range from 110 Hz to 4000 Hz. The phase shift signal is then normalized with the signal of a thermally thick glass sample (1 mm) of known thermal properties. Figure 8.16 shows a representative measurement curve together with the best fit. The fitting procedure was realized according to Singh et al.<sup>[45]</sup> Therefore, the generalized multilayer model of Hu et al.<sup>[40]</sup> is used. The model described the temperature distribution in the sample, assuming a one-dimensional heat transfer. The unknown parameters contact resistance between the gold layer and the sample, the thermal diffusivity of the sample, and the contact resistance between sample and substrate are fitted to match the experimental data. When fitting three parameters at the same time, the results for the individual parameters may not accurately be predicted.

However, it was found that the total layer resistance (consisting of all three parameters) can be estimated with high accuracy. The reason is the difference in sensitivity of the model on the individual parameters.<sup>[46]</sup> Hence, we report only the total layer resistance. In addition to that, we calculate the effective thermal conductivity of our samples. We estimated based on literature data<sup>[47,48]</sup> that the thermal interface resistance between the gold transducer layer and sample is on the order or less than  $10^{-8} \text{ K m}^2 \text{ W}^{-1}$ . We, consequently, do not expect a significant influence of this interface on our calculation of the effective thermal conductivity. The thermal conductivity is obtained by dividing the total layer resistance by the sample thickness. AFM measurements determined the sample thickness. We summarized the values of the total layer resistance, the sample thickness and the resulting effective thermal conductivity in Table 8.6.

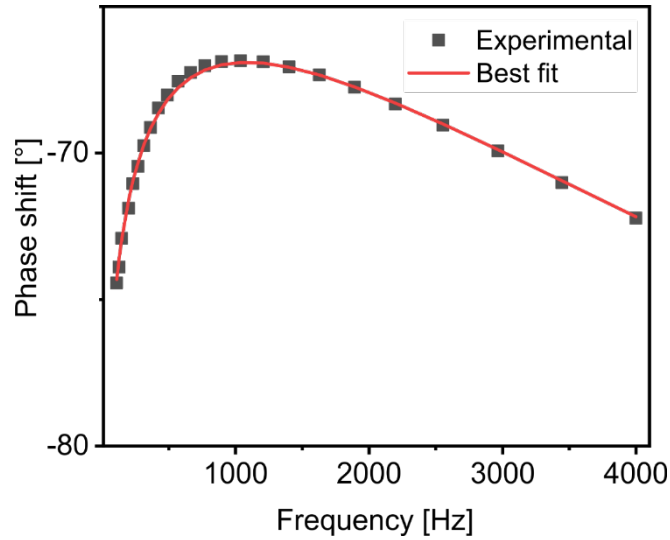


Figure 8.16: Representative photoacoustic measurement of the GO-syn sample with a thickness of 446 nm. Normalized photoacoustic phase signal is dependent on the frequency. The red line indicates the best fit.

Table 8.6: Summary of the photoacoustic measurements. The total layer resistance, the thickness, and the resulting effective cross-plane thermal conductivity are given for each sample.

Sample	Total layer resistance [mm <sup>2</sup> K W <sup>-1</sup> ]	Thickness [μm]	Effective cross-plane thermal conductivity [W m <sup>-1</sup> K <sup>-1</sup> ]
Hec-L	1.58	0.28	0.177
Hec-L	2.55	0.595	0.234
Hec-L	4.34	0.94	0.217
Hec-S	5.39	0.972	0.180
Hec-S	4.62	0.972	0.210
Hec-S	5.86	0.972	0.166
GO-syn	1.92	0.233	0.121
GO-syn	3.99	0.446	0.117
GO-syn	5.52	0.746	0.135
GO-com	1.43	0.179	0.125
GO-com	2.65	0.338	0.128
GO-com	4.50	0.589	0.131

## References

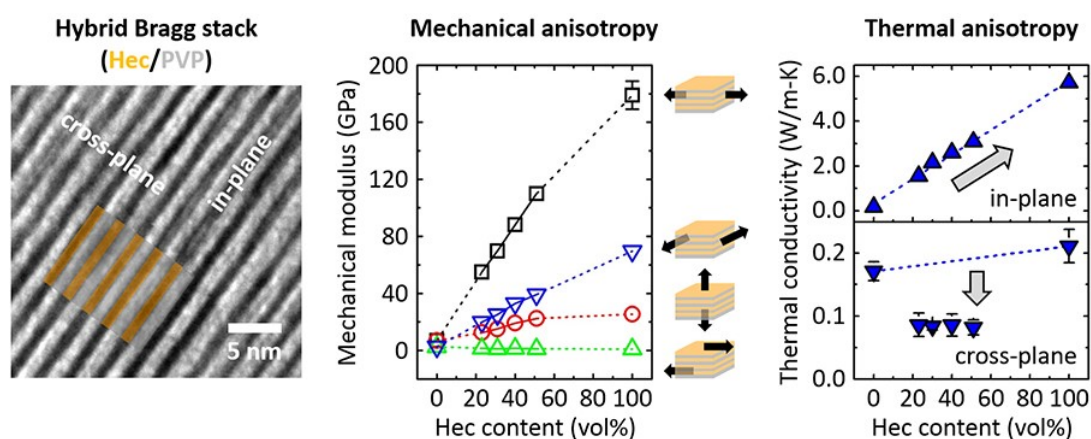
- [1] H. Song, J. Liu, B. Liu, J. Wu, H.-M. Cheng, F. Kang, *Joule* **2018**, *2*, 442–463.
- [2] J. Xiang, L. T. Drzal, *Carbon* **2011**, *49*, 773–778.
- [3] Y. Zhang, M. Edwards, M. K. Samani, N. Logothetis, L. Ye, Y. Fu, K. Jeppson, J. Liu, *Carbon* **2016**, *106*, 195–201.
- [4] K. M. Razeeb, E. Dalton, G. L. W. Cross, A. J. Robinson, *International Materials Reviews* **2018**, *63*, 1–21.
- [5] M. C. K. Swamy, Satyanarayan, *Journal of Electronic Materials* **2019**, *48*, 7623–7634.
- [6] R. Prasher, *Proceedings of the IEEE* **2006**, *94*, 1571–1586.
- [7] A. J. McNamara, Y. Joshi, Z. M. Zhang, *International Journal of Thermal Sciences* **2012**, *62*, 2–11.
- [8] Q.-L. Meng, H. Liu, Z. Huang, S. Kong, P. Jiang, X. Bao, *Chinese Chemical Letters* **2018**, *29*, 711–715.
- [9] J. D. Renteria, S. Ramirez, H. Malekpour, B. Alonso, A. Centeno, A. Zurutuza, A. I. Cocemasov, D. L. Nika, A. A. Balandin, *Advanced Functional Materials* **2015**, *25*, 4664–4672.
- [10] N. Song, D. Jiao, P. Ding, S. Cui, S. Tang, L. Shi, *Journal of Materials Chemistry C* **2016**, *4*, 305–314.
- [11] N. Song, D. Jiao, S. Cui, X. Hou, P. Ding, L. Shi, *ACS Appl. Mater. Interfaces* **2017**, *9*, 2924–2932.
- [12] L. Peng, Z. Xu, Z. Liu, Y. Guo, P. Li, C. Gao, *Advanced Materials* **2017**, *29*, 1700589.
- [13] P. Jiang, X. Qian, R. Yang, L. Lindsay, *Physical Review Materials* **2018**, *2*, 064005.
- [14] Y. Lin, T. V. Williams, T.-B. Xu, W. Cao, H. E. Elsayed-Ali, J. W. Connell, *The Journal of Physical Chemistry C* **2011**, *115*, 2679–2685.
- [15] B.-H. Xie, X. Huang, G.-J. Zhang, *Composites Science and Technology* **2013**, *85*, 98–103.
- [16] X. Zeng, L. Ye, S. Yu, H. Li, R. Sun, J. Xu, C.-P. Wong, *Nanoscale* **2015**, *7*, 6774–6781.
- [17] Y.-F. Huang, Z.-G. Wang, H.-M. Yin, J.-Z. Xu, Y. Chen, J. Lei, L. Zhu, F. Gong, Z.-M. Li, *ACS Appl. Nano Mater.* **2018**, *1*, 3312–3320.
- [18] O. H. Kwon, T. Ha, D.-G. Kim, B. G. Kim, Y. S. Kim, T. J. Shin, W.-G. Koh, H. S. Lim, Y. Yoo, *ACS Applied Materials & Interfaces* **2018**, *10*, 34625–34633.

- [19] J. Han, G. Du, W. Gao, H. Bai, *Advanced Functional Materials* **2019**, *29*, 1900412.
- [20] B. Fischer, M. Ziadeh, A. Pfaff, J. Breu, V. Altstadt, *Polymer* **2012**, *53*, 3230–3237.
- [21] M. R. Schütz, H. Kalo, T. Lunkenbein, J. Breu, C. A. Wilkie, *Polymer* **2011**, *52*, 3288–3294.
- [22] M. R. Schütz, H. Kalo, T. Lunkenbein, A. H. Gröschel, A. H. E. Müller, C. A. Wilkie, J. Breu, *Journal of Materials Chemistry* **2011**, *21*, 12110–12116.
- [23] E. S. Tsurko, P. Feicht, F. Nehm, K. Ament, S. Rosenfeldt, I. Pietsch, K. Roschmann, H. Kalo, J. Breu, *Macromolecules* **2017**, *50*, 4344–4350.
- [24] E. S. Tsurko, P. Feicht, C. Habel, T. Schilling, M. Daab, S. Rosenfeldt, J. Breu, *Journal of Membrane Science* **2017**, *540*, 212–218.
- [25] M. D. Losego, I. P. Blitz, R. A. Vaia, D. G. Cahill, P. V. Braun, *Nano Lett* **2013**, *13*, 2215–9.
- [26] Z. Wang, K. Rolle, T. Schilling, P. Hummel, A. Philipp, B. A. F. Kopera, A. M. Lechner, M. Retsch, J. Breu, G. Fytas, *Angew Chem Int Ed Engl* **2020**, *59*, 1286–1294.
- [27] P. Feicht, R. Siegel, H. Thurn, J. W. Neubauer, M. Seuss, T. Szabó, A. V. Talyzin, C. E. Halbig, S. Eigler, D. A. Kunz, A. Fery, G. Papastavrou, J. Senker, J. Breu, *Carbon* **2017**, *114*, 700–705.
- [28] C. Clauser, E. Huenges in *Rock Physics & Phase Relations*, AGU Reference Shelf, **2013**, pp. 105–126.
- [29] A. Tiwari, K. Boussois, B. Nait-Ali, D. S. Smith, P. Blanchart, *AIP Advances* **2013**, *3*, 112129.
- [30] U. Hofmann, E. König, *Zeitschrift für anorganische und allgemeine Chemie* **1937**, *234*, 311–336.
- [31] L.-Q. Dao, P. Delage, A.-M. Tang, Y.-J. Cui, J.-M. Pereira, X.-L. Li, X. Sillen, *Applied Clay Science* **2014**, *101*, 282–287.
- [32] M. Stöter, D. A. Kunz, M. Schmidt, D. Hirsemann, H. Kalo, B. Putz, J. Senker, J. Breu, *Langmuir* **2013**, *29*, 1280–1285.
- [33] S. Rosenfeldt, M. Stöter, M. Schlenk, T. Martin, R. Q. Albuquerque, S. Förster, J. Breu, *Langmuir* **2016**, *32*, 10582–10588.
- [34] H. A. Prescott, Z.-J. Li, E. Kemnitz, J. Deutsch, H. Lieske, *Journal of Materials Chemistry* **2005**, *15*, 4616–4628.
- [35] M. Wojciechowska, B. Czajka, M. Pietrowski, M. Zieliński, *Catalysis Letters* **2000**, *66*, 147–153.

- [36] A. A. Rywak, J. M. Burlitch, *Chemistry of Materials* **1996**, *8*, 60–67.
- [37] Z. Xu, C. Gao, *Nature Communications* **2011**, *2*, 571.
- [38] U. Hofmann, A. Frenzel, E. Csalán, *Justus Liebigs Annalen der Chemie* **1934**, *510*, 1–41.
- [39] A. Mendioroz, R. Fuente-Dacal, E. Apinaniz, A. Salazar, *Rev. Sci. Instrum.* **2009**, *80*, 074904.
- [40] H. P. Hu, X. W. Wang, X. F. Xu, *Journal of Applied Physics* **1999**, *86*, 3953–3958.
- [41] X. Wang, H. Hu, X. Xu, *Journal of Heat Transfer* **2001**, *123*, 138–144.
- [42] J. Breu, W. Seidl, A. J. Stoll, K. G. Lange, T. U. Probst, *Chem. Mater.* **2001**, *13*, 4213–4220.
- [43] A. Salazar, A. Mendioroz, R. Fuente, *Appl. Phys. Lett.* **2009**, *95*, 121905.
- [44] A. Philipp, N. W. Pech-May, B. A. F. Kopera, A. M. Lechner, S. Rosenfeldt, M. Retsch, *Anal. Chem.* **2019**, *91*, 8476–8483.
- [45] V. Singh, T. L. Bougher, A. Weathers, Y. Cai, K. Bi, M. T. Pettes, S. A. McMennamin, W. Lv, D. P. Resler, T. R. Gattuso, D. H. Altman, K. H. Sandhage, L. Shi, A. Henry, B. A. Cola, *Nat Nanotechnol* **2014**, *9*, 384–90.
- [46] X. Wang, B. A. Cola, T. L. Bougher, S. L. Hodson, T. S. Fisher, X. Xu in *Annual Review of Heat Transfer*, **2013**, pp. 135–157.
- [47] M. D. Losego, M. E. Grady, N. R. Sottos, D. G. Cahill, P. V. Braun, *Nat. Mater.* **2012**, *11*, 502–6.
- [48] V. Juvé, M. Scardamaglia, P. Maioli, A. Crut, S. Merabia, L. Joly, N. Del Fatti, F. Vallée, *Physical Review B* **2009**, *80*, 195406.

## 9 Tunable thermoelastic anisotropy in hybrid Bragg stacks with extreme polymer confinement

Zuyuan Wang, Konrad Rolle, Theresa Schilling, Patrick Hummel, Alexandra Philipp, Bernd A.F. Kopera, Anna M. Lechner, Markus Retsch, Josef Breu and George Fytas



Reprinted with permission from Wang et al., *Angew. Chem. Int. Ed.*, 2020, 59, 1286-1294. Copyright 2019 The Authors.

**Abstract:** Controlling thermomechanical anisotropy is important for emerging heat management applications such as thermal interface and electronic packaging materials. Whereas many studies report on thermal transport in anisotropic nanocomposite materials, a fundamental understanding of the interplay between mechanical and thermal properties is missing, due to the lack of measurements of direction-dependent mechanical properties. In this work, exceptionally coherent and transparent hybrid Bragg stacks made of strictly alternating mica-type nanosheets (synthetic hectorite) and polymer layers (polyvinylpyrrolidone) were fabricated at large scale. Distinct from ordinary nanocomposites, these stacks display long-range periodicity, which is tunable down to angstrom precision. A large thermal transport anisotropy (up to 38) is consequently observed, with the high in-plane thermal conductivity (up to  $5.7 \text{ W m}^{-1} \text{ K}^{-1}$ ) exhibiting an effective medium behavior. The unique hybrid material combined with advanced characterization techniques allows correlating the full elastic tensors to the direction-dependent thermal conductivities. We, therefore, provide a first analysis on how the direction-dependent Young's and shear moduli influence the flow of heat.

## 9.1 Introduction

Heat management is crucial in many applications important for fueling the growth of our technology-driven society. It needs to address not only very small length scales to dissipate the heat produced, for example, by electronic circuits, but also very large length scales to realize air conditioning, for instance, for commercial buildings. The ubiquity of heat makes it obvious that heat management is a key-technology to realize international long-term goals regarding global warming. Controlling the elusive flow of heat is a complex challenge across multiple materials, length scales, and ultimately devices. This results in stringent requirements for directional control over the heat flux based on advanced material design. Whereas heat transport represents an effective, far-field phenomenon, it is decisively governed by the material structure<sup>[1-3]</sup> and chemistry<sup>[4,5]</sup> on the microscale. Extreme phenomena of both heat dissipation and thermal insulation have been demonstrated in nanostructured and hybrid materials. For heat dissipation, surprisingly high thermal conductivities have been reported for one-dimensional (1D) fibers comprising synthetic<sup>[6]</sup> and natural polymers.<sup>[7,8]</sup> For thermal insulation, unusually low thermal conductivities have been shown for (disordered) stacks of two-dimensional (2D) materials.<sup>[9,10]</sup> Extremely efficient anisotropic thermal insulation materials have been demonstrated with various mixtures of polymers and nanoparticles or 2D materials.<sup>[11-13]</sup>

The combination of inherently different materials, such as soft and hard matter, is attractive, as new properties, deviating from those based on the simple linear interpolation, could emerge. This is often accompanied by improved processability, which is aided by the complementary properties of the constituent components. For instance, the soft component can serve as a binder to enable fabrication of large-area, thin films of an otherwise brittle, hard component. On the contrary, the expected effective material properties, such as mechanical reinforcement, optical transparency, and electrical or thermal conductivity, have been often found inferior to the high expectations. The reason for such shortcomings is that the nanocomposite structure, particularly the soft-hard interface, is poorly controlled. Furthermore, although many characterization techniques, such as tensile testing, indentation, and abrasion tests, are capable of assessing engineering properties, they are unsuitable for directly identifying and quantifying anisotropies or microscopic contributions to the effective properties.

Nevertheless, hybrid systems have been reported to drastically alter the materials' thermal transport properties,<sup>[6-13]</sup> depending on the geometry, dimensionality, crystallographic symmetry, and confinement. Interestingly, layered structures in-

herently exhibit structural anisotropy, a feature that can be detrimental or desirable depending on the application.<sup>[14]</sup> In particular, when polymer films are filled with nanosheets of huge aspect ratio, the resulting nanocomposite properties ought to be exceedingly anisotropic. Yet, only effective material properties such as electrical or thermal conductivity have been reported in a direction-dependent manner. Direction-dependent mechanical properties, which fundamentally translate into thermal transport properties are still missing. Strong anisotropies in hybrid materials are preferentially achieved at small stacking periodicities<sup>[10]</sup> or by combining components with a large property contrast.<sup>[15]</sup>

For a thorough characterization of such nanosheet/polymer stacks (also known as “nacre-mimics”<sup>[16–19]</sup>), macroscopically oriented and homogeneous systems are paramount. Such ideal model system should also exhibit translational crystallographic symmetry, tunability, and strong anisotropy. Direction-dependent studies benefit significantly from the availability of various lightscattering methods, rendering a transparent filler such as the synthetic clay hectorite with a mica-type structure desirable. For fundamental investigations of elastic properties, BLS has established itself as a technique of choice, as it allows for microscopic observations of high frequency (GHz) dynamics, at which viscoelasticity effects are usually negligible.<sup>[20,21]</sup> On the other hand, lock-in thermography and photoacoustic techniques have been proven reliable in accessing the in-plane and cross-plane thermal conductivities of thin films.<sup>[22,23]</sup>

Here, we show for the first time the complete mechanical properties of clay/polymer Bragg stacks that are fabricated using a uniquely defined, scalable spray-coating process meeting all aforementioned specifications of a suitable model system. We, therefore, introduce 1D hybrid Bragg stacks based on nacre-mimetic clay/polymer with small stacking periods and large property contrast. These Bragg stacks are scalable in both lateral extension and thickness, and they are macroscopically oriented. The fully controlled microstructure allows a detailed orientation dependent characterization of the thermal and mechanical properties. We couple the thermal and mechanical analyses to achieve an in-depth understanding of the interplay between the thermal conductivities and mechanical moduli in a direction-dependent manner. The extreme confinement of polymer between the clay sheets further prompts a question regarding the validity of continuum mechanics that we also address. The combination of unique hybrid materials and advanced characterization techniques provides an unprecedented insight into the physics of direction-dependent nanomechanical and thermal transport properties in strongly anisotropic materials with polymer confinement.

## 9.2 Results and Discussion

**Hybrid Bragg stacks with extreme polymer confinement.** The Bragg stacks comprise synthetic clay sodium fluorohectorite (Hec,  $[\text{Na}_{0.5}]^{\text{inter}}[\text{Mg}_{2.5}\text{Li}_{0.5}]^{\text{oct}}[\text{Si}_4]^{\text{tet}}\text{O}_{10}\text{F}_2$ ) and polyvinylpyrrolidone (PVP,  $M_w = 40000 \text{ g mol}^{-1}$ ). Like layered titanates<sup>[24]</sup> and antimony phosphates,<sup>[25]</sup> Hec belongs to a handful of compounds showing a rare phenomenon of osmotic swelling.<sup>[26]</sup> In contrast to mechanical exfoliation by e.g. sonication in the liquid phase, osmotic swelling is a thermodynamically favored, repulsive process,<sup>[27]</sup> allowing for complete and gentle delamination that preserves the diameter of the parent crystals. In general, exfoliation describes the process of slicing tactoids into thinner stacks, whereas by delamination, the layered material is exfoliated to the level of individual single nanosheets.<sup>[28]</sup> For Hec, nanosheets with a thickness of 10 Å and a median diameter of 20 μm (Figure 9.5) are obtained by simply immersing the material into deionized water.<sup>[29]</sup> Phase purity and a homogeneous charge density guaranteeing a uniform intracrystalline reactivity are prerequisite for such a well-controlled delamination. For Hec this is achieved by long-term annealing, while less uniform natural or other synthetic clays commonly applied for nacre-mimics comprise mixtures of auxiliary minerals, mono-, few- and multilayer stacks.<sup>[29]</sup>

Because of the large aspect (diameter to thickness) ratio, polar rotation of the nanosheets in suspension is hindered, leading to parallel nanosheets after osmotic swelling. Even dilute (< 1 vol%) suspensions of Hec represent nematic phases.<sup>[30]</sup> The parallel pre-orientation of adjacent nanosheets in the highly swollen dispersion is indispensable for the fabrication of homogenous and periodic Bragg stacks via spray coating. Similar to titanate nanosheets,<sup>[31]</sup> Hec nanosheets adopt this cofacial arrangement due to strong electrostatic repulsion with inter-nanosheet distances exceeding 50 nm. Polymers can easily diffuse into these spacious galleries. By mixing Hec suspensions with varying aliquots of an aqueous PVP solution, we obtained perfectly homogeneous, nematic dispersions, as evidenced by SAXS measurements (Figure 9.6).

Through spray coating of dilute nematic mixtures of high-aspectratio Hec nanosheets with PVP (1-2 wt% total solid content, see Section 9.5.1 highly coherent Bragg stack films with tunable gallery spacings are fabricated.<sup>[32]</sup> The transverse flexibility of clay monolayers<sup>[33]</sup> and their large aspect ratio are essentials assuring the high degree of precision obtained in the self-assembly.<sup>[34]</sup> Both, all nanosheets and the macroscopic film are aligned parallel to a polyethylene terephthalate substrate. The microscopic orientation of the Hec nanosheets prescribes the macroscopic film orientation, which is prerequisite for the direction-dependent measurements. The macro-

scopic film orientation is, consequently, equivalent to the microscopic polymer/clay direction and allows using far-field and integrating characterization techniques to reveal direction-dependent properties. After drying, self-supporting hybrid films with lateral extensions of several square centimeters are peeled off the substrate and used in the BLS and thermal conductivity measurements. Only by generating a nematic phase consisting of a homogeneous mixture of large aspect ratio and flexible nanosheets allows for fabrication of large area, self-standing 1D single crystals referred to in literature as Bragg-stacks or smectic films.<sup>[34]</sup> Furthermore, appropriate processing like spray coating fostering the thermodynamic equilibration of the hybrid structure during drying has to be employed.

In total, we prepared six samples: pure polymer, pure Hec, and four hybrid Bragg stacks, which are denoted as Hec0/PVP100, Hec100/PVP0, Hec23/PVP77, Hec31/PVP69, Hec40/PVP60, and Hec51/PVP49, respectively. Here, the numbers indicate the volume fractions (vol%) of Hec and PVP, as confirmed by thermogravimetric analysis (Table 9.1 and Figure 9.7).

The Hec surface is corrugated (Figure 9.1A) allowing for interdigitation and anchoring of PVP chains. Such interdigitation has been documented for intercalated molecular moieties, where structures based on single crystal data refinement are available.<sup>[35,36]</sup> An in-scale impression of the ultra-high aspect ratio provided by the Hec nanosheet gallery is shown in Figure 9.1B, where the length of the line corresponds to the typical lateral size of a clay nanosheet, and the thickness of the line to the height of a Hec/PVP/Hec layer. The magnifying lens highlights the extreme polymer confinement in the cross-plane direction. The perfect homogeneous arrangement of Hec nanosheets and PVP is demonstrated by TEM and SEM images over different dimensions (Figure 9.1C-E, Figure 9.11. Note that the lateral dimensions of the Hec nanosheets are much larger than the typical persistence and even contour lengths of the PVP chains. While for the polymer chains the Hec nanosheet confinement appears infinite, at the length scale of the Bragg-stack films extending over tens of centimeters, they are of course finite. At the magnification where single 1 nm thick nanosheets are observable (Figure 9.1C-E, Figure 9.9, the occurrence of nanosheet edges is very rare (fewer than one per  $2500 \text{ nm}^{-2}$ ). Careful inspection, however, reveals few (Figure 9.10) of these nanosheet edges. The clay nanosheets show in-plane crystalline order resembling the structure of mica. While mica possesses 3D crystalline order, our nanocomposite films belong to the transversely isotropic symmetry class, because the adjacent Hec nanosheets are positioned randomly in the lateral direction. However, all hybrid films show translational crystallographic symmetry along 001 (the cross-plane direction), as indicated by several orders of Bragg reflections (Figure 9.1C-E and Figure 9.9). By varying

the PVP content, the basal spacing was tuned in the range from 19 to 38 Å, leading to PVP layer thicknesses ranging from 9 to 28 Å. For all samples, the gallery height is, therefore, significantly smaller than the PVP chains' radius of gyration ( $R_{g,PVP} \approx 15 \text{ nm}^{[37]}$ ), implying strong polymer confinement.

In contrast to known nanocomposite films,<sup>[17,38]</sup> thermodynamically miscible over a wide range of compositions. This miscibility is a prerequisite for tuning the basal spacing over a wide range with angstrom precision, which typically is only observed when vapour-phase deposition techniques are applied.<sup>[9]</sup> The miscibility is also reflected in an agreement of the basal spacing observed by X-ray diffraction ( $d_{XRD}$ ) with the nominal values calculated based on the Hec and PVP volume fractions ( $d_{nominal}$ , Table 9.1). To the best of our knowledge, our Hec/PVP Bragg stack films are the first of its kind showing such an agreement. Because the polymer confinement, however, is getting to the point where the gallery height is on the order of the size of an individual polymer chain, it is not possible to vary the gallery height continuously but only in incremental steps that relate to the diameter of the polymer chain. Consequently, only discrete polymer volume fractions lead to essentially defect-free Bragg stacks, as seen in Hec40/PVP60 and Hec31/PVP69. XRD patterns reflect this with a rational 001-series, where the average basal spacing ( $d_{XRD}$ ) calculated from individual reflections shows a low coefficient of variation with the reflection peaks being sharp and intense (Table 9.1). The two gallery heights of the two defectfree hybrid materials (1.3 nm for Hec40/PVP60 and 2.0 nm for Hec31/PVP69) might be attributed to the elliptical nature of PVP chains with principle axes of 1.0 nm and 1.3 nm (Figure 9.8A). The observed gallery heights correspond to a monolayer with the longer principal axis (Figure 9.8B) oriented perpendicular to the Hec nanosheets and a bilayer with the longer principle axis (Figure 9.8C) lying in the plan of the Hec nanosheets, respectively.

In the two cases where the volume ratios do not happen to match (Hec23/PVP77 and Hec51/PVP49), the miscibility is nevertheless assured at small length scale by random interstratification of two gallery heights (Figure 9.1E; transmission electron microscopy (TEM) close-up), and the coefficient of variation of the 001-series increases<sup>[39]</sup> (Table 9.1) with the reflection peaks being less intense (Figure 9.1E and Figure 9.9).

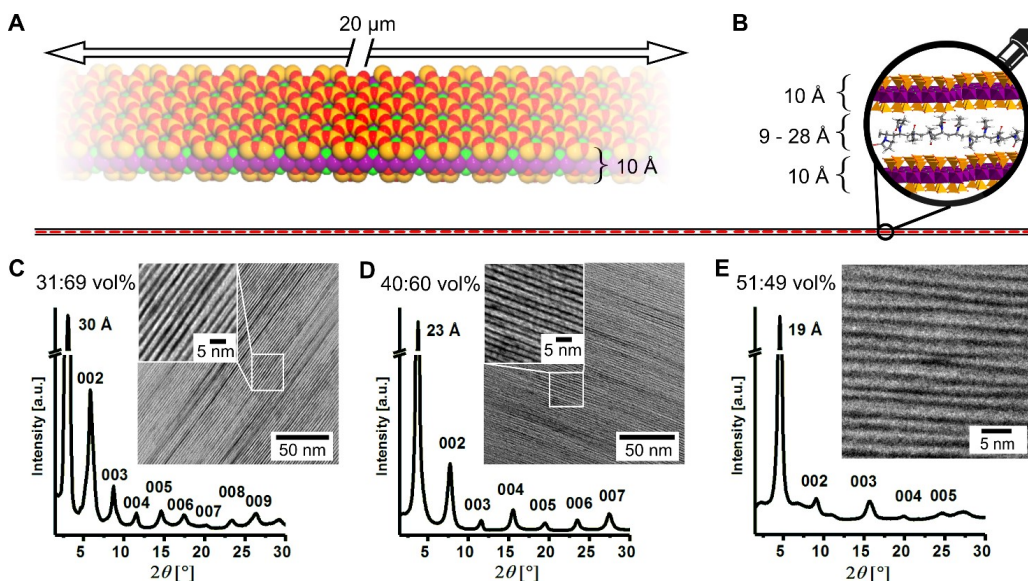


Figure 9.1: Schematic and microscopic images of ultra-anisotropic and extremely confined Hec/PVP Bragg stacks. (A) Space-filling model of one single Hec nanosheet emphasizing the anisotropy of the nanosheet and the corrugation of the clay nanosheet allowing for interdigitation with PVP. (B) True to scale schematic of the pronounced structural anisotropy. The ultra-high-aspect-ratio nanosheets stretch from left to right and have lateral dimensions much larger than the length of the PVP polymer chains. The gallery height is on the order of magnitude of the molecular dimensions. (C-D) XRD patterns of Hec31/PVP69 and Hec40/PVP60 (defect-free materials) showing intense 001-reflections and a rational series of basal reflections up to the ninth order. The cross-sectional TEM images show exceptionally periodic homogeneity of these hybrid films over large length scales. (E) XRD patterns and cross-sectional TEM image of Hec51/PVP49 displaying a random stacking of two gallery heights.

**In-plane and cross-plane thermal conductivities.** The in-plane and cross-plane thermal conductivities of the Hec/PVP hybrid Bragg stacks were characterized by lock-in thermography and photoacoustic measurements,<sup>[22,23,40]</sup> respectively. Since the density,  $\rho$ , and specific heat,  $c_p$ , are prerequisites for the thermal conductivity analysis, they were also determined experimentally by using helium pycnometry and differential scanning calorimetry (DSC) (Section 9.5.2), respectively. As the Hec volume fraction increases from 0 to 100%, the density increases from 1190 to 2730 kg m<sup>-3</sup> (Figure 9.2A). This is well captured by a volumefraction-based mixing model (dashed line in Figure 9.2A). Correspondingly, the specific heat decreases from 1140 to 890 J kg<sup>-1</sup> K<sup>-1</sup> (Figure 9.2B), which also follows the prediction by an effective medium model (Figure 9.12B). Both analyses indicate that despite the extreme polymer confinement the properties of the hybrid stacks could be described by linearly interpolating the properties of the two bulk constituents. The polymer confinement, however, leads to a significant increase in the glass transition temperature ( $T_g$ ) of PVP, with no discernable  $T_g$  below 250 °C even at the lowest Hec com-

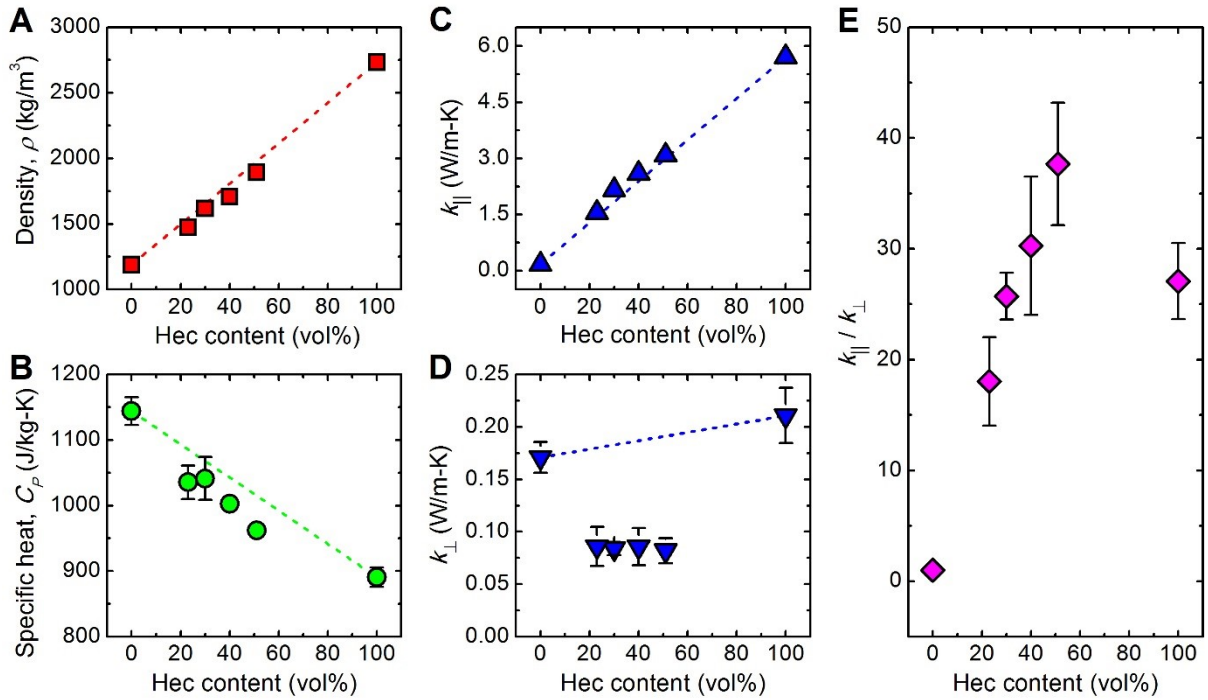


Figure 9.2: Direction-dependent thermal conductivities of Hec/PVP hybrid Bragg stacks. (A) Film density, (B) specific heat, and effective (C) in-plane and (D) cross-plane thermal conductivities, as a function of the Hec volume fraction. The red, green, and blue dashed lines in (A)-(D) show linear trends based on a simple mixing model,  $A(x) = (1-x)A(0\%) + xA(100\%)$ , where  $A$  represents  $\rho$ ,  $c_p$ ,  $k_{\parallel}$ , or  $k_{\perp}$ , and  $x$  denotes the Hec volume fraction. (E) Ratio of the in-plane to cross-plane thermal conductivities vs. the Hec volume fraction. For clarity, error bars smaller than the symbol size are not shown.

position (Figure 9.12A). Expectedly, the thermal conductivity of the Bragg stacks strongly depends on the direction. The in-plane thermal conductivity achieves its maximum,  $k_{\parallel,max} = 5.71 \text{ W m}^{-1} \text{ K}^{-1}$ , in Hec100/PVP0, which is even higher than typical in-plane thermal conductivities of natural micas (Figure 9.4A).<sup>[41]</sup> The lower end is given by the isotropic thermal conductivity of Hec0/PVP100, i.e.,  $k_{\parallel,min} = 0.17 \text{ W m}^{-1} \text{ K}^{-1}$  (only determined by photoacoustic characterization). The four hybrid Bragg stacks have in-plane thermal conductivities between these limiting values following a parallel mixing model (Figure 9.2C).

This is again surprising, as it implies that the confinement of PVP has no effect on the in-plane thermal conductivity of the Hec/PVP hybrid stacks compared to bulk PVP. The cross-plane thermal conductivity exhibits a broad minimum at  $k_{\perp} \approx 0.09 \text{ W m}^{-1} \text{ K}^{-1}$ , which is comparable to previously reported data for organo-clay laminates.<sup>[10]</sup> The deviation of the cross-plane thermal conductivities from an effective medium behavior (Figure 9.2D, dashed line) could be attributed to the Hec/PVP interfaces, which are the dominating contributors to the cross-plane thermal resistance, as discussed below. The thermal conductivity anisotropy,  $k_{\parallel}/k_{\perp}$ , de-

depends strongly on the hybrid composition, attaining a maximum of 38 in Hec51/PVP49 (Figure 9.2E). We note that this anisotropy is exceptionally high for electrically insulating hybrid materials<sup>[42]</sup> and outperforms natural nacre by a factor of  $\sim 20$ .<sup>[43]</sup> All in all, the structural perfection of the pure components and hybrid Bragg stacks translate into a record-high in-plane thermal conductivity and thermal transport anisotropy.

**Anisotropic mechanical properties.** The unique macroscopic orientation in the hybrid Bragg stacks allows us to track down the origin of their high thermal conductivity anisotropy by measuring their full mechanical tensors. The measurements were conducted by using BLS, which probes the phonon wave vector,  $\mathbf{q}$ , dependent sound velocity,  $\nu$ , through inelastic light scattering by thermally excited, high frequency (GHz) phonons.<sup>[20,21]</sup> Since the hybrid Bragg stacks are transversely isotropic, only  $\mathbf{q}$  vectors in a single plane containing the symmetry axis have to be considered. For such a  $\mathbf{q}$  vector, the direction can be denoted by  $\alpha$ , the angle between  $\mathbf{q}$  and the normal to the sample film, and because of symmetry  $\alpha$  can be restricted in the range from  $0^\circ$  to  $90^\circ$ . The measurements corresponding to  $\alpha = 0^\circ$ ,  $0^\circ < \alpha < 90^\circ$ , and  $\alpha = 90^\circ$  were conducted in the reflection, backscattering, and transmission scattering geometries, respectively, while the polarization of the phonon mode was selected using different incident and scattered light polarization configurations (e.g., VV for quasi-longitudinal (Q-L) and quasi-transverse (Q-T) modes, and VH for a pure-transverse (P-T) mode).<sup>[44]</sup> This flexibility of accessible parameters makes BLS particularly suitable for characterizing anisotropic or crystalline structures, as demonstrated in previous experiments on mica crystals. Since this work is the first one to apply the BLS technique to a hybrid Bragg stack material, we briefly outline the BLS measurement and data analysis.

Consider Hec31/PVP69 as an example. A typical BLS spectrum from the reflection geometry (inset to Figure 9.18A) displays a cross-plane longitudinal ( $L_\perp$ ) mode in the VV polarization configuration (Figure 9.18B). A typical BLS spectrum from the backscattering geometry (Figure 9.3A, top-right inset) depicts a Q-L and a Q-T mode in the VV polarization configuration (Figure 9.2A) and a weak P-T mode in the VH polarization configuration (Figure 9.3A, top-left inset). Comparatively richer information exists in a typical BLS spectrum from the transmission geometry (Figure 9.3B, top-right inset). In the VV polarization configuration, the BLS spectrum features an in-plane longitudinal ( $L_\parallel$ ) and a Q-L mode at a small laser incident angle,  $\beta$ , and an additional Q-T mode at a large  $\beta$  (Figure 9.3B). In the VH polarization configuration, a weak P-T mode at all  $\beta$  (Figure 9.3B, top-left inset) is clearly resolved. In the transmission BLS spectra, the intensity ratio of the Q-L and Q-T peaks yields additional information (Figure 9.19B) and the Q-T mode intensity increases

noticeably at higher Hec contents. By comparing the backscattering and transmission spectra, it becomes clear that the appearance of the Q-L and Q-T peaks in the latter (Figure 9.3B) results from the scattering of the laser beam internally reflected on the sample's backside.<sup>[45]</sup>

Based on the frequency shift,  $f$ , from the BLS spectrum and the phonon wave vector,  $\mathbf{q}$ , from the momentum conservation analysis, we calculated the sound velocity along a certain  $q$  as  $v = 2\pi f/|\mathbf{q}|$ . Whereas the reflection measurements give the  $v_{Q-L}$  at  $\alpha = 0^\circ$  and the transmission measurements result in the  $v_{Q-L}$  and  $v_{P-T}$  at  $\alpha = 90^\circ$ , the backscattering measurements provide sound velocities for all the Q-L, Q-T, and P-T modes at intermediate  $\alpha$  angles, as limited by the sample's refractive index. These direction-dependent sound velocities are reported in Figure 9.3C for Hec31/PVP69; additional data for the other samples are shown in Figure 9.20, A-D. Since sound velocities are intimately related to the elastic stiffness tensor in the framework of the Christoffel equation,<sup>[46,47]</sup> the availability of the former together with the measured sample densities (Figure 9.2A and Table 9.4) enables unique determination of the latter. For a transversely isotropic material, the elastic stiffness tensor contains five independent elastic constants (e.g.,  $C_{11}$ ,  $C_{12}$ ,  $C_{13}$ ,  $C_{33}$ , and  $C_{44}$ ).<sup>[48,49]</sup>

Through  $\chi^2$  fitting<sup>[50]</sup>, we obtained the elastic stiffness constants (Figure 9.20E and Table 9.4), which allow theoretical representation of the direction-dependent sound velocities (solid lines in Figure 9.3C and Figure 9.20, A-D) as well as determination of the engineering mechanical properties (Figure 9.3D and Table 9.5). In addition, we analyzed the error bars (standard deviations) of the quantities according to principles of uncertainty propagation (Section 9.5.5).

This analysis provides the first direction-dependent insights into the mechanical properties of hybrid Bragg stacks in general and of clay/polymer nanocomposites in particular. The Young's moduli,  $E_{\parallel}$  and  $E_{\perp}$ , and torsional shear modulus,  $G_{12}$ , all increase with increasing Hec volume fraction. The sliding shear modulus,  $G_{13}$ , however, decreases from 2.6 GPa in Hec0/PVP100 to 1.0 GPa in Hec100/PVP0. A reduction in polymer chain entanglement upon confinement could be the cause of the decrease in  $G_{13}$ . Since the elastic moduli of polymer nanocomposites depend on the specific filler-polymer and polymer-polymer interactions, a rationalization of the increase ( $E_{\parallel}$ ,  $E_{\perp}$ ,  $G_{12}$ ) or decrease (for  $G_{13}$ ) with Hec content would require computer simulations. All the mechanical moduli of the Bragg stacks display an effective medium behavior, assuming values between those of the two bulk components. We point out that even though the PVP chains are strongly confined between the adjacent Hec nanosheets (note  $R_{g,PVP} > 5(d_{XRD} - d_{Hec})$ ), bulk properties (e.g.,  $\rho_{PVP}$ ,  $\rho_{Hec}$ ) are sufficient to fully capture the BLS measurements. As expected from

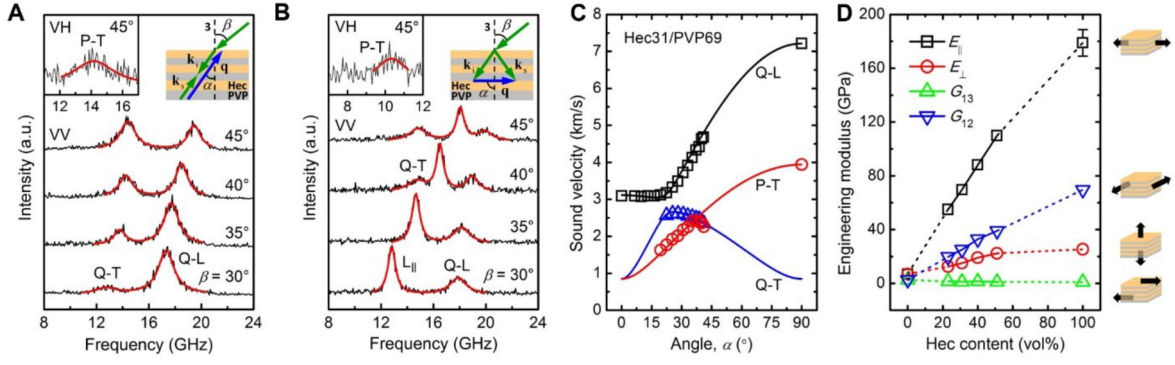


Figure 9.3: BLS measurements and strong mechanical anisotropy of Hec/PVP hybrid Bragg stacks. (A-B) Polarized BLS spectra (anti-Stokes side) of the Hec31/PVP69 hybrid stack film recorded in (A) the backscattering geometry with  $q$  forming a variable angle,  $\alpha$ , with the normal to the sample film (top-right inset to (A)) and (B) the transmission geometry with the phonon wave vector,  $q$ , directed in-plane ( $\alpha = 90^\circ$ ; top-right inset to (B)).  $k_i$  and  $k_s$  are the wave vectors of the incident and scattered light beams, respectively.  $\beta$  is the incident angle of the laser beam. The quasi-longitudinal (Q-L), quasi-transverse (Q-T), and in-plane longitudinal ( $L_{||}$ ) phonon modes are indicated in (A) and (B). The much weaker depolarized VH spectra of the pure transverse modes are shown in the top-left insets. Notice the correspondence between the Q-L and Q-T modes in (A) and those in (B). (C) Direction-dependent sound velocities of the observed acoustic phonons in the BLS spectra of Hec31/PVP69. The three solid lines indicate theoretical representations (Equations (S6)-(S8)) of the experimental sound velocities of the three modes. (D) Composition dependence of four engineering moduli. The moduli of the anisotropic hybrid films are extrapolated to those of the pure PVP and pure Hec films, as shown by the dashed lines. The four schematics beside (D) visualize the physical meanings of the corresponding moduli.

the structural anisotropy, the Young's moduli exhibit large differences between the in-plane and cross-plane directions (Figure 9.3D). As the Hec volume fraction increases from 0 to 100%, the mechanical anisotropy ratio,  $E_{||}/E_{\perp}$ , increases from 1 to 7. Concomitantly, the two characteristic Poisson's ratios,  $\nu_{13}$  and  $\nu_{12}$ , vary in ranges of 0.02-0.05 (nearly zero or cork-like values) and 0.34-0.41 (typical polymer values), respectively (Table 9.5). The reasonable values of the mechanical properties corroborate the validity of continuum mechanics at length scales of a few nanometers and in the presence of extreme polymer confinement.

In the last section, we summarize the new insights onto the anisotropic thermoelasticity that can be gained from this wholistic analysis. We firstly exploit the directly measured direction-dependent sound velocities, and secondly correlate the derived mechanical moduli to the direction-dependent thermal conductivities. We first apply a kinetic theory model,  $k = c_V \bar{v}_g \bar{\Lambda}/3$  to estimate the average phonon mean free path  $\bar{\Lambda}$  along different directions in the Bragg stacks.<sup>[51]</sup> We use  $C_V = C_P$  and  $\bar{v}_g = \bar{v}_{s,||} = (v_{Q-L,||} + v_{Q-T,||} + v_{P-T,||})/3$ ; a similar analysis is done for  $k_{\perp}$ .

The in-plane  $\bar{\Lambda}$  strongly depends on the hybrid composition, ranging from 14 Å for Hec100/PVP0 to 2 Å for Hec0/PVP100 (Figure 9.4A). We note that these Å values significantly underestimate the presence of longer ranged phonons, which are typically better described by a phonon mean free path accumulation function.<sup>[51,52]</sup> It is well known that thermal transport involves phonons over a wide range of frequencies which have different specific heat capacities, group velocities, and mean free paths. The underestimated  $\bar{\Lambda}$  in our analysis could be attributed to the from the BLS measurements, which mainly characterizes the propagation speed of a small fraction of the low frequency (long wavelength) phonons. These low frequency phonons carry only a negligible fraction of the overall heat. For the in-plane direction, the lateral size of the Hec nanosheets by far exceeds the average phonon mean free path. Hence, the high in-plane thermal conductivities are governed by the intrinsic material properties, not by the presence of grain boundaries between the aligned Hec nanosheets. The complementary analysis for  $k_{\perp}$  demonstrates a strong reduction of  $\bar{\Lambda}$  down to less than 1 Å (Figure 9.4B) with no discernible composition dependence along the cross-plane direction. Interfacial effects apparently dominate the thermal transport in this direction, which is better analyzed using a series resistance model (SRM, Figure 9.4C and F) as outlined by Losego et al.<sup>[10]</sup> The fitted value of the interfacial conductance,  $G_{Hec/PVP} = 89 \pm 8 \text{ MW m}^{-2} \text{ K}^{-1}$  (see Section 9.5.4), falls well into the range of reported values for other inorganic/organic interfaces.<sup>[4,53]</sup> The intercalation of PVP between the clay sheets leads to a strong reduction of the interfacial conductance, which is  $G_{Hec/Hec} = 219 \pm 28 \text{ MW m}^{-2} \text{ K}^{-1}$  for the pure hectorite.

We next address the correlation between the anisotropic mechanical moduli and thermal conductivities. Two distinct conclusions can be drawn. (i) In the direction parallel to the Hec nanosheets, a correlation between the thermal conductivity and all mechanical moduli is found. Along this direction the phonon mean free path is considerably shorter than the typical lateral size of a Hec nanosheet, rendering grain boundary effects insignificant. The influence of  $E_{\parallel}$ ,  $E_{\perp}$ , and  $G_{12}$  on the thermal transport dominates over  $G_{13}$  since the former moduli show a direct relation to the in-plane thermal conductivity.  $E_{\parallel}$  and  $G_{12}$  show a power scaling law close to one (0.93) between in-plane thermal conductivity and modulus ( $E_{\perp}$  scales with 0.38). Whereas we find a clear correlation between the moduli and the thermal conductivity, we cannot deduce which change in mechanical modulus causes which effect to the thermal transport. The applicability of a simple mixing model along the parallel direction as outlined in Figure 9.2 A-C is certainly surprising in view of the strong polymer confinement effect on the glass transition (Figure 9.12). (ii) In the direction perpendicular to the Hec nanosheets, the phonon mean free path is comparable to the periodicity of the Bragg stacks. Here, the composition dependence of

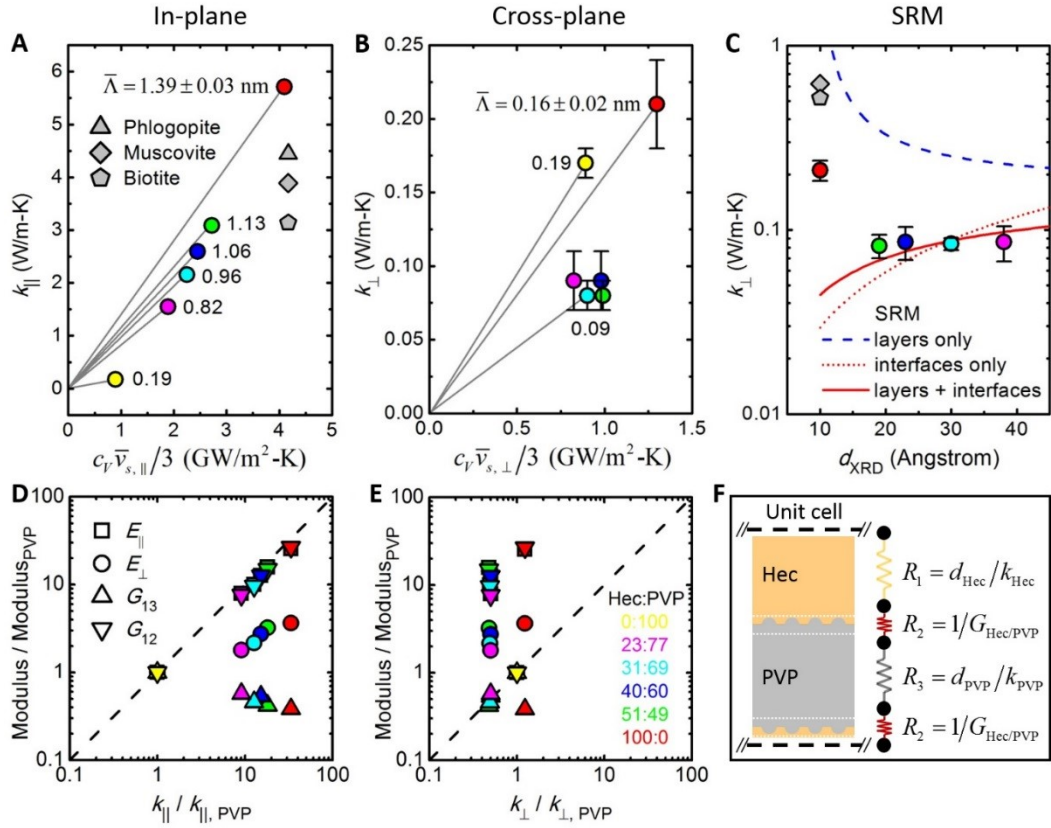


Figure 9.4: Analysis of anisotropic thermomechanical coupling in Hec/PVP hybrid Bragg stacks. (A) Effective in-plane thermal conductivity,  $k_{||}$ , vs.  $C_V \bar{v}_{S,||}/3$ . The yellow, purple, cyan, blue, green, and red colored symbols represent the Hec0/PVP100, Hec23/PVP77, Hec31/PVP69, Hec40/PVP60, Hec51/PVP49, and Hec100/PVP0 samples, respectively. The phlogopite data point is from our additional measurements; muscovite and biotite data points are from reference.<sup>[41]</sup> (B) Effective cross-plane thermal conductivity,  $k_{\perp}$ , vs.  $C_V \bar{v}_{S,\perp}/3$ . In (A) and (B), the numbers beside the data points indicate the average phonon mean free paths,  $\bar{\Lambda}$  (i.e., the slope of the gray lines). (C) Effective cross-plane thermal conductivity,  $k_{\perp}$ , vs. the basal spacing of the Bragg stacks. The red solid line is a fit to the experimental data based on the SRM shown in (F). As a comparison, the blue dashed line considers only the thermal resistances of the Hec and PVP layers, and the red dotted line considers only the thermal resistances of the Hec/PVP interfaces. (D) Normalized mechanical moduli vs. normalized effective in-plane,  $k_{||}$ . The dashed line shows a direct correlation between the two axes with a power of one. (E) Normalized mechanical moduli vs. normalized effective cross-plane thermal conductivity,  $k_{\perp}$ . In (D) and (E), the following values of the pure PVP film,  $E_{||} = E_{\perp} = 7.0$  GPa,  $G_{13} = G_{12} = 2.6$  GPa, and  $k_{||} = k_{\perp} = 0.17$  W m<sup>-1</sup> K<sup>-1</sup>, are used as references in the normalization. (F) A schematic of the SRM used to analyze the Hec/PVP interfacial thermal conductance.

the mechanical properties does not influence the reduction of the cross-plane thermal conductivity (vertical spread of the data points in Figure 9.4E). Thus, changes to the gallery height are insignificant, which indicates the overwhelming contribution of the interfacial conductance. Considering changes to the pure components we

find that reducing the sliding shear modulus  $G_{13}$  decreases the cross-plane thermal transport properties of the polymer component. The reduction in  $k_{\perp}$  of the hybrid stacks relative to pure hectorite correlates to losses in  $E_{\parallel}$ ,  $E_{\perp}$ , and  $G_{12}$  that apparently counteract the increase in  $G_{13}$ . Overall, the mechanical and thermal properties are uncorrelated along the perpendicular direction, and the thermal transport is governed by the Hec/PVP interfaces.

### 9.3 Conclusion

In conclusion, fully delaminated hectorite platelets can be processed into hybrid Bragg stacks with unique properties, with the polymer polyvinylpyrrolidone being the intercalated second component. Such long-range 1D ordered materials become accessible by simply spray coating the desired nematic dispersions of adjusted volume fractions, which at the same time controls the periodicity of the hybrid stacks down to the angstrom level. The macroscopic lattice alignment enables the determination of direction-dependent thermoelastic properties, which we assessed by thermal transport characterization techniques and Brillouin light spectroscopy. We found a record-high anisotropy between the in-plane and cross-plane thermal conductivities in clay/polymer hybrid materials. This is corroborated by the first report of direction-dependent Young's and shear moduli that are also strongly anisotropic. The effective gallery spacing, density, specific heat, and in-plane thermal conductivity were found to conform to composition-dependent simple mixing models. Despite the nanometer-level lattice periodicity and angstrom-level polymer confinement, the Christoffel-equation-based model, derived in the framework of continuum mechanics, remains applicable for determining the anisotropic elasticity. Of general relevance is the direction dependency of the way that the mechanical moduli and thermal conductivities correlate. In the in-plane direction, where grain boundaries are negligible relative to the phonon mean free path,  $E_{\parallel}$ ,  $E_{\perp}$ , and  $G_{12}$  directly correlate with the in-plane thermal conductivity. In the cross-plane direction, where the phonon mean free path is comparable to the lattice periodicity, the thermal transport is governed by the clay/polymer interfaces. We are convinced that a wholistic understanding of direction-dependent thermoelastic properties will have a broad impact on important applications such as electronic packaging and thermoelectrics. This contribution is only a first step towards this goal. More work needs to be done for the deterministic - maybe even independent - design of mechanical and thermal properties. Future studies should also address the role of enthalpic interaction at the clay/polymer interface, interdigitation of the confined polymer, size effects of the platelets, and other nanosheet materials.

## 9.4 Experimental Section

**Sample preparation.** The synthetic clay sodium fluorohectorite (Hec,  $[\text{Na}_{0.5}]^{\text{inter}}[\text{Mg}_{2.5}\text{Li}_{0.5}]^{\text{oct}}[\text{Si}_4]^{\text{tet}}\text{O}_{10}\text{F}_2$ ) was delaminated by immersing it into Millipore water (0.5 wt%). The aqueous PVP solution (1 wt%) was added in the desired weight ratio. The suspension was mixed for at least one day in an overhead shaker. The homogeneity of the suspension was crosschecked by SAXS measurements. Self-supporting films were prepared using a fully automatic spray coating system. Every spraying cycle is followed by a drying cycle of 90 s at a temperature of 55 °C. We prepared pure PVP, pure Hec, and four hybrid Hec/PVP films. The selfsupporting films were characterized by thermogravimetric analysis, XRD, and TEM. Additional information about the sample preparation can be found in Section 9.5.1.

**In-plane thermal conductivity measurements.** Lock-in thermography measures the temperature spreading across the free-standing samples upon thermal excitation by a focused laser beam with a modulated intensity. To prevent convective heat losses, the experiments are conducted in a vacuum chamber. The amplitude and phase data are extracted from the radial temperature distribution. The thermal diffusivity is then fitted by the slope method for thermally thin films. With the density, determined by helium pycnometry, and the specific heat, determined by DSC, the thermal conductivity can be calculated. More details are provided in Section 9.5.2.

**Cross-plane thermal conductivity measurements.** The photoacoustic method uses a modulated laser beam to periodically heat a transducer layer in intimate contact with the sample. The heat is converted into an acoustic wave propagating into a gas tight cell above the sample, which is filled with helium at 20 psi. A sensitive microphone detects the phase shift between the acoustic signal and the modulated laser by a lock-in amplifier. The frequency-dependent phase shift is then compared to a multilayer model, assuming one-dimensional heat transfer. Therefrom, the total layer resistance is obtained. With the film thickness determined by AFM, the effective thermal conductivity is calculated. More details are provided in Section 9.5.2.

**Brillouin light spectroscopy (BLS).** BLS measures the phonon dispersion,  $\omega(\mathbf{q})$ , by detecting the Doppler frequency shift,  $\omega$ , of the inelastically scattered light by sound waves (“phonons”) with a wave vector,  $\mathbf{q}$ . We recorded BLS spectra utilizing three scattering geometries (transmission, reflection, and backscattering) and two polarization configurations of the incident ( $\lambda = 532$  nm) and scattered light (polarized VV, depolarized VH), which allowed us to establish the nature of the observed phonons. We varied the incident angle to obtain the direction-dependent sound velocities necessary for the determination of the anisotropic elasticity. The elastic stiffness tensors were obtained from the representation of the direction-dependent sound velocities by the Christoffel equation assuming transverse isotropy. The characteristic Young’s moduli, shear moduli, and Poisson’s ratios of the Bragg stacks were subsequently calculated. More details can be found in Section 9.5.3.

**Acknowledgements:** We thank Sabine Rosenfeldt for conducting SAXS measurements on the gel samples. We also thank Marco Schwarzmann for preparing TEM samples and taking TEM micrographs. The Volkswagen Foundation funded this project through a Lichtenberg professorship. DFG RE 3550/2-1 provided additional support. Z.W., K.R., and G.F. acknowledge the financial support by ERC AdG SmartPhon (Grant No. 694977).

**Author Contributions:** M.R., J.B., and G.F. initialized the idea. T.S. explored and optimized the Hec/PVP system, fabricated the hybrid Bragg stacks, and characterized their structures. K.R. conducted the BLS experiments. A.P. conducted and analyzed the lock-in thermography measurements to obtain the in-plane thermal conductivity. P.H. performed and analyzed the photoacoustic characterization to obtain the cross-plane thermal conductivity and measured the sample densities. A.F.K. conducted additional lock-in thermography measurements and contributed to the lock-in thermography analysis. A.L. conducted and analyzed the DSC measurements to obtain the specific heat. Z.W. analyzed the BLS data and established the correlation between the mechanical moduli and thermal conductivity. Z.W., M.R., J.B., and G.F. wrote the manuscript. All authors have given approval to the final version of the manuscript.

**Conflict of interest:** The authors declare no conflict of interest.

## 9.5 Supporting Information

### 9.5.1 Sample preparation

#### Materials

The synthetic clay sodium fluorohectorite (Hec,  $[\text{Na}_{0.5}]^{\text{inter}}[\text{Mg}_{2.5}\text{Li}_{0.5}]^{\text{oct}}[\text{Si}_4]^{\text{tet}}\text{O}_{10}\text{F}_2$ ) was synthesized via melt synthesis followed by long-term annealing, according to an established procedure. The material featured a cation exchange capacity of  $1.27 \text{ mmol g}^{-1}$  (References<sup>[29,54]</sup>) Polyvinylpyrrolidone (PVP,  $M_w = 40000 \text{ g mol}^{-1}$ ) was provided by Sigma Aldrich.

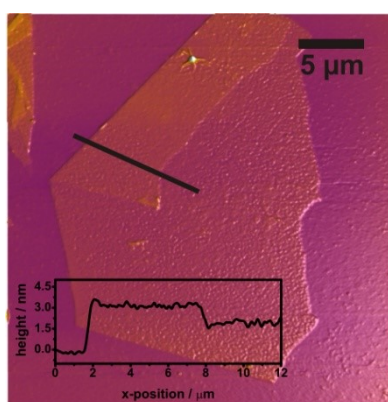


Figure 9.5: Atomic force microscopy image of a single delaminated Hec nanosheet. Reprinted with permission from Langmuir.<sup>[29]</sup> Copyright 2019 American Chemical Society.

#### Film preparation

For the delamination, the synthetic Hec was immersed into Millipore water (0.5 wt%). The complete delamination was studied by small angle X-ray scattering (SAXS).<sup>[30]</sup> The aqueous PVP solution (1 wt%) was added in the desired weight ratio. The suspension was mixed for at least 1 day in the overhead shaker. Homogeneity of the suspensions was cross-checked by SAXS measurements. All SAXS data were measured using the small-angle X-ray system “Double Ganesha AIR” (SAXSLAB, Denmark). The X-ray source of this laboratory-based system is a rotating anode (copper, MicroMax 007HF, Rigaku Corporation, Japan) providing a micro-focused beam. The data were recorded by a position sensitive detector (PILATUS 300 K, Dectris). To cover the range of scattering vectors between  $0.004\text{--}1.0 \text{ \AA}^{-1}$ , different detector positions were used. The measurements of the suspensions were done in 1 mm glass capillaries (Hilgenberg, code 4007610, Germany) at room temperature. To improve the detection limit of the in-house machine, the suspensions were first concentrated to  $\approx 10 \text{ wt\%}$  by centrifugation at 10000 rpm for 1 hour. A rational basal series was found for all suspensions, indicating that all clay nanosheets were

separated to exactly the same distance by water and PVP (Figure 9.6). Within experimental errors reaggregation to stacks of Hec can be excluded by the absence of a reflection typical for crystalline hydrated Hec phases at  $q = 0.65\text{-}0.41 \text{ \AA}^{-1}$ .

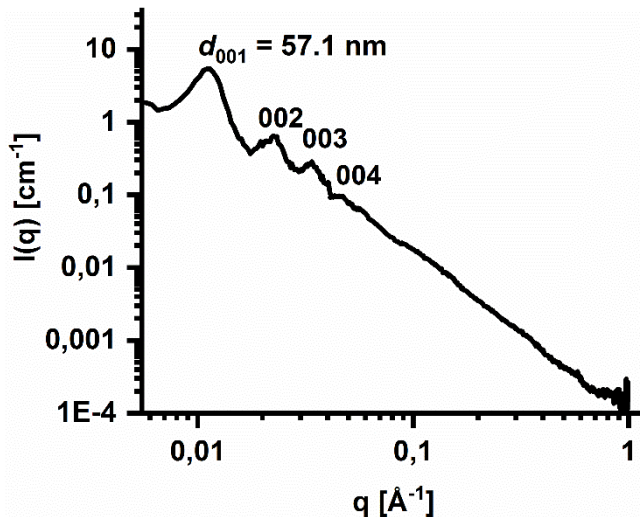


Figure 9.6: 1D SAXS pattern of the concentrated gel sample Hec40/PVP60.

The self-supporting films were prepared by spray coating. The fully automatic spray coating system was equipped with a SATA 4000 LAB HVLP 1.0 mm spray gun (SATA GmbH & Co. KG, Germany). Suspensions were sprayed on a corona-treated PET foil (optimont 501, bleher Folientechnik, Germany). The spraying and nozzle pressure were set constant at values of 2 and 4 bar, respectively. The round per flat fan control was set to 6 with a flow speed of  $3 \text{ mL s}^{-1}$ . The distance between the spraying gun and the substrate was 17 cm. The thickness of the suspension layer applied in one spraying step is  $\approx 2 \text{ }\mu\text{m}$  which corresponds to  $\approx 20 \text{ nm}$  dry nanocomposite film thickness. For drying the suspension layer, the sample is stopped under infrared lamps until evaporation of the solvent is complete. After every spraying cycle, a drying cycle of 90 s with a temperature of  $55 \text{ }^\circ\text{C}$  took place. The spraying/drying cycle is repeated until the desired barrier film thickness of  $50 \text{ }\mu\text{m}$  is obtained. Afterwards, the film was dried at  $100 \text{ }^\circ\text{C}$  for 3 days and peeled off from the PET foil to achieve self-supporting films. For characterization by photoacoustic analysis thinner films on the order of a few  $\mu\text{m}$  were spray coated onto clean 1 mm thick microscopy glass slides. In total, we prepared six samples, which are denoted as Hec0/PVP100, Hec23/PVP77, Hec31/PVP69, Hec40/PVP60, Hec51/PVP49, and Hec100/PVP0, respectively (Table 9.1). Throughout the manuscript, all samples are referred to by the nominal volume fractions (vol%) of Hec and PVP, respectively. To rule out compositional changes during spray coating, these ratios were cross-checked (Table 9.1) by TGA, using a Linseis STA PT 1600 (Linseis Messgeräte GmbH, Germany). Changes in mass observed upon heating in synthetic air up to  $800 \text{ }^\circ\text{C}$  were attributed to the combustion of PVP.

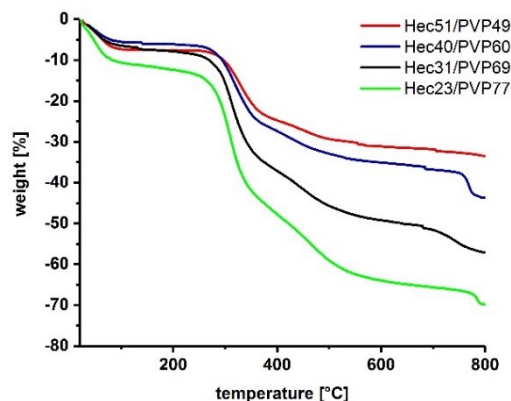


Figure 9.7: TGA curves of four hybrid Bragg stacks. The weight loss below 200 °C corresponds to the water.

XRD patterns for the films were recorded in Bragg-Brentano-geometry on an Empyrean diffractometer (PANalytical B.V.; the Netherlands) using Cu  $K_{\alpha}$  radiation ( $\lambda = 1.54187 \text{ \AA}$ ). The self-supporting films were placed on glass slides (Menzel-Gläser; Thermo Scientific). Prior to the XRD measurements, the samples were dried at 100 °C in a vacuum chamber for one week.

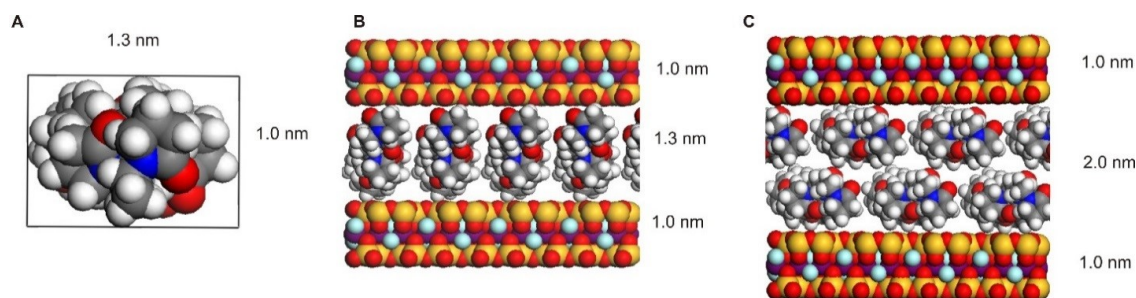


Figure 9.8: Space filling models. (A) PVP viewed along the polymer backbone chain. (B) Monolayer of PVP oriented with the longer principal axis perpendicular to the Hec nanosheet. (C) Bilayer of PVP lying in the plane of the Hec nanosheets.

As a measure of the quality of the one-dimensional crystallinity of the films, the coefficient of variation (CV) and the full width at half maximum (FWHM) were determined (Table 9.1). Large CV-values ( $\approx 3\%$ <sup>[39]</sup>) and large FWHM indicate non-rationality of the diffraction pattern as caused by a random interstratification of different interlayer heights. Assuming PVP and Hec densities of  $1.2 \text{ g cm}^{-3}$  and  $2.7 \text{ g cm}^{-3}$ , respectively, nominal d-spacings can be calculated for the various volume ratios ( $d_{\text{nominal}}$  in Table 9.1).<sup>[38]</sup> They agree reasonably with those obtained from XRD measurements ( $d_{\text{XRD}}$  in Table 9.1). In analyzing the cross-plane thermal conductivity using the series resistance model, we used the  $d_{\text{XRD}}$  values.

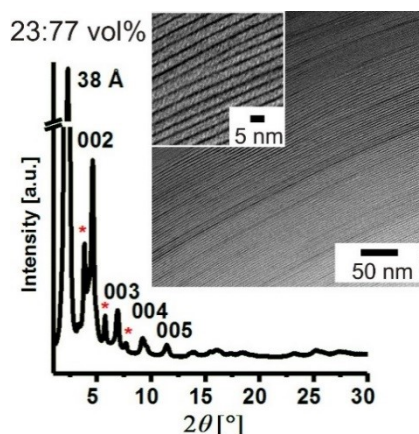


Figure 9.9: XRD pattern and TEM image of the nanocomposite film Hec23/PVP77. The red asterisks denote a second series of basal reflections of a minority phase ( $d = 2.3$  nm).

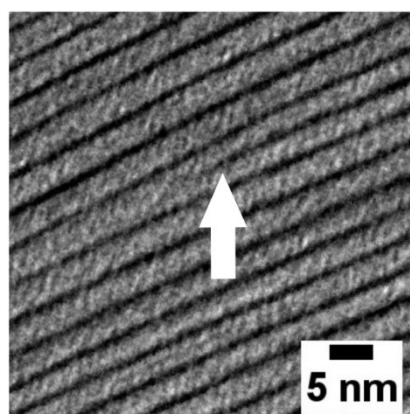


Figure 9.10: Lattice plane termination of a single Hec nanosheet.

Table 9.1: Overview of the structural and chemical characterization.

	nominal Hec:PVP ratio [wt%]	nominal Hec:PVP ratio [vol%]	PVP con- tent [ <sup>a</sup> ] [wt%]	PVP con- tent [ <sup>b</sup> ] [vol%]	$d_{nominal}$ [Å]	$d_{XRD}$ [Å]	gallery height (PVP) [ <sup>c</sup> ] [nm]	CV [%]	FWHM [° 2θ]
Hec100/PVP0	100:0	100:0	-	-	10	10	-	-	-
Hec51/PVP49	70:30	51:49	27	45	18	19	0.9	5.9	0.4
Hec40/PVP60	60:40	40:60	38	58	23	23	1.3	1.3	0.3
Hec31/PVP69	50:50	31:69	49	68	30	30	2.0	1.0	0.3
Hec23/PVP77	40:60	23:77	59	76	41	38	2.8	2.8	0.3
Hec0/PVP100	0:100	0:100	100	100	-	-	-	-	-

<sup>[a]</sup>determined by TGA; <sup>[b]</sup>calculated with the PVP content determined by TGA; <sup>[c]</sup>gallery height corresponds to the  $d$ -spacing minus the Hec platelt height of 1 nm.

SEM images were taken with a Zeiss LEO 1530 (Carl Zeiss AG, Germany) at an operating voltage of 3 kV. Cross sections were prepared by cutting with a razor blade. The samples with Hec were sputtered with 10 nm carbon.

Transmission electron microscopy (TEM) images were taken on a JEOL JEM-2200FS (JEOL GmbH, Germany) at an acceleration voltage of 200 kV. Cross-section pictures of the self-supporting films were prepared with a Cryo Ion Slicer IB-09060CIS (JEOL, Germany).

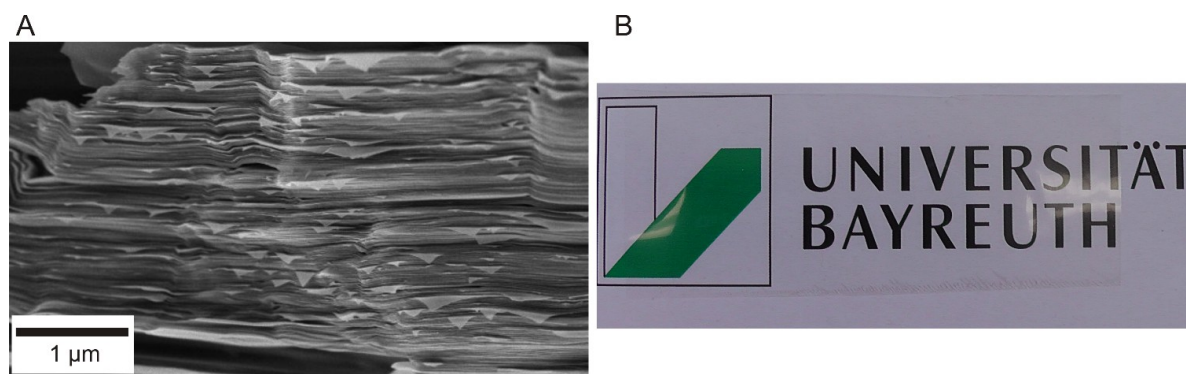


Figure 9.11: SEM image and photograph of the hybrid film. A) The SEM image displays the ordered arrangement of hectorite sheets at the macro-scale. B) As the hectorite platelets arrange highly ordered, light scattering is prevented and the films is transparent.

### 9.5.2 Thermal measurements

For the determination of the in-plane and cross-plane thermal conductivity, the density and the specific heat are needed. Therefore, Helium pycnometry and DSC were used. We determined the in-plane thermal diffusivity by lock-in thermography, and the cross-plane thermal conductivity by the photoacoustic method. Prior to the measurements, the samples were dried at 100 °C in a vacuum chamber for one week.

**Helium pycnometry** The density of the samples was measured by helium pycnometry. Therefore, an Ultrapyc 1200e (Quantachrome Instruments) was used. Prior to each measurement the volume of the empty measurement cell was measured. Afterwards, small pieces of the freestanding films were weighed into the sample cell with a nominal volume of 1.8 cm<sup>3</sup>. One hundred runs were performed to determine the volume of the films at room temperature. By knowing the mass (measured on a fine balance) and the volume, the density of the samples was calculated.

#### Differential scanning calorimetry

The specific heat was determined by DSC measurements according to the ASTM E1269 standard. The samples were freeze ground for better processability and con-

tact to the DSC pans. The measurements were performed on a TA instruments Discovery DSC 2500. An isothermal step (1h, 100 °C) was conducted prior to the measurement to ensure dry conditions. Then two heating cycles were used and only the second cycle evaluated. The temperature profile ranged from -40 to 250 °C using a heating rate of 20 K min<sup>-1</sup> with a nitrogen flow of 50 mL min<sup>-1</sup>.

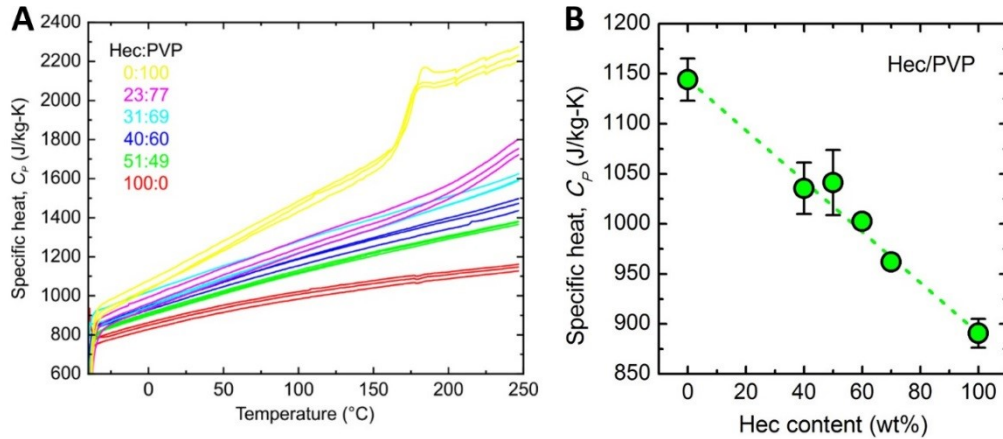


Figure 9.12: Temperature and composition dependencies of the specific heat. (A) Three samples per Hec/PVP composition were measured. The average specific heat at 25 °C was used to calculate the thermal conductivity. (B) The green dashed line shows the prediction by a simple mixing model,  $C_p(x) = (1-x)C_p(0\%) + xC_p(100\%)$ , with  $x$  being the hectorite weight fraction.

### Lock-in thermography

The in-plane thermal diffusivity of free-standing Hec/PVP stack films was obtained by lock-in thermography (LIT). The self-built LIT set-up is shown in Figure 9.13.

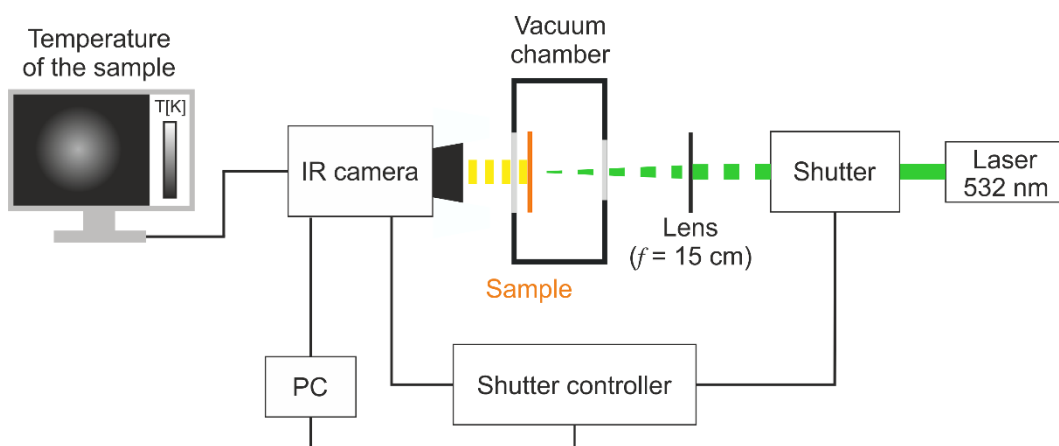


Figure 9.13: Scheme of the lock-in thermography set-up. The samples were measured in a vacuum chamber to avoid convective heat losses to the environment.

The sample is heated by a laser beam (Genesis MX 532-1000 SLM OPS, Coherent,  $\lambda = 532$  nm) focused onto the sample surface by a lens of 150 mm focal length. The intensity of the laser is modulated using a shutter (SH05/M, Thorlabs) controlled

by a shutter controller (SC10, Thorlabs). The emitted IR radiation of the sample surface is detected by an Infratec VarioCAM HD research IR camera (spectral window: 7.5-14  $\mu\text{m}$ ). The camera is equipped with a close-up lens. In this configuration, the minimum spatial resolution is 29  $\mu\text{m}$  (working distance: 33 mm). Since heat losses to the environment lead to an overestimation of the thermal diffusivity<sup>[23,55]</sup> all samples were measured under vacuum conditions ( $\sim 3 \times 10^{-3}$  mbar). Furthermore, all samples were coated with a 20 nm carbon layer for enhanced laser absorption. The coating of the sample was facing to the IR camera. LIT measurements were performed using Infratec's IRBISactiveonline software. Measurements were conducted at several lock-in frequencies between 0.219 and 1.765 Hz (depending on the Hec/PVP composition). Furthermore, each measurement was averaged over several (600-2000) lock-in periods to enhance the signal to noise ratio, with the first 60-100 periods being discarded. The software calculates automatically the amplitude and phase of the temperature oscillations (Figure 9.14). The red point marks the midpoint of the laser excitation and thus the midpoint of the radial distribution.

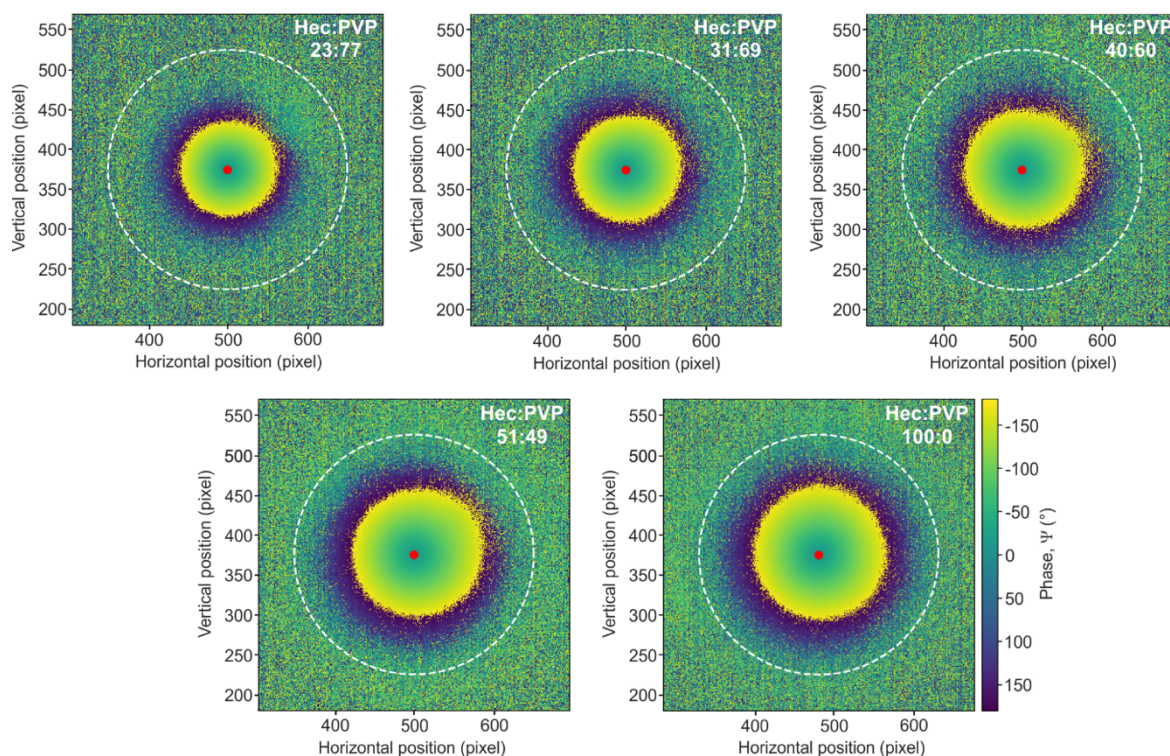


Figure 9.14: Exemplary two-dimensional phase images measured at a frequency of 1.111 Hz. The penetration depth of the temperature oscillations increases with increasing thermal diffusivity of the Hec/PVP films. The focal point of the laser is marked by a red point in the center of the IR image.

A self-written Python script is used to extract radial profiles for the phase and amplitude images (Figure 9.15). The thermal diffusivity is calculated from the phase and amplitude slopes according to the slope method of a thermally thin film<sup>[23]</sup>:

$$m_{\Psi} \cdot m_{\ln(T \cdot r^{0.5})} = \frac{\pi f_{lock-in}}{\alpha_{\parallel}} \quad (9.1)$$

Here,  $m_{\Psi}$  is the slope of the linear relation of the phase and the radial distance  $r$ ,  $m_{\ln(T \cdot r^{0.5})}$  is the slope of the linear relation of the natural logarithm of the amplitude  $T$  multiplied by the square root of the radial distance  $r$ ,  $f_{lock-in}$  is the lock-in frequency, and  $\alpha_{\parallel}$  is the in-plane thermal diffusivity.

Three films have been measured for each Hec/PVP composition. An average in-plane thermal diffusivity and a standard deviation were calculated for each composition, as summarized in Table 9.2.

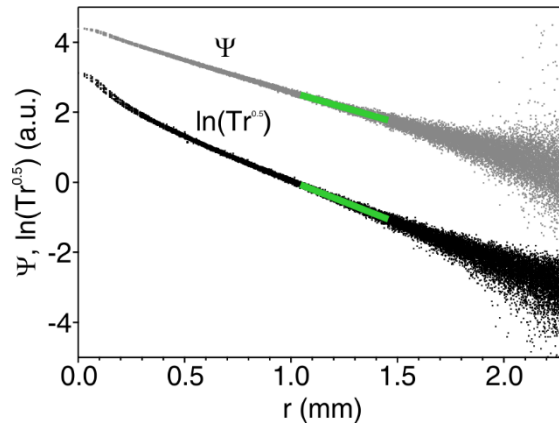


Figure 9.15: Exemplary phase  $\Psi$  and amplitude profiles. The green line indicates the region, where the linear fit was evaluated. This is sufficiently far away from the central excitation spot.

Table 9.2: In-plane thermal diffusivity values of Hec/PVP stack films. Three films per Hec/PVP composition were measured, based on which an average in-plane thermal diffusivity and a standard deviation were calculated.

Sample	In-plane thermal diffusivity ( $\text{mm}^2 \text{s}^{-1}$ )
Hec23/PVP77	$1.02 \pm 0.04$
Hec31/PVP69	$1.28 \pm 0.02$
Hec40/PVP60	$1.52 \pm 0.04$
Hec51/PVP49	$1.69 \pm 0.03$
Hec100/PVP0	$2.35 \pm 0.03$

The in-plane thermal conductivity was calculated from the in-plane thermal diffusivity ( $\alpha_{\parallel}$ ), density ( $\rho$ ), and specific heat ( $C_p$ ) as

$$k_{\parallel} = \alpha_{\parallel} \cdot \rho \cdot C_p \quad (9.2)$$

### Photoacoustic method

The cross-plane thermal conductivity was determined by the photoacoustic method. It uses the photoacoustic effect to determine the thermal properties of a sample. Therefore, a modulated laser beam ( $\lambda = 488 \text{ nm}$ ) periodically heats the sample. For good absorption of the laser energy a thin Au transducer layer ( $\sim 150 \text{ nm}$ ) was coated on the sample surface. For photoacoustic characterization, the samples were spray-coated on a glass substrate. The layout of the measurement cell above the sample is shown in Figure 9.16A. The gas tight cell is filled with a helium pressure of 20 psi. The microphone (Bruel&Kjaer, 4398-A-011) connected to the cell measures an acoustic wave, which is induced by the periodic heat conduction from the transducer layer surface to the gas phase. As shown in Figure 9.16B, the microphone is linked to a lock-in amplifier with integrated signal generator (Zurich instruments, HF2LI). The signal generator controls the electro-optic modulator (EOM, Conoptics, M25A) and therefore the frequency of the modulated laser beam. The acoustic signal detected by the microphone is then transferred into a phase and amplitude shift in relation to the modulation of the incident laser beam.

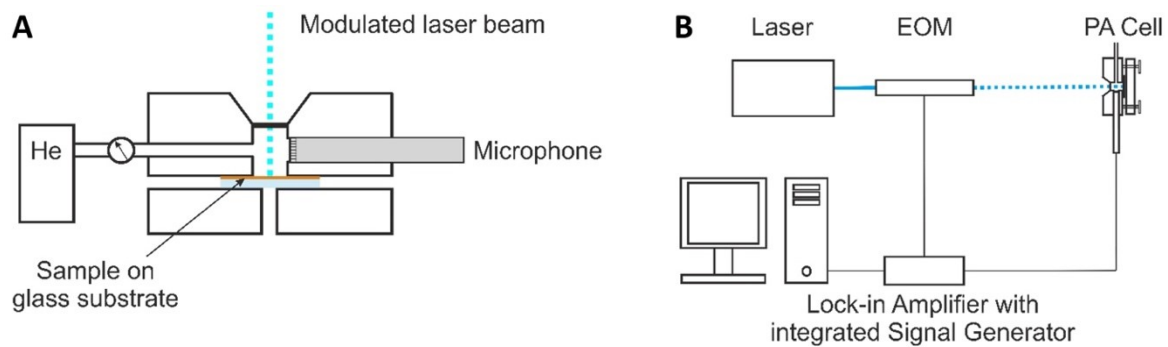


Figure 9.16: Scheme of photoacoustic measurements. (A) The photoacoustic cell. (B) The whole setup.

The phase shift is detected as a function of the frequency in a range from 110 Hz to 4000 Hz. The signal is then normalized with the phase shift signal of a thermally thick glass sample (1 mm) with known thermal properties. A representative frequency sweep is shown in Figure 9.17. The red line indicates the best fit according to the fitting procedure presented by Singh et al.<sup>[22]</sup> They used the generalized multilayer model of Hu et al.<sup>[56]</sup> assuming one-dimensional heat transfer. The unknown fitting parameters are the contact resistance between the gold layer and the

sample, the thermal diffusivity of the sample, and the contact resistance between sample and substrate. For thin films the fit is not very sensitive to the individual parameters, but to the total layer resistance. Therefore, only the total layer resistance is reported. From the total layer resistance it is possible to calculate the effective thermal conductivity by dividing with the thickness. The thickness of the samples was determined by AFM measurements. The values of the total layer resistance and sample thickness are summarized in Table 7.3. For each Hec/PVP ratio samples with three different thicknesses were measured to exclude influences from the sample thickness.

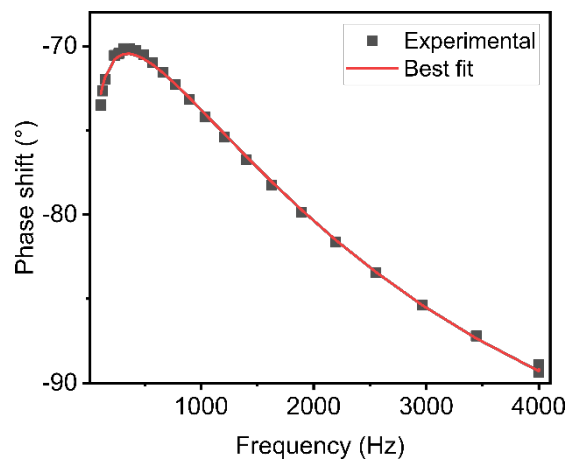


Figure 9.17: Normalized photoacoustic phase signal. Representative photoacoustic measurement of the Hec31/PVP69 sample with a thickness of  $1.979 \mu\text{m}$ . The red line shows the best fit.

### 9.5.3 Brillouin light spectroscopy

BLS measures the phonon dispersion, i.e., the wave vector,  $\mathbf{q}$ , dependent sound velocity,  $v_i(\mathbf{q})$ , by detecting the Doppler frequency shift,  $f$ , in laser light inelastically scattered by sound waves (“phonons”). Since the phonon modes in question are thermally populated, the Bragg condition for light scattering is satisfied independent of the scattering angle, in contrast to the kindred time-domain (“picosecond ultrasonic”) techniques that require external phonon injection via special sample preparation. Since the latter typically involves deposition of non-transparent metallic transducer films, they also do not readily allow for transmission and backscattering measurements, further limiting the potential of these techniques for probing anisotropic materials.

Assuming a planar sample, BLS can be conducted in three scattering geometries: transmission, reflection, and backscattering. For angle-dependent measurements in the transmission and reflection geometries, the laser source ( $\lambda = 532 \text{ nm}$ ) was

Table 9.3: Summary of the photoacoustic measurements. The total layer resistance, the thickness, and the resulting effective cross-plane thermal conductivity are given for each sample.

Sample	Total layer resistance [mm <sup>2</sup> K W <sup>-1</sup> ]	Thickness [ $\mu$ m]	Effective cross-plane thermal conductivity [W m <sup>-1</sup> K <sup>-1</sup> ]
Hec100/PVP0	1.58	0.28	0.177
Hec100/PVP0	2.55	0.595	0.234
Hec100/PVP0	4.34	0.94	0.217
Hec51/PVP49	3.69	0.255	0.069
Hec51/PVP49	7.74	0.722	0.093
Hec51/PVP49	11.53	0.957	0.083
Hec40/PVP60	6.54	0.463	0.071
Hec40/PVP60	14.03	1.139	0.081
Hec40/PVP60	18.96	1.987	0.105
Hec31/PVP69	8.20	0.744	0.091
Hec31/PVP69	17.58	1.382	0.079
Hec31/PVP69	24.06	1.979	0.082
Hec23/PVP77	8.81	0.568	0.064
Hec23/PVP77	17.45	1.677	0.096
Hec23/PVP77	26.37	2.568	0.097
Hec0/PVP100	2.26	0.351	0.155
Hec0/PVP100	4.50	0.792	0.176

<sup>[a]</sup>determined by TGA; <sup>[b]</sup>calculated with the PVP content determined by TGA; <sup>[c]</sup>gallery height corresponds to the  $d$ -spacing minus the Hec platelt height of 1 nm.

mounted on a goniometer and rotated around the sample, similar to a wide-angle X-ray (WAXS) setup. For the transmission geometry (top-right inset to Figure 9.3B), the propagation vector,  $\mathbf{q}$ , of the sound wave lies in the plane of the sample and its modulus,  $|\mathbf{q}|$ , is independent of the refractive index according to  $|\mathbf{q}|_{\parallel} = (4\pi/\lambda)\sin\beta$ , with  $\beta$  being the light incident angle. For the reflection geometry, the Bragg condition is fulfilled for sound waves with  $\mathbf{q}$  along the normal to the sample plane, so that  $|\mathbf{q}|_{\perp} = (4\pi/\lambda)\sqrt{n^2 - \sin^2\beta}$ , with  $n$  being the refractive index of the sample.<sup>[20]</sup> In order to find  $n$ , several points at different  $\beta$  were acquired, and then fit linearly;  $n$  was determined under the constraint that the fit has to pass through the ori-

gin (Figure 9.18A), and the obtained values are reported in Table 9.4. In contrast to the transmission geometry, the range of the dispersion relationship that can be scanned by varying  $|\mathbf{q}|_{\perp}$  is more restricted due to refraction of the laser beam at the air-sample boundary. Finally, backscattering measurements can be conducted, where the incident and scattered light traverse the same path, and the sample is mounted on a rotating stage with angular gradation marks. Only a single dispersion point, corresponding to  $\mathbf{q}$  directed opposite to  $\mathbf{k}_i$  in the film and of a magnitude,  $|\mathbf{q}| = (4\pi n/\lambda)$ , is accessible in the backscattering geometry, but all possible  $\mathbf{q}/|\mathbf{q}|$  directions can be probed. Because backscattering measurements use the same lens for focusing the incident and collimating scattered light, the alignment of the setup is generally much easier, so that all the backscattering spectra were acquired with microscope objectives (typically 10x) to reduce the spectrum accumulation time.

From the given formulas, it is easy to see that the Brillouin frequency shift does not exceed  $2nv/\lambda$ , where  $v$  is sound velocity. These frequencies render viscoelasticity effects negligible and are detected using a high-resolution six-pass Tandem Fabry Perot (TFP) interferometer (JRS Instruments, Switzerland) optimized for the 1-50 GHz range. Values still further out on the dispersion relationship can be accessed using, for example, picosecond ultrasonic interferometry (PUI), but at the expense of great effort and without any gain in information for the problem at hand.<sup>[57]</sup> Finally, BLS also offers direct access to the shear moduli, simply by analyzing scattered light in different polarizations: VV (i.e., vertical incident and vertical scattered light) corresponds to quasi-longitudinal and quasi-transverse phonon modes, and VH (i.e., vertical incident and horizontal scattered light) to the pure-transverse phonon mode (for transversely isotropic samples, HV does not show a transverse peak). Before the BLS measurements, the samples were dried at 100 °C in a vacuum chamber for one week to remove any residual water content.

Based on the BLS-measured direction-dependent sound velocities, we obtained the elastic tensor within the framework of the Christoffel equation.<sup>[46,47]</sup>

$$\begin{bmatrix} \Gamma_{11} - \rho v^2 & \Gamma_{12} & \Gamma_{13} \\ \Gamma_{21} & \Gamma_{22} - \rho v^2 & \Gamma_{23} \\ \Gamma_{31} & \Gamma_{32} & \Gamma_{33} - \rho v^2 \end{bmatrix} \begin{bmatrix} u_1 \\ u_2 \\ u_3 \end{bmatrix} = \begin{bmatrix} 0 \\ 0 \\ 0 \end{bmatrix}, \quad (9.3)$$

where  $\rho$  is the density of the sample,  $v$  is the sound velocity,  $\mathbf{u} = [u_1, u_2, u_3]^T$  is the displacement vector, and  $\Gamma_{ik}(i, k = 1, 2, 3)$  is the Christoffel stress, which is defined as

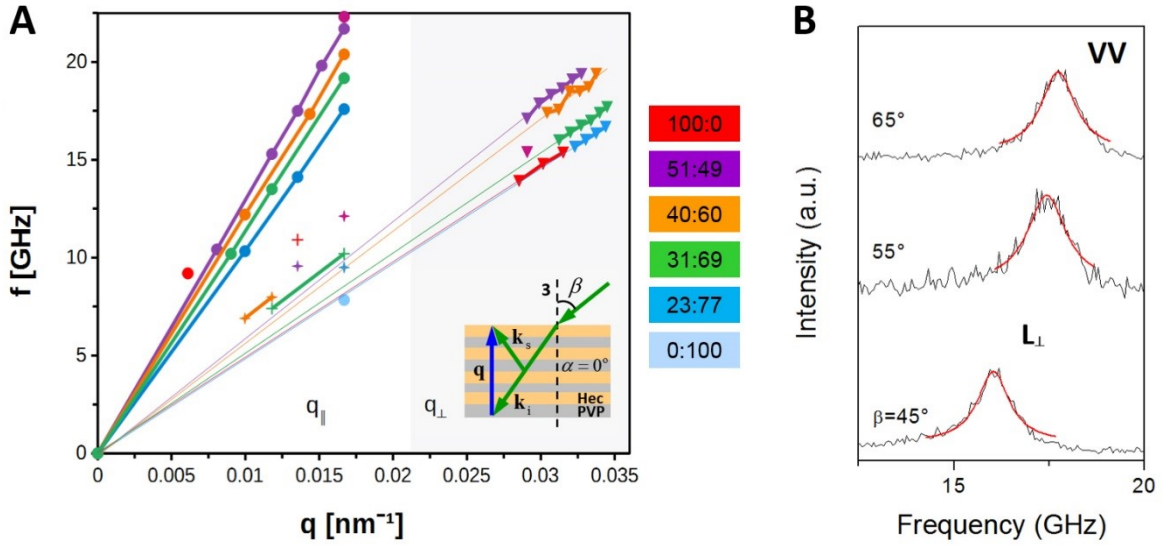


Figure 9.18: BLS experiments in the reflection geometry. (A) Dispersion (frequency vs. wave vector) of the longitudinal (L) and transverse (T) phonons in the hybrid stacks and the two constituent components (see the color code) obtained from the polarized (VV) and depolarized (VH) BLS spectra recorded in the reflection geometry (inset). (B) Typical VV spectra of the Hec31/PVP69 hybrid film at three laser incident angles.

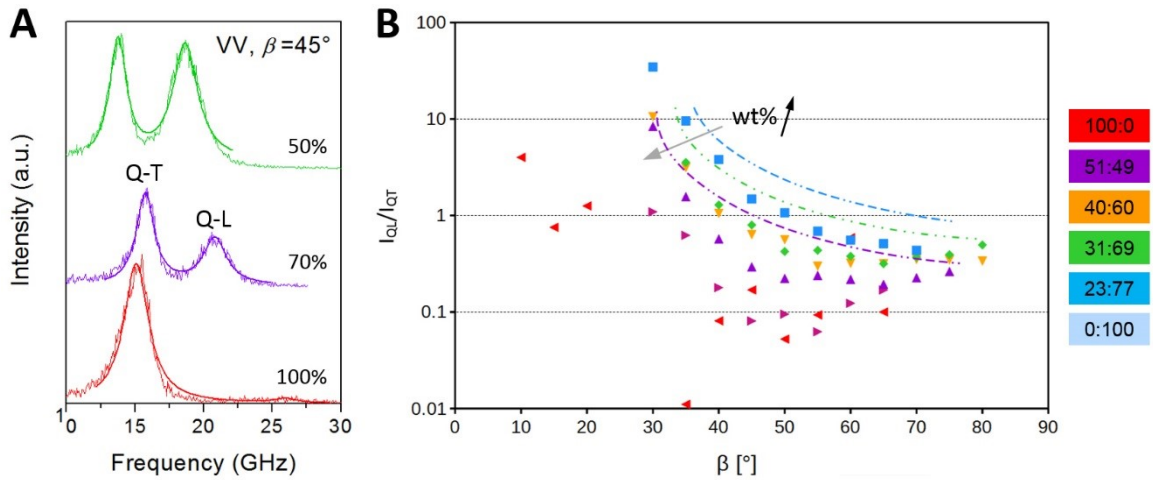


Figure 9.19: BLS spectra and peak intensity. (A) Polarized (VV) BLS spectra recorded in the backscattering geometry (inset to Figure 9.3A) for two hybrid stacks and the pure Hec film at an incidence angle of  $45^\circ$ . (B) The intensity ratio of the Q-L to Q-T peaks in (A) vs. the laser incident angle.

$$\Gamma_{ik} = \sum_{j=1}^3 \sum_{l=1}^3 C_{ijkl} n_j n_l. \quad (9.4)$$

Here,  $C_{ijkl}$  denotes an element of the 4<sup>th</sup> rank elastic tensor, and  $\mathbf{n} = [n_1, n_2, n_3]^T$  represents the phonon propagation direction. For a transversely isotropic material,

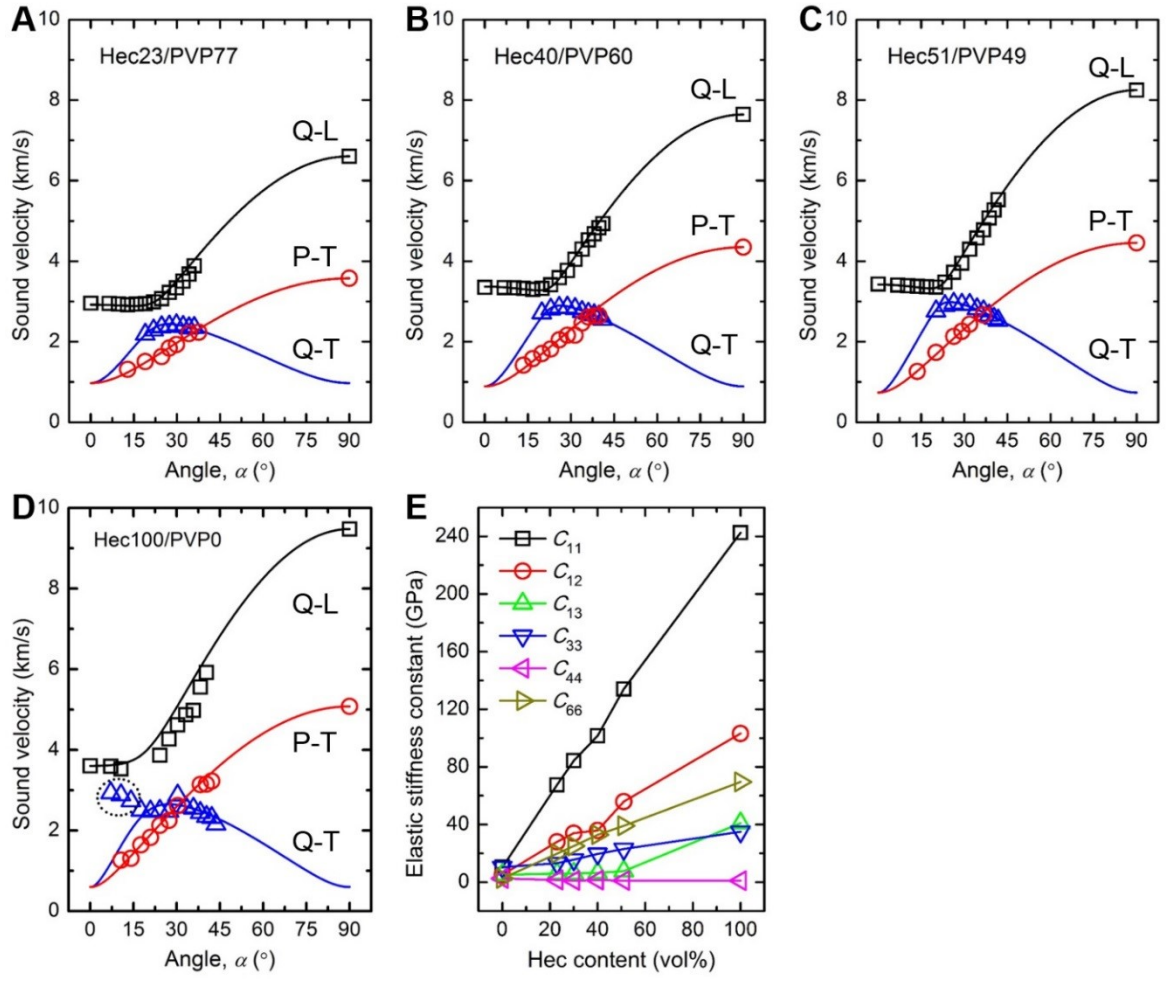


Figure 9.20: Direction-dependent sound velocities of hybrid stack films. (A) Hec23/PVP77, (B) Hec40/PVP60, (C) Hec51/PVP49, and (D) Hec100/PVP0 (the data points in the dotted circle were not used in the fitting). Q-L, P-T, and Q-T represent the quasi-longitudinal, pure-transverse, and quasi-transverse phonon modes, respectively. (E) Variation of the elastic stiffness constants with the Hec volume fraction.

the elastic tensor, in the Voigt notation, has the following form.<sup>[48]</sup>

$$C = \begin{bmatrix} C_{11} & C_{12} & C_{13} & & & \\ C_{12} & C_{11} & C_{13} & & & \\ C_{13} & C_{13} & C_{33} & & & \\ & & & C_{44} & & \\ & & & & C_{44} & \\ & & & & & C_{66} = \frac{C_{11}-C_{12}}{2} \end{bmatrix}, \quad (9.5)$$

and contains five independent stiffness constants. After some algebra, the sound velocities of the Q-L, Q-T, and P-T modes along a direction defined by  $\alpha$  can be represented as follows,

$$v_{Q-L}(\alpha) = \sqrt{\frac{-A_1 + \sqrt{A_1^2 - 4A_2}}{2\rho}} \quad (9.6)$$

$$v_{Q-T}(\alpha) = \sqrt{\frac{-A_1 + \sqrt{A_1^2 - 4A_2}}{2\rho}} \quad (9.7)$$

$$v_{P-T}(\alpha) = \sqrt{\frac{A_3}{\rho}} \quad (9.8)$$

where,

$$A_1 = -(\sin^2\alpha C_{11} + \cos^2\alpha C_{33} + C_{44}) \quad (9.9)$$

$$A_2 = \sin^4\alpha C_{11}C_{44} + \sin^2\alpha \cos^2\alpha (C_{11}C_{33} - C_{13}^2 - 2C_{13}C_{44}) + \cos^4\alpha C_{33}C_{44}. \quad (9.10)$$

$$A_3 = \sin^2\alpha C_{66} + \cos^2\alpha C_{44}. \quad (9.11)$$

Through nonlinear  $\chi^2$  fitting of the BLS-measured sound velocities (i.e.,  $v$  vs.  $\alpha$ ) with Equations 9.6-9.8, we obtained the elastic stiffness constants as well as their uncertainties.<sup>[50]</sup> The  $\chi^2$  is defined as

$$\chi^2 = \sum_i \frac{[v_{i,fit}(C_{11}, C_{12}, C_{13}, C_{33}, C_{44}, \alpha) - v_{i,exp}(\alpha)]^2}{(\Delta v_{i,exp})^2}, \quad (9.12)$$

where  $v_{i,fit}$  and  $v_{i,exp}$  are the fitted and experimental sound velocities, respectively,  $\Delta v_{i,exp}$  is the uncertainty of the measured sound velocity, and the summation is over all experimental sound velocities. By considering the uncertainties of the measured angles, refractive indices, and phonon frequencies, we estimated  $\Delta v_{i,exp}$  to be  $0.02v_{i,exp}$ . We imposed the following constraints for the elastic stiffness constants<sup>[58]</sup>: (1)  $C_{11} > |C_{12}|$ , (2)  $C_{44} > 0$ , and (3)  $C_{33}(C_{11} + C_{12}) > 2C_{13}^2$ , which ensures positive Young's and shear moduli. The availability of experimental data for all the Q-L, Q-T, and P-T modes allows unique determination of  $C_{11}$ ,  $C_{12}$ ,  $C_{13}$ ,  $C_{33}$ , and  $C_{44}$ .

After that, we calculated the engineering mechanical properties,<sup>[48]</sup> which include the in-plane Young's modulus ( $E_{\parallel}$ ), cross-plane Young's modulus ( $E_{\perp}$ ), sliding shear modulus ( $G_{13}$ ), torsional shear modulus ( $G_{12}$ ), and two characteristic Poisson's ra-

tios ( $u_{13}$  and  $u_{12}$ ). Note that only five of the engineering mechanical properties are independent (typically,  $E_{\parallel}$ ,  $E_{\perp}$ ,  $G_{13}$ ,  $G_{12}$ , and one of  $u_{13}$  and  $u_{12}$  are chosen). Also note that to be consistent with the direction-dependent thermal conductivity results, we used subscripts, “ $\parallel$ ” and “ $\perp$ ”, to represent directions parallel and perpendicular to the sample film, respectively, rather than directions parallel and perpendicular to the “3”-axis (i.e., the symmetry axis), as seen in typical analysis of transversely isotropic materials. The relevant mechanical properties are summarized in Tables 9.4 and 9.4.

Table 9.4: Summary of elastic stiffness constants. Composition (Hec vol%, Hec wt%), density ( $\rho$ ), refractive index (n), and elastic stiffness constants ( $C_{11}$ ,  $C_{22}$ ,  $C_{33}$ ,  $C_{44}$ ,  $C_{55}$ ,  $C_{66}$ ) of the Hec/PVP hybrid Bragg stack films.

Sample ID	Hec vol%	Hec wt%	$\rho$ (g/cm <sup>3</sup> )	n	$C_{11}$ (GPa)	$C_{22}$ (GPa)	$C_{33}$ (GPa)	$C_{44}$ (GPa)	$C_{55}$ (GPa)	$C_{66}$ (GPa)
Hec0/PVP100	0	0	1.20	1.53*	10.4	5.2	5.2	10.4	2.6	2.6
Hec23/PVP77	23	40	1.55	1.54	67.6 $\pm 1.7$	28.0 $\pm 1.9$	6.0 $\pm$ 1.2	13.2 $\pm 0.3$	1.5 $\pm$ 0.1	19.8 $\pm 0.5$
Hec31/PVP69	31	50	1.62	1.50	84.3 $\pm 1.5$	34.0 $\pm 1.8$	6.1 $\pm$ 1.5	15.7 $\pm 0.3$	1.2 $\pm$ 0.2	25.1 $\pm 0.5$
Hec40/PVP60	40	60	1.74	1.47	101.6 $\pm 1.8$	35.9 $\pm 2.2$	6.5 $\pm$ 1.8	19.7 $\pm 0.4$	1.4 $\pm$ 0.1	32.9 $\pm 0.6$
Hec51/PVP49	51	70	1.97	1.45	134.1 $\pm 2.2$	55.9 $\pm 2.9$	7.7 $\pm$ 2.3	23.0 $\pm 0.5$	1.1 $\pm$ 0.1	39.1 $\pm 0.9$
Hec100/PVP0	100	100	2.70	1.40	242.5 $\pm 6.2$	103.2 $\pm 6.7$	40.9 $\pm 5.2$	35.0 $\pm 0.9$	1.0 $\pm$ 0.1	69.6 $\pm 1.2$

\*Source:

<https://refractiveindex.info/?shelf=organic&book=polyvinylpyrrolidone&page=Konig>.

#### 9.5.4 Evaluation of interfacial thermal conductance

The SRM shown in Figure 9.4F illustrates a hybrid stack unit cell consisting of one Hec layer and one PVP layer. We describe the corrugation of the Hec nanosheet (Figure 9.1B) by a thermal interface conductance,  $G_{Hec/PVP}$ . For the unit cell in Figure 9.4F, the total thermal resistance can be calculated as  $\frac{d_{XRD}}{k_{\perp}} = \frac{d_{Hec}}{k_{Hec}} + \frac{d_{PVP}}{k_{PVP}} + \frac{2}{NG_{Hec/PVP}}$ , where  $d_{XRD}$  is the basal spacing as determined by XRD (Table 9.1),  $k_{\perp}$  is the effective cross-plane thermal conductivity,  $d_{Hec} = 10 \text{ \AA}$ , and  $d_{PVP} = d_{XRD} - d_{Hec}$ . For the thermal conductivity of the two components, we used the following values:  $k_{Hec} = 5.71 \text{ W m}^{-1} \text{ K}^{-1}$ , and  $k_{PVP} = 0.17 \text{ W m}^{-1} \text{ K}^{-1}$ . The Hec/PVP interfacial

Table 9.5: Summary of engineering mechanical properties. Composition (Hec vol%, Hec wt%) and engineering mechanical properties of the Hec/PVP hybrid Bragg stack films.  $E_{\parallel}$ : in-plane Young's modulus;  $E_{\perp}$ : cross-plane Young's modulus;  $G_{13}$ ,  $G_{23}$ : sliding shear moduli;  $G_{12}$ : torsional shear modulus;  $\nu_{13}$ ,  $\nu_{23}$ ,  $\nu_{12}$ : Poisson's ratios ( $\nu_{13}$  represents the strain response in the  $j$ -direction due to a stress in the  $i$ -direction).

Sample ID	Hec vol%	Hec wt%	$E_{\parallel}$ (GPa)	$E_{\perp}$ (GPa)	$E_{\parallel}/E_{\perp}$	$G_{13} = G_{23}$ (GPa)	$G_{12}$ (GPa)	$\nu_{13} = \nu_{23}$	$\nu_{12}$
Hec0/PVP100	0	0	7.0	7.0	1	2.6	2.6	0.33 (assumed)	0.33 (assumed)
Hec23/PVP77	23	40	55.0 ± 2.5	12.5 ± 0.4	4.4	1.5 ± 0.1	19.8 ± 0.5	0.06 ± 0.01	0.39 ± 0.03
Hec31/PVP69	31	50	69.7 ± 2.3	15.1 ± 0.4	4.6	1.2 ± 0.2	25.1 ± 0.5	0.05 ± 0.01	0.39 ± 0.02
Hec40/PVP60	40	60	88.1 ± 2.6	19.1 ± 0.5	4.6	1.4 ± 0.1	32.9 ± 0.6	0.05 ± 0.01	0.34 ± 0.02
Hec51/PVP49	51	70	109.9 ± 3.5	22.4 ± 0.6	4.9	1.1 ± 0.1	39.1 ± 0.9	0.04 ± 0.01	0.41 ± 0.02
Hec100/PVP0	100	100	178.9 ± 9.9	25.4 ± 2.6	7.0	1.0 ± 0.1	69.6 ± 1.2	0.12 ± 0.02	0.29 ± 0.06

conductance,  $G_{Hec/PVP}$ , is determined by least squares fitting of the experimental  $k_{\perp}$  data (red solid line in Figure 9.4C) to be  $89 \pm 8 \text{ MW m}^{-2}\text{K}^{-1}$ , which falls well into the range of interfacial conductance reported for inorganic/organic interfaces.<sup>[4,53]</sup> We also obtained the Hec/Hec interfacial conductance,  $G_{Hec/Hec} = 219 \pm 28 \text{ MW m}^{-2}\text{K}^{-1}$ , by considering a unit cell consisting of one Hec layer and one Hec/Hec interface (i.e.,  $\frac{d_{XRD}}{k_{\perp}} = \frac{d_{Hec}}{k_{Hec}} + \frac{1}{G_{Hec/Hec}}$ ).

### 9.5.5 Uncertainty analysis

The uncertainties (standard deviations) of the data reported in this work were analyzed by taking into account the instrument accuracy, repetitive measurements, and propagation of uncertainties. The sound velocities were estimated to have an error bar of 2%. The uncertainties of the elastic stiffness constants were determined according to Zgonik et al.<sup>[50]</sup> The uncertainties of the engineering mechanical properties were calculated according to principles of uncertainty propagation. For instance,

$$E_{\perp} = C_{33} - \frac{2C_{13}^2}{C_{11} + C_{12}} \quad (9.13)$$

$$\Delta E_{\perp} = \sqrt{\sum_{ij=11,12,13,33} \left( \frac{\delta E_{\perp}}{\delta C_{ij}} \right)^2 (\Delta C_{ij})^2 + \sum_{\substack{ij,kl=11,12,13,33 \\ ij < kl}} 2 \frac{\delta E_{\perp}}{\delta C_{ij}} \frac{\delta E_{\perp}}{\delta C_{kl}} \Delta C_{ij|kl}} \quad (9.14)$$

where  $\frac{\delta E_{\perp}}{\delta C_{11}} = \frac{2C_{13}^2}{(C_{11}+C_{12})^2}$ ,  $\frac{\delta E_{\perp}}{\delta C_{12}} = \frac{2C_{13}^2}{(C_{11}+C_{12})^2}$ ,  $\frac{\delta E_{\perp}}{\delta C_{13}} = \frac{4C_{13}}{C_{11}+C_{12}}$ , and  $\frac{\delta E_{\perp}}{\delta C_{33}} = 1$ . Similar expressions can be derived for the other engineering moduli and the Poisson's ratios.

The uncertainties of the thermal measurement results are analyzed in a similar way, i.e., by considering uncertainty propagation. For example,

$$k_{\parallel} = \alpha_{\parallel} \rho C_p \quad (9.15)$$

$$\Delta k_{\parallel} = \sqrt{\left( \frac{\delta k_{\parallel}}{\delta \alpha_{\parallel}} \right)^2 (\Delta \alpha_{\parallel})^2 + \left( \frac{\delta k_{\parallel}}{\delta \rho} \right)^2 (\Delta \rho)^2 + \left( \frac{\delta k_{\parallel}}{\delta C_p} \right)^2 (\Delta C_p)^2} \quad (9.16)$$

where  $\frac{\delta k_{\parallel}}{\delta \alpha_{\parallel}} = \rho C_p$ ,  $\frac{\delta k_{\parallel}}{\delta \rho} = \alpha_{\parallel} \rho$ , and  $\frac{\delta k_{\parallel}}{\delta C_p} = \alpha_{\parallel} \rho$ . Here we assumed negligible covariance terms. Similar expressions can be derived for  $k_{\text{perp}}$ ,  $k_{\text{parallel}}/k_{\text{perp}}$ ,  $\bar{\Lambda}$ , etc.

The uncertainties of the data are reported as error bars in the figures shown in the main text and Supporting Information. For clarity, error bars smaller than the symbol size are not shown.

## References

- [1] B. Graczykowski, A. El Sachat, J. S. Reparaz, M. Sledzinska, M. R. Wagner, E. Chavez-Angel, Y. Wu, S. Volz, Y. Wu, F. Alzina, C. M. Sotomayor Torres, *Nat. Commun.* **2017**, *8*, 415.
- [2] M. E. Siemens, Q. Li, R. Yang, K. A. Nelson, E. H. Anderson, M. M. Murnane, H. C. Kapteyn, *Nat. Mater.* **2010**, *9*, 26–30.
- [3] J. A. Tomko, A. Pena-Francesch, H. Jung, M. Tyagi, B. D. Allen, M. C. Demirel, P. E. Hopkins, *Nature Nanotechnology* **2018**, *13*, 959–964.
- [4] M. D. Losego, M. E. Grady, N. R. Sottos, D. G. Cahill, P. V. Braun, *Nat. Mater.* **2012**, *11*, 502–6.
- [5] G. H. Kim, D. Lee, A. Shanker, L. Shao, M. S. Kwon, D. Gidley, J. Kim, K. P. Pipe, *Nat Mater* **2015**, *14*, 295–300.
- [6] S. Shen, A. Henry, J. Tong, R. Zheng, G. Chen, *Nat. Nanotechnol.* **2010**, *5*, 251–255.
- [7] X. Huang, G. Liu, X. Wang, *Adv. Mater.* **2012**, *24*, 1482–1486.
- [8] R. Fuente, A. Mendioroz, A. Salazar, *Mater. Lett.* **2014**, *114*, 1–3.
- [9] C. Chiritescu, D. G. Cahill, N. Nguyen, D. Johnson, A. Bodapati, P. Keblinski, P. Zschack, *Science* **2007**, *315*, 351–353.
- [10] M. D. Losego, I. P. Blitz, R. A. Vaia, D. G. Cahill, P. V. Braun, *Nano Lett* **2013**, *13*, 2215–9.
- [11] B. Wicklein, A. Kocjan, G. Salazar-Alvarez, F. Carosio, G. Camino, M. Antonietti, L. Bergström, *Nat. Nanotechnol.* **2015**, *10*, 277–283.
- [12] T. Li, J. Song, X. Zhao, Z. Yang, G. Pastel, S. Xu, C. Jia, J. Dai, C. Chen, A. Gong, F. Jiang, Y. Yao, T. Fan, B. Yang, L. Wagberg, R. Yang, L. Hu, *Sci. Adv.* **2018**, *4*, eaar3724.
- [13] M. Chau, B. A. F. Kopera, V. R. Machado, S. M. Tehrani, M. A. Winnik, E. Kumacheva, M. Retsch, *Mater. Horiz.* **2017**, *4*, 236–241.
- [14] X. Tian, M. E. Itkis, E. B. Bekyarova, R. C. Haddon, *Sci. Rep.* **2013**, *3*, 1710–1715.
- [15] N. Song, D. Jiao, S. Cui, X. Hou, P. Ding, L. Shi, *ACS Appl. Mater. Interfaces* **2017**, *9*, 2924–2932.
- [16] A. Eckert, T. Rudolph, J. Guo, T. Mang, A. Walther, *Adv Mater* **2018**, *30*, e1802477.
- [17] T. Verho, M. Karesoja, P. Das, L. Martikainen, R. Lund, A. Alegría, A. Walther, O. Ikkala, *Adv. Mater.* **2013**, *25*, 5055–5059.

- [18] T. Szabó, M. Szekeres, I. Dékány, C. Jackers, S. De Feyter, C. T. Johnston, R. A. Schoonheydt, *J. Phys. Chem. C* **2007**, *111*, 12730–12740.
- [19] Z. Tang, N. A. Kotov, B. Magonov, B. Ozturk, *Nat. Mater.* **2003**, *2*, 413–418.
- [20] T. Still, *High frequency acoustics in colloid-based meso- and nanostructures by spontaneous Brillouin light scattering*, 1st ed., Springer-Verlag Berlin Heidelberg, **2010**.
- [21] E. Alonso-Redondo, M. Schmitt, Z. Urbach, C. M. Hui, R. Sainidou, P. Rembert, K. Matyjaszewski, M. R. Bockstaller, G. Fytas, *Nat. Commun.* **2015**, *6*, 8309.
- [22] V. Singh, T. L. Bougher, A. Weathers, Y. Cai, K. Bi, M. T. Pettes, S. A. McMenamin, W. Lv, D. P. Resler, T. R. Gattuso, D. H. Altman, K. H. Sandhage, L. Shi, A. Henry, B. A. Cola, *Nat Nanotechnol* **2014**, *9*, 384–90.
- [23] A. Mendioroz, R. Fuente-Dacal, E. Apinaniz, A. Salazar, *Rev. Sci. Instrum.* **2009**, *80*, 074904.
- [24] L. Wang, T. Sasaki, *Chem. Rev.* **2014**, *114*, 9455–9486.
- [25] P. Davidson, C. Penisson, D. Constantin, J.-C. P. Gabriel, *PNAS* **2018**, *115*, 6662–6667.
- [26] A. Lerf, *Dalton Trans.* **2014**, *43*, 10276–10291.
- [27] M. Daab, N. J. Eichstaedt, A. Edenharter, S. Rosenfeldt, J. Breu, *RSC Adv.* **2018**, *8*, 28797–28803.
- [28] J. E. F. C. Gardolinski, G. Lagaly, *Clay Miner.* **2018**, *40*, 547–556.
- [29] M. Stöter, D. A. Kunz, M. Schmidt, D. Hirsemann, H. Kalo, B. Putz, J. Senker, J. Breu, *Langmuir* **2013**, *29*, 1280–1285.
- [30] S. Rosenfeldt, M. Stöter, M. Schlenk, T. Martin, R. Q. Albuquerque, S. Förster, J. Breu, *Langmuir* **2016**, *32*, 10582–10588.
- [31] K. Sano, Y. S. Kim, Y. Ishida, Y. Ebina, T. Sasaki, T. Hikima, T. Aida, *Nat. Commun.* **2016**, *7*, 12559.
- [32] H. Kalo, W. Milius, J. Breu, *RSC Adv.* **2012**, *2*, 8452–8459.
- [33] D. A. Kunz, J. Erath, D. Kluge, H. Thurn, B. Putz, A. Fery, J. Breu, *ACS Applied Materials & Interfaces* **2013**, *5*, 5851–5855.
- [34] M. Wong, R. Ishige, K. L. White, P. Li, D. Kim, R. Krishnamoorti, R. Gunther, T. Higuchi, H. Jinnai, A. Takahara, R. Nishimura, H. J. Sue, *Nat. Commun.* **2014**, *5*, 3589.
- [35] W. Seidl, J. Breu, *Z. Kristallogr.- Cryst. Mater.* **2005**, *220*, 169–176.

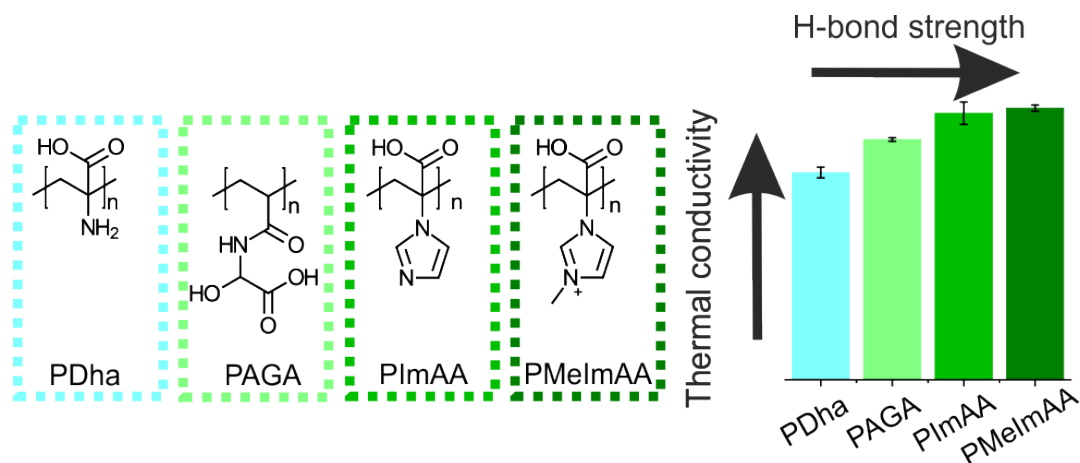
- [36] A. Baumgartner, K. Sattler, J. Thun, J. Breu, *Angew. Chem. Int. Ed.* **2008**, *47*, 1640–1644.
- [37] N. L. McFarlane, N. J. Wagner, E. W. Kaler, M. L. Lynch, *Langmuir* **2010**, *26*, 13823–13830.
- [38] E. S. Tsurko, P. Feicht, F. Nehm, K. Ament, S. Rosenfeldt, I. Pietsch, K. Roschmann, H. Kalo, J. Breu, *Macromolecules* **2017**, *50*, 4344–4350.
- [39] D. M. Moore, R. C. Reynolds, D. M., *X-ray Diffraction and the Identification and Analysis of Clay Minerals*, Oxford University Press, Oxford, U.K., **1997**.
- [40] A. Philipp, N. W. Pech-May, B. A. F. Kopera, A. M. Lechner, S. Rosenfeldt, M. Retsch, *Anal. Chem.* **2019**, *91*, 8476–8483.
- [41] C. Clauser, E. Huenges in *Rock Physics & Phase Relations*, AGU Reference Shelf, **2013**, pp. 105–126.
- [42] Y.-F. Huang, Z.-G. Wang, H.-M. Yin, J.-Z. Xu, Y. Chen, J. Lei, L. Zhu, F. Gong, Z.-M. Li, *ACS Appl. Nano Mater.* **2018**, *1*, 3312–3320.
- [43] L. P. Tremblay, M. B. Johnson, U. Werner-Zwanziger, M. A. White, *J. Mater. Res.* **2011**, *26*, 1216–1224.
- [44] R. W. Gammon, *Brillouin scattering experiments in the ferroelectric crystal triglycine sulfate*, PhD thesis, John Hopkins University, **1967**.
- [45] J. Krüger, L. Peetz, M. Pietralla, *Polymer* **1978**, *19*, 1397–1404.
- [46] S. P. Cheadle, R. J. Brown, D. C. Lawton, *Geophysics* **1991**, *56*, 1603–1613.
- [47] M. Mah, D. R. Schmitt, *Geophysics* **2001**, *66*, 1217–1225.
- [48] S. Cusack, A. Miller, *J. Mol. Biol.* **1979**, *135*, 39–51.
- [49] Y. C. Chu, S. I. Rokhlin, *J. Acoust. Soc. Am.* **1994**, *96*, 342–352.
- [50] M. Zgonik, P. Bernasconi, M. Duelli, R. Schlessler, P. Günter, M. H. Garrett, D. Rytz, Y. Zhu, X. Wu, *Phys. Rev. B* **1994**, *50*, 5941–5949.
- [51] G. A. Elbaz, W. L. Ong, E. A. Doud, P. Kim, D. W. Paley, X. Roy, J. A. Malen, *Nano Lett.* **2017**, *17*, 5734–5739.
- [52] A. S. Henry, G. Chen, *J. Comput. Theor. Nanosci.* **2008**, *5*, 1–12.
- [53] W. L. Ong, S. M. Rupich, D. V. Talapin, A. J. McGaughey, J. A. Malen, *Nat. Mater.* **2013**, *12*, 410–5.
- [54] J. Breu, W. Seidl, A. J. Stoll, K. G. Lange, T. U. Probst, *Chem. Mater.* **2001**, *13*, 4213–4220.
- [55] A. Salazar, A. Mendioroz, R. Fuente, *Appl. Phys. Lett.* **2009**, *95*, 121905.
- [56] H. P. Hu, X. W. Wang, X. F. Xu, *Journal of Applied Physics* **1999**, *86*, 3953–3958.

- [57] C. Klieber, *Ultrafast photo-acoustic spectroscopy of super-cooled liquids*, Massachusetts Institute of Technology, **2010**.
- [58] F. Mouhat, F.-X. Coudert, *Phys. Rev. B* **2014**, *90*, 4104.



## 10 Thermal Transport in Ampholytic Polymers: The Role of Hydrogen Bonding and Water Uptake

Patrick Hummel, Anna M. Lechner, Kai Herrmann, Philip Biehl, Carsten Rössel, Lisa Wiedenhöft, Felix H. Schacher and Markus Retsch



Reprinted with permission from Hummel et al., *Macromolecules* **2020**, 53, 5528-5537. Copyright 2020 American Chemical Society.

**Abstract:** The low thermal conductivity of amorphous polymers typically prevents their usage in thermal management applications. Therefore, increasing their intrinsic thermal conductivity poses an interesting scientific challenge. One approach is to promote attractive interchain interactions. Here, we investigate the thermal conductivity of several ampholytic polymers. This unique class of polymers offers H-bond donor and acceptor groups in each repeat unit and constitutes a one-component system. We use IR spectroscopy to characterize the bonding strength and motifs based on the carbonyl peak. For the dry ampholytic polymers, we find a correlation between H-bond strength and thermal conductivity. We also characterized the influence of hydration under various relative humidity conditions. There, an increase in thermal conductivity is observed, which can be well-described by a parallel mixing model, indicating the uptake of water in a percolating fashion.

## 10.1 Introduction

Easy processability, lightweight, low cost, and electrical insulation make polymers promising candidates for various applications in electronic devices. The continuously increasing energy density in such electronic devices demands a wholistic concept for thermal management at the same time.<sup>[1]</sup> The usually low thermal conductivity of polymers represents a major obstacle in this context.

For that reason, the ambiguous goal of polymer chemists is to create thermally highly conducting polymers. Similar to the discovery of (semi)conducting polymers, this would open up an entirely new space for the application of amorphous polymers. Two general strategies have been pursued to reach this goal: the creation of polymer (nano)composites and polymer processing. In the case of processing a variety of methods such as mechanical stretching<sup>[2,3]</sup>, electro-spinning<sup>[4]</sup>, and nano-templating<sup>[5]</sup> have been investigated. In these cases, an increase in thermal conductivity is mostly attributed to a high chain orientation.<sup>[6,7]</sup> The polymer chain orientation is often accompanied by some degrees of crystallization. The chain extension can be further enhanced by the proper design of the polymer backbone to promote stiffer polymer chains.<sup>[8]</sup> Consequently, impressively high thermal conductivities, of around  $20 \text{ Wm}^{-1}\text{K}^{-1}$ , were measured along the axis of crystalline polymer fibers with a high modulus.<sup>[2]</sup> However, the radial thermal conductivity stays low.<sup>[9]</sup> This anisotropy, along with a properly stretched polymer film and its ensuing crystallinity are already established in a commercial product. The organic heat spreader Temprion OHS (DuPont) with a crystallinity of 99.9 % demonstrates a remarkable in-plane thermal conductivity of  $45 \text{ Wm}^{-1}\text{K}^{-1}$  and a typical polymer-like cross-plane thermal conductivity of  $0.2 \text{ Wm}^{-1}\text{K}^{-1}$ . Amorphous polymers, in general, have a lower thermal conductivity than crystalline ones. Yet, their heat spreading capabilities would be less affected by the orientation in space owing to the random polymer coiling. Furthermore, the processing of amorphous polymers is less sophisticated because of the lack of a nucleation and growth phase compared to (semi)crystalline samples. Ways to beat the intrinsically low thermal conductivity of amorphous polymers are mixing with highly conducting components or the introduction of functional groups.

In that regard, the field of (nano)composite materials have been strongly investigated over the past years. The effective material properties strongly depend on a multitude of parameters such as the filler shape and composition, the interfacial interaction between the filler and matrix, and the filler concentration.<sup>[10,11]</sup> Depending on the filler shape, anisotropic thermal transport properties may evolve at the same time.<sup>[12,13]</sup>

The introduction of functional groups to the polymer backbone or its side-groups is an alternative approach to increase the thermal conductivity. The main driving force for an increased thermal conductivity is stretching of the polymer to a more elongated conformation and an improved interchain transfer of heat. Amorphous polymers with hydrogen bond-forming functional groups are consequently well-suited to realize improved thermal conductivities.<sup>[14]</sup> The strong hydrogen bonding between adjacent polymer chains could improve the transfer of thermal energy. In addition to this, the thermal conductivity can be further increased by the use of polyelectrolytes.<sup>[34,35]</sup> Polyelectrolytes react sensitively to external stimuli such as ionic strength or pH, which influence the polymer conformation and polymer packing.

The engineering of these interchain interactions can lead to high thermal conductivities of up to  $1.5 \text{ Wm}^{-1}\text{K}^{-1}$ , as shown in amorphous polymer blends.<sup>[15]</sup> However, demixing is a considerable issue in polymer blends, and controversial findings were published.<sup>[14]</sup> Miscibility is always an enormous challenge in polymer blends, and the resulting microstructure can be hard to characterize.

In this work, we present a new approach to prevent the issue of miscibility. Ampholytic polymers exhibit donor and acceptor groups for the formation of H-bonds covalently attached to one polymer chain, which inevitably prevents demixing. We studied five different ampholytic polymers regarding their microstructure (measured by IR spectroscopy) and thermal conductivity (measured by the photoacoustic method).

## 10.2 Materials and Methods

### *Polymer synthesis*

Synthesis of poly(2-(imidazol-1-yl)acrylic acid) (PIImAA). The synthesis of ethyl 2-(imidazol-1-yl)acrylate (EImA) and anionic polymerization in tetrahydrofuran (THF) with potassium *tert*-butoxide (KO*t*Bu) as an initiator, as well as the polymer modifications, were performed as described in the literature.<sup>[16]</sup> The polymers were characterized by <sup>1</sup>H NMR (300 MHz, D<sub>2</sub>O) and SEC (0.1 M NaCl/0.3 % TFA in water, P2VP calibration).

Synthesis of polydehydroalanine (PDha): PDha was synthesized as reported by Günther et al. or von der Lühe et al.<sup>[17,18]</sup> Briefly, a solution of 2.9 mg (0.0084 mmol) of Lucirin TPO in 300  $\mu$ L of 1,4-dioxane was added to 300 mg (1.49 mmol) of *tert*-butoxycarbonylaminoethyl acrylate (*t*BAMA; M/I = 200:1). The mixture was placed in an UV cube (100 W) for 5 min. Afterward, the polymer was precipitated in 4 mL of *n*-hexane and subsequently deprotected. Therefore, 500 mg of the obtained *Pt*BAMA was dissolved in 7.5 mL of trifluoroacetic acid and stirred at 50 °C for 1 h. The mixture was precipitated in methanol. The so obtained PAMA was dissolved in 10 mL of 1,4-dioxane, and a saturated solution of LiOH (10 mL) was added. The mixture was stirred at 100 °C for 3 h and neutralized with diluted HCl<sub>aq</sub>. During neutralization, PDha precipitated. PDha was characterized by <sup>1</sup>H NMR (300 MHz, D<sub>2</sub>O/NaOD, pH 8).

Synthesis of poly(2-acrylamido glycolic acid) (PAGA): 2-acryloylamido glycolic acid was synthesized as described in the literature.<sup>[19]</sup> Reversible addition-fragmentation chain transfer (RAFT) polymerization was performed according to a previously published protocol<sup>[20]</sup> with [M]/[CTA]/[I] = 145:1:0.3. PAGA was characterized by <sup>1</sup>H NMR (D<sub>2</sub>O, 300 MHz) and SEC (0.1 M NaNO<sub>3</sub>/ 0.05 % NaN<sub>3</sub>, PEO calibration).

Synthesis of poly(methyl methacrylate) (PMMA): The RAFT synthesis of PMMA was adapted from Mayadunne et al.<sup>[21]</sup> Therefore, 38.25 g (0.382 mol) of MMA, 750.6 mg (2.17 mmol) of 2-cyano-2-propyl dodecyl trithiocarbonate (CPDTTC), 3.7 mg (0.0225 mmol) of azobisisobutyronitrile (AIBN), and 11.9 g (0.129 mol) of toluene were placed in a flask. The mixture was heated to 80 °C for 33.5 h. The polymer was precipitated in methanol.

Poly(acrylic acid) (PAA) was purchased from Sigma-Aldrich as a sodium salt solution. The pH of the solution was adjusted to 1. The sodium ions were removed by dialysis of the solution against Milli-Q water until constant pH.

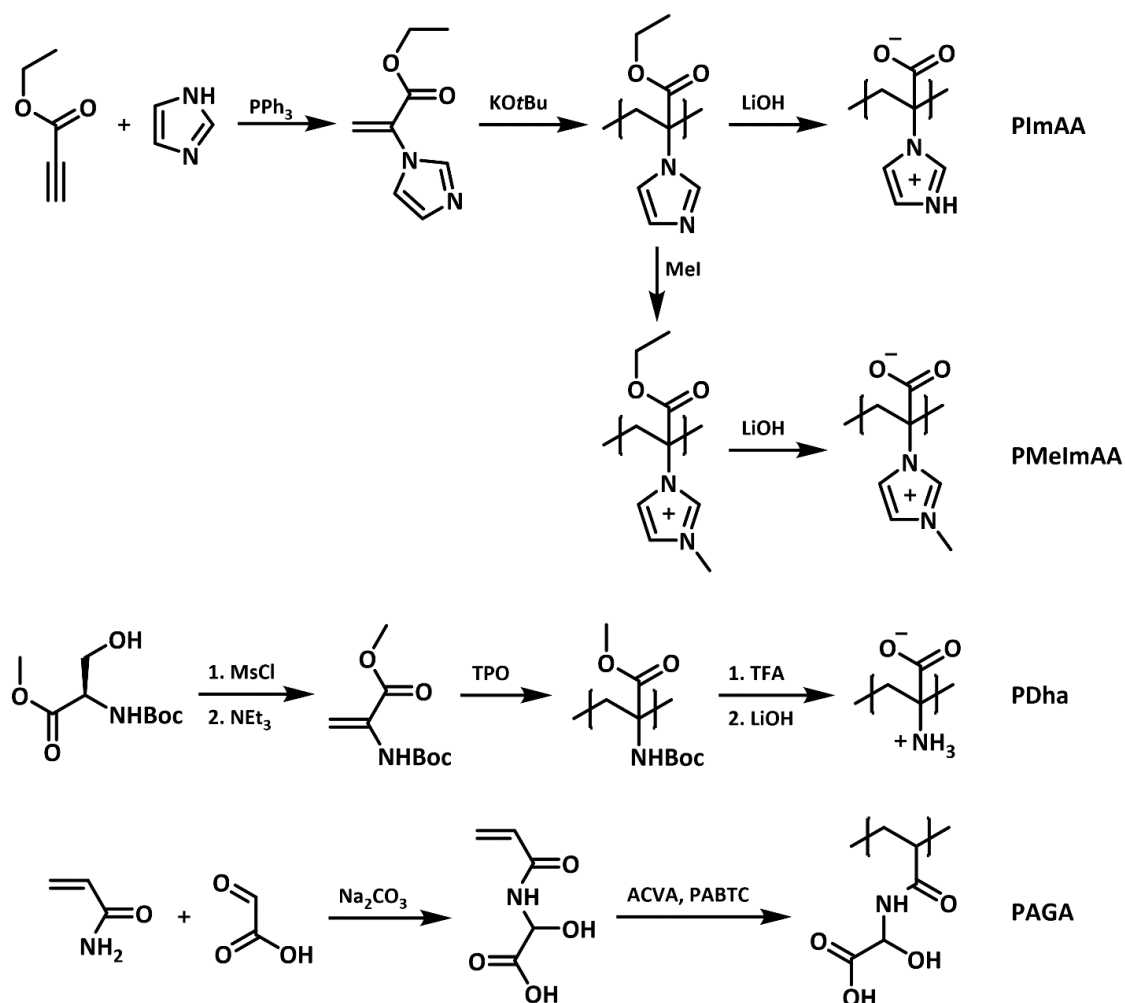


Figure 10.1: Synthesis of poly(2-(imidazol-1-yl)acrylic acid) (PImAA), poly(2-(3-methylimidazolium-1-yl)acrylic acid) (PMeImAA), poly(dehydroalanine) (PDha), and poly(2-acrylamido glycolic acid) (PAGA).

## Sample preparation

### *Spin-coating*

The polymers were dissolved in the respective solvent to achieve concentrations between 15 wt% and 25 wt%. PMMA was dissolved in toluene and PDha was dissolved in dimethyl sulfoxide (DMSO), while all other polymers were processed from water. The solutions were then spin-casted on glass substrates with dimensions of 25x25 mm at 3000 rpm for 150 s. These samples were used for thermal conductivity measurements and IR investigations.

### *Humidity annealing*

Saturated salt solutions in a desiccator achieved different relative humidities. We

Table 10.1: Summary of the measured polymer properties. The density and  $c_p$  values were used for the determination of thermal conductivity.

Name	Mn [g · mol <sup>-1</sup> ]	PDI	Density [g · cm <sup>-3</sup> ]	$c_p$ [J · g <sup>-1</sup> · K <sup>-1</sup> ]
PIImAA	5,500 <sup>a)</sup>	1.31 <sup>a)</sup>	1.48	1.045
PMeImAA	3,300 <sup>a)</sup>	1.45 <sup>a)</sup>	1.37	0.896
PDha	13,000 <sup>b)</sup>	2.5 <sup>b)</sup>	1.24	1.009
PAGA	28,500 <sup>c)</sup>	1.32 <sup>c)</sup>	1.22	1.245
PAA	15,000	-	1.258	1.202
PMMA	17,400 <sup>d)</sup>	1.15 <sup>d)</sup>	1.152	1.217

<sup>a)</sup> Determined by SEC using aqueous 0.3 % TFA/0.1 M NaCl as an eluent and calibrated against P2VP standards; <sup>b)</sup> Determined for the protected precursor of PDha by SEC using 0.1 % LiCl in DMAc as an eluent and calibrated against PMMA standards; <sup>c)</sup> Determined by SEC using 0.1 M NaNO<sub>3</sub>/ 0.05 % NaN<sub>3</sub> as an eluent and calibrated against PEO standards, <sup>d)</sup> Determined by SEC using THF as an eluent and calibrated against PMMA standards.

used MgCl<sub>2</sub>, NaCl, and K<sub>2</sub>SO<sub>4</sub> for relative humidities of 45 %, 77 %, and 92 %, respectively.<sup>[22]</sup> The spin-cast samples were equilibrated in the humid atmosphere for 24 h prior to further investigations. The transducer layer surface is shown in Figure 10.16 and demonstrates holes or cracks. Therefore, equilibration with the environment is not prevented by the evaporated transducer layer on top of the polymer. PA, AFM, and IR measurements were conducted immediately after receiving the samples from the humidity adjusted desiccator.

#### *Thermal conductivity measurements*

The PA method was used to determine the thermal conductivity of the spin-coated polymer films.<sup>[23,24]</sup> A gold transducer layer was applied to the top of the sample prior to the measurement. The sample is fixed to the measurement cell. The cell is gas-tight and filled with 20 psi helium. A modulated laser heats the transducer layer periodically. The induced temperature change on the surface of the sample leads to an acoustic wave propagating into the gas. The acoustic signal is detected using a microphone and coupled to a lock-in amplifier. The frequency-dependent phase shift between the modulated laser beam and the acoustic wave is measured. The experimental data are fitted using a multilayer model, describing the temperature distribution in the sample. The primary fitting result is the total layer resistance. Dividing the total layer resistance by the film thickness, the effective thermal conductivity is obtained. Each sample was measured three times. The mean values of

these measurements are presented with the standard deviations as error bars. The humidity dependent data were measured without additional external control of the surrounding humidity. We did not observe a drift in the photoacoustic signal during the measurement time and conclude that the humidity water uptake remains constant for this duration (Figure 10.7c). More details can be found in the Supporting information section 10.5.1.

#### *Fourier-transform infrared spectroscopy*

The Fourier-transform infrared (FTIR) measurements were conducted on a Bruker (Billerica, MA, USA) Vertex 70 IR spectrometer with an attenuated total reflection (ATR) measurement unit. The measurements were performed from  $380\text{ cm}^{-1}$  to  $4000\text{ cm}^{-1}$  with a resolution of  $4\text{ cm}^{-1}$  and 128 scans. The samples were taken from the desiccators or vacuum oven, respectively, and directly measured under ambient conditions. Normalized spectra were used to calculate the difference spectra relative to the dry polymer samples.<sup>[25]</sup> Therefore, the normalized spectrum of the dry sample was subtracted from the spectra at the different relative humidities. The  $\text{CH}_2$  deformation vibration at  $1450\text{ cm}^{-1}$  was used as reference peak for normalization, which is unaffected by water adsorption.

#### *Fourier self-deconvolution*

Fourier self-deconvolution (FSD) is a mathematical method to increase the spectral resolution. By this, it is possible to separate overlapping absorption bands in an IR spectrum.<sup>[26]</sup> We applied the FSD according to Hu et al.<sup>[27]</sup> The software OPUS 7.5 (Bruker, Billerica, MA, USA) was used for all steps. First, the carbonyl region (between  $1800\text{ cm}^{-1}$  and  $1540\text{ cm}^{-1}$ ) was cut-off. A baseline correction with one iteration was performed, and the spectrum was smoothed by 5-9 points. In the next step, the FSD was performed with a Lorentzian shape with a half-bandwidth of 25, and a noise reduction of 0.30. Another baseline correction was conducted, before the peaks were selected according to the minima of the second derivative of the initial spectrum. Finally, the peaks were fitted with a Gaussian profile with the Levenberg-Marquardt method.

#### *Differential scanning calorimetry*

Differential scanning calorimetry (DSC) measurements were performed on a TA instruments Discovery DSC 2500. Two heating cycles were conducted; only the second cycle was used for evaluation. The temperature profile ranged from  $-40\text{ }^\circ\text{C}$  to  $140\text{ }^\circ\text{C}$  using a heating rate of  $10\text{ K min}^{-1}$  with a nitrogen flow of  $50\text{ mL min}^{-1}$ . The measurements are shown in Figure 10.14.

Modulated DSC (MDSC) measurements were performed to determine the  $c_p$  of the samples. The optimum MDSC parameters have been calculated and evaluated fol-

lowing the instructions described in literature.<sup>[28]</sup> The modulations in the transition-range and the modulation period were controlled and adjusted to a heating rate of  $2 \text{ K min}^{-1}$ , a period of 80 s, and an amplitude of 1.6 K. The final samples were measured in hermetic pants to avoid loss of water during the measurement. The experiments were performed in a temperature range from 5 to 60 °C. The  $c_p$  at 25 °C of each polymer is given in Table 10.1.

#### *Helium pycnometer*

An Ultrapyc 1200e (Quantachrome Instruments, Boynton Beach, FL, USA) was used for the determination of the density of the dry samples. Before each run, the volume of the measurement cell was calibrated. Subsequently, a defined mass of the polymer was put into the cell. The volume of the polymer was determined by 100 runs. The density was calculated by the division of mass and volume. The obtained values are summarized in Table 10.1.

### **10.3 Results and Discussion**

We investigate the effective thermal conductivity of four different ampholytic polymers, PDha, PAGA, PImAA, and its methylated derivative PMeImAA (Figure 10.2a). All polymers have at least two different functional groups per repetition unit. We also analyzed PAA with only one functional group, which was reported to play a crucial role in the formation of a highly conducting pathway.<sup>[15]</sup> PMMA is not able to form hydrogen bonds and was also measured as a reference system.

We start our analysis by the polymer characterization under dry conditions, that is, after storing the samples in a vacuum oven. In the IR spectra shown in Figure 10.2b, it can be seen that, except PMMA, all polymers form intra- and intermolecular hydrogen bond interactions as indicated by the broad bands between  $2500 \text{ cm}^{-1}$  and  $3600 \text{ cm}^{-1}$ . These bands originate from the O-H and N-H stretching vibrations. OH-wagging at  $900 \text{ cm}^{-1}$  is another indicator for the presence of COOH under these vacuum-dried conditions. This band is broad due to various spatial orientations of the H-bond-forming functional groups. Because of this variety of possible bonds, the underlying C-H stretching vibrations, and several overtones, this region of an IR spectrum is very difficult to evaluate.

We, consequently, focus our analysis on another strong peak connected to hydrogen bonds: the carbonyl stretching vibration around  $1700 \text{ cm}^{-1}$ . This peak is very strong, possesses a small FWHM, and is sensitive to the local environment.<sup>[27,29,30]</sup> Therefore, it provides a suitable target for further investigations of H-bonds. Furthermore, it was shown that the absorption coefficient of the carbonyl stretching

vibration, in comparison with the O-H and N-H stretching, does not depend significantly on the strength of the H-bonds.<sup>[31,32]</sup> One disadvantage is that H-bonds between functional groups without a carbonyl group contribution cannot be resolved. A first indication of the strength of a hydrogen bond is the position of the carbonyl peak whereby lower frequencies indicate an increasing strength of the H-bond.<sup>[33]</sup> We see a systematic shift of the carbonyl peak from PAA to PMeImAA, indicating an overall increase in strength of the carboxylic H-bonds.

The effective thermal conductivities (Figure 10.2c) show typical values for water-soluble amorphous polymers compared to values reported in the literature (shaded area).<sup>[14]</sup> Comparing our values for PMMA ( $0.16 \text{ Wm}^{-1}\text{K}^{-1}$ ) and PAA ( $0.31 \text{ Wm}^{-1}\text{K}^{-1}$ ) with the literature ( $0.20 \text{ Wm}^{-1}\text{K}^{-1}$ <sup>[14]</sup> and  $0.34 \text{ Wm}^{-1}\text{K}^{-1}$ <sup>[34]</sup>/ $0.37 \text{ Wm}^{-1}\text{K}^{-1}$ <sup>[14]</sup>) we find slightly lower values. The lower values are reasonable because the PA method determines the total layer resistance of the sample. The effective thermal conductivity is calculated based on the polymer film thickness and also takes the thermal resistances between the polymer layer and the support structure and transducer layer, respectively, into account. We attribute the relatively large standard deviation of the PImAA sample to the lowest layer thickness ( $< 1 \mu\text{m}$ ) of the PImAA sample, which reduces the fitting accuracy.

Considering the systematic increase in H-bond strength derived from the carbonyl peak position, we find the expected increase in thermal conductivity for the ampholytic samples under investigation. Rather unexpected from this point of view is the exceptionally high thermal conductivity of PAA.

For further insight into the strength of the H-bonds, we provide a detailed analysis of the IR spectra. We base our analysis on FSD of the carbonyl resonance between  $1600$  and  $1750 \text{ cm}^{-1}$ , according to Hu et al.<sup>[27]</sup> The fitted spectra are shown in Figure 10.3. The peaks are assigned to different configurations of the carbonyl group. Dark yellow are anhydrides ( $1805 \text{ cm}^{-1}$  to  $1760 \text{ cm}^{-1}$ ), green are free carbonyl groups ( $1740 \text{ cm}^{-1}$  to  $1730 \text{ cm}^{-1}$ ), cyan is the terminal oligomeric form of carboxylic acid ( $1716 \text{ cm}^{-1}$  to  $1680 \text{ cm}^{-1}$ ), blue is the cyclic dimer ( $1700 \text{ cm}^{-1}$  to  $1665 \text{ cm}^{-1}$ ) and gray-blue is the inner oligomeric form ( $1675 \text{ cm}^{-1}$  to  $1650 \text{ cm}^{-1}$ ). These peaks can be found in all samples containing a carboxylic acid group. The assignment is based on Dong et al.<sup>[29]</sup>, who investigated different H-bond motifs in PAA samples. The introduction of amino-groups in our ampholytic polymers introduces additional peaks marked in purple, ascribed to H-bonds with primary or secondary amino-groups (PDha and PAGA). A final category of H-bonds is assigned to the interaction of the carbonyl group with the imidazole ring in PImAA and PMeImAA depicted in dark blue. Further contributions arising from vibrations other than the carbonyl stretching, such as NH bending vibration/Amide II and

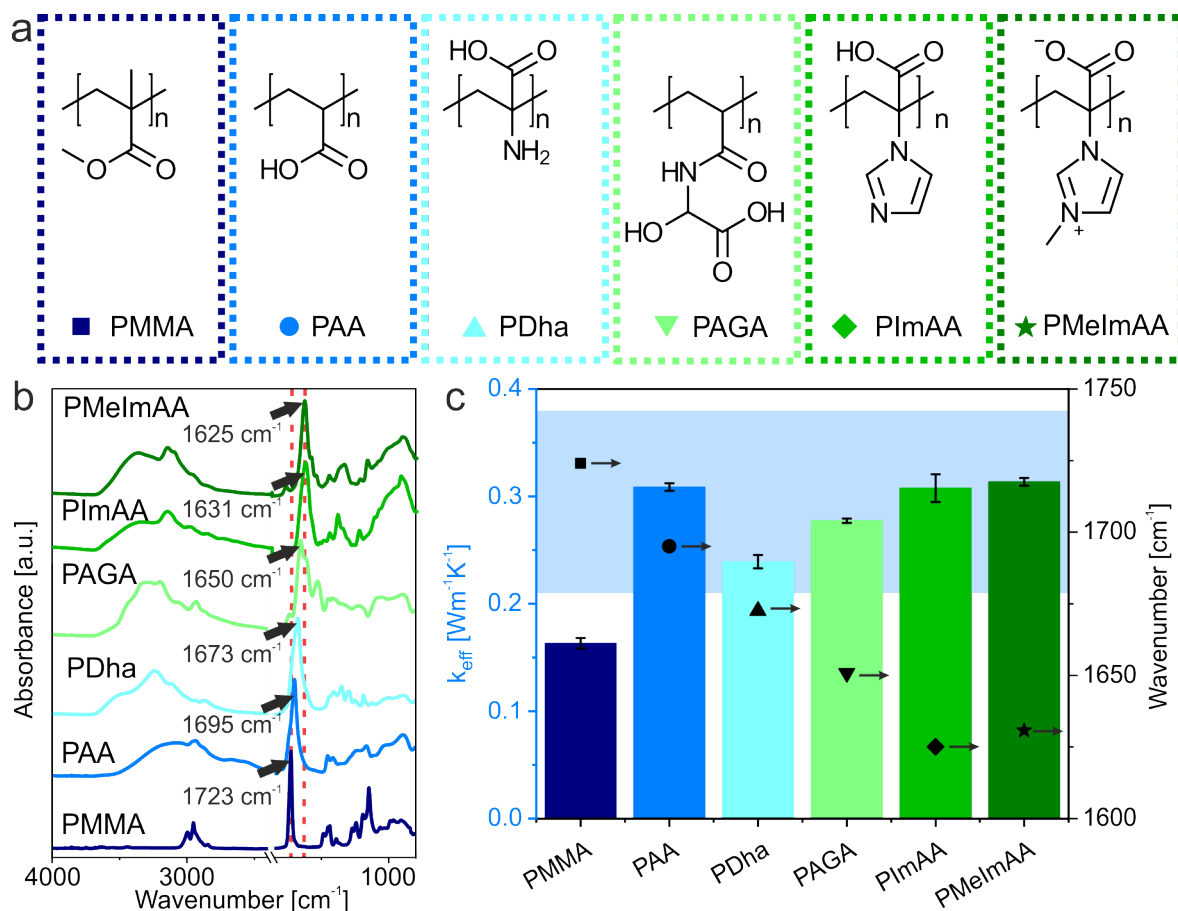


Figure 10.2: (a) Structure of the ampholytic polymers and the reference polymers PAA and PMMA. The ampholytic polymers have at least two functional groups per repetition unit. (b) IR spectra of all investigated polymer samples in the dry state. The red dashed lines present the carbonyl peak position of PMMA and PMelAA, respectively. (c) Measured effective thermal conductivity of all samples (solid bars). The thermal conductivity correlates with the peak position (black squares) of the carbonyl band measured by IR spectroscopy (except for PAA). The light blue area indicates the range of literature values for amorphous, water-soluble polymers.<sup>[14]</sup>

vibrations of the aromatic ring, are summarized in orange. As a consequence, the orange bands were excluded for the evaluation of the carbonyl ratio.

The relative contribution of all these different classes of hydrogen bonds is summarized in Figure 10.3b. Most notably, PAA comprises a range of strongly coordinated H-bonds (dimer, inner, terminal) and even covalently condensed moieties (anhydride). The interplay of these structural motifs facilitates thermal transport between the polymer chains. Please note that the strength of the H-bond is the lowest in the case of PAA compared to all other ampholytic polymers (Figure 10.2b, 1723 cm<sup>-1</sup> peak position of the carbonyl band). Thus, the bonding scheme in PAA may additionally facilitate an elongated conformation, which also improves thermal transport. As soon as an additional functional group is introduced (NH<sub>2</sub> in the case

of PDha), the thermal conductivity drops considerably, although the nature of the H-bond environment is still comparable to PAA. Merely, the anhydride and free-carboxyl bonds are replaced by O-H-N moieties (“other bonds” in Figure 10.3b). The overall stiffer carbonyl peak ( $1695\text{ cm}^{-1}$ ) should even favor a higher thermal conductivity. Thus it is difficult to unambiguously relate the thermal conductivity reduction to subtle differences in the way hydrogen bonds are formed in the respective polymers. Additional contributions, such as the side chain structure<sup>[35]</sup> or the influence of the side groups on the polymer morphology<sup>[8]</sup>, are important at the same time. Thus, the alleged beneficial influence of additional hydrogen bonds to the primary amino-group is counteracted by conformational changes that cannot be resolved by IR characterization. The transition from PDha to PAGA, PImAA and PMeImAA demonstrates a monotonic increase in the class of other hydrogen bonds. Along this direction, the strength of the carbonyl bond also increases. The combination of both effects translates into the general trend of an increasing thermal conductivity.

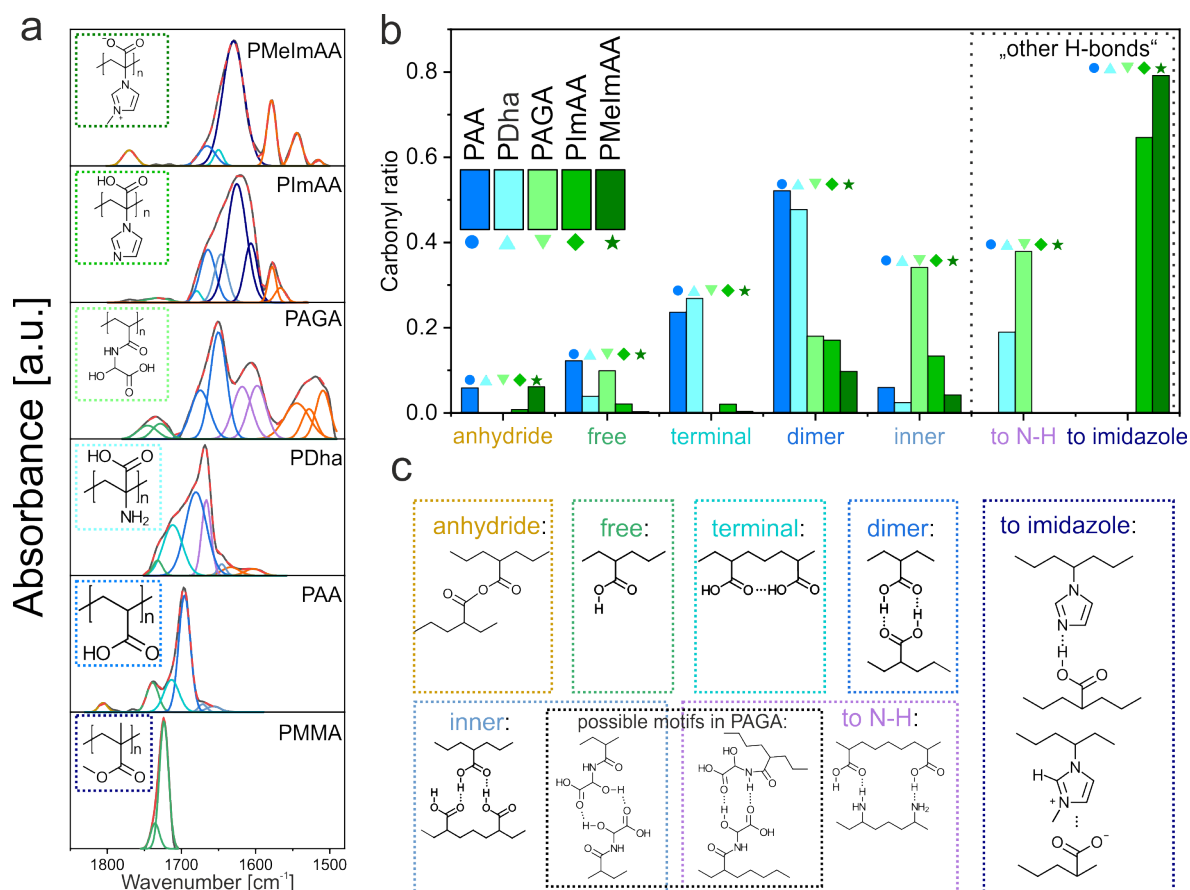


Figure 10.3: (a) Deconvoluted IR spectra of all investigated samples. The films were dried before the measurements. (b) Relative ratio of different motifs of the carbonyl bond. (c) Schematic illustration of different H-bond motifs.

PAA and all herein used ampholytic polymers are strongly sensitive to humidity. We, consequently, determined its influence on the effective thermal conductivity. We gravimetrically measured the moisture content after prolonged exposure to specific humidities (Figure 10.4a). PMMA as a control demonstrates, as expected, no sensitivity to increasing humidity. PAA exhibits a considerable absorption of water on the order of 40 %, whereas in case of the herein used ampholytic polymer values from 35 % to 60 % are found. The quaternized PMeImAA exhibits the most significant water uptake and doubles its weight. These mass changes are comparable to literature data on PAA<sup>[36]</sup> and other polyelectrolytes<sup>[Wieland2020]</sup>, respectively. The uptake of water influences not only the H-bonding within the polymers, but also the specific heat capacity and density. Both quantities are highly relevant when determining the thermal conductivity under these conditions. The measurement of the effective polymer density under various humidity conditions is not possible in a direct manner. We, therefore, used the measured moisture content to calculate the humidity dependent density. The specific heat capacity was determined experimentally by MDSC measurements, using hermetic pans (Figure 10.4b). The shaded areas indicate the expected  $c_p$  based on a mass-weighted mixing model considering the measured moisture contents. Although the overall trend of an increasing  $c_p$  is well captured in all cases, some degree of variability in a range of  $\sim 20\%$  is seen. This variation can be explained by the difficulty of accurately retaining the moisture uptake and polymer conformation during the measurement itself.

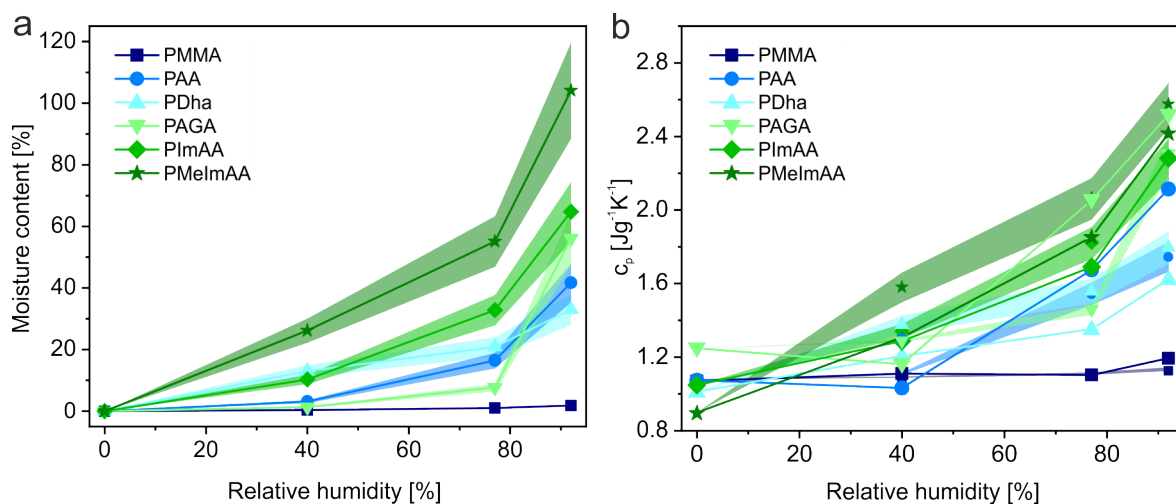


Figure 10.4: Humidity dependence of the samples. (a) Moisture content increases with humidity for all polymers with functional groups. Shaded areas mark the variability. (b)  $c_p$ , measured by MDSC, increases with humidity (solid lines and symbols). Shaded areas rationalize the expected trend of the  $c_p$  based on the water uptake in (a) calculated using a mass-weighted mixing model.

The uptake of water also affects the polymer microstructure and H-bond environment. Consistently with our previous analysis, we used FSD of the carbonyl peak of our FTIR spectra. Figure 10.5 summarizes three distinct cases: PAA, PImAA, and PMeImAA. The spectra show a distinctly different way of water uptake in the case of PAA compared to PImAA and PMeImAA. In the literature, there is a differentiation between unbound and bound water.<sup>[36,37]</sup> We define bound water as directly coordinated to the polymer, while unbound water interacts with other water molecules and forms clusters.

Our results of the absorbed amount of water in PAA (moisture content of 0.42 g/g polymer) are in good agreement with the literature value (0.47 g/g polymer).<sup>[36]</sup> Also the FTIR difference spectrum is in good agreement with the findings of Danil-iuc et al.<sup>[36]</sup> They reported a negative contribution in the difference spectra for free C=O (around 1735 cm<sup>-1</sup>) and dimer (around 1700 cm<sup>-1</sup>) and a positive peak between 1672 and 1634 cm<sup>-1</sup>. The negative contributions are attributed to disconnected polymer-polymer interactions, while the positive contributions are newly formed polymer-water interactions.<sup>[36]</sup> They interpret the spectra such that only bound water exists in their PAA sample.

Despite a higher moisture content, the difference spectra of PImAA and PMeImAA show overall fewer variations. Although the negative contributions between 1675 cm<sup>-1</sup> and 1600 cm<sup>-1</sup> represent disconnected polymer-polymer interactions, the overall lack of significant positive contributions indicates that the water is adsorbed in a less bound state in the case of PImAA and PMeImAA. The variation between these two polymers is smaller because polymers with similar functional groups show similar peaks in IR spectroscopy when adsorbing/absorbing water.<sup>[38]</sup> The same data evaluation and representation for PDha and PAGA are summarized in Figure 10.14.

When considering the deconvoluted peaks (right panels of Figure 10.5), one has to be cautious while interpreting the respective contributions. The major difficulty is that the thermal conductivity is governed by various parameters, which were already pointed out in the discussion of the dry samples. We can, however, extract reasonable trends. PAA shows that the adsorption of bound water hardly influences the thermal conductivity. Consequently, bound water intercalates tightly between the PAA chains without affecting its conformation nor impeding interchain thermal transport. The IR spectra of PImAA do not show significant changes in the carbonyl peak region. Consequently, the uptake of bound and unbound water itself seems to be the driving force for the monotonic increase in thermal conductivity. Finally, PMeImAA hints towards the fact that the creation of inner oligomeric groups on the expense of anhydride, cyclic dimer, and charged heterocycle interactions impedes

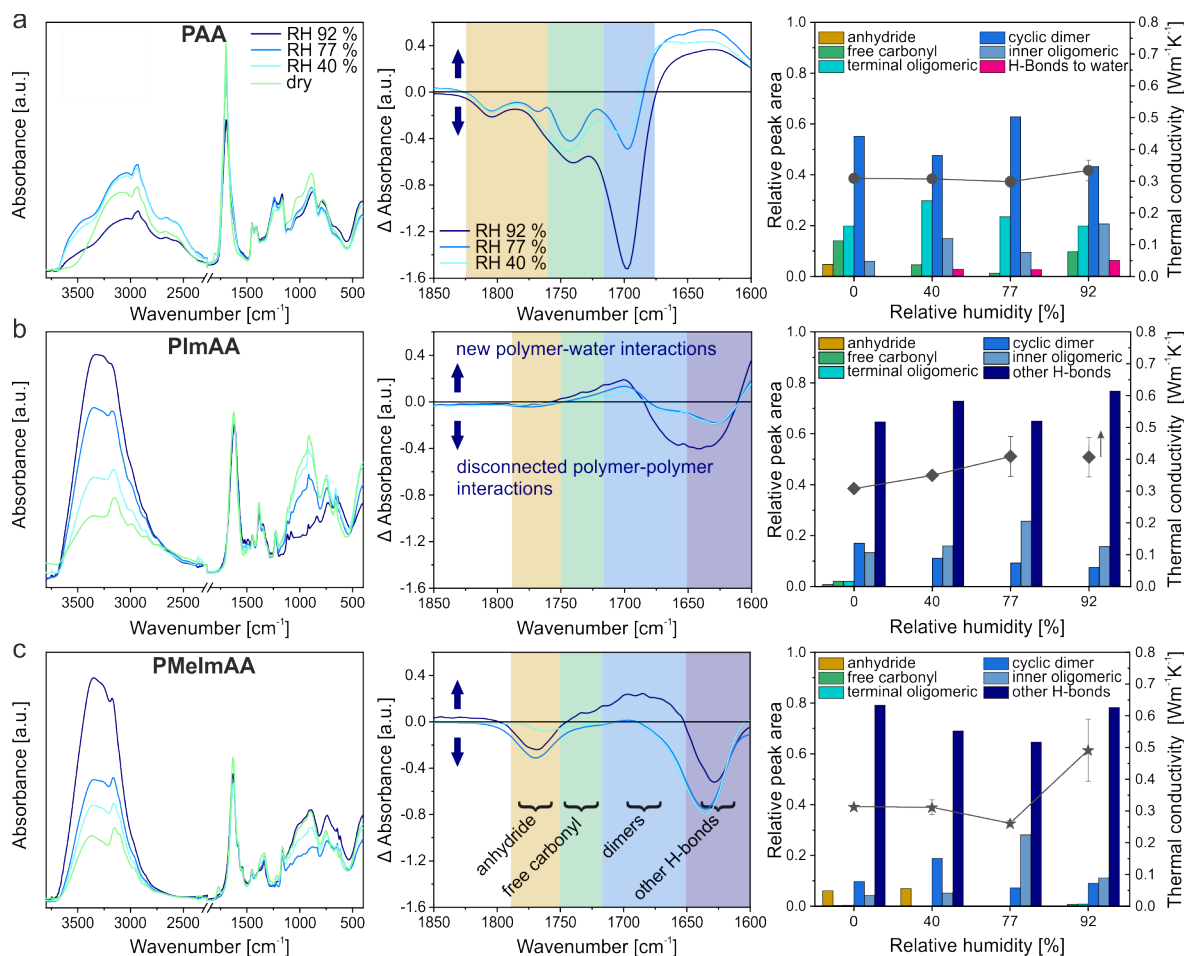


Figure 10.5: From left to right: IR-spectra of samples stored at different relative humidities. Difference spectra in the region of the carbonyl stretching vibration. The relative peak area of different H-bond structures dependent on the relative humidity. (a) PAA, (b) PImAA and (c) PMeImAA.

thermal transport up to the humidity of  $Rh \sim 77\%$ . Lastly, considering reports in the literature, the uptake of water was also reported to strongly increase the effective thermal conductivity. Mehra et al.<sup>[39]</sup> worked with polyvinylalcohol and ascribed the thermal conductivity increase to the formation of thermal bridges by bound water molecules. All these examples demonstrate that the influence of humidity on the thermal transport in hydrophilic is hard to predict and certainly depends on the specific polymer-water combination.

Although the previous discussion focused on a microscopic interpretation of inter- and intramolecular interaction between the constituting polymers, we also want to draw the attention to an alternative consideration comprising a much more coarse-grained point of view. The uptake of unbound water can be understood as a way to generate a two-phase material, where water clusters are formed.<sup>[37]</sup> This heterogeneous material can then be analyzed in a similar way to other nanocomposite materials using simple, effective medium models as described by Carson<sup>[41]</sup>. For this,

we use the vacuum (dry) polymer thermal conductivity as the pure phase of one component and literature data of the thermal conductivity of water as the second component. In combination with our data of the moisture uptake (Figure 10.4a) and two volume-weighted mixing models (parallel mixing model and effective medium model<sup>[41]</sup>), the humidity-dependent thermal conductivity is calculated (Figure 10.6). For PDha, PAGA, and PImAA, both mixing models describe the experimental data adequately well, particularly when considering the accuracy of the mixing models themselves and the thermal conductivity determination. For the case of PAA, where a high amount of bound water can be expected, both mixing models systematically overestimate the effective thermal conductivity.

The parallel mixing model is based on the presence of extended percolation paths through the entire polymer structure. In contrast, if the water uptake happened in a random and dispersed fashion within the polymer, it should be better represented by the EMT mixing model (also compared to the schematic depiction in the inset of Figure 10.6a). The small difference between the pure polymer and the pure water thermal conductivity prevents an unambiguous judgment on the presence of dispersed or percolated water inside the polymer. Both mixing models, however, support the straightforward interpretation in the sense of a water-polymer nanocomposite material. Only the ionic PMeImAA sample deviates strongly from the mixing models, which could be understood in a way that the uptake of water first disrupts thermal transport pathways. Once water condensation sets in at very high humidity ( $RH \sim 92\%$ ), the thermal conductivity is again dominated by the water-phase again.

## 10.4 Conclusions

We employed a set of polyampholytes featuring a high density of functional groups to investigate how thermal transport can be controlled by hydrogen bonding in amorphous polymers. We, therefore, compared four types of ampholytic polymers to PAA and PMMA as reference materials. The investigation of ampholytic polymers is particularly interesting because this opens an elegant pathway to study the influence of H-donor and H-acceptor groups in a one-phase system. We employed a detailed IR spectroscopy investigation for a wholistic understanding of the involved H-bond motifs.

In summary, we can deduce three major trends. First, PAA is an exceptionally well-conducting hydrophilic polymer, which we attribute to a stretched polymer conformation. Second, for all ampholytic polymers, we find an overall trend of increasing thermal conductivity along with an increase in the H-bond strength under

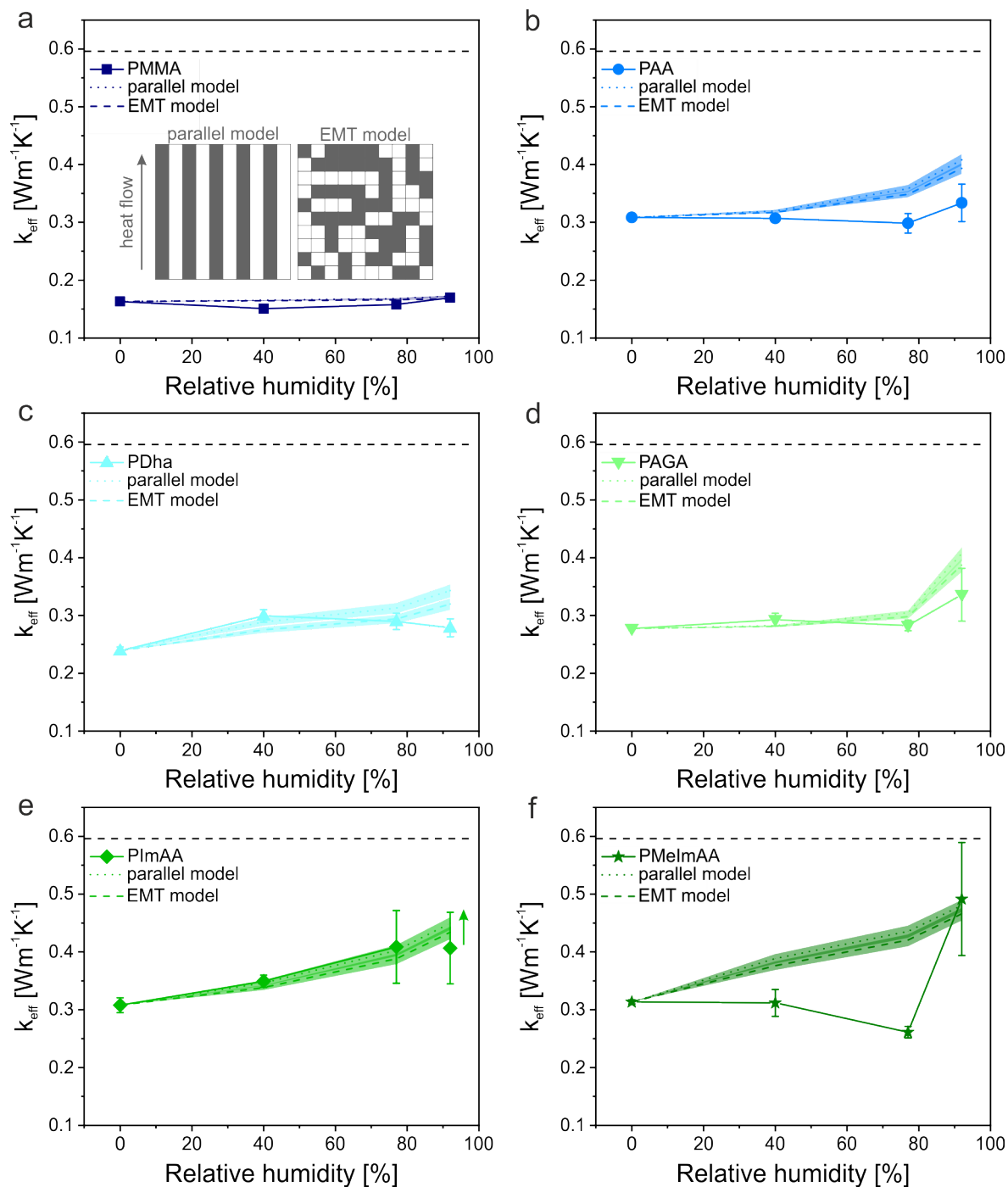


Figure 10.6: Effective thermal conductivity versus relative humidity for all investigated polymer samples. From (a) to (f) PMMA, PAA, PDha, PAGA, PImAA, and PMeImAA. The solid symbols depict the experimental data, while the dashed and dotted lines are calculated values using the parallel and the EMT mixing model, respectively. A schematic illustration of these models is shown as an inset in (a). The shaded areas consider the variability due to the deviation of the moisture content determination. The dashed black line represents the thermal conductivity of water.

dry conditions. This can be deduced from a systematic red-shift of the carbonyl peak. Third, the presence of humidity leads to a polymer-specific uptake of wa-

ter and, consequently, to a variety of changes to the H-bond motifs. However, the thermal transport in ampholytic polymers can be well-described using an effective medium model, where water is treated as a percolating phase. Deviations from this straight-forward description are PAA, where a high amount of strongly bound water is observed, and for PMeImAA, where ionic interactions are dominant. The deconvolution of the carbonyl resonance peak demonstrates a range of binding motifs between the respective polymers. However, an unambiguous assignment of a particular H-bond moiety to an increased or decreased thermal transport behavior is not possible. Additional factors such as scattering effects along the polymer backbone or on polymer side groups have to be taken into account, as well as subtle changes to the polymer conformation. Overall, our contribution adds to a better understanding of the role of H-bonds for thermal transport in polymer materials.

Most importantly, not only the specific design of H-bond motifs determines the capability to conduct thermal energy. Even in the case of one-phase systems, the various influences of polymer conformation, side-groups, and interaction have to be balanced. We are still far away from a predictive model to molecularly design amorphous polymers to a certain high or low thermal conductivity. This is an ongoing challenge to be addressed by polymer chemists and engineers over the next years.

## **Supporting information**

thermal conductivity measurements, IR spectroscopy of individual polymers, DSC measurements, and effective medium mixing model

## **Acknowledgments**

This project was funded by The Volkswagen Foundation through a Lichtenberg professorship and by the German Research Foundation by the SFB 840 (project B7). Additional support was provided by DFG RE3550/2-1, SCHA1640/12-1, and the collaborative research center SFB 1278 “PolyTarget” (project number 316213987, project C03). P. B. (Landesgraduiertenstipendium) and L. W. (Carl-Zeiss-Foundation) are grateful for PhD fellowships.

## **Notes**

The authors declare no competing financial interests.

## 10.5 Supporting information

### 10.5.1 Thermal conductivity measurements

The thermal conductivity was determined by the photoacoustic method. For photoacoustic characterization, the samples were spin-coated on glass substrates. The layout of the measurement set-up is described in literature.<sup>[13]</sup> The frequency-dependent phase-shift is plotted in Figure 10.7 - two measurement curves and the respective fits are shown Figure 10.7a and b. They correspond to the dry and the RH 77 % PImAA sample, respectively. The phase shift data are fitted by a multilayer model developed by Hu et al.<sup>[23]</sup> The fit was performed according to Singh et al.<sup>[5]</sup>, which yields the total layer resistance. Figure 10.7c shows three consecutive measurements. The change of the phase shift is minimal. Therefore, we conclude that the moisture content keeps constant over the course of at least three measurements, which corresponds to about 30 min. For the fit, the sample thickness, the specific heat capacity, and the density are necessary. The thickness was obtained by AFM measurements (Table 10.2). For each humidity condition, a separate and individual sample was prepared using the same stock solution and spin coating parameters. Overall the layer thicknesses show a good consistency from sample to sample. The applied humidity conditions do not lead to an excessive degree of swelling. Only for PImAA, the layer thickness at RH 92 % could not be quantified by AFM directly. The low molecular weight of PImAA (5500 g/mol) - in comparison to the other polymer samples (13000 – 28000 g/mol) - led to a viscous polymer film that prevented the evaluation of the step height at a scratch in the sample. Consequently, we provide for this single case a lower estimate of the thermal conductivity based on the dry polymer layer thickness of  $\sim 900$  nm. The humidity dependent specific heat capacity was determined by MDSC measurements. The density of the dry samples was measured with a helium pycnometer. The density of the samples with absorbed water was calculated from the moisture content, and the bulk densities of water and the polymers. Dividing the total layer resistance by the sample thickness leads to the effective thermal conductivity. All relevant data are shown in Table 10.2.

### 10.5.2 IR Spectroscopy of dry samples

#### PAA

In Figure 10.8 the IR spectrum of a dry PAA film in the region of the C=O stretching vibration is shown. We attributed the different peaks in the deconvoluted spectrum to certain configurations of the C=O bond, according to Dong et al.<sup>[29]</sup>. Therefore, we could distinguish between the free, the dimeric, and two oligomeric forms of the

Table 10.2: Summary of the measured polymer properties. The density and  $c_p$  values were used for the determination of thermal conductivity.

Sample	Relative humidity [%]	SD	Total layer resistance [ $\text{mm}^2 \cdot \text{K} \cdot \text{W}^{-1}$ ]	SD	Thickness [ $\mu\text{m}$ ]	SD	Effective thermal conductivity [ $\text{W} \cdot \text{m}^{-1} \cdot \text{K}^{-1}$ ]
PMMA	0	9.44	0.28	1.540	0.071	0.163	0.005
PMMA	45	10.41	0.11	1.569	0.011	0.151	0.002
PMMA	77	9.94	0.17	1.569	0.024	0.158	0.003
PMMA	92	9.26	0.25	1.570	0.016	0.170	0.004
PAA	0	3.74	0.18	1.182	0.010	0.309	0.004
PAA	45	4.10	0.06	1.258	0.052	0.307	0.005
PAA	77	4.26	0.25	1.270	0.005	0.299	0.017
PAA	92	4.56	0.42	1.511	0.197	0.334	0.032
PDha	0	7.10	0.19	1.697	0.017	0.239	0.006
PDha	45	6.28	0.20	1.680	0.022	0.299	0.011
PDha	77	5.96	0.29	1.724	0.025	0.290	0.014
PDha	92	6.20	0.33	1.723	0.020	0.279	0.016
PAGA	0	5.70	0.04	1.580	0.194	0.277	0.002
PAGA	45	5.77	0.22	1.688	0.108	0.293	0.011
PAGA	77	6.50	0.21	1.838	0.143	0.283	0.009
PAGA	92	3.31	0.42	1.100	0.016	0.336	0.046
PImAA	0	2.87	0.12	0.881	0.035	0.307	0.013
PImAA	45	2.57	0.08	0.891	0.024	0.349	0.011
PImAA	77	2.45	0.35	0.983	0.071	0.409	0.062
PImAA	92	2.25	0.33	> 0.900	-	0.407	0.061
PMeImAA	0	3.54	0.04	1.110	0.048	0.314	0.004
PMeImAA	45	3.64	0.28	1.132	0.170	0.312	0.023
PMeImAA	77	4.08	0.16	1.064	0.071	0.261	0.010
PMeImAA	92	2.47	0.35	1.200	0.096	0.492	0.098

C=O bond. The peak with the highest wavenumber of  $1735 \text{ cm}^{-1}$  is attributed to the free monomer of the COOH group. Whereas the peak at around  $1700 \text{ cm}^{-1}$  repre-

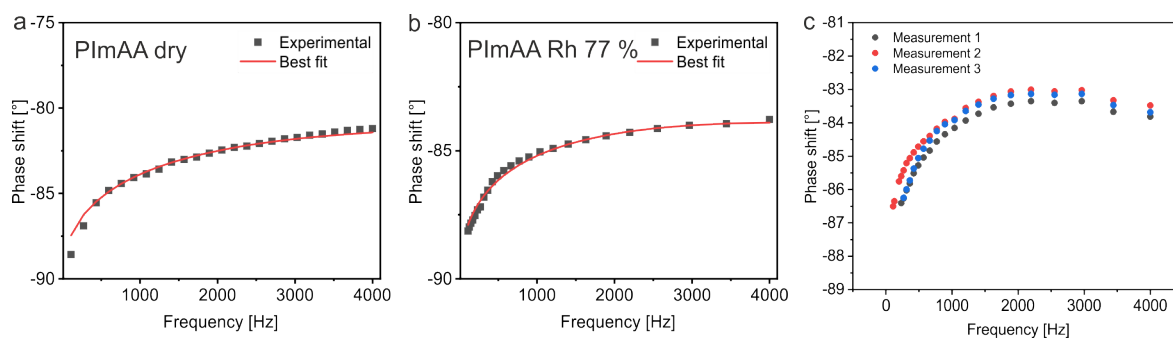


Figure 10.7: Frequency-dependent phase shift of (a) the dry PImAA sample and (b) the PImAA sample at 77 % humidity. The red lines present the best fit.

sents the cyclic dimer. The linear oligomeric forms of the terminal COOH groups lie in between, at  $1716\text{ cm}^{-1}$ , while the inner COOH appears at two peaks with the lowest wavenumbers around  $1674\text{ cm}^{-1}$ . The H-bond conformations are illustrated in Figure 10.9. At least some anhydride groups have formed due to the drying process as indicated by the bands at  $1806\text{ cm}^{-1}$  and  $1765\text{ cm}^{-1}$ .

Extending the assignment from Dong et al., we attributed different forms of H-bonds in the other investigated polymers.

### PDha

Compared to PAA, an amino-group is added to the repetition unit of PDha. Therefore, more motifs to form H-bonds are available. Similar peaks as for the PAA sample could be detected (Figure 10.10). However, we found a slight shift to lower frequencies of all peaks. While the shift is only a few wavenumbers for the free C=O stretching and the terminal H-bonds, the shift is  $20\text{ cm}^{-1}$  and  $50\text{ cm}^{-1}$  for the cyclic dimers and the inner H-bonds. The shift is an incidence of the increased strength of the H-bonds.

Furthermore, new peaks arose at  $1667\text{ cm}^{-1}$ ,  $1634\text{ cm}^{-1}$ , and  $1603\text{ cm}^{-1}$ . The peak at  $1667\text{ cm}^{-1}$  is ascribed to the H-bonds formed between the carbonyl and the amino-group. The peaks at  $1634\text{ cm}^{-1}$  and  $1603\text{ cm}^{-1}$  belong to the  $\text{NH}_2$  deformation vibration and are, therefore, excluded from the evaluation of the C=O stretching vibration. We want to note that it is also possible that H-bonds between two amino-groups are formed. The analysis of these H-bonds is not approachable by the investigation of the carbonyl stretching vibration.

### PAGA

Due to the presence of two different carbonyl groups, the spectrum of PAGA exhibits many peaks in the region between  $1500\text{ cm}^{-1}$  and  $1800\text{ cm}^{-1}$ . Besides the carboxylic acid group, also another carbonyl group is located in the amide bond. As a consequence, we detect amide I and amide II vibrations. While the amide I band

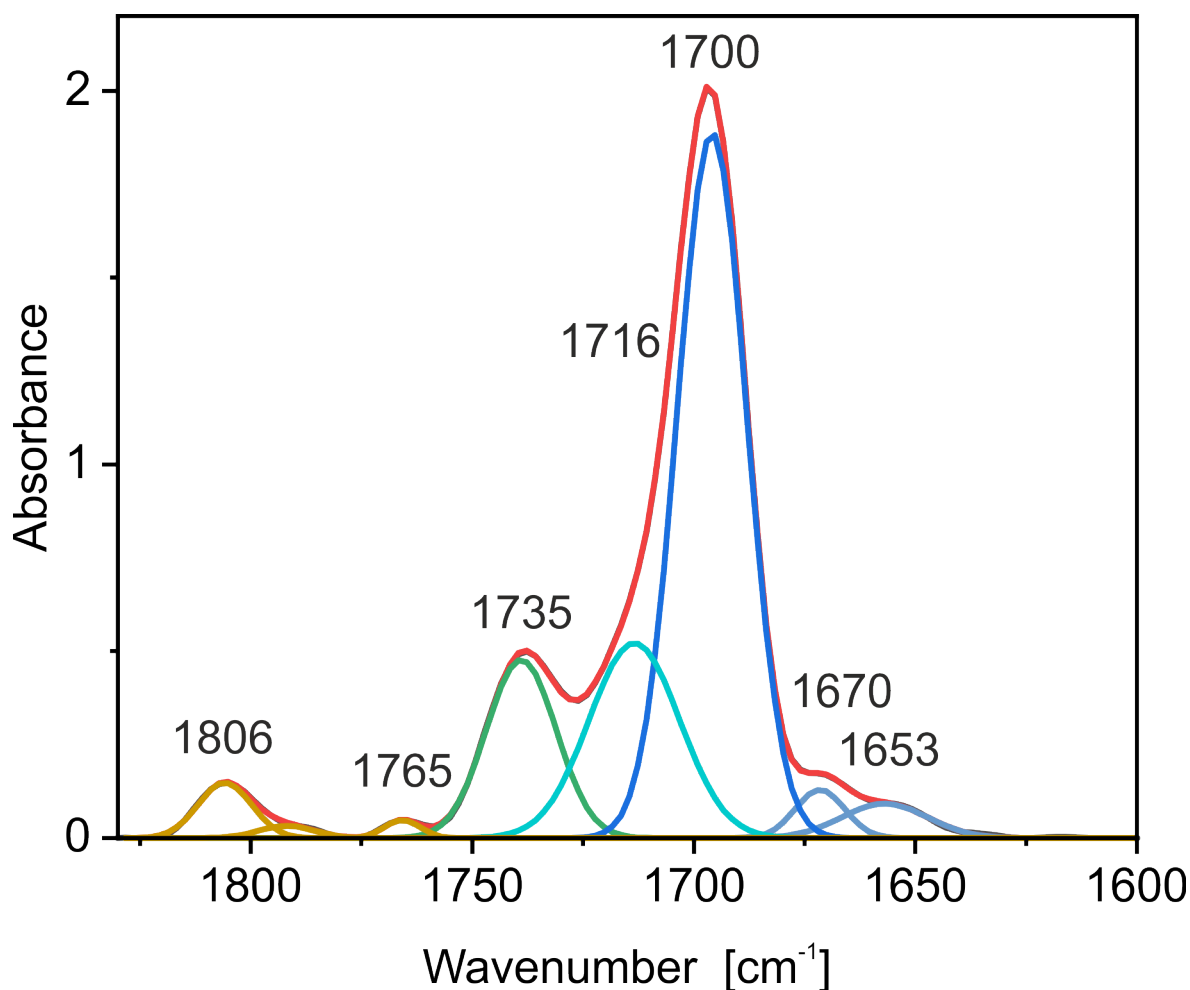


Figure 10.8: IR spectrum of PAA in the region of the C=O band. The spectrum was deconvoluted for better interpretation. The bands were attributed to distinct configurations of the C=O bond, according to Ref.<sup>[29]</sup>

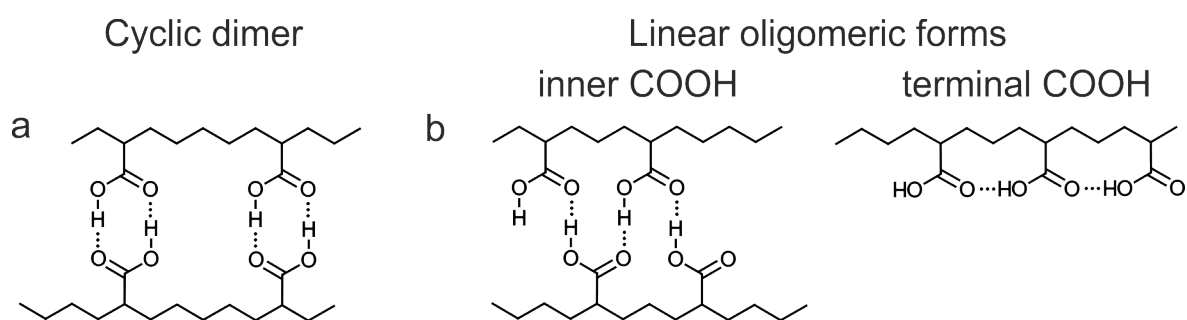


Figure 10.9: Forms of hydrogen bonding in PAA.<sup>[29]</sup>

derives from the C=O stretching of the amide carbonyl group, the amide II band consists of N-H bending and C-N stretching. Therefore, the amide II band is not relevant for the H-bond analysis, which is focused on the carbonyl bands. Stretching vibrations of free carbonyl groups from the carboxylic acid appear at  $1735\text{ cm}^{-1}$ . The peak at  $1675\text{ cm}^{-1}$  is attributed to the carboxylic acid dimer as this is a wavenumber comparable to the other samples. The band at  $1650\text{ cm}^{-1}$  is ascribed to the inner

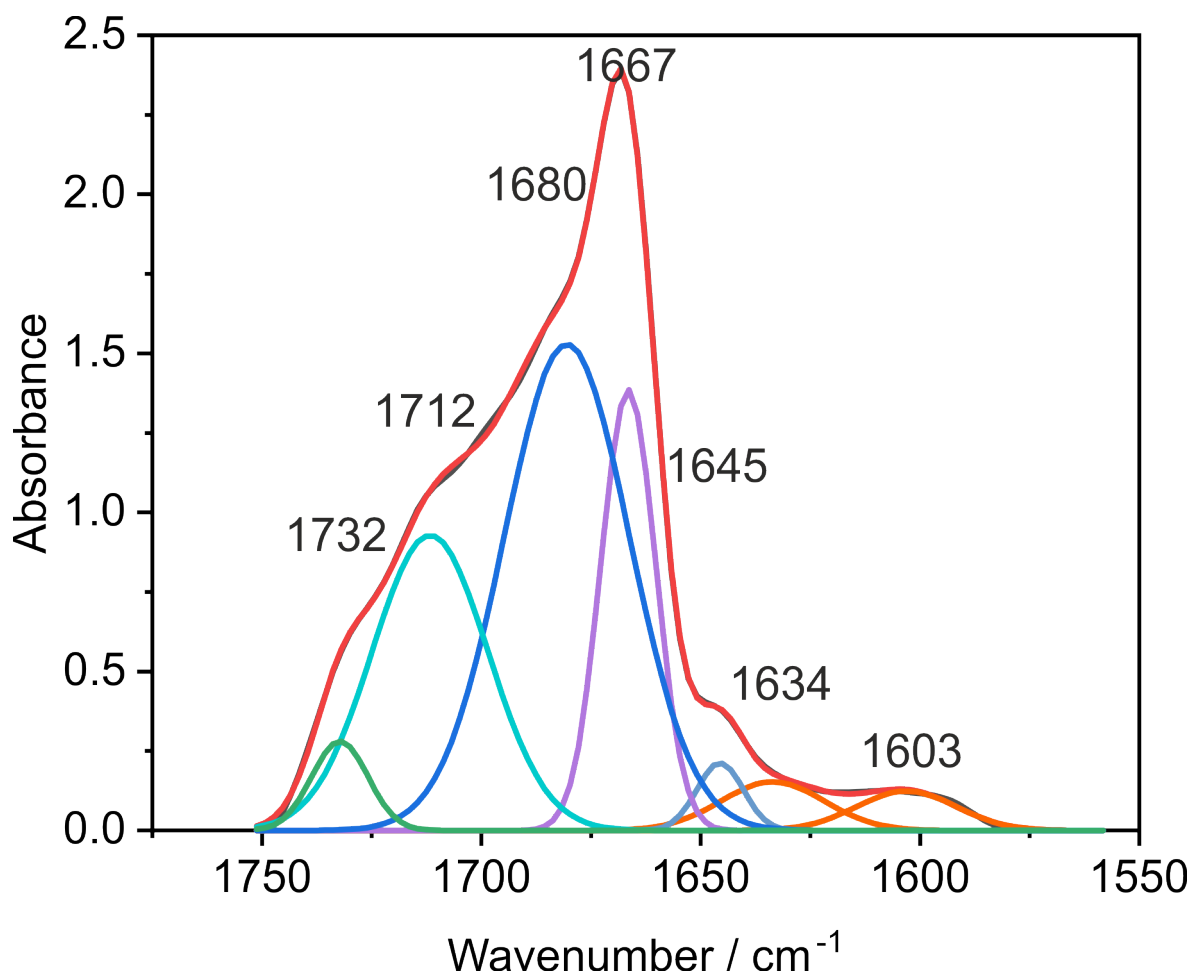


Figure 10.10: Deconvoluted IR spectrum of the dry PDha sample in the region of the C=O stretching vibration.

H-bonds of the COOH group. Additional H-bonds to the single OH group could be a reason for the exceptional strength of this band. The two bands at  $1618\text{ cm}^{-1}$  and  $1598\text{ cm}^{-1}$  belong to different conformations of H-bonds but are not easily distinguishable.

### PImAA

In the literature, it has been described that mixing PAA with poly(vinyl imidazole) (PVI) leads to a decrease of the carbonyl band of the PAA at  $1716\text{ cm}^{-1}$  and to a new peak at  $1547\text{ cm}^{-1}$ . The new peak is explained by the exchange of the proton from the carboxylic acid group to the imidazole group. Hence, the new peak is ascribed to the asymmetric stretching vibration of  $\text{COO}^-$ .<sup>[40]</sup>

In comparison, the PImAA film shows a strong carbonyl stretching peak at  $1625\text{ cm}^{-1}$ . The peak  $1578\text{ cm}^{-1}$  is ascribed to the C=C and C=N stretching in the aromatic ring. We do not attribute any of those peaks to the asymmetric stretching vibration of  $\text{COO}^-$ , because of the high wavenumber of the first and the missing of the symmet-

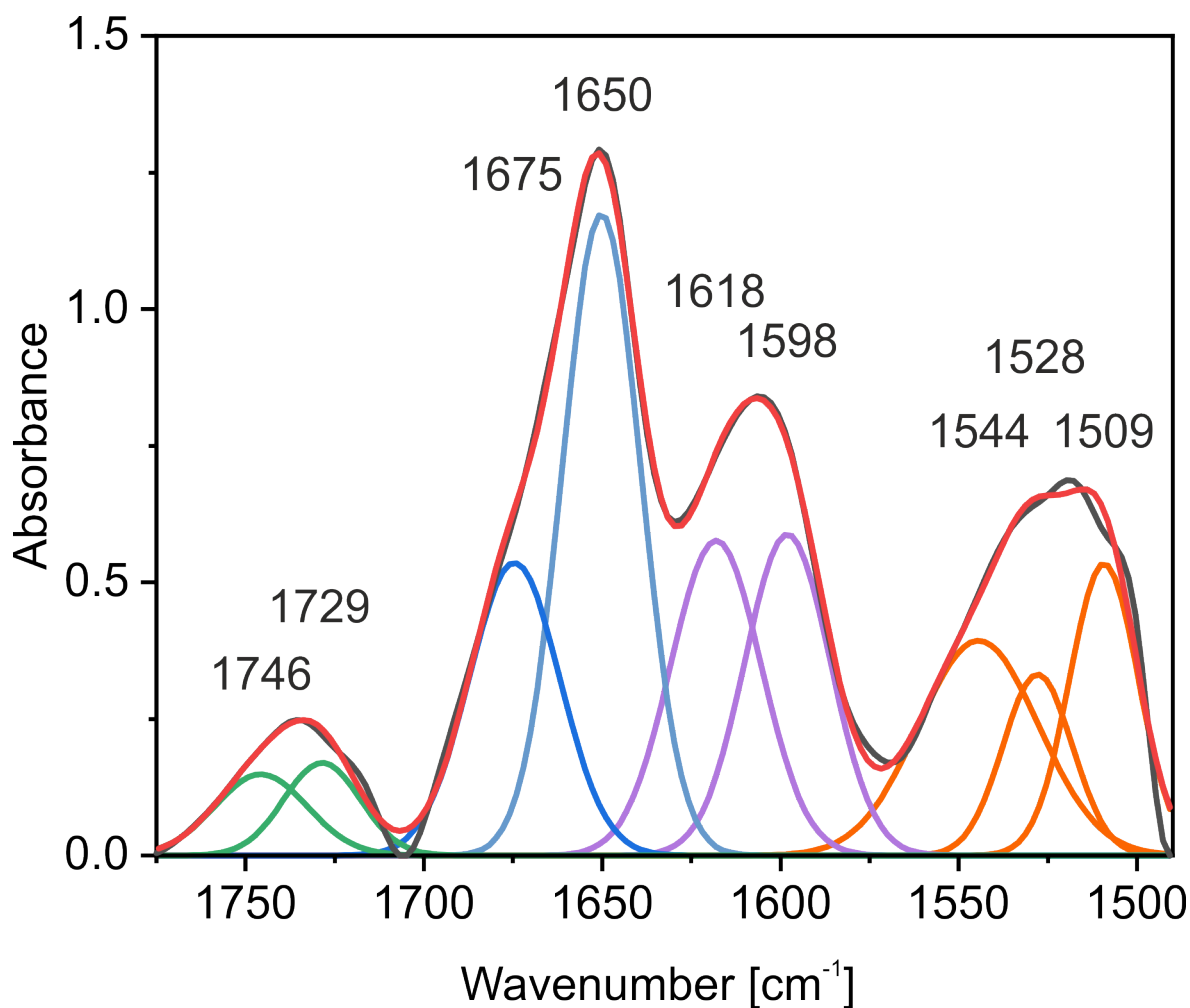


Figure 10.11: Deconvoluted IR spectrum of the dry PAGA sample in the region of the C=O stretching vibration.

ric stretching vibration around  $1330\text{ cm}^{-1}$ . Nevertheless, the low frequency of the C=O peak is an incident for a strong interaction between the carboxylic acid and the imidazole groups. This band, in turn, is relatively broad, which indicates a variety of interactions with different coordinations and bond strengths. The two peaks with the highest wavenumbers at  $1770\text{ cm}^{-1}$  and  $1732\text{ cm}^{-1}$  are ascribed to anhydride bonds and free carbonyl groups, respectively. Both show a very weak intensity and are almost overlooked. Accordingly, most of the carbonyl groups participate in H-bond interactions. We distinguish the H-bonds in two categories. H-bonds between acid groups like in PAA ( $1680\text{ cm}^{-1}$ ,  $1664\text{ cm}^{-1}$ , and  $1647\text{ cm}^{-1}$ ) and H-bonds between the carboxylic acid and an imidazole group (“other H-bonds”,  $1625\text{ cm}^{-1}$  and  $1606\text{ cm}^{-1}$ ).

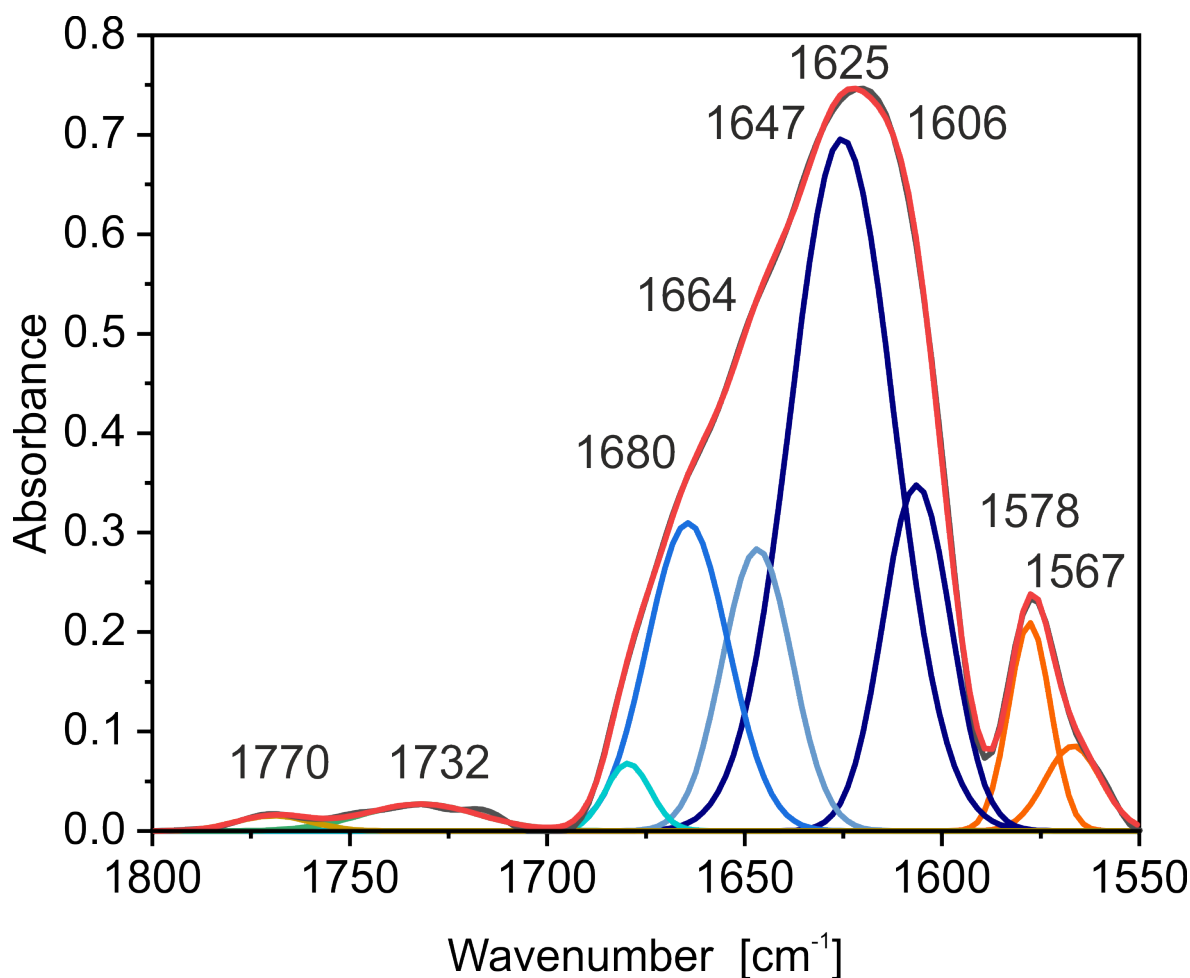


Figure 10.12: Deconvoluted IR spectrum of the dry PImAA sample in the region of the C=O stretching vibration.

### PMeImAA

In comparison to PImAA, PMeImAA has a methyl group attached to the imidazole ring, leading to a positive charge. Consequently, there is no free electron pair available at the nitrogen. The C=O band is again composed of different parts. At  $1770\text{ cm}^{-1}$  a relative strong anhydride band is detected. Whereas the vibration of free carbonyl at  $1733\text{ cm}^{-1}$  is only marginal. Also, the H-bonds between the carboxylic acid groups decreased in intensity. The very narrow peak at  $1629\text{ cm}^{-1}$  is ascribed to the interactions between carbonyl and imidazole ring. The narrow width of the peak indicates a relative uniform strength and conformation of the interactions. The bands at  $1579\text{ cm}^{-1}$  and  $1515\text{ cm}^{-1}$  are ascribed to the C=C and C=N stretching in the aromatic ring.

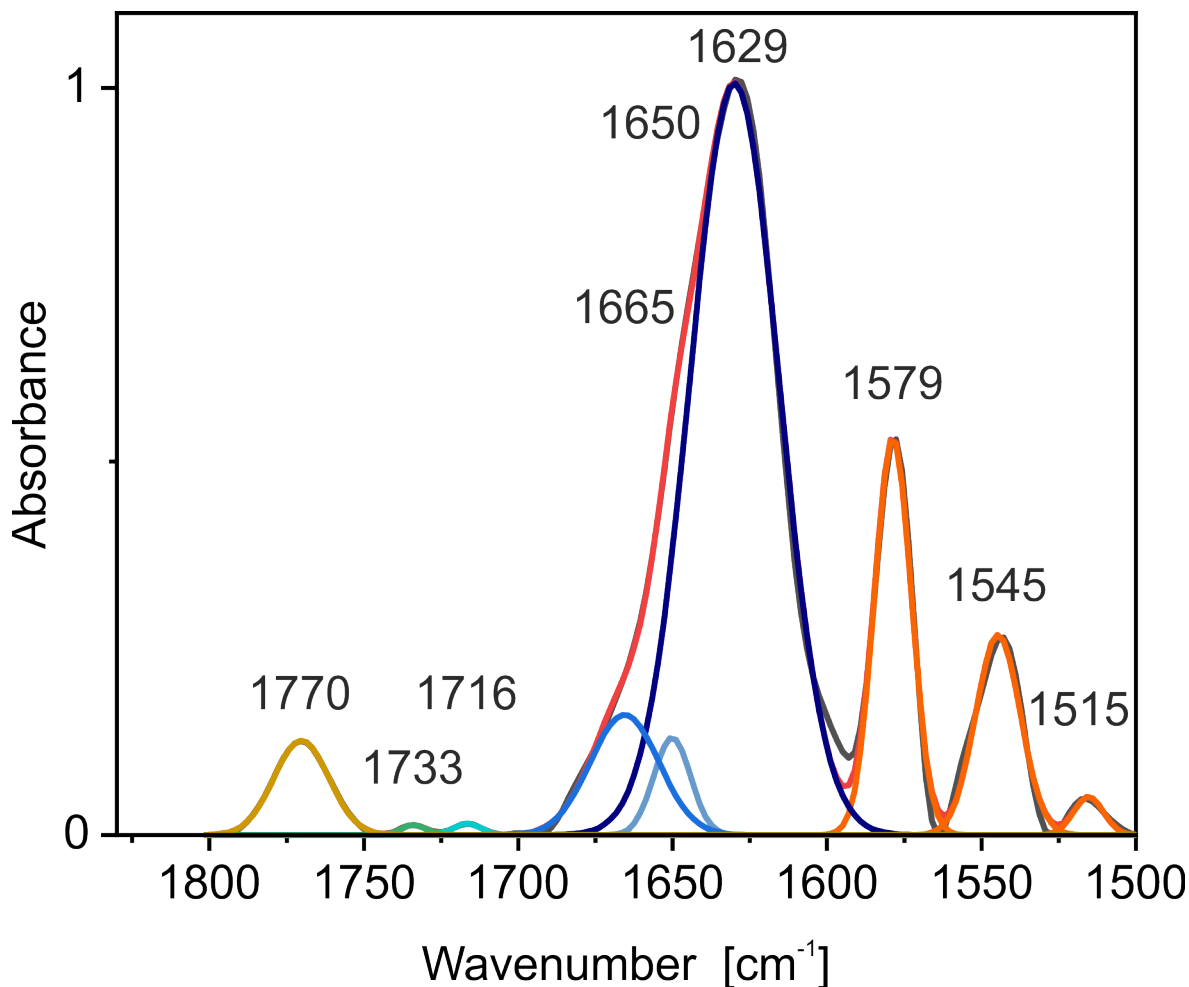


Figure 10.13: Deconvoluted IR spectrum of the dry PMeImAA sample in the region of the C=O stretching vibration.

### 10.5.3 Humidity dependent IR spectra

Figure 10.14 shows the humidity dependent IR analysis for PDha and PAGA analogous to the presentation in Figure 10.5 in the main manuscript. PDha shows a comparable behavior to PAA. The difference IR spectra show negative and positive contributions in the same wavenumber regions. However, the effects are less pronounced. This indicates a similar mechanism of water absorption in PAA and PDha. PAGA shows moderate water uptake for RH 40 % and RH 77 %. At RH 92 %, the moisture content strongly increases. This behavior is also observed in the IR spectrum, with a drastic increase of the OH stretching vibration at  $3500\text{ cm}^{-1}$ . The difference spectra in the carbonyl region show small deviations. The spectra for RH 40 % and RH 77 % show a slight decrease in H-bonds, whereas a small positive contribution is observed for the RH 92 % sample. The newly formed interactions probably also lead to a slight increase in thermal conductivity at RH 92 %.

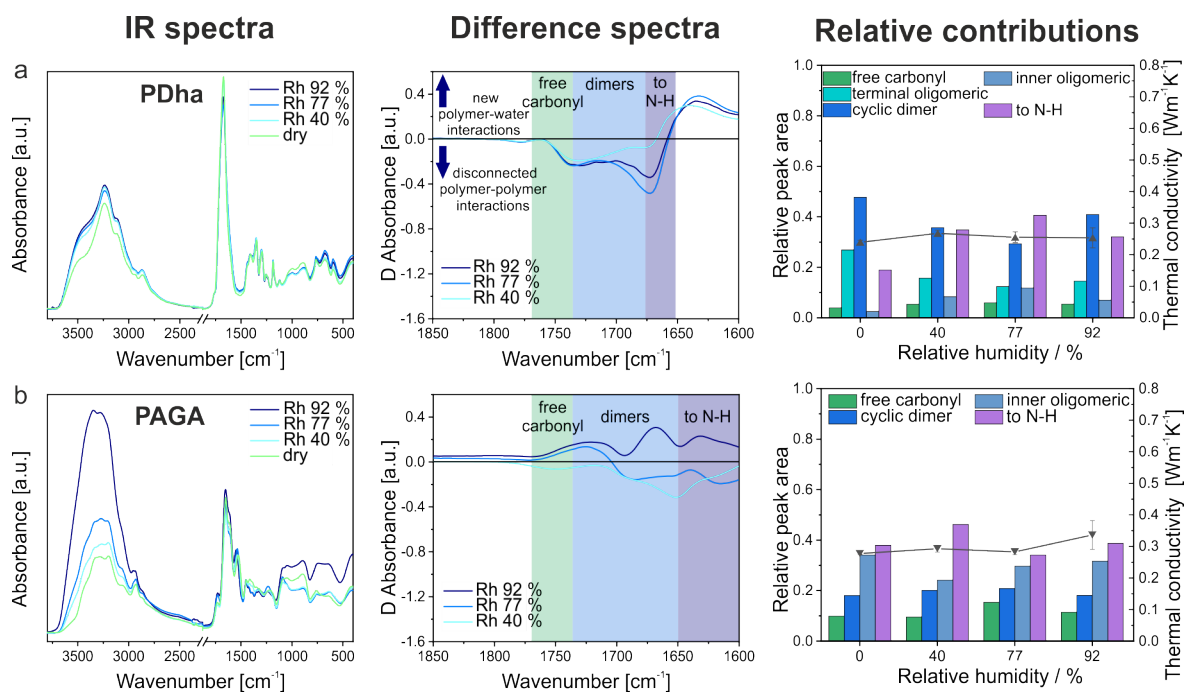


Figure 10.14: (a) PDha, and (b) PAGA. From left to right: IR-spectra of samples with various humidity exposure. Difference spectra in the region of the carbonyl stretching vibration. The relative peak area of different H-bond structures dependent on the relative humidity.

#### 10.5.4 DSC measurements

Besides the MDSC measurements, to determine the  $c_p$  of all samples, we performed DSC measurements of the dry samples in the range between  $-40$  °C and  $140$  °C. Figure 10.14 shows direct DSC measurements with a heat rate of  $10$  K min<sup>-1</sup>. The absence of melting peaks demonstrates the amorphous nature of all samples.

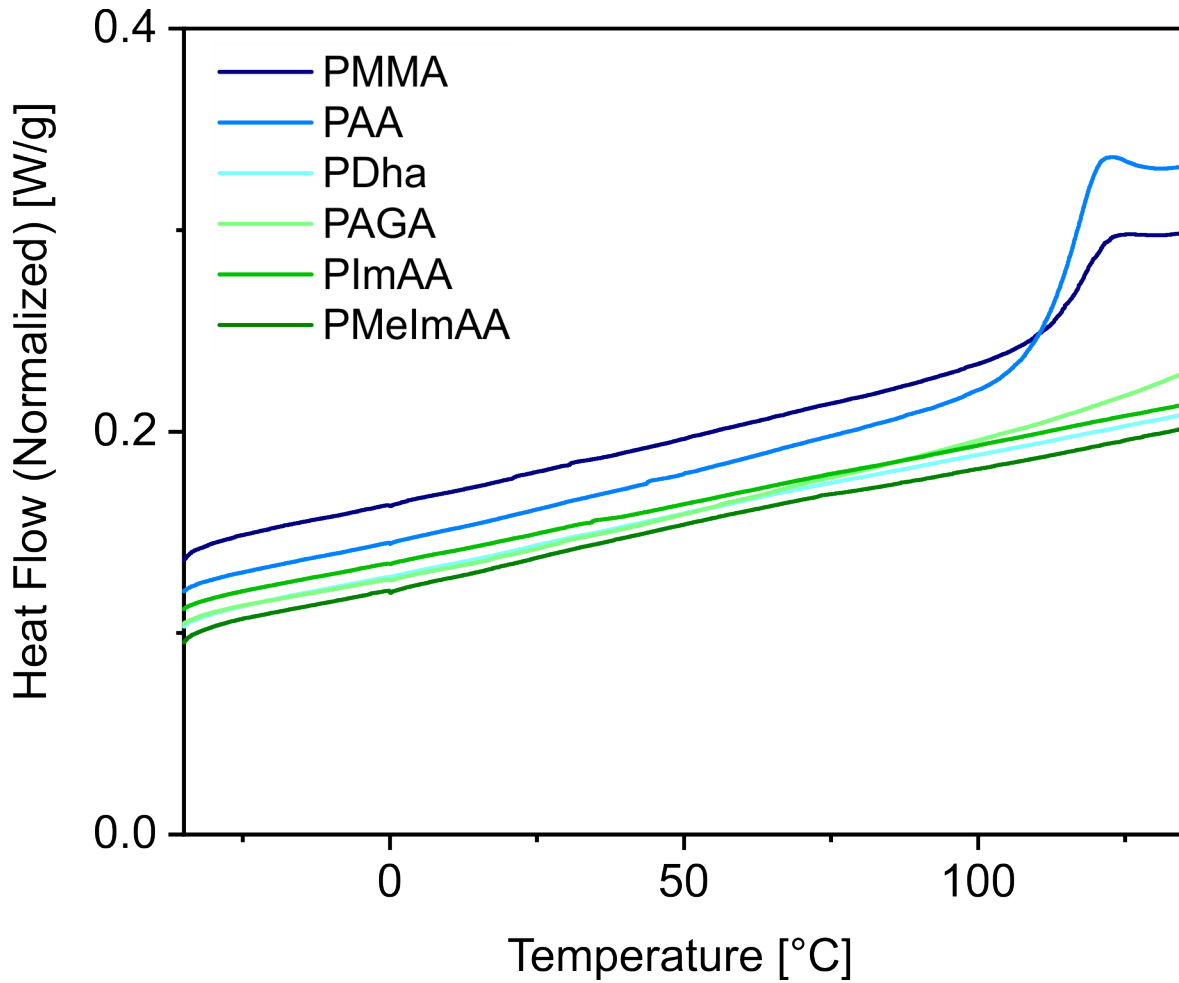


Figure 10.15: DSC measurements of dry polymer samples. The experiments were performed in the range from -40 °C to 140 °C with a heating rate of 10 K/min under nitrogen atmosphere.

### 10.5.5 Polymer / water effective medium model (EMT)

The following equations were used to calculate the values for the parallel mixing model and the effective medium model, according to Carson et al.<sup>[41]</sup>

Parallel mixing model:

$$k_{parallel} = (1 - x_2)k_1 + x_2k_2 \quad (10.1)$$

Effective medium model:

$$k_{EMT} = \frac{1}{4} \left( (3x_2 - 1)k_2 + [3(1 - x_2) - 1]k_1 + \sqrt{[(3x_2 - 1)k_2 + (3(1 - x_2) - 1)k_1]^2 + 8k_1k_2} \right) \quad (10.2)$$

With  $x_{1,2}$  and  $k_{1,2}$ , the volume ratio, and the thermal conductivity of components 1 and 2, respectively.

### 10.5.6 Transducer layer

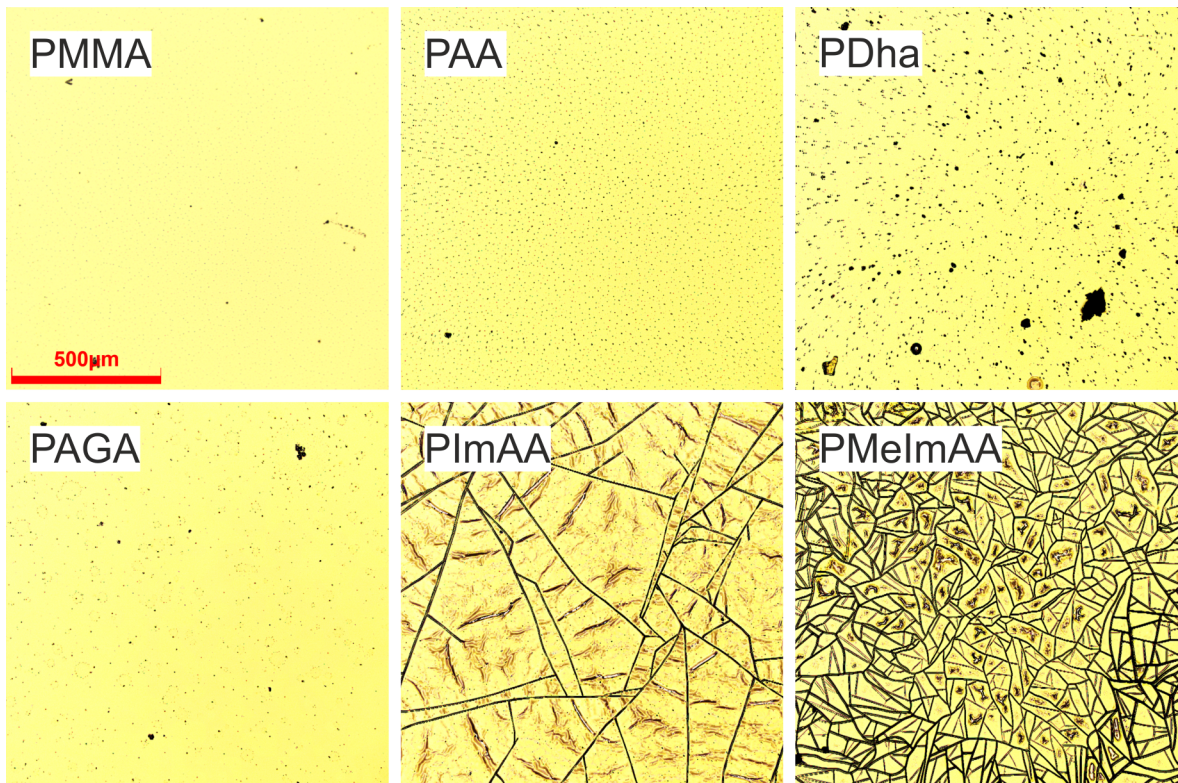


Figure 10.16: Optical microscopy of the surface of the Au transducer layer after measuring at humid conditions. Dark speckles and cracks indicate imperfections in the Au transducer layer, which facilitates equilibration to environmental conditions.

## References

- [1] A. L. Moore, L. Shi, *Materials Today* **2014**, *17*, 163–174.
- [2] X. J. Wang, V. Ho, R. A. Segalman, D. G. Cahill, *Macromolecules* **2013**, *46*, 4937–4943.
- [3] S. Shen, A. Henry, J. Tong, R. Zheng, G. Chen, *Nat. Nanotechnol.* **2010**, *5*, 251–255.
- [4] Z. Zhong, M. C. Wingert, J. Strzalka, H.-H. Wang, T. Sun, J. Wang, R. Chen, Z. Jiang, *Nanoscale* **2014**, *6*, 8283–8291.
- [5] V. Singh, T. L. Bougher, A. Weathers, Y. Cai, K. Bi, M. T. Pettes, S. A. McMenamin, W. Lv, D. P. Resler, T. R. Gattuso, D. H. Altman, K. H. Sandhage, L. Shi, A. Henry, B. A. Cola, *Nat Nanotechnol* **2014**, *9*, 384–90.
- [6] A. Henry, G. Chen, *Physical Review Letters* **2008**, *101*, 235502.
- [7] J. Liu, R. Yang, *Physical Review B* **2012**, *86*, 104307.
- [8] T. Zhang, T. Luo, *The Journal of Physical Chemistry B* **2016**, *120*, 803–812.
- [9] Y. Lu, J. Liu, X. Xie, D. G. Cahill, *Acs Macro Letters* **2016**, *5*, 646–650.
- [10] C. Huang, X. Qian, R. Yang, *Materials Science and Engineering: R: Reports* **2018**, *132*, 1–22.
- [11] H. S. Kim, J.-u. Jang, H. Lee, S. Y. Kim, S. H. Kim, J. Kim, Y. C. Jung, B. J. Yang, *Advanced Engineering Materials* **2018**, *20*, 1800204.
- [12] N. Song, D. Jiao, S. Cui, X. Hou, P. Ding, L. Shi, *ACS Appl. Mater. Interfaces* **2017**, *9*, 2924–2932.
- [13] Z. Wang, K. Rolle, T. Schilling, P. Hummel, A. Philipp, B. A. F. Kopera, A. M. Lechner, M. Retsch, J. Breu, G. Fytas, *Angew Chem Int Ed Engl* **2020**, *59*, 1286–1294.
- [14] X. Xie, D. Y. Li, T. H. Tsai, J. Liu, P. V. Braun, D. G. Cahill, *Macromolecules* **2016**, *49*, 972–978.
- [15] G. H. Kim, D. Lee, A. Shanker, L. Shao, M. S. Kwon, D. Gidley, J. Kim, K. P. Pipe, *Nat Mater* **2015**, *14*, 295–300.
- [16] C. Rössel, M. Billing, H. Görls, G. Festag, M. Grube, P. Bellstedt, I. Nischang, F. H. Schacher, *Polymer* **2017**, *127*, 182–191.
- [17] U. Günther, L. V. Sigolaeva, D. V. Pergushov, F. H. Schacher, *Macromolecular Chemistry and Physics* **2013**, *214*, 2202–2212.
- [18] M. von der Lühe, A. Weidner, S. Dutz, F. H. Schacher, *ACS Applied Nano Materials* **2018**, *1*, 232–244.

- [19] Y. Sidot, C. Christidis, Amides  $\alpha,\beta$ -ethyleniques N-alcoylolees et leur procede de fabrication, Patent, **1964**.
- [20] L. Volkmann, M. Köhler, F. H. Sobotta, M. T. Enke, J. C. Brendel, F. H. Schacher, *Macromolecules* **2018**, *51*, 7284–7294.
- [21] R. T. A. Mayadunne, E. Rizzardo, J. Chiefari, J. Krstina, G. Moad, A. Postma, S. H. Thang, *Macromolecules* **2000**, *33*, 243–245.
- [22] P. W. Winston, D. H. Bates, *Ecology* **1960**, *41*, 232–237.
- [23] H. P. Hu, X. W. Wang, X. F. Xu, *Journal of Applied Physics* **1999**, *86*, 3953–3958.
- [24] X. Wang, H. Hu, X. Xu, *Journal of Heat Transfer* **2001**, *123*, 138–144.
- [25] Y. Park, S. Lee, S. S. Ha, B. Alunda, D. Y. Noh, Y. J. Lee, S. Kim, J. H. Seol, *Polymers* **2019**, *11*, 858.
- [26] J. K. Kauppinen, D. J. Moffatt, H. H. Mantsch, D. G. Cameron, *Applied Spectroscopy* **1981**, *35*, 271–276.
- [27] X. Hu, D. Kaplan, P. Cebe, *Macromolecules* **2006**, *39*, 6161–6170.
- [28] L. C. Thomas, Modulated DSC Basics; Optimization of MDSC Experimental Conditions, Electronic Article, **2005**.
- [29] J. Dong, Y. Ozaki, K. Nakashima, *Macromolecules* **1997**, *30*, 1111–1117.
- [30] M. M. Coleman, M. Sobkowiak, G. J. Pehlert, P. C. Painter, T. Iqbal, *Macromolecular Chemistry and Physics* **1997**, *198*, 117–136.
- [31] D. J. Skrovanek, S. E. Howe, P. C. Painter, M. M. Coleman, *Macromolecules* **1985**, *18*, 1676–1683.
- [32] D. J. Skrovanek, P. C. Painter, M. M. Coleman, *Macromolecules* **1986**, *19*, 699–705.
- [33] Z. Shen, F. Luo, H. Bai, P. Si, X. Lei, S. Ding, L. Ji, *RSC Advances* **2016**, *6*, 17510–17518.
- [34] A. Shanker, C. Li, G.-H. Kim, D. Gidley, K. P. Pipe, J. Kim, *Science Advances* **2017**, *3*, e1700342.
- [35] X. Xie, K. Yang, D. Li, T.-H. Tsai, J. Shin, P. V. Braun, D. G. Cahill, *Physical Review B* **2017**, *95*, 035406.
- [36] L. Daniliuc, C. David, *Polymer* **1996**, *37*, 5219–5227.
- [37] S. Popineau, C. Rondeau-Mouro, C. Sulpice-Gaillet, M. E. R. Shanahan, *Polymer* **2005**, *46*, 10733–10740.
- [38] K. Ichikawa, T. Mori, H. Kitano, M. Fukuda, A. Mochizuki, M. Tanaka, *Journal of Polymer Science Part B: Polymer Physics* **2001**, *39*, 2175–2182.

- [39] N. Mehra, L. Mu, T. Ji, Y. Li, J. Zhu, *Composites Science and Technology* **2017**, *151*, 115–123.
- [40] A. Arslan, S. Kiralp, L. Toppare, A. Bozkurt, *Langmuir* **2006**, *22*, 2912–2915.
- [41] J. K. Carson, S. J. Lovatt, D. J. Tanner, A. C. Cleland, *International Journal of Heat and Mass Transfer* **2005**, *48*, 2150–2158.

## 11 Conclusion and Outlook

In conclusion, this thesis elaborated on thermal transport in polymers and polymeric hybrid materials. The work focused on materials with particular functionality and exceptional structural control to investigate fundamental parameters in thermal transport. However, these materials are limited to small sample geometries. Therefore, a technique to characterize the thermal conductivity of small sample amounts and geometries was necessary. The herein developed and implemented photoacoustic (PA) method can determine the cross-plane thermal conductivity of thin films on substrates. Further advantages of this method are the simple setup, and the handling of a diversity of samples (e.g., electrical conductive samples and low restrictions regarding surface roughness).

However, in thin samples the thermal conductivity cannot be fitted directly. Rather, an effective thermal conductivity is determined by fitting the total layer resistance of the multilayer sample. Here, the contact resistances between the different layers could play a role. The accuracy could be optimized regarding the interplay of sample thickness, frequency range, and contact resistance. Moreover, the addition of a heat stage would allow temperature dependent measurements, that would make the PA method even more powerful.

In the following, the implementation of the PA set-up allowed studying the thermal conductivity in materials with a structural control down to the molecular level. The first material was made of Ag NPs functionalized by a polystyrene (PS) brush. The interparticle distance (IPD) could be adjusted from 2 nm to 16 nm by choosing different molecular weights of the ligands. Thermal conductivity studies showed the influence of the phonon scattering at the interfaces induced by the nanoparticles (NPs). The versatility of the presented ligand exchange method allows studying an almost endless combination of materials. By this, the influence of the surface chemistry at the interface between ligand and particle could be targeted in future research studies.

The second material class investigated in this work is characterized by its anisotropic sheet structure. This anisotropy was also observed in the thermal conductivity of the layered samples of graphene oxide (GO) and the synthetic clay sodium fluorohectorite. In the next step, an organic-inorganic hybrid material was prepared from synthetic clay and polyvinylpyrrolidone (PVP). The implementation of hard-soft interfaces further increased the thermal conductivity anisotropy ratio. Due to the extremely low cross-plane thermal conductivity for a solid material of around  $0.09 \text{ W m}^{-1} \text{ K}^{-1}$ , and an anisotropy ratio of 38, this material is a promising candidate for thermal management applications. In future studies, the surface chemistry

between the polymer and the clay could be addressed. Furthermore, the strict periodicity of the basal spacing could be varied. Different heights of the polymer phase between the clay platelets could lead to a deliberate disorder in the stacks, and further decrease the cross-plane thermal conductivity.

The last topic of this thesis demonstrated that heat transport could be influenced by interactions between functional groups. Four ampholytic polymers with various functional groups were investigated. The thermal conductivity correlated with the hydrogen bond (H-bond) strength, determined by IR spectroscopy. In humidity dependent measurements, a composite like behavior was observed.

Overall, the work gave fascinating insights into the thermal transport in nanostructured materials. The impact of the enormous number of interfaces and the surface chemistry were demonstrated. Future studies could be linked to the presented results for a better understanding of thermal transport in nanostructured materials.

## Danksagung

Ich möchte diesen Abschnitt dazu nutzen, um mich bei allen zu bedanken, die mich auf dem Weg dieser Arbeit begleitet haben.

Als erstes gilt mein Dank natürlich meinem Doktorvater Prof. Dr. Markus Retsch. Ich möchte mich für die Möglichkeit bedanken, die Promotion in seiner Arbeitsgruppe durchzuführen. Er gab mir während meiner Promotion nicht nur den nötigen Freiraum, sondern war auch jederzeit für Fragen erreichbar und bot mir immer die bestmögliche Unterstützung.

Selbstverständlich bedanke ich mich auch bei allen Kooperationspartnern, die an Publikationen in dieser Arbeit mitgewirkt haben und dementsprechend auch einen maßgeblichen Anteil zu dieser Arbeit geleistet haben. Ich möchte mich aber auch bei all denen bedanken, die ohne eine Autorenschaft Teil meiner Arbeit waren. Ob es nun eine Einweisung, Messungen oder Diskussionen waren. Diese Zusammenarbeiten, ohne messbaren Wert, sehe ich als wichtigste Grundvoraussetzung für effektive Forschung. Nicht nur innerhalb der Arbeitsgruppe hat dies hervorragend funktioniert, auch lehrstuhlübergreifend an der ganzen Uni Bayreuth.

Ebenso möchte ich mich bei allen Kollegen am Lehrstuhl für Physikalische Chemie bedanken. Ihr habt die Promotion für mich zu einer besonderen Zeit gemacht. Ob bei Grillabenden, Kickerturnieren oder einfach nur Kaffeepausen. Hervorheben möchte ich an dieser Stelle Pia, Fabi, Astrid, Kristina, Alex, Kirsten, Felix, Arne, Bernd, Anna, Tanja und jeden Freitag Thomas, meine besonderen Laborfreunde Christian und Tobi, meinen 12. besten Freund Andi und Captain Kai.

Mein allergrößter Dank geht natürlich an meine Familie und meine Frau Miriam die mich immer unterstützt haben.

Vielen Dank.



## Eidesstattliche Versicherungen und Erklärungen

§8 Satz 2 Nr. 3 PromO BayNAT

Hiermit versichere ich eidesstattlich, dass ich die Arbeit selbstständig verfasst und keine anderen als die von mir angegebenen Quellen und Hilfsmittel benutzt habe (vgl. Art. 64 Abs 1 Satz 6 BayHSchG).

§8 Satz 2 Nr. 3 PromO BayNAT

Hiermit erkläre ich, dass ich die Dissertation nicht bereits zur Erlangung eines akademischen Grades eingereicht habe und dass ich nicht bereits diese oder eine gleichartige Doktorprüfung endgültig nicht bestanden habe.

§8 Satz 2 Nr. 4 PromO BayNAT

Hiermit erkläre ich, dass ich Hilfe von gewerblichen Promotionsberatern bzw. -vermittlern oder ähnlichen Dienstleistern weder bisher in Anspruch genommen habe noch künftig in Anspruch nehmen werde.

§8 Satz 2 Nr. 7 PromO BayNAT

Hiermit erkläre ich mein Einverständnis, dass die elektronische Fassung meiner Dissertation unter Wahrung meiner Urheberrechte und des Datenschutzes einer gesonderten Überprüfung unterzogen werden kann.

§8 Satz 2 Nr. 8 PromO BayNAT

Hiermit erkläre ich mein Einverständnis, dass bei Verdacht wissenschaftlichen Fehlverhaltens Ermittlungen durch universitätsinterne Organe der wissenschaftlichen Selbstkontrolle stattfinden können.

Bayreuth, den \_\_\_\_\_

\_\_\_\_\_

Patrick Hummel